UNIVERSITAT POLITÈCNICA DE CATALUNYA BARCELONATECH

Development of new algorithms for depth of anesthesia monitoring integrating cerebral blood flow estimations

Carmen González Pijuan

Thesis for Doctoral Degree (Ph.D.)
2019

Doctoral Program in Biomedical Engineering

Development of new algorithms for depth of anesthesia monitoring integrating cerebral blood flow estimations

Carmen González Pijuan

Dissertation Supervisors:

Dr. Erik Weber Jensen**,** Quantium Medical
Dr. Montserrat Vallverdú Ferrer**,** Universitat Politècnica de Catalunya

Barcelona, Spain, July 2019

UNIVERSITAT POLITÈCNICA DE CATALUNYA
BARCELONATECH
Departament d'Enginyeria de Sistemes,
Automàtica i Informàtica Industrial

Universitat Politècnica de Catalunya · Barcelona**TECH**

Department of Automatic Control (ESAII)
Research Center for Biomedical Engineering (CREB)
Bioinformatics and Biomedical Signals Laboratory (B2SLab)
CIBER in Bioengineering, Biomaterials and Nanomedicine (CIBER-BBN)

Quantium Medical · **Fresenius Kabi** group

Development of new algorithms for depth of anesthesia monitoring integrating cerebral blood flow estimations

Doctoral Program in Biomedical Engineering

Dissertation Supervisors

Dr. Erik Weber Jensen**,** Quantium Medical
Dr. Montserrat Vallverdú Ferrer**,** Universitat Politècnica de Catalunya

This thesis was supported by the Industrial PhD Program DI-2015/033 (Secretaria d'Universitats i Recerca del Departament d'Economia i Coneixement, Generalitat de Catalunya, Spain), Quantium Medical SLU (Spain), Universitat Politècnica de Catalunya (UPC, Spain) and the European Social Fund of the European Union. CIBER of Bioengineering, Biomaterials and Nanomedicine is an initiative of ISCIII.

A mi madre

Acknowledgement

I would like to dedicate this Thesis to my mother. We did not have the opportunity to share these years, but you are part of this Thesis. For all I learnt from you and with you, personally and professionally, for all those unforgettable moments that I keep as my most valuable treasure, thank you.

This Doctoral Thesis is the result of several years of research and cooperation between different research teams. With these words, I would like to acknowledge the work, support and advise I received from all those who have collaborated with this project.

First of all, I would like to thank my supervisors, Dr.Montserrat Vallverdú and Dr.Erik Weber Jensen, for their guidance and support during these years, and for presenting me with the opportunity to participate in such a challenging project, combining two different approaches that have enriched this experience.

I am also grateful to each institution involved in this project: the Regional Government of Catalonia (through the Industrial PhD program), the Universitat Politècnica de Catalunya (UPC), Quantium Medical (QM) and the Fresenius Kabi Group.

Besides the two institutions leading this industrial PhD program, UPC and QM, the close cooperation with Hospital CLÍNIC de Barcelona was key in the development of this research project. I would like to thank all the staff in the CMA operating rooms for their involvement, specially Dr. Pedro Gambús, for more than 10 years of cooperation with countless challenges and clinical advice.

Thanks to Pedro Amorim and Sérgio Vide for sharing their ideas and dedicate their time to endless discussions on cerebral blood flow and hemodynamics during anesthesia. I also like to thank Jeremy Wheeler for his valuable insights throughout the development of this work.

I would also like to acknowledge the support and help of all my colleagues in Quantium Medical who have accompanied me during these years. Jesús Escrivá, for all the conversations and shared experiences during our research projects. Claus Lindner, for all the advice and the valuable discussions on cerebral blood flow we had. Manuel Villegas, Patricia Capsi and Anaïs Espinoso, for being part of the research team. George Forrest, Beatriz Sanaú, Umberto Melia, Miguel Rueda, Marina Zamora and, especially Sandra Cortés, whose encouragement, either professional or personal, was fundamental.

I am grateful to my parents for their continuous support, their dedication, their advice and for the constant efforts they undertook to provide me with all the tools I needed to chase up my dreams - a true proof of unselfish love.

I am grateful to my sister Irene, who has always encouraged me to engage in this project and to finish it. And to my nieces Helena and Berta, who in the most stressful periods of these last years, without even being conscious of it, helped me carrying on.

To the rest of my family and friends, thank you very much.

And last, but not least, to Rui. For his comprehension, for his support, for being always there.

To all of you, my deepest gratitude.

Abstract

Cerebral blood flow (CBF) reflects the rate of delivery of arterial blood to the brain. Since no nutrients, oxygen or water can be stored in the cranial cavity due to space and pressure restrictions, a continuous perfusion of the brain is critical for survival. Anesthetic procedures are known to affect cerebral hemodynamics, but CBF is only monitored in critical patients due, among others, to the lack of a continuous and affordable bedside monitor for this purpose.

This Doctoral Thesis proposes a potential solution through bioelectrical impedance technology, also known as rheoencephalography (REG), that could fill the existing gap for a low-cost and effective CBF monitoring tool. The underlying hypothesis is that REG signals carry information on CBF that might be recovered by means of the application of advanced signal processing techniques, allowing to track CBF alterations during anesthetic procedures.

In the first place, a thorough literature review is presented, providing the relevant clinical and technical information related to other CBF monitoring techniques and potential signal processing algorithms suitable to be applied to REG signals. Subsequently, clinical data collected under the scope of this project and used to develop and validate the techniques applied to REG signals are described.

As a first step in the analysis of REG signals, different filter options for noise removal are presented, in the linear and nonlinear domain. The performance of a nonlinear filter applied to the signal attractor demonstrated a better accuracy in recovering useful information from REG signals, especially in very noise environments. Nonetheless, its computational burden compromises its use in real time monitoring of physiological signals.

The analysis of REG signals starts with the use of geometric features extracted from the time domain, since this is the standard processing strategy for this type of physiological data. Geometric features are tested for their ability to detect apneas in young healthy volunteers and to distinguish between different anesthetic depths. Their performance is poor in apnea detection, but those features are capable of tracking cerebral hemodynamic changes during anesthesia.

A new approach is proposed, based on the assessment of nonlinear dynamics of REG signals. The descriptors of the attractors reconstructed form REG signals show significant differences between apnea and baseline recordings, as well as between different anesthetic states. This is a key finding, providing an alternative to standard processing of REG signals.

A third analysis technique is presented, using entropy metrics to characterize cerebral impedance signals. Those metrics are also capable of detecting apneas and differences among anesthetic states, providing an extra tool for REG analysis, even though their elevated computational times are not suitable for real time applications.

The results of the analysis of geometric features, Poincaré plot descriptors and entropy rates suggest that REG signals do carry CBF information. Among those features, those allowing real time data processing are used to classify REG recordings collected in awake and anesthetized patients. Their statistical diagnosisAn accuracy of 70% is reached, indicating that CBF changes in REG are related to the anesthetic state of the patient but presenting large variabilities.

Nonetheless, REG parameters should not aim at replacing depth of anesthesia monitoring but should rather help maintaining cerebral hemodynamic stability during anesthetic procedures. For that purpose, the relationship between global hemodynamics, cerebral hemodynamics and EEG based parameters are analyzed, looking for causal relationships among them. Interactions are detected during anesthetic drug infusion and patient positioning, providing evidence of the coupling between hemodynamics and brain activity.

As a conclusion, this Doctoral Thesis provides alternative methods for REG signal processing that confirm the hypothesis that REG signals carry information on CBF. The simplicity of the technology, together with its low cost and easily interpretable outcomes, should provide a new opportunity for REG to reach standard clinical practice. Moreover, causal relationships among the hemodynamic physiological signals and brain activity are assessed, suggesting that the inclusion of REG information in depth of anesthesia

monitors could be of valuable use for an affordable, noninvasive bedside tool to prevent unwanted CBF alterations during anesthetic procedures.

UNESCO codes: 240602 (Bioelectricity), 331110 (Medical Instruments), 241103 (Cardiovascular Physiology).

Resum

El flux sanguini cerebral (FSC) reflexa la taxa de lliurament de sang arterial al cervell. Com que no es poden emmagatzemar nutrients, oxigen ni aigua a la cavitat cranial a causa de restriccions d'espai i pressió, una perfusió cerebral contínua és essencial per a la supervivència. És sabut que els procediments anestèsics afecten l'hemodinàmica cerebral, però el FSC només es controla en pacients crítics degut, entre d'altres, a la manca d'un aparell adient, de monitorització contínua, de capçalera i de cost assequible.

Aquesta Tesi Doctoral proposa una possible solució mitjançant la tecnologia d'impedància bioelèctrica, també coneguda com a rheoencefalografia (REG), que podria omplir el buit existent per a una eina de control de FSC de baix cost i eficaç. La hipòtesi subjacent és que els senyals REG porten informació sobre FSC que es podria recuperar mitjançant l'aplicació de tècniques avançades de processament de senyals, permetent fer un seguiment de les alteracions del FSC durant procediments anestèsics.

En primer lloc, es presenta una revisió exhaustiva de la literatura que proporciona informació clínica i tècnica rellevant relacionada amb altres tècniques de control de FSC i possibles algoritmes de processament de senyals adequats per aplicar-se a senyals REG. Posteriorment, es descriuen dades clíniques recollides en l'àmbit d'aquest projecte i que s'utilitzen per a desenvolupar i validar les tècniques aplicades als senyals REG.

Com a primer pas en l'anàlisi dels senyals REG es presenten diferents opcions de filtrat per a l'eliminació del soroll, en el domini lineal i no lineal. El filtre no lineal aplicat a l'atractor del senyal mostra una millor precisió a l'hora de recuperar informació útil dels senyals REG, especialment en entorns amb

molt de soroll. No obstant això, la seva càrrega computacional compromet el seu ús en monitoratge de senyals fisiològics en temps real.

L'anàlisi de senyals REG s'inicia amb l'ús de característiques geomètriques extretes del domini temporal, ja que aquesta és l'estratègia de processament estàndard d'aquest tipus de dades fisiològiques. S'avalua la capacitat de les característiques geomètriques dels senyals REG per detectar apnees en joves voluntaris sans i per distingir diferents profunditats anestèsiques. El seu rendiment és deficient en la detecció de l'apnea, però aquestes característiques poden fer un seguiment dels canvis hemodinàmics cerebrals durant l'anestèsia.

Es proposa també un nou enfocament basat en l'avaluació de la dinàmica no lineal dels senyals REG. Els descriptors de la reconstrucció de l'atractor dels senyals REG mostren diferències significatives entre l'apnea i els valors basals, així com entre diferents estats anestèsics. Es tracta d'una troballa clau que proporciona una alternativa al processament estàndard de senyals REG.

Es presenta una tercera tècnica d'anàlisi mitjançant mesures d'entropia per caracteritzar els senyals d'impedància cerebral. Aquestes mètriques també són capaces de detectar apnees i diferències entre els estats anestèsics, proporcionant una eina addicional per a l'anàlisi de REG, tot i que la seva elevada complexitat computacional no és adequada per a aplicacions en temps real.

Els resultats de l'anàlisi de característiques geomètriques, els descriptors de Poincaré i les taxes d'entropia suggereixen que els senyals REG porten informació de FSC. Entre aquestes característiques s'utilitzen aquelles que permeten processar dades en temps real per classificar els enregistraments REG recollits en pacients desperts i anestesiats. S'aconsegueix una precisió del 70%, cosa que indica que els canvis de FSC en REG estan relacionats amb l'estat anestèsic del pacient però presenten gran variabilitat.

No obstant això, els paràmetres REG no tenen com a objectiu substituir la monitorització de la profunditat de l'anestèsia, sinó que haurien d'ajudar més aviat a mantenir l'estabilitat hemodinàmica cerebral durant els procediments anestèsics. Per a aquest motiu, s'analitzen les interaccions entre l'hemodinàmica global, l'hemodinàmica cerebral i els paràmetres basats en EEG, buscant relacions causals entre ells. Es detecten interaccions durant la infusió de medicaments anestèsics i en el posicionament del pacient, la qual cosa evidencia la interacció entre l'hemodinàmica i l'activitat cerebral.

A mode de conclusió, aquesta Tesi Doctoral proporciona mètodes alternatius per al processament dels registres de REG que confirmen la

hipòtesi que els senyals REG contenen informació sobre FSC. La senzillesa de la tecnologia, juntament amb el seu baix cost i resultats fàcilment interpretables, hauria de proporcionar una nova oportunitat per als senyals REG d'arribar a la pràctica clínica estàndard. A més, s'avaluen les relacions causals entre els senyals fisiològics hemodinàmics i l'activitat cerebral, amb resultats que suggereixen que la inclusió d'informació REG en monitors de profunditat anestèsica podria ser clau per a una eina no invasiva, i assequible, que evités alteracions del FSC no desitjades durant els procediments anestèsics.

Codis UNESCO: 240602 (Bioelectricitat), 331110 (Instruments mèdics), 241103 (Fisiologia cardiovascular).

Resumen

El flujo sanguíneo cerebral (FSC) refleja el suministro de sangre arterial al cerebro. Como no se pueden guardar nutrientes, oxígeno ni agua en la cavidad craneal debido a restricciones de espacio y presión, una circulación sanguínea continua es fundamental para la supervivencia. Los procedimientos anestésicos afectan la hemodinámica cerebral, pero el FSC sólo se monitoriza en pacientes críticos porque, entre otros motivos, no existen dispositivos de cabecera, con monitorización continua y a precios asequibles.

Esta Tesis Doctoral propone una posible solución a través de la tecnología de impedancia bioeléctrica, también conocida como rheoencefalografia (REG), que puede ocupar el vacío existente en la monitorización del FSC efectiva y de bajo coste. La hipótesis subyacente es que la señal REG transporta información de FSC que podría recuperarse mediante la aplicación de técnicas avanzadas de procesado de señal, permitiendo el seguimiento de las alteraciones del FSC durante los procedimientos anestésicos.

En primer lugar, se presenta una exhaustiva revisión de la literatura, ofreciendo información clínica y técnica relevante relacionada con otras técnicas de monitorización del FSC y con posibles algoritmos de procesado de señal aplicables a señales REG. A continuación, se describen los datos clínicos recogidos en el ámbito de este proyecto y utilizados para desarrollar y validar las técnicas aplicadas a señales REG.

Como primer paso en el análisis de las señales REG, se presentan distintas opciones de filtros de eliminación de ruido, en el dominio lineal y no lineal. El filtro no lineal aplicado al atractor de la señal ofrece una mayor precisión al recuperar información útil de la señal REG, especialmente en ambientes muy ruidosos. No obstante, la carga computacional que supone compromete su utilización en la monitorización en tiempo real de señales fisiológicas.

El análisis de las señales REG empieza con la utilización de características geométricas extraídas del dominio temporal, ya que ésta es la estrategia de procesado más común para este tipo de datos fisiológicos. Se evalúa La capacidad de dichas características para detectar apneas en voluntarios jóvenes sanos y para distinguir entre distintas profundidades anestésicas. Su rendimiento es pobre en la detección de apneas, pero esas características son capaces de detectar cambios hemodinámicos cerebrales durante la anestesia.

Se propone un nuevo enfoque, basado en la evaluación de dinámicas no lineales de señales REG. Los descriptores de los atractores reconstruidos a partir de señales REG muestran diferencias significativas entre apneas y registros basales, así como entre diferentes estados de anestesia. Éste es un hallazgo clave que proporciona una alternativa al procesado estándar de señales REG.

Se presenta también una tercera técnica de análisis, utilizando medidas de entropía para caracterizar señales de impedancia cerebral. Dichas métricas son también capaces de detectar apenas y diferencias entre estados de anestesia, proporcionando una herramienta adicional para el análisis REG, aunque tienen tiempos computacionales elevados no adecuados para aplicaciones en tiempo real.

Los resultados de los análisis de características geométricas, de los descriptores del grafico de Poincaré y de las tasas de entropía sugieren que las señales REG realmente transportan información del FSC. Entre esas características, aquellas que posibilitan el procesado de datos en tiempo real son utilizadas para clasificar registros REG recogidos en pacientes despiertos y anestesiados. Se obtiene una precisión del 70%, indicando que los cambios de FSC detectados en señales REG están relacionados con el estado de anestesia del paciente, aunque presentan una gran variabilidad.

Sin embargo, los parámetros REG no deben tener como propósito sustituir la monitorización de la profundidad de la anestesia, pero sí deben ayudar al mantenimiento de la estabilidad hemodinámica durante los procedimientos anestésicos.

Para alcanzar este objetivo, se analizan las posibles interacciones entre la hemodinámica global, la hemodinámica cerebral y parámetros basados en EEG, buscando relaciones de causalidad entre ellos. Se detectan interacciones durante la administración de anestésicos y cambios de posición del paciente, demostrando que existe una interacción entre la hemodinámica y la actividad cerebral.

En conclusión, esta Tesis Doctoral proporciona métodos alternativos para el procesado de señal REG que confirman la hipótesis de que las señales REG contienen información sobre el FSC. La simplicidad de la tecnología, junto con el bajo precio y los resultados fácilmente interpretables, deben proporcionar una nueva oportunidad para REG alcanzar la práctica clínica habitual. Además, las relaciones de causalidad entre la señal fisiológica hemodinámica y la actividad cerebral sugieren que la inclusión de información REG en monitores de profundidad de anestesia puede ser útil para un monitor de cabecera no invasivo y asequible para prevenir alteraciones FSC durante los procedimientos anestésicos.

Códigos UNESCO: 240602 (Bioelectricidad), 331110 (Instrumentos médicos), 241103 (Fisiología cardiovascular).

Contents

Acknowledgement ..... **v**
Abstract ..... **vii**
Resum ..... **x**
Resumen ..... **xiii**
Contents ..... **xvii**
List of Figures ..... **xxiii**
List of Tables ..... **xxxiii**
Abbreviations ..... **xxxviii**
1. Introduction **1**
1.1 Introduction 2
1.2 Background 2
1.3 Objectives 3
1.4 Research Framework 4
1.5 Thesis Outline 5
2. Clinical and Technical Background **7**
2.1 Introduction 8
2.2 Cerebral hemodynamics 8
2.3 CBF monitoring techniques 15
2.2.1 Near Infrared Spectroscopy 19
2.2.2 Transcranial Doppler 21
2.2.3 Rheoencephalography 22
2.3 Cerebral blood flow and general anesthesia 28
2.3.1 Cerebral blood flow during anesthesia 28
2.3.2 EEG monitoring 33

2.3.3 Propofol pharmacokinetic models 34
2.4 Signal processing techniques for REG analysis 38
3. Clinical Datasets 41
3.1 Introduction to Clinical Trials 42
3.2 Ethical Considerations 42
3.3 Apnea-Baseline Database 42
3.3.1 Clinical Protocol Rationale 42
3.3.2 Recorded Data Description 43
3.4 General Anesthesia Dataset 1 44
3.4.1 Aims of the Protocol 44
3.4.2 Recorded Data Description 44
3.5 General Anesthesia Dataset 2 46
3.5.1 Aims of the Protocol 46
3.5.2 Recorded Data Description 46
4. Optimal parameters for noise reduction algorithm based on local geometric projections of REG signals 49
4.1 Introduction 50
4.2 Methods 51
4.2.1 Classical time domain filters 51
4.2.2 The nonlinear filter 54
4.2.3 Experimental dataset 57
4.2.4 Evaluation of the performance of the filters under test 58
4.3 Results 61
4.4 Conclusions 69
5. Geometric features extraction from REG signals 71
5.1 Introduction 72
5.2 Methods 74
5.2.1 Geometric features extraction 74
5.2.2 Experimental datasets 77
5.2.3 Data analysis for apnea detection 78
5.2.4 Data analysis for general anesthesia recordings 79

5.3 Results for apnea detection 80
5.3.1 With linear filter 80
5.3.2 With nonlinear filter 81
5.4 Results for general anesthesia 83
5.4.1 With linear filter 83
5.4.2 With nonlinear filter 86
5.4.3 Confounding factors 89
5.5 Discussion of the results obtained in apnea detection 96
5.6 Discussion of the results obtained in anesthesia 98
5.7 Conclusions 99
6. Poincaré Plot Analysis of REG Signals 101
6.1 Introduction 102
6.2 Methods 104
6.2.1 Poincaré plot analysis 104
6.2.2 Experimental datasets 108
6.2.3 Data analysis for apnea detection 108
6.2.4 Data analysis for general anesthesia recordings 109
6.3 Results for apnea detection 110
6.3.1 With linear filter 110
6.3.2 With nonlinear filter 118
6.3.3 Selection of τ ranges optimizing apnea detection 122
6.4 Results for general anesthesia 125
6.4.1 With linear filter 125
6.4.2 With nonlinear filter 131
6.4.3 Confounding factors 136
6.5 Discussion of the results obtained in apnea detection 141
6.6 Discussion of the results obtained in anesthesia 144
6.7 Conclusions 146
7. Entropy Analysis of REG Signals 147
7.1 Introduction 148
7.2 Methods 150

7.2.1 Entropy definitions 150
7.2.2 Experimental protocols 157
7.2.3 Data analysis for apnea detection 158
7.2.4 Data analysis for general anesthesia recordings 159
7.3 Results for apnea detection 160
7.3.1 With linear filter 160
7.3.2 With nonlinear filter 169
7.4 Results for general anesthesia 177
7.4.1 With linear filter 177
7.4.2 With nonlinear filter 179
7.4.3 Confounding factors 181
7.5 Discussion of the results obtained in apnea detection 186
7.6 Discussion of the results obtained in anesthesia 190
7.7 Conclusions 192
8. Classification of REG signals during general anesthesia 193
8.1 Introduction 194
8.2 Methods 195
8.2.1 Features selection 195
8.2.2 Classification algorithms 196
8.2.3 Experimental dataset 197
8.2.4 Data processing 198
8.3 Classification results 199
8.4 Discussion of the results 204
8.5 Conclusions 205
9. Causality analysis between EEG, REG and hemodynamics during anesthesia 207
9.1 Introduction 208
9.2 Methods 211
9.2.1 Granger Causality 211
9.2.2 Experimental dataset 216
9.2.3 Data processing 217

9.3 Results 220
9.3.1 Steady state anesthesia 220
9.3.2 Propofol infusion 232
9.3.3 Remifentanil infusion 238
9.3.4 Atropine infusion 244
9.3.5 Ephedrine infusion 248
9.3.6 Trendelenburg position 251
9.3.7 Passive Leg Raise 256
9.4 Discussion 259
9.5 Conclusions 263
10. Conclusions and Future Work 265
10.1 Conclusions 266
10.2 Future work 270
Publications, Patents and Conference Contributions 271
References 273

List of Figures

Figure 2-1 Circle of Willis (from [3]). 9
Figure 2-2 Autoregulation mechanism illustration (from [7]). 10
Figure 2-3 Relationship between cerebral blood flow (CBF) and CMRO2 (from [5]). Vertical and horizontal lines refer to average resting values. 12
Figure 2-4 Blood pressure (BP), $PaCO_2$ and PaO_2 effects on cerebral blood flow (CBF) (from [9]). 12
Figure 2-5 Cerebral blood flow velocity (CBFv) recorded by means of Doppler spectra during a breath holding test (from [18]). 14
Figure 2-6 Placement of thermal diffusion flowmetry (TDF) probe (from [30]). 16
Figure 2-7 Perivascular Flow Probe (from [31]). 17
Figure 2-8 Absorption for main substances as a function of light wavelength (from [39]). 20
Figure 2-9 Cerebral Impedance pulse (from [53]). 24
Figure 2-10 Geometric values calculated in a rheoencephalographic curve by a particular software tool, RHEOSYS (from [53]). 24
Figure 2-11 Optimal frequency for REG (from [52]). 25
Figure 2-12 Description of one compartment. 35
Figure 2-13 Three compartment model. 35
Figure 3-1 Sequence of breath holding (apnea) and baseline episodes. 43
Figure 4-1 Example of magnitude responses for the digital low pass filters (a) Butterworth, (b) Chebyshev Type I, (c) Chebyshev Type II and (d) Elliptic. 52
Figure 4-2 Nonlinear filter algorithm description: (a) original time series, (b) reconstructed attractor, (c) identification of neighborhoods, (d) new projection of neighborhoods, (e) final attractor after 8 iterations, (f) filtered time series. 55
Figure 4-3 Processing applied to the recorded REG signals to obtain the input dataset y(t), consisting on a high pass filter (HPF) with cut-off frequency 0.1 Hz, the application of the nonlinear filter with parameters m=400, τ=1, v=300, k=0.95 and 100 iterations, and the addition of white noise. 58

Figure 4-4 Inclusion of a Butterworth second order low pass filter (LPF) with cut-off frequency at 4Hz in the steps followed to create the set of synthetic signals. 60
Figure 4-5 Frequency responses of the optimal time domain filters. 61
Figure 4-6 PRD of the filtered signal as a function of: (a) the number of iterations (with v=120 and m=50), (b) the number of neighbors (with m=150 and 40 iterations) and (c) the number of embedded dimensions (with v=120 and 40 iterations). 62
Figure 4-7 Number of iterations needed (a) and PRD error (b) obtained for each v and m combination. 63
Figure 4-8 PRD errors of the signals filtered with each filter under test in the training set (a) and the validation set (b). 64
Figure 4-9 Example of a reference signal REG(t) (a), signal y(t) with white noise (b), sREC(t) result after applying a Butterworth filter (c) and sREC(t) result obtained with the nonlinear filter (d). 65
Figure 4-10 PRD errors of the signals filtered with each filter under test in the training set (a) and the validation (b) set, after the inclusion of a Butterworth filter in the generation of the synthetic signals dataset. 66
Figure 4-11 Effect of different SNR levels in the performance of the filters, by comparing median and interquartile values of the PRD error (curves from Chebyshev type I and elliptic filters are overlapped). 67
Figure 4-12 Execution time of each filter as a function of the SNR value. 68
Figure 4-13 Effects of the input signal length on the performance of the filters, by comparing median and interquartile values of the PRD error (curves from Chebyshev type I and elliptic filters are overlapped). 69
Figure 4-14 Execution time of each filter as a function of the input signal length N. 70
Figure 5-1 Features extracted from REG wave and its derivative. 74
Figure 5-2 Graphical representation of LVET in the derivative of the ICG curve (from [177]). 76
Figure 5-3 Regression curves for the relationship between HR and LVET (from [179]). 76
Figure 5-4 Experimental datasets to be processed. 78
Figure 5-5 Receiver Operating Characteristic curves of AreaSyst in the linearly and nonlinearly filtered dataset. 83
Figure 5-6 Trends (mean and standard deviation) of the parameters showing statistically significant differences for the transitions between the defined anesthetic states: (a) Range, (b) AreaSyst, (c) δmax, (d) δrange, (e) CBVrel and (f) CBFest. 85
Figure 5-7 Trends (mean and standard deviation) of the parameters showing statistically significant differences for the transitions between the defined

anesthetic states when using the nonlinear filter for data preprocessing: (a) Range, (b) Δtmin-max, (c) AreaSyst, (d) δmax, (e) δrange and (f) CBVrel. 88
Figure 5-8 Spearman correlation values matching with colors and qualitative level. 91
Figure 6-1 SD1, SD2 and ellipse fitting of a REG signal. 106
Figure 6-2 Example of the application of the Complex Correlation Measure (CCM) algorithm in a subset of 5 data points..... 107
Figure 6-3 Poincaré plot reconstruction of apnea and baseline signals. Apnea signal (a,b,c) and baseline signal (d,e,f) for different time lags: τ=5 samples (a,d), τ=10 samples (b,e) and τ=70 samples (c and f). 112
Figure 6-4 Comparison of the results obtained for apnea and baseline periods (median values, interquartile range and statistical significance) of all tested features in function of the time lag τ. (a) SD1; (b) SD2; (c) SDarea; (d) SDratio; (e) R; (f) CCM. Grey solid color corresponds to statistical significance level of p-value<0.025. 113
Figure 6-5 Statistical significance levels (p-value) for SDratio, CCM and R, as a function of the time lag τ when comparing apnea and baseline segments. R and SDratio curves are overlapped for almost all values. The dotted horizontal black line shows significance when applying Bonferroni correction. Vertical lines indicate the different criteria commonly used to determine τ. 114
Figure 6-6 Correlations between R, CCM and SDratio. (a) R and CCM, (b) SDratio and CCM, and (c) CCM and R..... 115
Figure 6-7 Sensitivity and specificity of apnea and baseline classification as a function of the time lag values (τ). (a) SDratio, (b) R and (c) CCM. 116
Figure 6-8 AUC of the Receiver Operating Characteristic for SDratio, CCM and R, as a function of the time lag. AUC for R and SDratio are overlapped. 117
Figure 6-9 Accuracy of SDratio, CCM and R, as a function of the time lag τ.... 117
Figure 6-10 Comparison of the results obtained for apnea and baseline periods after nonlinear filtering (median values, interquartile range and statistical significance) of all tested features in function of the time lag τ. (a) SD1; (b) SD2; (c) SDarea; (d) SDratio; (e) R; (f) CCM. Grey solid color corresponds to statistical significance level of p-value<0.025. 118
Figure 6-11 Statistical significance levels (p-value) for SDratio, CCM and R, as a function of the time lag τ when comparing apnea and baseline segments extracted from REG signals nonlinearly filtered. R and SDratio curves are overlapped for almost all values. The dotted horizontal black line shows significance when applying Bonferroni correction..... 119
Figure 6-12 Sensitivity and specificity of apnea and baseline classification as a function of the time lag values (τ) for signals processed with the nonlinear filter. (a) SDratio, (b) R and (c) CCM..... 120

Figure 6-13 AUC of the Receiver Operating Characteristic for SDratio, CCM and R, when computed from nonlinearly filtered data, as a function of the time lag τ. AUC for R and SDratio are overlapped. 121
Figure 6-14 Accuracy of SDratio, CCM and R, after preprocessing with the nonlinear filter. 121
Figure 6-15 Summary of SDratio performance assessed by means of p-value (a,b), AUC (c,d) and accuracy (e,f) as a function of τ, when data were filtered with the linear filter (a,c,e) and the nonlinear filter (b,d,f). 122
Figure 6-16 Summary of R performance assessed by means of p-value (a,b), AUC (c,d) and accuracy (e,f) as a function of τ, when data were filtered with the linear filter (a,c,e) and the nonlinear filter (b,d,f). 123
Figure 6-17 Summary of CCM performance assessed by means of p-value (a,b), AUC (c,d) and accuracy (e,f) as a function of τ, when data were filtered with the linear filter (a,c,e) and the nonlinear filter (b,d,f). 124
Figure 6-18 Evolution of SD1, SD2, SDratio, SDarea, CCM and R as a function of τ for the set of anesthesia states under analysis: awake, LOC, anesthesia, BSR and LOC. Median values are graphed, together with the 25th and 75th quartiles represented with dashed lines. 126
Figure 6-19 Statistical significance (p-values) obtained for the comparison of the median values of each Poincaré feature among consecutive anesthesia states. Grey areas represent intervals in which the graphed parameter shows statistical significance of p-value<0.01. 128
Figure 6-20 Trends for (a) SD1, (b) SD2, (c) SDratio, (d) SDarea, (e) CCM and (f) R across the different anesthesia states for τ=20 samples, represented as mean ± standard deviation. 130
Figure 6-21 Evolution of SD1, SD2, SDratio, SDarea, CCM and R as a function of τ for the nonlinearly filtered REG signals collected in the anesthesia states under analysis: awake, LOC, anesthesia, BSR and LOC. Median values are graphed, together with the 25^{th} and 75^{th} quartiles represented with dashed lines. 132
Figure 6-22 Statistical significance (p-values) obtained for the comparison of the median values of each Poincaré feature among consecutive anesthesia states, computed on the nonlinearly filtered dataset. Grey areas represent intervals in which the graphed parameter shows statistical significance of p-value<0.01. 133
Figure 6-23 Trends for (a) SD1, (b) SD2, (c) SDratio, (d) SDarea, (e) CCM and (f) R across the different anesthesia states for τ=20 samples, represented as mean ± standard deviation. 135
Figure 6-24 Spearman correlation values matching with colors and qualitative level. 137
Figure 7-1 Corrected Conditional Entropy (CCE(N, m, ε)) values of apnea and baseline recordings as a function of a) the quantification intervals (ε), b) the embedding dimension (m) and c) the signal length (N). The corresponding

statistical significance (p-value) of the differences between apnea and baseline recordings is presented in d), e) and f), respectively. 161
Figure 7-2 The influence of the signal length and the number of quantization levels in the Regularity index (ρ(N, ε)) is analyzed in: (a) values of ρ as a function of the number of quantification intervals (ε) and (b) values of ρ as a function of the signal length (N). The results of the statistical analysis (p-value) comparing apnea and baseline signals using this entropy indexes are shown in: (c) p-values versus the number of quantification intervals and (d) p-values versus the signal length..... 162
Figure 7-3 Values of the entropy CCE(N,m,ε) with ε=20 and N=2000 as a function of the embedding dimension m for all apnea (a) and baseline (b) recordings, including their median values (thick black line). 163
Figure 7-4 Values of the entropies ApEn, SampEn and FuzzyEn as a function of the number of samples (N) and the dimension (m), with r=0.3 and n=2 for FuzzyEn, for apnea (solid line) and baseline segments (dashed line). 164
Figure 7-5 Entropy values of ApEn(m,r,N), SampEn(m,r,N) and FuzzyEn(m,r,,n,N) as a function of r with m=2, n=2 and N=2000 for apnea and baseline recordings (a-c) and the corresponding p-values (d-f)..... 165
Figure 7-6 Fuzzy entropy (FuzzyEn(m,r, n,N)) (a) FuzzyEn(2,0.25, n, 2000) values as a function of n, including the 25-75 interquartile range (colored area); (b) standard deviation of FuzzyEn(2,0.25, n, 2000) as a function of n; (c) p-value obtained comparing FuzzyEn(2,0.25, n, 2000) values in apnea and baseline groups as a function of n. 166
Figure 7-7 Standard deviation of ApEn(m, r, N), SampEn(m, r, N) and FuzzyEn(m, r, n, N) as a function of r comparing baseline and apnea segments, with m=2, n=2, N=2000. 167
Figure 7-8 Receiver Operating Characteristic curves of all entropy metrics providing statistically significant differences between apnea and baseline recordings..... 169
Figure 7-9 Boxplot of all selected entropy metrics, showing the median values (horizontal red lines) and outliers (red crosses): ApEn (m, r, N), SampEn (m, r, N), FuzzyEn(m, r, n, N), CCE (N, m, ε) and ρ (N, ε), with m=2, r=0.25, N=2000, n=2 and ε=20. 170
Figure 7-10 Values of CCE(N,m,ε), ρ(N,ε) and CCEmin(N,ε) position median and interquartile values as a function of N, m and ε for apnea and baseline signals: (a) CCE(2000,m,20), (b)CCE(N,2,20), (c) ρ(N,20), (d) CCEmin(N,20), (e) CCE(2000, 2,ε), (f) ρ(2000,ε), (g) CCEmin(2000,ε). 171
Figure 7-11 Analysis of the statistical significance (p-value) for apnea detection of CCE(N,m,ε), ρ(N,ε) and CCEmin(N,ε) as a function of N, m and ε: (a) CCE(2000,m,20), (b)CCE(N,2,20), (c) ρ(N,20), (d) CCEmin(N,20), (e) CCE(2000, 2,ε), (f) ρ(2000,ε), (g) CCEmin(2000,ε). 172

Figure 7-12 Boxplot showing the distribution of CCE(N,m,ε) and ρ(N,ε) when N=2000, m=2 and ε=20 for data preprocessed with linear filters (LF) and nonlinear filters (NLF). Median values are indicated with horizontal lines, and mean values with circles. 173
Figure 7-13 ApEn(m,r,N), SampEn(m,r,N) and FuzzyEn(m,n,r,N) values as a function of the embedding dimension (m) (a,b,c,), the signal length (N) (d,e,f) and the threshold r (g,h,i). 174
Figure 7-14 Analysis of the statistical significance (p-value) for apnea detection of ApEn(m,r,N), SampEn(m,r,N) and FuzzyEn(m,n,r,N) as a function of m, N and r. 175
Figure 7-15 Boxplot of the distribution of ApEn(m,r,N), SampEn(m,r,N) and FuzzyEn(m,r,n,N) when m=2, r=0.25, n=2, and N=2000 and for data preprocessed with linear filters (LF) and nonlinear filters (NLF). Median values are indicated with horizontal lines, and mean values with circles..... 175
Figure 7-16 Receiver Operating Characteristic curves of all entropy metrics providing statistically significant differences between apnea and baseline recordings in the nonlinear filter dataset. 177
Figure 7-17 Mean and standard deviation values in each clinical state of the anesthetic process for the entropies (a) ApEn, (b) SampEn, (c) FuzzyEn, (d) CCE and (e) ρ. 178
Figure 7-18 Mean values in each clinical state for (a) ApEn, (b) SampEn, (c) FuzzyEn, (d) CCE and (e) ρ. 180
Figure 7-19 Spearman correlation values matching with colors and qualitative level. 183
Figure 8-1 Weights calculated with the Relief algorithm for the geometric features (GEOM) and the Poincaré plot descriptors (Poincaré). 200
Figure 8-2 Sensitivity (a), specificity (b) and accuracy (c) of the logistic regression, naïve Bayes and classification tree, as a function of the number of parameters used as inputs in the classifier, following the order provided by the Relief algorithm. 201
Figure 8-3 Weights calculated with the Relief algorithm for the demographic variables (DEMOG), the geometric features (GEOM) and the Poincaré plot descriptors (Poincaré). 202
Figure 8-4 Sensitivity (a), specificity (b) and accuracy (c) of the logistic regression, naïve Bayes and classification tree, as a function of the number of parameters used as inputs in the classifier, following the order provided by the Relief algorithm when demographic variables were included..... 203
Figure 9-1 (a) Normalized qCON data and (b) normalized propofol effect site concentration recorded during a general anesthesia procedure. 214
Figure 9-2 BIC values as a function of the selected xlag for the restricted AR model. 214

Figure 9-3 BIC values as a function of the selected ylag for the unrestricted AR model..... 215
Figure 9-4 Example of clinical data recorded during an anesthetic procedure: (a) qCON index, (b) EEG frequency bands, (c) propofol and remifentanil effect site concentrations, (d) heart rate and mean arterial pressure and (e) δmax and SDratio REG features. 219
Figure 9-5 Optimal time lags for the GC caused variable (x lag) in the unrestricted AR model during steady state anesthesia. Columns contain the causing variables and rows the caused ones. 221
Figure 9-6 Optimal time lags for the GC causing variable (y lag) in the unrestricted AR model during steady state anesthesia. Columns contain the causing variables and rows the caused ones. 222
Figure 9-7 Causal relationships diagram between MAP and REG geometric features, where n represents the number patients presenting each causal interaction. 223
Figure 9-8 Causal relationships diagram between HR and REG geometric features, where n represents the number patients presenting each causal interaction.224
Figure 9-9 Causal relationships diagram between MAP and HR and REG Poincaré plot descriptors features, where n represents the number patients presenting each causal interaction..... 225
Figure 9-10 Causal relationships diagram between the energy of the EEG bands and REG geometric features, where n represents the number patients presenting each causal interaction..... 226
Figure 9-11 Causal relationships diagram between the energy of the EEG bands and REG Poincaré plot descriptors, where n represents the number patients presenting each causal interaction. 227
Figure 9-12 Causal relationships diagram between the qCON index and REG geometric features, where n represents the number patients presenting each causal interaction. 228
Figure 9-13 Causal relationships diagram between the qCON index and REG Poincaré plot descriptors, where n represents the number patients presenting each causal interaction..... 229
Figure 9-14 Main interactions between global hemodynamics (HR and MAP), EEG features and REG geometric features (CBF lin) and REG Poincaré plot (CBF PP) parameters during steady state anesthesia. 230
Figure 9-15 Optimal time lags for the GC caused variable (x lag) in the unrestricted AR model during changes in propofol concentration. Columns contain the causing variables and rows the caused ones. 233
Figure 9-16 Optimal time lags for the GC causing variables (y lag) in the unrestricted AR model during changes in propofol concentration. Columns contain the causing variables and rows the caused ones. 234

Figure 9-17 Causal interactions from CePropo to (a) EEG and global hemodynamics, (b) REG geometric features and (c) REG Poincaré plot descriptors. 235
Figure 9-18 Causal interactions between EEG parameters, HR, MAP, REG geometric features (CBF lin) and REG Poincaré plot descriptors (CBF PP) during changes in propofol concentration. 236
Figure 9-19 Optimal time lags for the GC caused variable (x lag) in the unrestricted AR model during changes in remifentanil concentration. Columns contain the causing variables and rows the caused ones. 239
Figure 9-20 Optimal time lags for the GC causing variable (y lag) in the unrestricted AR model during changes in remifentanil concentration. Columns contain the causing variables and rows the caused ones. 240
Figure 9-21 Causal interactions from CeRemi to (a) EEG related parameters ang global hemodynamics, (b) REG geometric features and (c) REG Poincaré plot descriptors. 241
Figure 9-22 Causal interactions between EEG parameters, HR, MAP, REG geometric features (CBF lin) and REG Poincaré plot descriptors (CBF PP) during changes in remifentanil concentration. 242
Figure 9-23 Optimal time lags for the GC caused variable (x lag) in the unrestricted AR model during atropine infusion. Columns contain the causing variables and rows the caused ones. 244
Figure 9-24 Optimal time lags for the GC causing variable (y lag) in the unrestricted AR model during atropine infusion. Columns contain the causing variables and rows the caused ones. 245
Figure 9-25 Causal interactions between EEG parameters, HR, MAP, REG geometric features (CBF lin) and REG Poincaré plot descriptors (CBF PP) during atropine infusion. 246
Figure 9-26 Optimal time lags for the GC caused variable (x lag) in the unrestricted AR model during ephedrine infusion. Columns contain the causing variables and rows the caused ones. 248
Figure 9-27 Optimal time lags for the GC causing variable (y lag) in the unrestricted AR model during ephedrine infusion. Columns contain the causing variables and rows the caused ones. 249
Figure 9-28 Causal interactions between EEG parameters, HR, MAP, REG geometric features (CBF lin) and REG Poincaré plot descriptors (CBF PP) during ephedrine infusion. 250
Figure 9-29 Optimal time lags for the GC caused variable (x lag) in the unrestricted AR model during Trendelenburg positioning. Columns contain the causing variables and rows the caused ones. 252
Figure 9-30 Optimal time lags for the GC causing variable (y lag) in the unrestricted AR model during Trendelenburg positioning. Columns contain the causing variables and rows the caused ones. 253

Figure 9-31 Causal interactions between EEG parameters, HR, MAP, REG geometric features (CBF lin) and REG Poincaré plot descriptors (CBF PP) during Trendelenburg positioning. 254
Figure 9-32 Optimal time lags for the GC caused variable (x lag) in the unrestricted AR model during passive leg raising. Columns contain the causing variables and rows the caused ones. 256
Figure 9-33 Optimal time lags for the GC causing variable (y lag) in the unrestricted AR model during passive leg raising. Columns contain the causing variables and rows the caused ones. 257
Figure 9-34 Causal interactions between EEG parameters, HR, MAP, REG geometric features (CBF lin) and REG Poincaré plot descriptors (CBF PP) during passive leg raising. 258

List of Tables

Table 2-1 Rheoencephalographic devices used for REG clinical trials and excitation frequency used in each case [51]. 23
Table 2-2 Angiographic and REG results (from [66]). 27
Table 2-3 Effects of anesthetic agents on vasodilation / vasoconstriction (CVR), CPP, CAR and CO2 reactivity [72]. 29
Table 2-4 EEG frequency bands. 33
Table 2-5 Compartment volumes in Marsh and Schnider models. 36
Table 2-6 Kij values for Marsh and Schnider models. 37
Table 3-1 Participants demographic data 43
Table 3-2 Patients demographic data 44
Table 3-3 Drugs administered during surgical procedures. 45
Table 3-4 Patients demographic data 46
Table 3-5 Drugs administered during surgical procedures. 47
Table 4-1 Time domain filters tested for REG signals in the training set. 59
Table 4-2 Statistical significance p-value of the paired t-student test comparing the PRD errors of the nonlinear filter with the one obtained with each classical filter. 64
Table 4-3 Statistical significance p-value of the paired t-student test comparing the PRD errors of the nonlinear filter with the one obtained with each classical filter. 66
Table 5-1 Description of the signals belonging to General Anesthesia Dataset 1: sample size, dynamic range (95% confidence interval), cardiac cycle duration and p-value obtained from the comparison with values in the following clinical state. 80

Table 5-2 Results of geometric features using classical filters: average values (mean ± standard deviation) for apnea and baseline recordings and statistical significance of their difference (p-value). 81
Table 5-3 Results of geometric features using the nonlinear filter: average values (mean ± standard deviation) for apnea and baseline recordings and statistical significance of their difference (p-value). 82
Table 5-4 Comparison of the performance of AreaSyst with the linear and nonlinear filter. 82
Table 5-5 Average values (mean, standard deviation) of all the extracted geometric features in each anesthesia state for REG data preprocessed with the linear filter. 84
Table 5-6 Statistical significance (p-value) of the differences in every transition of anesthetic states. Significant values ($p<0.01$) are indicated in bold type..... 86
Table 5-7 Average values (mean, standard deviation) of all the extracted geometric features in each anesthesia state for REG data preprocessed with the nonlinear filter. 87
Table 5-8 Statistical significance (p-value) of the differences in every transition of anesthetic states when preprocessing with the nonlinear filter. Significant values ($p<0.01$) are indicated in bold type. 89
Table 5-9 Spearman correlation of each geometric feature with patient demographics for every clinical state, either using the linear filter or the nonlinear filter. Cells are colored as indicated in **Figure 5-8** and statistical significance ($p<0.05$) is indicated in bold. 90
Table 5-10 Spearman correlation between patient demographics and differences in geometric features for every transition between consecutive clinical states analyzed, either using the linear filter (left side) or the nonlinear filter (right side). Cells are colored as a function of the correlation value (see **Figure 5-8**) and statistical significance ($p<0.05$) of the correlations is indicated in bold type. ... 93
Table 5-11 Spearman correlation between clinical variables related to depth of anesthesia and hemodynamics and differences in geometric features for every transition between consecutive clinical states analyzed, either using the linear filter (left side) or the nonlinear filter (right side). Cells are colored as a function of the correlation value (see **Figure 5-8**) and statistical significance ($p<0.05$) of the correlations is indicated in bold type. 95
Table 6-1 Tau values (in samples) calculated from the REG signals following the criteria recommended in literature. 111
Table 6-2 Performance of SDratio, CCM and R in apnea detection for τ values between 1 and 20 samples. 125
Table 6-3 Average values (mean ± standard deviation) of each Poincaré plot feature in the selected anesthesia states considering $\tau = 20$ samples. 129

Table 6-4 Statistical significance (p-value) of the differences between consecutive anesthesia states for the Poincaré plot extracted features, considering τ=20 samples..... 131
Table 6-5 Average values (mean ± standard deviation) of each Poincaré plot feature in the selected anesthesia states considering τ = 20 samples. 134
Table 6-6 Statistical significance (p-value) of the differences between consecutive anesthesia states for the Poincaré plot extracted features, considering τ=20 samples..... 135
Table 6-7 Spearman correlation of each Poincaré feature with patient demographics for every clinical state, either using the linear filter or the nonlinear filter. Cells are colored as indicated in **Figure 6-24** and statistical significance is indicated in bold..... 136
Table 6-8 Spearman correlation between patient demographics and differences in Poincaré plot descriptors for every transition between consecutive clinical states analyzed, either using the linear filter (left side) or the nonlinear filter (right side). Cells are colored as a function of the correlation value (see **Figure 6-24**) and statistical significance of the correlations is indicated in bold type. 139
Table 6-9 Spearman correlation between clinical variables related to depth of anesthesia and hemodynamics and differences in Poincaré plot descriptors for every transition between consecutive clinical states analyzed, either using the linear filter (left side) or the nonlinear filter (right side). Cells are colored as a function of the correlation value (see **Figure 6-24**) and statistical significance of the correlations is indicated in bold type..... 140
Table 7-1 Parameter combinations used to calculate each entropy metric.... 159
Table 7-2 Parameter combination used to calculate each entropy metric. 164
Table 7-3 Mean values and standard deviation of all entropy metrics when comparing apnea and baseline recordings. The values of the set of parameters that best describe these entropies are included. Statistics as p-value, AUC and accuracy (acc) are provided to assess the ability of the entropy metrics to distinguish between apnea and baseline..... 168
Table 7-4 Mean values and standard deviation of all entropy metrics when comparing apnea and baseline recordings using the nonlinear filter. The values of the set of parameters that best describe these entropies are included. Statistics as p-value, AUC and accuracy (acc) are provided to assess the ability of the entropy metrics to distinguish between apnea and baseline..... 176
Table 7-5 Average entropy values for each clinical state and each entropy metric. 178
Table 7-6 Statistical significance (p-value) of each entropy metric reflecting the ability to distinguish between consecutive anesthesia stages..... 179

Table 7-7 Average values (mean ± standard deviation) for all entropy metrics in each anesthetic states when preprocessing signals with the nonlinear filter. 180
Table 7-8 Statistical significance (p-value) of each entropy metric reflecting the ability to distinguish between consecutive anesthesia stages..... 181
Table 7-9 Spearman correlation of each entropy metric with patient demographics for every clinical state analyzed, either using the linear filter (left side) or the nonlinear filter (right side). Cells are colored (see **Figure 7-19** for its meaning) as a function of the correlation value and statistical significance of the correlations is indicated in bold type. 182
Table 7-10 Spearman correlation between patient demographics and differences in entropy metrics for every transition between consecutive clinical states analyzed, either using the linear filter (left side) or the nonlinear filter (right side). Cells are colored (see **Figure 7-19** for its meaning) as a function of the correlation value and statistical significance of the correlations is indicated in bold type.184
Table 7-11 Spearman correlation between clinical variables related to depth of anesthesia and hemodynamics and differences in entropy metrics for every transition between consecutive clinical states analyzed, either using the linear filter (left side) or the nonlinear filter (right side). Cells are colored (see **Figure 7-19** for its meaning) as a function of the correlation value and statistical significance of the correlations is indicated in bold type. 185
Table 8-1 Geometric and Poincaré parameters extracted from REG signals to be used as inputs for the classifier. 198
Table 8-2 Number of input parameters needed for each classifier to reach at least an accuracy of 70%. 201
Table 8-3 Number of input parameters needed for each classifier to reach at least an accuracy of 70% when including the demographic variables as inputs of the classifier. 203
Table 9-1 Statistical differences of the hypothesis testing comparing the age, height, weight and BMI of patients presenting causal relationships among pairs of variables during steady state anesthesia with patients not presenting them. 231
Table 9-2 Statistical differences of the hypothesis testing comparing the age, height, weight and BMI of patients presenting causal relationships among pairs of variables during changes in propofol concentration with patients not presenting them. 237
Table 9-3 Spearman correlation between the causality indices and patient demographic presenting statistical significance ($p<0.01$) during changes of propofol effect site concentration. 238

Table 9-4 Spearman correlation between the causality indices and patient demographic presenting statistical significance ($p<0.01$) during changes of remifentanil effect site concentration. 243
Table 9-5 Spearman correlation between the causality indices and patient demographic presenting statistical significance ($p<0.01$) during atropine infusion. 247
Table 9-6 Spearman correlation between the causality indices and patient demographic presenting statistical significance ($p<0.01$) during ephedrine infusion. 251
Table 9-7 Spearman correlation between the causality indices and patient demographic presenting statistical significance ($p<0.01$) during Trendelenburg positioning. 255

Abbreviations

ApEn	Approximate Entropy
AUC	Area Under the Curve
$AVDO_2$	Arteriovenous Differences of Oxygen
BMI	Body Mass Index
BP	Blood Pressure
BSR	Burst Suppression Rate
CAR	Cerebral Autoregulation
CBF	Cerebral Blood Flow
CBFv	Cerebral Blood Flow Velocity
CBV	Cerebral Blood Volume
CE	Conditional Entropy
Ce	Effect-site concentration
CePropo	Propofol effect-site concentration
CeRemi	Remifentanil effect-site concentration
$CMRO_2$	Cerebral Metabolic Rate of Oxygen
Cp	Plasmatic Concentration
CPP	Cerebral Perfusion Pressure
CREB	Biomedical Engineering Research Centre
CT	Computed Tomography
CVR	Cerebrovascular Resistance
DBP	Diastolic Blood Pressure
ECG	Electrocardiogram
EEG	Electroencephalogram
EMG	Electromyogram
ESAII	Enginyeria de Sistemes, Automàtica i Informàtica Industrial
EU	European Union
FDA	Food and Drug Administration
FuzzyEn	Fuzzy Entropy
GC	Granger Causality
HPF	High Pass Filter
HR	Heart Rate
HRV	Heart Rate Variability
iREG	Intracranial Rheoencephalography
ICP	Intracranial Pressure
ISO	International Organization for Standardization

LF	Linear Filter
LMA	Laryngeal Mask Airway
LPF	Low Pass Filter
LOC	Loss of Consciousness
MAC	Minimum Alveolar Concentration
MAP	Mean Arterial Pressure
MBP	Mean Blood Pressure
MRI	Magnetic Resonance Imaging
NIRS	Near Infrared Spectroscopy
NLF	Nonlinear filter
NMBA	Neuromuscular Blocking Agents
OEF	Oxygen Extraction Fraction
OR	Operating Room
PPG	Photoplethysmography
PRD	Percentile Root Mean Square Difference
rCBF	Regional Cerebral Blood Flow
$rCMRO_2$	Regional Cerebral Metabolic Rate of Oxygen
REG	Rheoencephalography
REM	Rapid Eye Movement
ROC	Recovery of Consciousness
ROI	Region of Interest
rSO_2	Regional Oxygen Saturation
SampEn	Sample Entropy
SAP	Systolic Arterial Pressure
SBP	Systolic Blood Pressure
SE	Shannon Entropy
SEP	Somatosensory Evoked Potentials
STD	Standard Deviation
SNR	Signal-to-Noise Ratio
TCD	Transcranial Doppler
TCI	Target Controlled Infusion
TDF	Thermal Diffusion Flowmetry
TIVA	Total Intravenous Anesthesia
UPC	Universitat Politècnica de Catalunya
US	United States

Chapter 1

Introduction

Abstract

This chapter presents the main research hypothesis of this Doctoral Thesis, focusing on the principal and intermediate objectives, and providing an overview of the contents of the Thesis and how those are structured. Moreover, a description of the research framework in which this project has been carried out is presented.

1.1 Introduction

Chapter 1 aims at presenting the research hypothesis this Doctoral Thesis is based on and provides the relevant information regarding the research environment in which it was developed. For that purpose, the main hypothesis will be formulated, followed by the specific objectives of this project. Finally, the institutions involved will be presented, as well as the structure of this Thesis.

1.2 Background

In the last decades, medical devices have flooded operating theaters to provide healthcare professionals updated and reliable information on patient vital signs, as well as advanced algorithms aiming at improving patient care. Nonetheless, certain clinical signs are not included in standard patient monitoring during surgeries under general anesthesia, such as cerebral blood flow (CBF). Even though CBF is monitored in critical patients, it is not part of the standard of care, one of the reasons for that being that there is no current bedside monitor, non-invasive and affordable, to collect and display this information.

General anesthetics are known to affect hemodynamics, provoking changes in CBF that might interfere in the transit times of the anesthetics towards the target organ, the brain. The main research hypothesis of this dissertation suggests that CBF plays an important role in anesthesia and might be useful to enhance current algorithms used for depth of anesthesia monitoring. Moreover, to be accepted for standard clinical practice, a CBF monitor to be used for anesthesia titration should be easy to use, non-invasive and cost-effective, provide real time information and guarantee that it does not cause alterations in blood flow during its use.

Rheoencephalography (REG), a blood flow monitoring technique based on bioimpedance, would comply with those requirements. However, its clinical relevance has not been confirmed. The possibility of providing a low-cost tool to allow the inclusion of CBF monitoring in routine clinical practice has led to the main research hypothesis in this Doctoral Thesis: REG signals carry information on CBF that might be recovered by means of the application of advanced signal processing techniques, allowing to track CBF alterations during anesthetic procedures. To provide an answer to this research question, several intermediate objectives were set up, bearing in mind the requirements for bedside monitoring of CBF signals.

1.3 Objectives

The main objective of this project is to assess REG technology as a candidate for intra-operative CBF monitoring, using advanced signal processing techniques to extract relevant clinical information from REG waves and show its relationship with changes during anesthetic procedures.

The detailed objectives of this Doctoral Thesis are:

- Research on available techniques for CBF monitoring currently used in clinical practice, in order to assess the feasibility of a REG based monitor as a bedside tool for CBF measurements.

- Research on signal processing techniques applied to REG signals and alternative methods to extract clinical information form REG waves that have not been used for this application and could improve the correlation of REG signals with CBF alterations.

- Design and execution of clinical trials including the collection of REG data under simple respiratory challenges and during anesthetic procedures, to be used to develop new methodologies for their processing.

- Evaluation of the best filtering strategy to remove high frequency noise and drift oscillations from REG signals prior to their analysis.

- Analysis of REG signals using the classical approach based on the extraction of geometrical properties in the time domain, including the assessment of their performance during breath holding episodes and general anesthesia.

- Analysis of REG signals by alternative methodologies to be compared to the classical approach based on geometric features extraction: nonlinear features extraction by Poincaré plot analysis and Entropy metrics calculation. Those analyses are to be applied to both breath holding and anesthesia scenarios. For each methodology proposed, the set of parameters needed for its implementation shall be evaluated and specific guidelines on how to apply them to REG signals provided. Finally, their suitability for REG analysis in anesthesia must be assessed.

- Selection of the best methodology from the ones proposed (or a combination of them) to track CBF changes during anesthesia by means of REG signals.

- Analysis of causal relationships between the characteristics extracted from REG signal processing and other clinical variables recorded during general anesthesia procedures, such as EEG, infused drugs, heart rate and mean arterial pressure.

1.4 Research Framework

This Doctoral Thesis has been developed under the scope of the Industrial PhD program of the regional Catalan Government (Programa de Doctorats Industrials, Generalitat de Catalunya, DI-2015). This initiative intends to reinforce the collaboration between the Catalan Universities and Industry, increasing the innovation capabilities of the University, providing the Industry with cutting-edge technologies developed in the Education Centers and allowing the PhD students to benefit from this interaction.

Quantium Medical is dedicated to the research, design and development of innovative non-invasive monitoring solutions, focused mainly in the field of anesthesia. Since 2016, Quantium Medical is part of Fresenius Kabi, a global health care company that specializes in lifesaving medicines and technologies for infusion, transfusion and clinical nutrition. In this thesis, Quantium Medical has provided an extensive market knowledge in noninvasive monitoring, as well as instrumentation and know-how from previous products applicable to this research project. Those contributions were combined with the deep knowledge on signal processing techniques in the Automatic Control Department (Enginyeria de Sistemes, Automàtica i Informàtica Industrial, ESAII) and Biomedical Engineering Research Centre (CREB), as well as their experience with a variety of physiological signals and disease conditions. Both entities belong to the Universitat Politècnica de Catalunya (UPC), institution hosting the Doctoral School of Biomedical Engineering in which this PhD Thesis is developed.

Even though the Industrial PhD program was led by Quantium Medical and the referred departments of UPC, the role of Hospital CLÍNIC de Barcelona does also deserve to be outlined. Research in the medical field needs to be driven as well by qualified medical staff, since monitoring solutions can only succeed when they meet the expectations of the end users, the clinicians. Hospitals should therefore be integrated as key players in the ecosystem of

innovation related to medical devices, to foster the multidisciplinary approach underlying the design and development of this equipment and to contribute, as in this particular project, to the continuous innovation in patient care.

1.5 Thesis Outline

The contents of this thesis are distributed in 10 chapters. After this introduction stating the research hypothesis of this dissertation as well as the main objectives of the thesis, Chapter 2 provides background information from both clinical and technical perspectives, presenting as well an overview of the current devices used for CBF monitoring.

Chapter 3 contains the description of the clinical databases used along this thesis. Clinical protocol preparation and data collection are part of this project and were developed in cooperation with the Hospital CLÍNIC de Barcelona. A brief description of the protocols, data collected, and patient characteristics is provided for the three datasets processed.

Chapter 4 discusses the best filtering algorithm to be used for REG signals, comparing the performance of classical filters with an alternative nonlinear approach based on the reconstruction of the signal attractor. The selected optimal filters were used along this project for data preprocessing.

Chapter 5 contains the analysis of REG signals in the temporal domain by means of the selection of features related to the geometry of the REG pulse wave. This technique is applied to two sets of data, one based on healthy young volunteers performing a respiratory exercise consisting in breath holding, and a second one based on the analysis of REG data from patients undergoing elective surgeries under general anesthesia. Results from this chapter are to be considered as a reference for comparison with other techniques applied in this thesis, since those are based on the classical analysis of REG waveforms.

Chapter 6 proposes a new approach to REG signals processing, based on the extraction of Poincaré plot descriptors obtained from the signal attractor. This nonlinear technique will be applied to REG signals recorded during breath holding episodes in a first step, to assess its feasibility. Subsequently, the same descriptors will be applied to data recorded during general anesthesia procedures to analyze their performance under those circumstances.

Chapter 7 reproduces the structure in Chapters 5 and 6, applying entropy metrics to the breath holding and anesthesia recordings, to assess the ability of entropy metrics to track CBF changes through REG signals.

After the application of time domain features extraction, Poincaré plot analysis and entropy algorithms, the results from those techniques proving to contain information on changes in CBF and capable of providing real time information will be used together in Chapter 8 to implement a classifier capable of distinguishing between different periods in anesthesia management and thus proposing a new tool for anesthesia monitoring based on REG signals.

In Chapter 9, interactions between depth of anesthesia monitoring, general hemodynamics and REG based variables are analyzed by means of causality techniques. This step aims at detecting cause-effect relationships taking place during general anesthesia procedures and involving interactions between different physiological systems to better characterize the effect of anesthetics on brain hemodynamics.

Finally, Chapter 10 contains the conclusions of this thesis, focusing as well on the future steps needed to enhance REG based systems for its application in monitoring anesthetic procedures.

Chapter 2

Clinical and Technical Background

Abstract

This chapter focuses on the existing clinical and technical background related to cerebral blood flow (CBF), including an overview of the systems currently used to monitor CBF and a review of signal processing techniques suitable for rheoencephalography (REG) analysis.

2.1 Introduction

This chapter contains a review of the most relevant clinical and technical aspects related to CBF monitoring and REG technology. The first section is dedicated to summarize the basic concepts on cerebral hemodynamics, followed by an overview of the monitoring systems used in clinical practice, focusing on REG.

Additionally, information on CBF changes during anesthesia is provided, together with a review of anesthesia monitoring techniques that will be referred along this Thesis. Finally, signal processing techniques used for REG and other physiological signals will be described, in order to select the most appropriate ones to be applied to REG signals to explore their ability to correlate with clinical changes in CBF.

2.2 Cerebral hemodynamics

This section describes the main anatomical and physiological characteristics of the brain and its perfusion, in order to provide an overview of the circulatory subsystem that will be studied during this Doctoral Thesis.

The brain is an organ with unique properties from a hemodynamic point of view: even though it represents only 2% of the body weight in humans, it receives up to 20% of the total cardiac output [1]. This suggests that the brain has large metabolic needs and, as it is an organ that has no mechanism to store nutrients, oxygen or water, it needs to receive a large and uninterrupted blood supply.

The brain is perfused with blood coming from the carotid arteries (70%) and from the vertebrobasilar system (30%). Interrupting the blood supply to the brain for more than 5 minutes causes neuronal death [2]. Therefore, security mechanisms need to protect the brain from such a deleterious condition. One of the mechanisms used to guarantee as much as possible the brain perfusion is the vascular structure known as the circle of Willis [1] (**Figure 2-1**): blood vessels responsible for brain perfusion are interconnected in order to provide an alternative path for blood in case one of the main arteries is obstructed.

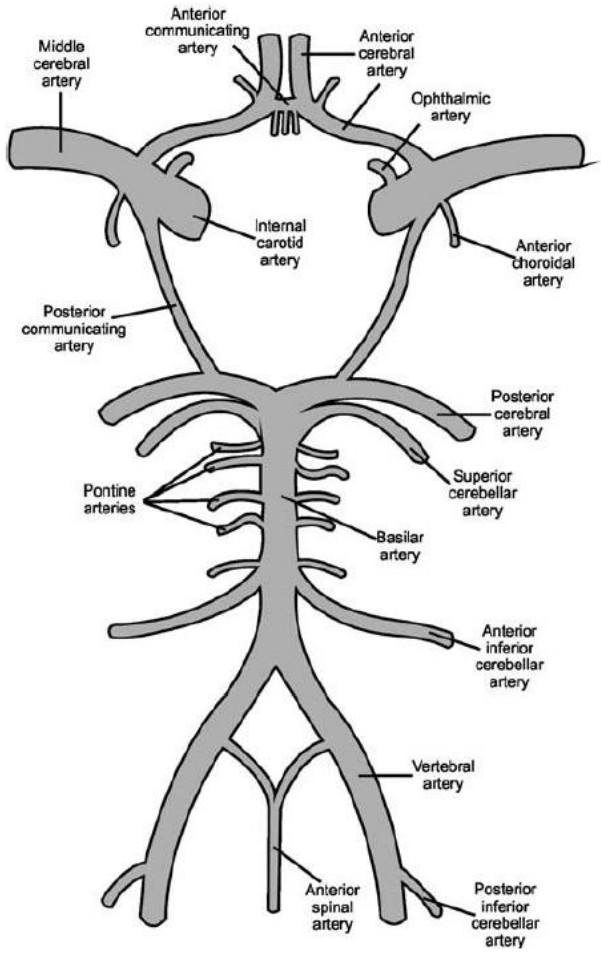

Figure 2-1 Circle of Willis (from [3]).

The volume of blood reaching the brain per minute is the cerebral blood flow (CBF). Generally, it has been accepted that in adults the value of CBF is around 750 ml per minute or 15% of the cardiac output. This leads to an average perfusion of 50 ml of blood per 100 g of brain tissue per minute[4], which also reflects the high oxygen consumption of the brain, known as cerebral metabolic rate for oxygen or $CMRO_2$, that reaches a 20% of the total body consumption.

Brain perfusion depends on the cerebral perfusion pressure (CPP), which is the gradient between intracranial pressure (ICP) and mean arterial pressure (MAP) (equation 2.1). ICP is usually less than 13mmHg while MAP is around

90 mmHg [5]. Equation 2.2 relates CBF with CPP, reflecting the brain's ability to maintain constant CBF over a range of cerebral perfusion (or mean arterial pressures) by means of adapting the cerebrovascular resistance (CVR) [6].

$$\mathrm{CPP} = \mathrm{MAP} - \mathrm{ICP} \tag{2.1}$$

$$\mathrm{CBF} = \frac{\mathrm{CPP}}{\mathrm{CVR}} \tag{2.2}$$

As deducted from equation 2.2, cerebral blood flow changes can be triggered by two different factors: CVR and CPP. CBF changes provoked by MAP alterations and subsequent CPP adaptions are illustrated in **Figure 2-2**. For a MAP range between 60 mmHg and 150 mmHg, CBF is kept constant by means of vasoconstriction or dilatation, i.e. modifying the CVR. In other words, increases in MAP produce CPP increases that are compensated by a reduction in blood vessels diameter (increased CVR) due to the cerebral autoregulation (CAR) mechanism; for MAP values below the autoregulation limits, brain ischemia takes place as vessels cannot achieve a higher dilation, while for MAP values above the upper limit vessels cannot continue reducing their diameter and brain edema or brain hemorrhage would occur.

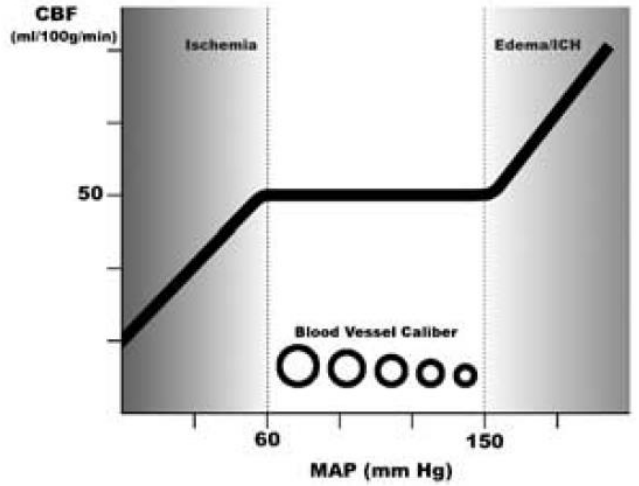

Figure 2-2 Autoregulation mechanism illustration (from [7]).

As stated below, changes in the radius of blood vessels would also modify CBF. In some literature, brain blood flow is modeled as a flow in a tube with the assumptions that it is steady, laminar, and uniform through thinned-walled

non-distensible tubes. However, these assumptions do not apply to large arteries that have thick walls or in the microcirculation in which flow is non-Newtonian [8].

Blood flow can be estimated by Poiseuielle's law, which states that flow is directly related to ΔP (equivalent to CPP in the brain), blood viscosity (η), the length of the vessel (L, assumed to be constant) and the vessel radius (R) to the fourth power [9]:

$$CBF = \frac{CPP\ \pi\ R^4}{8\ \eta\ L} \tag{2.3}$$

Equation 2.3 illustrates the main role of blood vessels diameter in the CBF: even small changes in diameter have significant effects on cerebral blood flow, and it is by this mechanism that vascular resistance can change rapidly to alter regional and global cerebral blood flow. The most relevant factors for vessel caliber changes for the proposed research project are: (a) cerebral metabolism, (b) CO_2 and O_2 blood pressures, and (c) the previously mentioned autoregulation mechanism, but some others such as blood viscosity and temperature are also responsible for the vessel radius. Therefore, a more detailed analysis of those factors is herein provided.

a) Cerebral metabolism: Some authors consider there is a flow-metabolism coupling such that when the brain has an increased demand of glucose and oxygen, CBF raises in a linear fashion in order to be able to supply the substances needed [5] (**Figure 2-3**). However, other authors rely on non-linear models for this coupling, as short oxygen demanding tasks provoke high CBF increases with low $CMRO_2$ changes, while others even state that such coupling does not exist [10][11].

b) CO_2 and O_2 partial pressures: The partial carbon dioxide arterial pressure ($PaCO_2$) shows a sigmoidal relationship with CBF (see **Figure 2-4**): for a very wide range of mean arterial pressures CBF increases linearly with $PaCO_2$ having doubled when the partial CO_2 pressure reaches around 80mmHg. However, if $PaCO_2$ gets very reduced, vasoconstriction is activated to the point that it

could provoke cerebral ischemia [5]. Therefore, $PaCO_2$ has immediate effects in vessel radius and CBF. Nonetheless, partial pressure of oxygen (PaO_2) has little effects, showing a constant behavior while autoregulation is preserved [9].

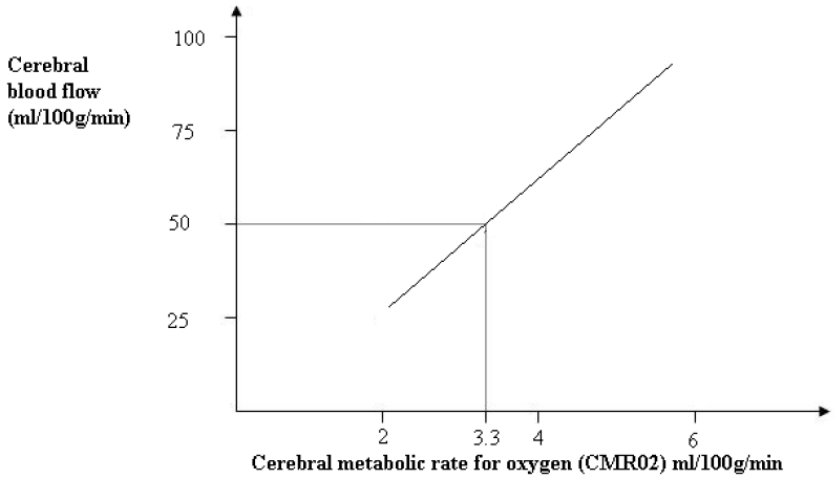

Figure 2-3 Relationship between cerebral blood flow (CBF) and CMRO2 (from [5]). Vertical and horizontal lines refer to average resting values.

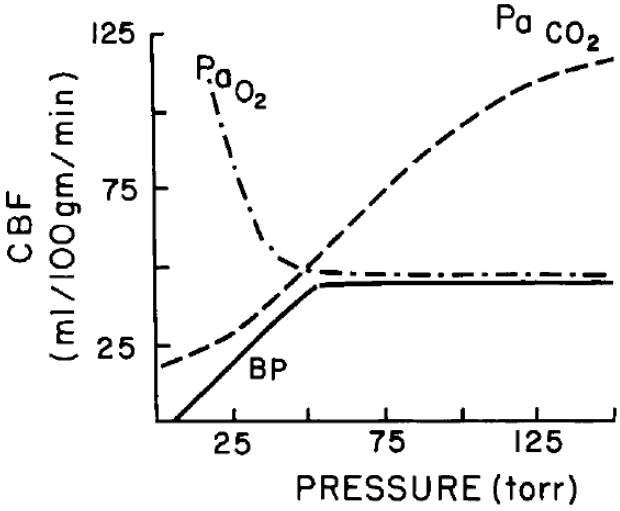

Figure 2-4 Blood pressure (BP), $PaCO_2$ and PaO_2 effects on cerebral blood flow (CBF) (from [9]).

c) Autoregulation: CBF has to be regulated with precision as too much blood can raise intracranial pressure (ICP), which can compress and damage delicate brain tissue, and too little results in ischemia and tissue death. As stated previously, cerebral blood flow autoregulation may be defined as the mechanism that protects the brain against the dangers of hypoxia at low perfusion pressures and against the risks of brain edema at high arterial pressures. Autoregulation therefore serves as a line of defense by helping to maintain constant the cerebral capillary pressure, assuring a steady supply of essential metabolites and simultaneously protecting the blood-brain barrier. Cerebral blood vessels are able to change the flow of blood through them by altering their diameters in a process called autoregulation; they constrict when systemic blood pressure is raised and dilate when it is lowered.

In order to provide some clarifying examples on how CBF gets adapted through autoregulation mechanisms, scenarios of hypercapnia, hyperventilation and apnea will be succinctly described. Those methods are often used for CVR assessment and applied to clinical practice aiming to compensate CBF alterations in critical or anesthetized patients.

Hypercapnia: Carbon dioxide CO_2 has a profound and reversible effect on cerebral blood flow as it causes marked dilation of cerebral arteries and arterioles and increased blood flow, whereas hypocapnia causes constriction and decreased blood flow. A known side effect of hypercapnia is ICP elevation as a consequence of elevated CBF values [12]. In several studies, rheoencephalographic signals (see section 2.2.4) were used to evaluate the role of CO_2 inhalation for the measurement of cerebrovascular vasomotor reactivity [13]. It was seen that the increase of CO_2 inhalation markedly affected the REG signal amplitude, indicating increased CBF. A linear relationship could be established between CO_2 concentration and REG peak amplitude and the raise time of the curve. During the inhalation, increases in REG were significant, while carotid flow and systemic arterial pressure decreased.

Hyperventilation: Acute hyperventilation causes an immediate vasoconstriction effect because of the reduction in CO_2 arterial pressure [14] and the subsequent decrease of CBF. Several studies have published CBF data obtained during hyperventilation episodes: Settakis et al. measured flow velocity during hyperventilation concluding that the maximal effect took place 20 seconds after starting the procedure and at this time it reached a constant value for 40 seconds, time at which the experiment ended. Afterwards, flow velocities recovered achieving the baseline values [15]. Kety and Schmidt [16] published results from passive and active hyperventilation, concluding that both reduced cerebral blood flow while maintained blood pressure values.

Apnea: Episodes of apnea or breath holding reduce the amount of O_2 in blood and therefore $PaCO_2$ increases provoking increases in CBF. Kastrup et al. [17] quantified the effect of an apnea procedure in regional cerebral blood flow measured with magnetic resonance imaging and in average found a regional CBF (rCBF) increase of 47-87%, dependent on apnea duration. This dependence on apnea duration has been confirmed by posterior measurements performed using transcranial Doppler (see **Figure 2-5**) [18]. Apneas and CO_2 inhalation tests for CVR evaluation purposes have been compared in order to find out if results were equivalent and therefore breath holding would be the selected choice as it does not require any CO_2 inhalation: even though both episodes showed comparable images using the blood oxygenation level dependent technique, CBF changes from both tests were not correlated [19].

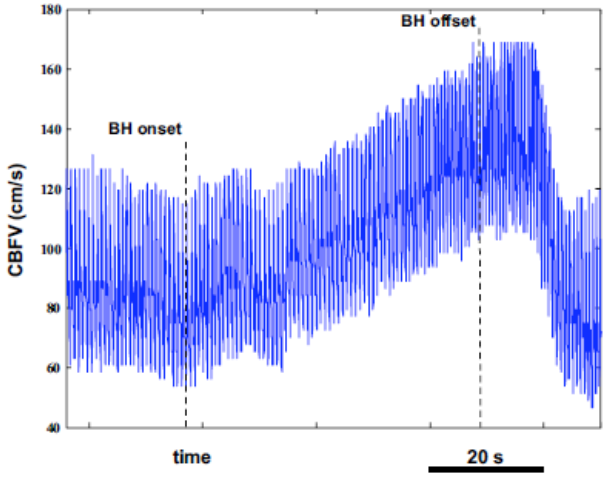

Figure 2-5 Cerebral blood flow velocity (CBFv) recorded by means of Doppler spectra during a breath holding test (from [18]).

2.3 CBF monitoring techniques

The first validated method for cerebral blood flow assessment was developed by Kety and Schmidt in 1945 [20]. Several methods have been developed since then, in order to either quantitatively or qualitatively monitor CBF or its surrogates. This section presents a review on the basic techniques and devices developed for this purpose. As many efforts have been done in this area, the most relevant techniques for the purpose of this project will be analyzed in more detail while others will be just succinctly herein described.

Xenon-133: This is one of the most widely used methods of intraoperative CBF measurement, even considered by many authors as the gold standard [21]. This technique consists in the injection into the internal carotid artery of the radiopharmaceutical Xe133, which is a radioactive agent [22], and its assessment through a Computed Tomography (CT) system. This isotope is a low-energy gamma emitter that diffuses freely through the brain, is temporarily retained in brain tissue and finally released through veins. Thus, it allows to image the lungs and blood flow, particularly in the brain, making it an ideal agent for measurement of CBF or different lung diseases [23]. Nowadays, this technique can be used with inhaled Xe133, making it a non-invasive tool for CBF assessment; however, xenon provokes changes in blood velocity that might influence results [24] and requires the use of a radioactive agent and therefore radiation exposure needs to be taken into account and reduced as much as possible [25].

Magnetic Resonance Imaging (MRI): Even though by the end of the XXth century MRI techniques were not enough developed for brain hemodynamics assessment, they were clearly identified as a very promising tool [25]. Since then, several MRI based techniques have been published for CBF monitoring and quantification, which are extensively used in clinical trials looking for a deeper understanding on brain hemodynamics. They allow both regional and global CBF measurements and are non-invasive, fast and accurate, which makes them a very interesting choice also for diagnostic procedures [26]. Some techniques, as for example dynamic susceptibility weighted imaging, are based on tracing agents followed by MRI imaging, while arterial spin labelling is based on magnetization labeling of water molecules.

Intraoperative Angiography: This method allows to visualize the blood vessels and blood flow during surgery to ensure normal vascular flow before a procedure has been completed, this technique uses a contrasting agent and X-rays to see how blood flows through the brain[27]. Therefore, it is an invasive method that allows a qualitative assessment of the presence and adequacy of CBF. The intraoperative angiography requires of specific settings as the head needs to be fixed and the image intensifier must be placed. The puncture can be done through the carotid or the femoral artery.

Thermal Diffusion Flowmetry (TDF): It is one of the most common invasive methods for monitoring CBF. It is widely used for long-term bedside monitoring of CBF in comatose patients, patients with brain injuries, both during and after surgery. The CBF is determined by measuring the effective thermal conductivity of the cortical tissue, which changes with CBF, using a temperature microprobe implanted in the cerebral region of interest (ROI) (see **Figure 2-6**). Temperature gradients are induced in a volume of interest and the temperature variations recorded [28]. It then measures dynamic changes in cerebral perfusion by converting the value of temperature gradient to ml of blood per 100g of brain tissue per min, ml/(100g.min), in real-time [29]. However, by nature of its design, it could accurately reflect relative changes but not absolute values. Care must be taken not to place the probe on any major surface vessel and the probe must be in contact with the tissue surface to provide valid temperature measurements. Besides its invasiveness, the main disadvantage of thermal diffusion techniques is that they measure cortical blood flow, which is not always representative of total CBF.

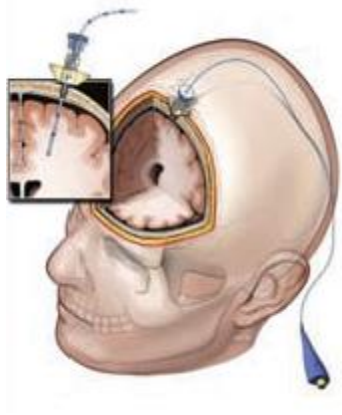

Figure 2-6 Placement of thermal diffusion flowmetry (TDF) probe (from [30]).

Perivascular Flow Probe: This technique has been used routinely for measuring blood flow intraoperatively. It is an invasive method, based on a probe consisting of an electronic flow detection unit and a flow sensing perivascular one, and has a semicircular tip which is positioned in such a way that it contains the vessel of interest within its diameter (see **Figure 2-7**). It then uses ultrasound transit time to measure the blood flow, obtaining a quantitative measure of CBF independent of the flow velocity profile, turbulence or hematocrit [31].

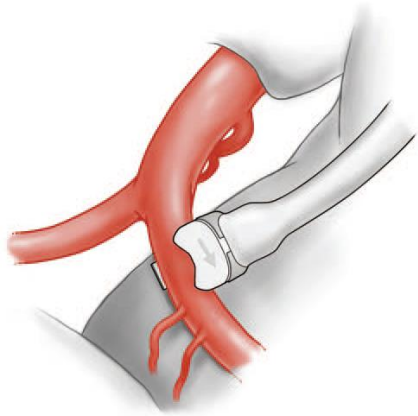

Figure 2-7 Perivascular Flow Probe (from [31]).

Laser Doppler Flowmetry: When using a monochromatic laser light, reflections from moving cells create a frequency shift while other tissues reflect light with the original frequency. Following this principle, laser Doppler flowmetry is able to measure movements from red blood cells. Three variables are provided: the concentration of moving cells (CMBC), their velocity and the flow, which is the multiplication of the other two. Computed values are relative and even though absolute values can be deducted they must be interpreted carefully. It is an invasive technology because it requires probes implantation but has been designed for bedside monitoring [25][21].

Diffuse Correlation Spectroscopy (DCS): This technique uses near infrared light to measure local microvascular CBF. Although it is based on similar principles as the ones applied for Near-Infrared Spectroscopy (NIRS) (see section 2.2.1), the properties of the emerging light provide different results and allow for $CMRO_2$ measurements as well [32]. Even though it can

be applied to different tissues, it has revealed to be useful for CBF assessment, both in CVR challenges [33] and during general anesthesia [34]. It is a non-invasive technology as it uses two probes placed on the forehead, but it is only useful for assessing relative changes in blood flow.

Jugular Bulb Oximetry: This is an invasive method which indicates changes in CBF without its direct measurement. The jugular bulb is the dilated portion of the jugular vein just below the base of the skull and is the preferred site for blood sampling. Here, jugular venous oxygen is an indirect assessment of cerebral oxygen use. It measures arterio-jugular differences of oxygen ($AVDO_2$) and relies on the assumption that CBF and $CMRO_2$ are coupled and therefore related by equation 2.4: if $CMRO_2$ is constant, $AVDO_2$ decreases imply higher CBF. When demand exceeds supply, the brain extracts a bigger amount of oxygen, resulting in a decrease of jugular bulb oxygen saturation. If CBF decreases, a point is eventually reached at which the brain can no longer completely compensate by a further increase in oxygen extraction. At this point, oxygen consumption decreases and anaerobic metabolism starts. On the other hand, when cerebral oxygen supply exceeds demand, oxygen saturation of jugular bulb blood is increased [35]. This technique is invasive and measurements might be influenced by extracranial venous blood, distorting results [25].

$$\mathrm{CMRO_2} = \mathrm{CBF} \times \mathrm{AVDO_2} \tag{2.4}$$

Besides all these relevant techniques, it is also necessary to introduce the utility of electroencephalography (EEG) and somatosensory evoked potentials (SEP) in CBF monitoring. Even though these monitors have not been developed for CBF monitoring purposes, they might be used as surrogates of CBF and for that reason will be included in this review. Brain function is represented in the EEG by neural oscillations at certain frequencies, and due to the fact that pyramidal neurons are exquisitely sensitive to conditions of low oxygen, EEG changes are strongly correlated to CBF decreases. When normal CBF declines, the EEG first loses faster frequencies, then as the CBF decreases, slower frequencies gradually increase. Therefore, EEG detects changes in CBF within seconds and allows for continuous monitoring of these changes over time, which makes it an indirect, non-invasive and qualitative measurement of CBF in patients undergoing surgery. Nevertheless, raw EEG requires interpretation, which is ultimately

subjective, by trained experts, being this the main limitation to this method [36].

SEP consist on the application of an electrical stimulation on the patient's skin over the trajectory of peripheral nerves and the response is monitored, therefore the technique is a non-invasive mean of assessing somatosensory system functioning. Nowadays, SEP are a standard tool for intraoperative neurophysiological monitoring. It is used for clinical diagnosis in patients with neurologic diseases, to evaluate patients with sensory symptoms that might be psychogenic, for prognostication in comatose patients, and for intraoperative monitoring during surgeries that place parts of the somatosensory pathways at risk [37]. But SEP monitoring has also been used to assess the adequacy of CBF, relating the lack of detection of SEP to an insufficient blood perfusion to the brain. Some studies show that, thanks to being relatively resistant to the effect of metabolic insults and drug effects, this technique has a similar or even lower threshold for failure compared to the EEG.

Having briefly described these methods for CBF measurement or assessment, the following sections will introduce the technologies that are most commonly used for noninvasive CBF monitoring (Near Infrared Spectroscopy and Transcranial Doppler), as well as the one this project is based on, rheoencephalography.

2.2.1 Near Infrared Spectroscopy

In 1977 Jobsis [38] first published that brain tissues characteristics made possible a non-invasive measurement of tissue oxygen saturation in real time by means of light in the near infrared spectrum. However, the first United States Food and Drug Administration (FDA) approved device appeared in 1993, was named INVOS 3100® and was developed by Somanetics Corporation (United States)[39].

Near-infrared spectroscopy (NIRS) measures regional brain tissue oxygen saturation (rSO_2) via an emitted near-infrared light that penetrates the scalp and underlying brain tissue and detects the absorption of oxygenated haemoglobin compared with deoxygenated haemoglobin [40]. However, the extent to which light can penetrate in the brain depends on the thickness of

the skull and for this reason this technology works better with neonates than adults, as for neonates [25] penetration is deeper.

Wavelengths used in NIRS are in the 700-850 nm range, as for these light wavelengths the separation between oxygenated and deoxygenated haemoglobin is maximized (see **Figure 2-8**). Even though these wavelengths also prevent from overlap with water, they are quite sensitive to melanin [39].

The measured rSO2 refers to the percentage of oxygenated haemoglobin within the total amount of haemoglobin and is therefore related to the tissue oxygen extraction fraction (OEF). Equation 2.5 [41], where Ca corresponds to average capillary oxygen concentration, illustrates the relationship between the OEF coefficient, cerebral metabolism $CMRO_2$ and cerebral blood flow CBF, from which it can be deducted that NIRS devices measure in fact a surrogate of CBF.

$$\mathrm{OEF} = \frac{\mathrm{CMRO_2}}{\mathrm{CBF} \cdot \mathrm{Ca}} \tag{2.5}$$

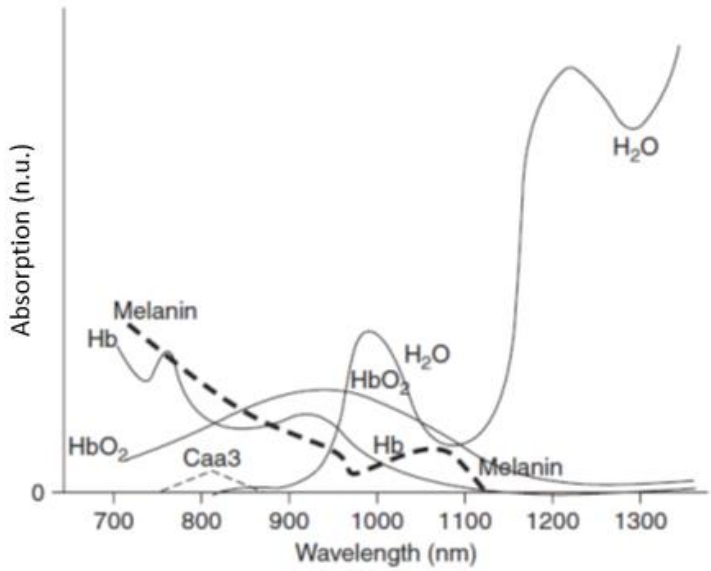

Figure 2-8 Absorption for main substances as a function of light wavelength (from [39]).

NIRS technology is affected by several confounding factors that might be responsible for distorted outputs. For example, the separation between transmitter and receptor is critical: short distances provide low penetrations while longer distances would demand higher power with risk of tissue damage [42] and therefore high penetrations cannot be achieved in adults. Furthermore, in 1996 a clinical study was published in which NIRS measurements were performed in human cadavers [43]: values provided by NIRS technology for one third of the cadavers were values previously obtained for normal subjects. Even though it can be explained by the fact that venous cerebral vessels could still contain blood, it questions the specificity of the technology.

However, a considerable amount of clinical studies have been performed using NIRS technology with promising results. McCormick et al. [44] reported NIRS to be at least as sensitive as EEG for hypoxia detection. Moreover, the use of NIRS as continuous monitoring under coronary artery bypass trying to maintain patients baseline has shown a significant reduction of adverse clinical events [45] and in patients with subarachnoid hemorrhage, vasospasms were associated to reductions in NIRS signal [46].

NIRS provides a non-invasive, real-time, bedside monitoring tool of cerebral oximetry, without exposing patients to radiation as happened with the xenon-133 technique; however, some controversies exist around its ability to assess CBF as it measures a surrogate of blood flow.

2.2.2 Transcranial Doppler

Transcranial Doppler ultrasound (TCD) or Transcranial Doppler sonography was first introduced in 1982 by Aaslid, Markwalder and Nornes [25]. This is a non-invasive technique that measures blood flow velocities in cerebral arteries with high temporal resolution. It uses ultrasound transducers in contact with the surface of the head. When ultrasound waves are reflected by moving objects, a frequency shift takes place allowing the detection of tissue motion and blood flow. As ultrasound waves need to penetrate the skull and lower waves present better penetration, low ultrasound 2MHz waves are used [47]. Applying the Doppler spectral envelope detection technique to the flow returning from the middle cerebral artery, flow indices can be calculated

and displayed in real time providing information concerning perturbations in CBF [48].

The most frequent measurement place is the temporal window as usually the main arteries supplying blood to the brain can be identified in this region [26]. Even though the middle cerebral artery is the one monitored most often, the internal carotid and anterior cerebral arteries can be measured as well.

One of the main disadvantages of TCD is that it measures velocity, not flow, hence it is a surrogate measure for CBF. In an artery with lumen area A, blood flow can be expressed as $BF=V \cdot A$, where V is the cross-sectional flow velocity. However, as vessels anatomy is complex and different among individuals, the obtained values for blood flow are difficult to interpret and not always reliable [25]. Besides this information, TCD also offers three indices related to CVR: a pulsatility index, a resistance index and the ratio between CPP and flow velocity [49].

It is a well-used method for clinical studies although, as mentioned before, it only provides a relative index of CBF with the problematic of not being always reliable. Even so, as equipment evolves, this technique has been used more frequently as an intraoperative monitoring system, as it is portable, non-invasive and allows continuous monitoring. Moreover, it is considered a very useful tool in order to measure anesthetic effects on brain hemodynamics[50].

2.2.3 Rheoencephalography

A rheoencephalograph is defined by the United States Food and Drug Administration (FDA) as "a device used to estimate a patient's cerebral circulation (blood flow in the brain) by electrical impedance methods with direct electrical connections to the scalp or neck area". Therefore, rheoencephalography (REG) is an explorative method of cerebral circulation that measures electrical impedance which allows a continuous observation of the blood flow in different cerebral regions. The principle of this method is that blood is a good electrical conductor, therefore any increase in blood volume will lead to a reduction of the brain electrical resistance, and this will be reflected in a decrease of REG pulse amplitude given a constant current.

The main limitations of REG data processing are the need to clean the signal from various artifacts, such as respiration or movements, the

differences in tissue conductivity, and the lack of absolute measurements of CBF. However, it is a very low cost technique and this is the main reason why it is still attractive for researchers[51]. REG was extensively used during the 60s and 70s, but afterwards its popularity decayed because the provided results were not conclusive from a clinical point of view. Nowadays, with more precise electronics, software capabilities and newer methods for CBF assessment, investigations on REG seem to have restarted [52]. Nevertheless, it is only being used in some countries, as China and Russia, while in the EU and the US is almost ignored. **Table 2-1** shows the rheoencephalographic devices that have been referred in publications of clinical data since the early clinical trials and have been listed and published by Bodo [51].

Table 2-1 Rheoencephalographic devices used for REG clinical trials and excitation frequency used in each case [51].

NAME	FREQUENCY (KHZ)	COUNTRY
Galileo	45	Italy
Medicor	160	Hungary
Cereberus	125	Hungary
UFI	50	US
MIC	100	US

Figure 2-9 shows an average cerebral impedance pulse as recorded by means of a rheoencephalograph, where Δz, the maximum change of blood volume in a heartbeat, is indicated. In order to obtain this results and readings from a REG signal, its amplitude, its first derivative and its integral measurement are most commonly used. This is due to the fact that the information of the signal resides in the variation of the distance between minimum and maximum points of the REG pulse wave, which refers to heart and respiratory activity as well as brain vasoconstriction and vasodilatation [51]. However, as shown in **Figure 2-10**, several extra parameters are extracted from REG curves.

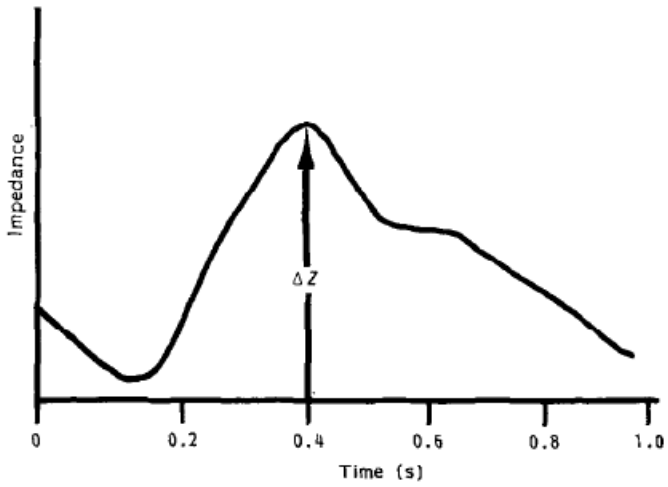

Figure 2-9 Cerebral Impedance pulse (from [53]).

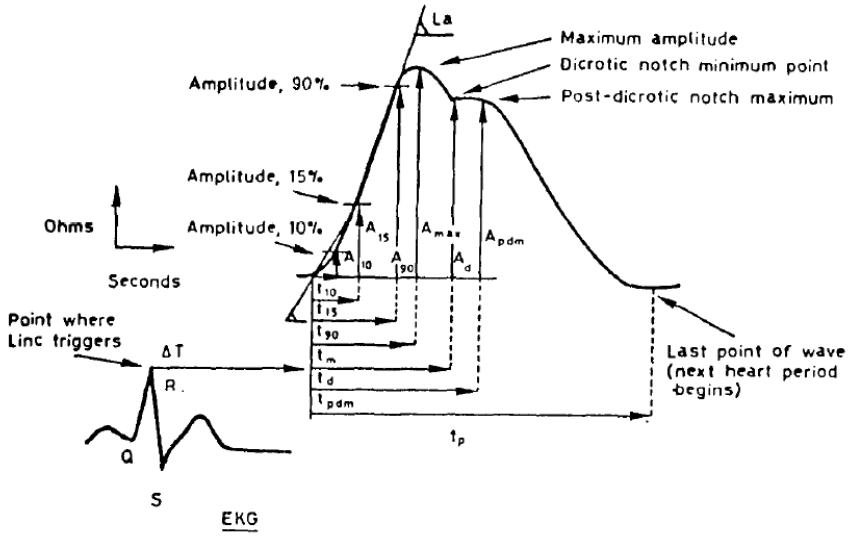

Figure 2-10 Geometric values calculated in a rheoencephalographic curve by a particular software tool, RHEOSYS (from [53]).

The REG technology

Two different configurations have been used for REG devices: the bipolar (REGI) and tetrapolar (REGII) configurations. REGI uses a single

pair of electrodes and impedance is measured with bridge systems, allowing for interferences in between electrodes when placed close, while REGII uses a different pair of electrodes for sending current and sensing impedance, improving the quality of the collected data [54]. For that reason, in this project, a REGII configuration was used for data recording.

Figure 2-11 shows the optimal frequency range to be used for REG recordings, that ideally should be between 60kHz and 100kHz but can be reduced down to 20kHz.These frequencies are determined as a function of γm/γs which is the ratio of electrical conductivity of extracranial tissues (muscles and skin), γf/γp, which is the ratio of electrical conductivities of fluid and structural intracranial compounds, γb which represents changes of electrical conductivity of moving blood and %, that accounts for changes of electrical sensitivity of head skin [52].

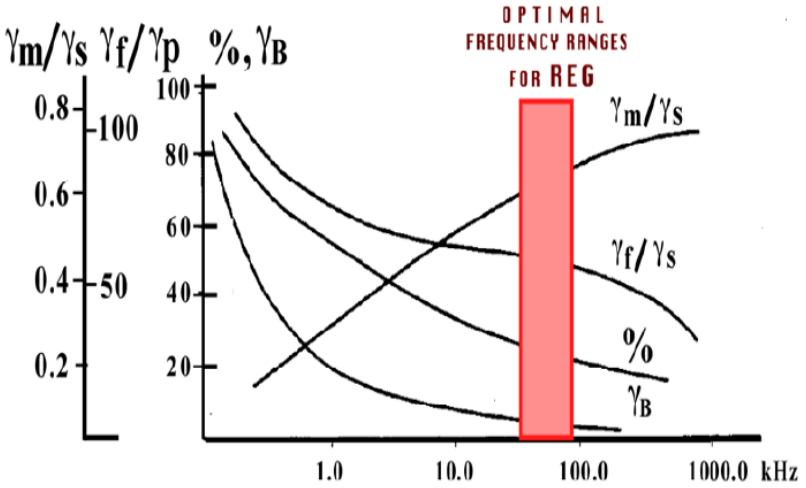

Figure 2-11 Optimal frequency for REG (from [52]).

Lately, several multifrequency approaches have been developed under the assumption that tissues will provide different impedances depending on the signal frequency and therefore recording the cerebral bioimpedance with several frequencies, usually three or four, will provide information on the contribution of each tissue into the final recorded values [55].

One of the problems that REG technologies need to face is the contamination from extracranial tissue in the final readings, as happened with NIRS devices as well [56]. Efforts have been made in order to distinguish from brain tissue and external tissue contribution, developing advanced signal processing algorithms that have the ability to account for those two factors[54], [57], [58]. Besides those solutions, intracranial REG (iREG) measurements have also been performed in animals to overcome this issue [59][60]. However, iREG technique is invasive and is not suitable for CFB monitoring in standard clinical practice.

Clinical studies performed with REG devices

Pathological conditions in the brain typically involve changes in fluid content caused by bleeding, vascular reaction, cerebral volume changes and vessel wall hardening. These changes can cause an increase in ICP and a resulting decrease in CBF. With this in mind, several studies tried to find a relationship between REG and ICP or arterial blood pressure in order to confirm whether this parameter could be used to assess the state of CAR. There is no clear consensus, although in some animal studies, in which REG was used to monitor the lower limit of CAR, correlations between REG and measurements of carotid flow and ICP were confirmed [61].

As mentioned before, a direct correspondence between REG and ICP would allow the use of this methodology as assessment of CAR. That is why there are many studies on this subject, such as one that compared estimates of the lower limit of CAR based on REG signal, with data based on the pressure-reactivity index and visual assessment by an expert in animals during exsanguination [59]. Exsanguination is commonly chosen as a model for CAR assessment as it causes Systolic Arterial Pressure (SAP) to gradually lower and cerebral arteries to maximally dilate until the autoregulation is exhausted. The results obtained were promising as it was observed that amplitude changes in the intracranial REG signal reflected changes in cerebral vascular resistance. These studies confirmed that both REG and iREG reflected CAR and were useful for detecting spreading depression, vasospasm and the lower limit of CAR [62].

It has also been observed that REG pulse amplitude increased as SAP decreased due to arteriolar vasodilation and increased blood volume within the skull. The increased blood volume is demonstrated by increased REG pulse amplitude, due to the fact that blood and even more cerebrospinal fluid

are better conductors than brain tissue [63]. REG has revealed to be useful in assessing cerebrovascular reactivity (CVR) and very useful when combined with functional testing (such as Valsalva, apnea or hyperventilation)[64].

Several trials have compared REG measurements to other methods: it has been published that correlation between cerebral blood flow assessed by transcranial Doppler and the the Xe133 clearance method have shown high correlations, between 0.75 and 0.92. When validating REGII with rCBF obtained with the Xe133 clearance method, a close correlation between both was detected [65]. Another clinical trial with 60 patients suffering from cerebrovascular diseases [66] compared the information provided by cerebral angiography and REG. Results are summarized in **Table 2-2**, suggesting that a high correlation exists between diagnosis performed with the two methods, and with clinical findings as well.

Table 2-2 Angiographic and REG results (from [66]).

CLINICAL, ANGIOGRAPHIC AND REG CORRELATION IN SYMPTOMATIC CEREBRAL VASCULAR DISEASE

Group	*Description*	*Number*
I	Correlation of REG with arteriographic and clinical findings	40
II	Correlation of REG with clinical findings but not with arteriography	6
III	Correlation of REG with arteriography but not with clinical findings	3
IV	No correlation between REG and arteriographic and clinical findings	11

REG assessment has also been evaluated during mental tasks. In a two volunteers study performed during mental tasks and postural stress [67], pulsatile resistance changes (ΔR) and its first derivative ($\Delta R/\Delta T$) were extracted from REG recordings and assessed during the completion of a defined mental task, both being reduced during the procedure. However, EEG changes were not consistent among the two studied subjects. In a larger study, including data from 10 volunteers [53], task complexity was observable in REG recordings as well as in EEG, suggesting that REG and EEG combination might provide valuable information regarding the compensatory responses of the brain.

REG technology has been investigated and applied for combat casualties monitoring. Provided that clinical tests in rats allow to conclude that REG might be a non-invasive tool for global assessment of CBF and not just

regional [68], REG was considered to be a cost effective option for monitoring CBF impairments in soldiers. Even though it cannot compete with MRI or TCD as a diagnosis tool [69], it could be a useful and cost-effective technology as well for continuous CBF monitoring during surgery, to prevent or at least detect brain perfusion changes than could eventually put patients at risk.

2.3 Cerebral blood flow and general anesthesia

2.3.1 Cerebral blood flow during anesthesia

Autoregulation of cerebral blood flow is a fundamental property of the cerebral vascular system to assure adequate oxygenation and metabolism of the brain under changing physiological conditions. In spite of this, the impact of factors such as age or anesthesia on autoregulation remains unclear, although it is a sensitive mechanism and it has been observed to be impaired by different pathologies and by general anesthesia. Anesthetics are known to decrease cerebral metabolism and therefore CBF in a dose-dependent manner, however those effects can be modulated by other factors during anesthesia [70]. Regulation of CO_2 partial pressures have also a direct impact in CBF, suggesting that during anesthesia altering respiratory conditions or administering vasoactive drugs might help maintaining CBF in the adequate range.

There are differences in the influence of anesthetic agents that are currently used in hospitals on cerebrovascular autoregulation, and some studies suggest that volatile anesthetics lead to an impairment of CAR, while intravenous anesthetics preserve it. However, both of them have been proved to reduce cerebral blood flow assessed by transcranial Doppler [71].

Table 2-3 shows the effects of different anesthetics in CVR, CPP, CAR and CO_2 reactivity. It can be deduced from those data published by Engelhard and Werner in 2009 [72], that depending on the anesthetics to be used in a surgical procedure, consequences at a brain perfusion level might be different. This section will review the effects of the most common anesthesia regimens in brain hemodynamics.

Table 2-3 Effects of anesthetic agents on vasodilation / vasoconstriction (CVR), CPP, CAR and CO2 reactivity [72].

	Dilation/Constriction of cerebral vessels	CPP	Cerebrovascular autoregulation	CO_2-reactivity
propofol	vasoconstriction	↑↓	intact	intact
thiopental	vasoconstriction	↑↓	intact	intact
desflurane	vasodilation	↓	impaired	intact
isoflurane	vasodilation	↓	impaired	intact
sevoflurane	(vasodilation)	(↓)	(impaired)	intact
ketamine	vasodilation	↑	intact	intact
dexmedetomidine	vasoconstriction	↓	intact	intact

Sevoflurane anesthesia

Sevoflurane has been proved to provoke a decrease in systemic blood pressure and therefore a decrease in cerebral blood flow and an increase in cerebrovascular resistance [73]. The range of effective CBF autoregulation appears shortened in both young and older patients under sevoflurane anesthesia. Nonetheless, no significant differences have been recorded in the effect of sevoflurane anesthesia on the limits of CAR or the regulatory range for different ages. However, this anesthesia generally results in a shortening of the autoregulatory plateau when compared to awake subjects. Studies have shown an influence of inhalational anesthesia on CBF autoregulation. However, it is not yet clear if the autoregulatory response is altered by aging alone, or due to a combination of aging and inhalational anesthesia [74].

The attenuation of autoregulatory capacity, is a known dose dependent effect of most volatile anesthetics (such as halothane, isoflurane, and desflurane) [75], and is likely due to the strong vasodilatory properties of these volatiles. Therefore, with a higher concentration of a volatile anesthetic, CBF becomes more pressure passive and varies linearly with cerebral perfusion pressure (CPP).

Propofol anesthesia

Compared to inhaled anesthetics, which generally have a depressive effect on autoregulation (except sevoflurane), propofol preserves autoregulation

both at high and low doses in healthy individuals. However, high doses of propofol have been shown to impair cerebrovascular autoregulation in head-injured patients, although this needs to be verified in more studies [76]. In patients with increased intracranial elastance, elevated ICP or in which complex surgical approaches require intraoperative monitoring, propofol intravenous anesthesia remains the first choice. Additionally, hypercapnia has been shown to increase CBF velocity during propofol sedation [77].

When remifentanil is used together with propofol, it induces a dose-dependent reduction of CBF while preserving CBF autoregulation. Therefore, comparing it to other inhaled agents at comparable doses, propofol results in a more profound cerebral vasoconstriction and it does not impair cerebrovascular autoregulation [6]. Total intravenous anesthesia (TIVA) with propofol and remifentanil reduces mean flow velocity when anesthetic dosages are increased and therefore BIS values decreased, suggesting also a reduction of blood flow along with neuronal activity [78].

Comparison between propofol and sevoflurane

Propofol and sevoflurane are the most widely used intravenous and inhaled agents for general anesthesia respectively. They both decrease regional cerebral blood flow (rCBF) in a set of cortical regions and the thalamus [79] at certain concentrations: at 1 minimum alveolar concentration (MAC) for sevoflurane and at the median effective concentration (EC50) dose for propofol. At deeper levels only minor changes were observed, suggesting that drug induced decrease in metabolism or blood flow is related to level of consciousness. Propofol reduced rCBF and $rCMRO_2$ comparably at a BIS value of 40 while sevoflurane reduced rCBF less than propofol but $rCMRO_2$ to a comparable level [80].

Therefore, it can be concluded that at standard dosages for surgery, both preserve autoregulation while decreasing rCBF and $rCMRO_2$. However, for higher concentrations and for brain injured patients, propofol has demonstrated to be safer as it fully preserves the autoregulation mechanisms.

Other anesthetic regimens

Halothane and enflurane are two inhaled general anesthetics. They are no longer in common use, as they have the capability to impair the CAR mechanism. A small dose of this anesthetic reduces the effective range of

MAP over which CBF is regulated. Increasing the depth of anesthesia to 1 MAC at normocapnia totally eliminates effective cerebral autoregulation [81].

Hypotensive epidural anesthesia (HEA) is a technique that reduces blood loss during an operation by significantly lowering the mean arterial pressure (MAP), while providing circulatory support with the simultaneous infusion of epinephrine. Therefore, there is a risk that CBF might be reduced lower than the limit of autoregulation of CBF by this technique in some patients.

A study showed that during an HEA regimen that included circulatory support, CBF was on average well maintained despite the MAP reduction. However, responses were very variable to HEA, leading to a 12% of subjects experiencing a reduction of CBF velocity greater than 30% and were therefore, probably close to the limits of cerebral ischemia.

Spinal anesthesia is regional and involves the injection of a local anesthetic into the subarachnoid space. It has been documented that a small dose of this anesthesia induces a significant modification in CBF in very elderly patients. These results lead to think that higher doses may be harmful to the autoregulation in elderly patients, as it has been demonstrated for global hemodynamic changes after spinal anesthesia [82].

In conclusion, this type of anesthesia induces a statistically significant reduction in middle cerebral artery velocity in elderly patients. This could be explained by a decrease in arterial blood pressure which then impairs CAR in elderly subjects. However, this small changes in CBF velocity are not likely to have relevant clinical consequences.

Additional drugs administered during general anesthesia

General anesthesia has three main components: hypnosis, responsible for patient's unconsciousness, analgesia, to prevent pain, and muscular blockade, to facilitate intubation and to avoid any involuntary movements interfering with the surgery. The combination of these three components is necessary to guarantee a safe and effective anesthesia. Moreover, since the drugs used for this purpose might provoke hemodynamic changes, several other drugs are administered during anesthesia to ensure hemodynamic stability.

The effects of propofol - and its combination with remifentanil – in CBF have been previously discussed. Regarding the use of Neuromuscular

Blocking Agents (NMBA), one the most commonly used is rocuronium, a non-depolarizing agent with quick onset and intermediate duration [83]. Several authors have analyized the effects of rocuronium and other NMBA on hemodynamics, concluding that even tough it can potentially increase heart rate, it does not provoke any clear hemodynamic instability at intubation dosages[83]–[85], even in critically ill patients undergoing cardiac surgeries.

During anesthesia, together with the drugs needed to provoke hypnosis, analgesia and muscular block, vasoactive drugs are administered to maintain stable hemodynamic conditions. For instance, atropine is used to recover from bradycardia, which is often provoked by the hypnotic propofol [86]. The effects of atropine in CBF remain unclear: a clinical study in baboons concluded that atropine did not have any effect in CBF [87] while a study in humans suggested that atropine attenuated cerebral vasodilation response [88]. Since atropine provokes an increase in HR, its administration will be considered as a possible factor for CBF regulation in this Thesis.

Another drug commonly used during anesthesia is ephedrine, which is administered to prevent or compensate for hypotension and bradycardia produced by hypnotics and opioids [89]. Ephedrine during general anesthesia has proved to increase MAP but without affecting CBF and cerebral oxygenation[90], [91].

Besides the effect of the drugs administered during general anesthesia in CBF, other events might also alter the blood supply to the brain, as for example patient positioning [92]. Kose at el. [93] published the influence of head and body position in CBFv, concluding that it affects cerebral perfusion and ICP. Kim et al. [94] analyzed the effect of patient positioning in gynecological laparoscopic surgeries, proving an association between the Trendelenburg position and cerebral desaturation, changes in ICP and CBF. Furthermore, passive leg raise (PLR) rest is used as a ressucitation technique since it has proved to help out increasing cerebral perfusion improving the CBF conditions in critically ill patients [95].

Considering all those factors affecting brain perfusion during anesthesia, CBF should be the result of the effects of positional changes, selection of drugs used and their dosages, cerebral metabolsim and other aspects related to pateint condition and the type of surgery being carried out.

2.3.2 EEG monitoring

The electroencephalogram (EEG), which results from the addition of the activity of millions of neurons in cerebral cortex [96], is known to reflect changes provoked by anesthetics in the brain. In 1950, Falconer and Bickford [97] related EEG electrical power with changes in anesthetic dosages using a time domain approach and this is still nowadays a research topic in the biomedical field.

EEG is divided in several frequency bands which are representative of different patterns and are widely used by the scientific community (see **Table 2-4**) [98]. EEG changes produced by anesthetics are based on frequency shifts among the referred bands as well as amplitude changes.

Table 2-4 EEG frequency bands.

NAME	FREQUENCIES (HZ)
Delta (δ)	0.5 – 3.5
Theta (θ)	3.5 – 7.0
Alpha (α)	7.0 – 13.0
Beta1 (β1)	13.0 – 30.0
Beta2 (β2)	30.0 - 50.0

Awake humans, while maintaining eyes closed to avoid blinking artefacts, present a predominant rhythmic α activity [99]. When low doses of propofol are administered, energy in the β bands paradoxically increases, as this reaction is common during excitation states [100]. Increased propofol dosages will provoke a shift towards α, θ and δ bands with simultaneous amplitude increases, as well as an increase of the full power of the EEG spectrum [101]. Administering even more propofol would elicit a burst suppression pattern, which consists on the alternation of almost flat EEG sequences and bursts. Those frequency patterns herein described, and the corresponding amplitude shifts, are reversed at recovery of consciousness.

Besides the analysis of the changes in each frequency band, two parameters have also been studied as indicators of loss of consciousness: the spectral edge frequency and the median frequency, corresponding to the frequencies below which 95% and 50% of the total power of the spectrum is

confined. Both of them are decreased during anesthesia induction and increased at recovery [98] [102].

During the last decades several indices have been developed based on EEG analysis and aiming to reflect patient brain status during general anesthesia and sedation. The most widely used depth of anesthesia index is the bispectral index, BIS, developed by Aspect Medical. It is based on bispectral analysis of the EEG [98][103] and has been used as a reference for evaluating the pharmacodynamics of propofol [104]. The qCON index (Quantium Medical, Mataró, Spain) is another index for depth of anesthesia assessment that uses spectral EEG analysis to evaluate the effects of hypnotics in the brain and has been proved to be equivalent to BIS in loss of consciousness detection [105]. The qCON index, as well as the energy in the aforementioned frequency bands, will be used in the scope of this project to assess depth of anesthesia and to related it to cerebral blood flow changes.

2.3.3 Propofol pharmacokinetic models

Propofol is one of the most used anaesthetic agents in clinical practice, because of the short action, fast effect and few side effects [106]. It is administered intravenously, often combined with intravenous opioids such as remifentanil, resulting in a total intravenous anesthesia (TIVA).

Different pharmacokinetic models have been developed in order to describe how propofol is distributed through the human body. The most commonly used are the Marsh model [107] and the Schnider model [108]. They are both based on a three-compartment model, i.e. a system composed by homogeneous units (or compartments) that exchange substances based on the principle of mass conservation. **Figure 2-12** shows an example of a compartment i receiving a determined amount of drug (d(t)), with current concentration (C_i), eliminating part of it with a k_{i0} rate, and exchanging the substance with another compartment j (with rates k_{ij} for the drug going from i to j and rate k_{ji} for the drug going from j to i).

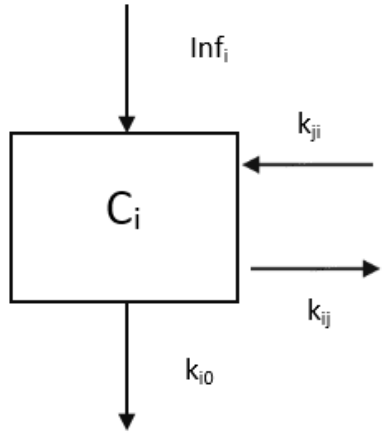

Figure 2-12 Description of one compartment.

As stated before, both Marsh and Schnider models are based in a three-compartment approach, in which compartment 1 corresponds to the central compartment (plasma), compartment 2 to highly perfused tissues and compartment 3 to scarcely perfused tissues. Propofol is therefore directly administered to compartment 1 and redistributed among compartments 2 and 3 while a percentage of it is achieving the target organ, in this case, the brain (**Figure 2-13**).

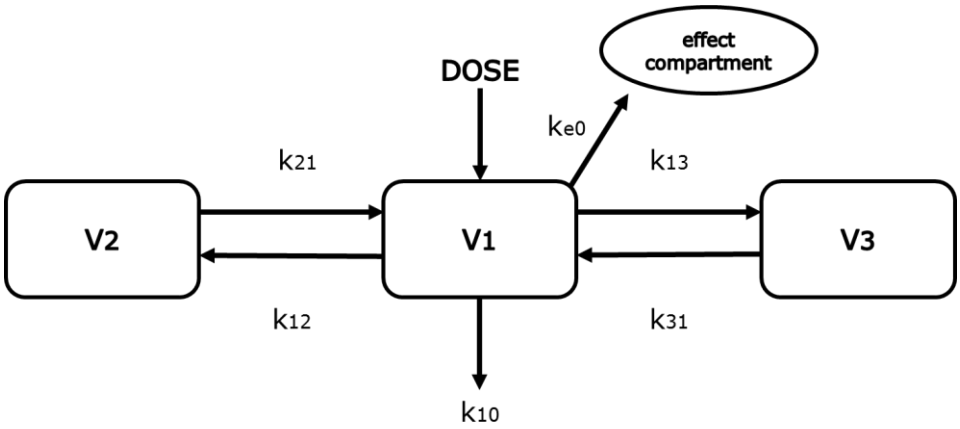

Figure 2-13 Three compartment model.

Under those assumptions, a differential equations system is defined accounting for all the drug exchanges among compartments for each time interval, resulting in the final equations 2.6 and 2.7 used to compute the plasmatic and effect site concentration values. The plasmatic concentration (C_p) refers to the concentration in the first compartment while the effect site concentration (C_e) refers to the concentration in the target organ.

$$\frac{dC_p(t)}{dt} = \dot{C}_1(t) \tag{2.6}$$

$$\frac{dC_e(t)}{dt} = k_{e0}C_1(t) - k_{e0}C_e(t) \tag{2.7}$$

Even though both Marsh and Schnider models rely in the same three compartment assumption, their performance is different because the constants that characterize the model are not coincident. While the Marsh model uses constant k_{ij} rates for drug transfer among compartments and compartment volumes only depending on the patient weight, the Schnider model adapts those transfer rates to patient characteristics and considers different compartment volumes (See **Table 2-5** and **Table 2-6** for details).

Table 2-5 Compartment volumes in Marsh and Schnider models.

COMPARTMENT	MARSH MODEL (L/KG)	SCHNIDER MODEL (L)
V1	0.228	4.27
V2	0.463	18.9-0.39*(age-53)
V3	2.893	238

Table 2-6 Kij values for Marsh and Schnider models.

TRANSFER RATES	MARSH MODEL (MIN^{-1})	SCHNIDER MODEL (MIN^{-1})
K_{10}	0.119	0.443+0.0107*(weight-77)-0.0159*(LBM-59) + 0.0062*(height-177)
K_{12}	0.112	0.302-0.0056*(age-53)
K_{13}	0.042	0.196
K_{21}	0.055	(1.29-0.024*(age-53))/(18.9-0.391*(age-53))
K_{31}	0.0033	0.0035
K_{e0}	0.26	0.465

Those differences in model definitions are responsible for the differences in the predicted plasmatic and effect site concentrations. Several clinical studies have been designed in order to evaluate the differences between the two models, mainly when anesthesia is administered via target control infusion (TCI): a system that given the target concentration desired in the target organ computes de infusion rate needed for that purpose.

For instance, Absalom et al. [109] concluded that in determined set of patients both models can differ substantially and attention should be payed when used under TCI conditions because performances were very different and for example the Schnider model should not be used with target C_p concentrations. Sivasubramaniam [110], in his review of pharmacokinetic models for TCI, clearly stated that due to the differences between the two models, Marsh model should be used with plasmatic concentration targets while the Schnider model was most suitable for effect site concentration targets.

Besides the comparison between the two models, several publications have debated the appropriate value for the k_{e0} constant, which is the rate that

modulates propofol going from the first compartment to the target organ and is therefore related to the propofol time effect as well as to the equilibrium between plasmatic and effect site concentrations (see equation 2.6). The original model from Schnider proposed a k_{e0} value of 0.456 min-1 [108], while Gambús et al. obtained 0.122 min^{-1} [104]; furthermore other studies have published 0.16 min-1 for young adults [111] and 0.3 min^{-1} in different age groups [112]. In each case different populations and surrogates have been used to obtain the final k_{e0}. It is also known that pharmacokinetic models present a significant accuracy errors when evaluated on a particular population sample [113] and this would also explain those differences.

It is common to use EEG changes and/or depth of anesthesia indices as the reference for k_{e0} calculations, as they are considered surrogates of the anesthetic effect. Moreover, as stated before, propofol is known to decrease $CMRO_2$ and CBF, and these effects are translated into EEG alterations. Therefore, one could consider that k_{e0} should not be constant but dependent on the cerebral blood flow, which is one of the hypothesis evaluated along this Doctoral Thesis.

2.4 Signal processing techniques for REG analysis

As previously presented in this chapter, signal processing applied to REG recordings has been based in the extraction of geometric features from its pulse wave and the study of their evolution over time under certain clinical conditions. This is a similar approach to the one taken for thoracic bioimpedance [114], [115] and photoplethysmography recordings [116], [117], that share with REG a similar pulse waveform. However, other signal processing techniques are needed to further explore in depth the ability of REG waves to reflect CBF changes.

Biomedical signals, due to their intrinsic characteristics, often require to be processed with alternative methods to extract the information they contain. For instance, signal processing in the frequency domain is usually performed applying the Fast Fourier Transform (FFT). However, this technique requires stationarity and linearity, while physiological signals are typically stochastic, nonlinear and not stationary [118]. Therefore, different approaches in the frequency domain have been developed to overcome those constraints and

have been extensively applied to biomedical signals, such as Time Frequency Distributions (TFD) and wavelets.

For example, wavelets have been used to identify epileptic seizures in EEG signals [119] and to enhance peaks detection in photoplethysmography [120]. In other publications, TFD were successfully used to model upper airway obstructions when applied to respiratory signals [121] or were part of an EEG based emotions recognition system [122].

Even though results provided relevant clinical outcomes, elevated computational times are required by both wavelet [123] and TFD analysis [124]. Since algorithms developed under the scope of this Thesis are to be applied to a real time CBF monitor, techniques with low computational efforts are needed to be able to monitor patients in real time. For that reason, other options suitable for real time monitoring of physiological signals should be explored.

Biomedical signals are typically nonlinear and can be defined as the result of the combination of the action of many multidimensional control loops [125]. Therefore, nonlinear signal processing techniques might be an appropriate strategy to analyze REG signals and explore the possibility of using them as an additional source of information for anesthesiologists to monitor the effects of anesthesia in patients undergoing clinical procedures.

Within the field of time series nonlinear analysis, many features have been developed for signals characterization, such as the Lyapunov exponents, fractal dimension, Poincaré plot analysis or entropy. Lyapunov exponents, fractal dimension and the entropy metric ApEn were successfully applied to EEG signals for epilepsy detection [126] and to HRV signals to measure the effects of mobile phone radiation in cardiac health [127]. However, both the fractal dimension calculation [128] and the determination of the Lyapunov exponents require extensive computational efforts [129]. Hence, they could be a powerful tool for post-hoc analysis but are not the optimal solution for patient bedside monitoring. In contrast, within the set of nonlinear algorithms applied to biomedical signals, Poincaré plot analysis has shorter computation times and has also been extensively used in physiological signal processing, namely in HRV analysis [130], hence being a suitable tool for REG analysis.

Even though none of those algorithms has been applied to REG signals, some authors have studied their performance in processing similar data, such

as intracranial pressure (ICP) recordings. Di Ieva et al. [131], in their review of existing methods for ICP analysis, concluded that the analysis of the nonlinear dynamics is a promising research field to improve patient bedside monitoring. Moreover, other authors have published their investigations on the nonlinear processing of ICP signals. For instance, Lu at al. [132] used multiscale entropy applied to ICP recordings to study their complexity in brain injured patients, concluding that multiscale entropy was a good predictor of mortality and favorable outcome in those patients. Another entropy metric, Apen, was selected by Hornero et al. [133] to analyze ICP signals in the pediatric population, providing evidence that decreased complexity in ICP was related to events of intracranial hypertension.

In the scope of this Doctoral Thesis, considering the underlying nonlinear behavior governing biomedical signals and the need for real time algorithms to be embedded in a standalone device, the selected algorithms for REG signal processing were Poincaré plot analysis and entropy, since they have proved to be effective for HRV and EEG monitoring even when there is no clear evidence on the chaotic behavior of the signals [134]. Therefore, algorithms for Poincaré plot analysis and entropy metrics were developed to quantify their ability to track CBF changes. Moreover, the performance of those nonlinear techniques was compared to the outcome of the traditional REG processing by means of the extraction of geometric features from the time domain signal.

Chapter 3

Clinical Datasets

Abstract

This chapter aims to present all datasets used for the development of the algorithms contained in the present PhD Thesis. Information on the clinical trials design, data collection methodology and a general description of the recorded data are provided.

3.1 Introduction to Clinical Trials

Due to the lack of publicly available datasets of REG signals, the design and execution of clinical trials was performed under the scope of this Doctoral Thesis. The common objective of the three clinical trials herein presented was the collection and analysis of REG signals under clinical conditions known to provoke changes in brain hemodynamics. The two scenarios chosen for that purpose were (a) awake healthy subjects carrying out breath holding exercises and (b) patients undergoing elective surgeries under general anesthesia.

All the clinical trials were designed and executed in cooperation with Hospital CLÍNIC de Barcelona. The specification of the primary and secondary objectives, the study population to be enrolled, the study design and methodology and all safety concerns and risk analysis were defined by the multidisciplinary team involved in this research project. The main design details, as well as the methodology and the description of the collected data, are presented along this chapter.

3.2 Ethical Considerations

All clinical trials under the scope of this thesis have been performed following the principles of the Declaration of Helsinki [135] and the ISO standard on *Clinical investigation of medical devices for human subjects -- Good clinical practice*, ISO 14155:2011 [136]. Clinical protocols were approved by the Ethical Committee of the Hospital CLÍNIC de Barcelona with protocol number (2013/8356). All participants were informed about the study and gave their written consent prior to participation.

3.3 Apnea-Baseline Database

3.3.1 Clinical Protocol Rationale

The objective of this clinical trial was to record REG data during a respiratory challenge, consisting on the alternation between apnea and resting periods, to analyze the differences in REG waves provoked by the apnea episodes. In order to limit the number of possible confounding factors, inclusion criteria required healthy young volunteers, with ages on the range of 18 to 40 years old. The study was observational and retrospective.

3.3.2 Recorded Data Description

Sixteen young healthy volunteers were enrolled in this observational study. Details of the participants are reported in **Table 3-1**.

Table 3-1 Participants demographic data. Gender is provided as an absolute frequency. Age, height, weight and body mass index (BMI) are provided as mean ± standard deviation.

APNEA-BASELINE PARTICIPANTS DEMOGRAPHIC DATA	
Gender (male/female)	8/8
Age (years)	25.4 ± 3.6
Height (cm)	166.8 ± 8.3
Weight (kg)	59.6 ± 6.8
BMI (kg/m^2)	21.3 ± 2.1

The qCO monitor (Quantium Medical, Barcelona, Spain) was used to monitor the cerebral bioimpedance signal for CBF estimation. Four pre-gelled standard Ag/AgCl ECG electrodes were placed on the subject temples and connected to the qCO monitor through a patient cable. Data from the monitor were continuously collected at a sampling rate of 250Hz.

The subjects were monitored in supine position for 8 minutes repeating twice the sequence of 3 minutes at rest followed by 1 minute of breath holding (**Figure 3-1**). Subjects were asked to avoid talking, movements and blinking, since those would provoke artifacts in the recorded signals. Apneas were planned to stand for 1 minute, however volunteers were instructed to stop earlier if needed and raise their hand to communicate to the investigator that the apnea period was over.

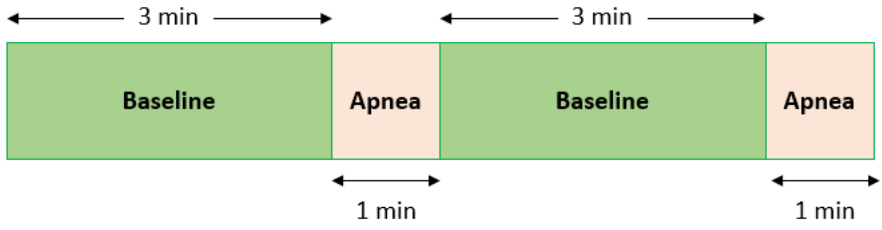

Figure 3-1 Sequence of breath holding (apnea) and baseline episodes.

All events susceptible of creating artefacts in the signal, such as coughing or swallowing, were annotated in a customized software developed for qCO data collection to guarantee synchronism with the recorded REG signals. In addition, events corresponding to the beginning and to the end of the apnea period were also annotated.

REG recordings and demographic data of the patients were anonymized and assessed for completeness and integrity prior to their analysis through advanced signal processing techniques.

3.4 General Anesthesia Dataset 1

3.4.1 Aims of the Protocol

The objective of this clinical trial was to record REG data during elective surgeries performed under general anesthesia and analyze their evolution when compared to the events taking place along the surgery and other physiological data recorded simultaneously. Exclusion criteria considered were cardiac or neurosurgeries, as well as traumatic brain injuries. This clinical trial was observational and retrospective: no clinical decisions were made based on the output of the qCO monitor.

3.4.2 Recorded Data Description

Forty female patients undergoing elective surgeries were enrolled in this clinical trial. A summary of the demographic data of the participants in the study is provided in **Table 3-2**. All patients were scheduled for elective gynecological surgeries under TIVA with propofol and remifentanil.

Table 3-2 Patients demographic data. Age, height, weight and body mass index (BMI) are provided as mean ± standard deviation.

GENERAL ANESTHESIA DATASET 1 PATIENT DEMOGRAPHIC DATA	
Age (years)	50.9 ± 15.9
Height (cm)	160.7 ± 6.5
Weight (kg)	68.9 ± 13.4
BMI (kg/m^2)	26.7 ± 5.0

At their arrival in the operating room (OR), all sensors needed for patient monitoring were prepared and attached to the patient. Additionally, an intravenous cannula was placed to allow the administration of anesthesia and

other drugs as required. Anesthesia was induced by means of a TCI system (Base Primea, Fresenius Kabi, Germany), with an average target dose of 5.9 μg/mL of propofol (ranging from 5 to 7μg/mL) and 3.7 ng/mL of remifentanil (ranging from 2 to 6.2 ng/mL). Once loss of consciousness was assessed as the loss of eyelash reflex, patients were preoxygenated to prepare for intubation. Laryngoscopies were only performed in case the use of laryngeal masks (LMA) was not recommended. In those cases, patients received a 30mg bolus of rocuronium 2 minutes before intubation. Airway management through LMA required lower bolus of either 10mg or 20mg of rocuronium in 8 patients.

After intubation, anesthetic dosages were reduced for maintenance to an average propofol concentration of 3.4 μg/mL of propofol (from 2.5 to 4.3 μg/mL) and 3.4 ng/mL of remifentanil (from 2.3 to 4.5 ng/mL). The dosages of both drugs were adjusted as required during the whole anesthetic procedure. Patients were placed in supine position for the surgery: 25% of them (10 out of 40) remained in the horizontal plane for the whole procedure while 12.5% (5 out of 40) were placed in the Trendelenburg position and in 62.5% of cases (25 out of 40) patient legs were raised during the procedure.

During the surgeries, other drugs were administered either to prevent pain (Methadone) or to preserve hemodynamic stability (Atropine, Ephedrine). **Table 3-3** presents the occurrence of the administration of those drugs.

Table 3-3 Drugs administered during surgical procedures.

DRUGS ADMINISTERED	
Propofol	40/40 (100%)
Remifentanil	40/40 (100%)
Rocuronium	18/40 (45%)
Atropine	9/40 (22.5%)
Ephedrine	3/40 (7.5%)
Methadone	10/40 (25.0%)

Patient monitoring consisted on the use of a Depth of Anesthesia device, the Conox (Fresenius Kabi, Germany), an electrical bioimpedance monitor for REG data collection, the qCO (Quantium Medical, Barcelona, Spain) and a hemodynamic monitor providing information on the heart rate, systolic

blood pressure (SBP), diastolic blood pressure (DBP) and mean blood pressure (MBP).

Data from those monitors, as well as data from the TCI pumps, were recorded through the RugloopII© software (Demed, Belgium). Moreover, annotation of relevant events during the surgical procedure was performed through the same software, to make sure the occurrence of those events was synchronized with all other clinical data. Once patients were discharged, collected data were checked for anonymization and recorded for further analysis. No adverse events were detected throughout the clinical trial.

3.5 General Anesthesia Dataset 2

3.5.1 Aims of the Protocol

The objective of this clinical trial was to extend the available dataset of REG signals during general anesthesia and to confirm the findings with the previous dataset and increase the statistical power of the results obtained. As for the other clinical protocols described in this section, this clinical trial was observational and retrospective: no clinical decisions were made based on the output of the qCO monitor.

3.5.2 Recorded Data Description

Ninety female patients were enrolled in this clinical trial. Two of them were discarded due to technical reasons, resulting in a final dataset composed by 88 patients. Summarized demographic data are provided in **Table 3-4**.

Table 3-4 Patients demographic data. Age, height, weight and body mass index (BMI) are provided as mean ± standard deviation.

GENERAL ANESTHESIA DATASET 2 PATIENT DEMOGRAPHIC DATA	
Age (years)	49.5 ± 16.4
Height (cm)	161.3 ± 7.0
Weight (kg)	68.1 ± 13.9
BMI (kg/m^2)	26.2 ± 5.2

The clinical procedures and the protocols for data collection in this clinical study are analogous to those previously presented for the General Anesthesia Dataset1. Initial dosage of propofol at anesthesia induction was 5.8 μg/mL (ranging from 4.8 to 7 μg/mL) and was administered together with

remifentanil targeted at 3.8 ng/mL (ranging from 2 to 6.2 ng/mL). After induction, those target dosages for propofol and remifentanil were reduced to 3.4 μg/mL (from 2.5 to 4.3 μg/mL) and to 3.4ng/mL (from 2.3 to 4.5 ng/mL), respectively. From the 88 patients suitable for analysis, 22 were intubated through laryngoscopy while in the remaining 66 an LMA was used. Regarding patient positioning, 24 patients (27.3%) were kept in the horizontal plane for the whole procedure, while passive leg raising took place in 51 cases (57.9%) and 13 participants (14.8%) were placed in Trendelenburg position.

The same set of drugs was used for anesthesia management and control of hemodynamics. The occurrence of administration of each drug is specified in **Table 3-5**.

Table 3-5 Drugs administered during surgical procedures.

DRUGS ADMINISTERED	
Propofol	88/88 (100%)
Remifentanil	88/88 (100%)
Rocuronium	43/88 (48.9%)
Atropine	16/88 (18.2%)
Ephedrine	7/88 (7.9%)
Methadone	16/88 (18.2%)

All patients were monitored from 3 min prior to the anesthesia induction until 3 minutes after extubating. At that time, sensors were disposed, patients discharged, and data anonymized and stored for retrospective analysis. No adverse events were detected throughout the clinical trial.

Chapter 4

Optimal parameters for noise reduction algorithm based on local geometric projections of REG signals

Abstract

Physiological signals are known to be affected by noise. This chapter compares several methods for signal preprocessing to filter out interferences from REG signals collected during anesthetic procedures, in order to identify the algorithm and parameters optimizing the noise cancellation process.

4.1 Introduction

The recording and processing of biomedical signals in the operating rooms have improved patient care during the last decades. One of the most critical steps for vital signs monitoring is the identification and rejection of noise embedded in the recorded signals. In clinical settings, the noise sources can be classified into noise coming from the electronics used by the recording system, environmental noise provoked by power line and other devices emitting radiations, and interferences originated by physiological processes other than the one under assessment [137].

In particular, REG signals are affected by electrooculogram, respiration, movements and facial electromyography, as well as by surrounding electrical equipment and power line interferences. Literature on the noise embedded in REG signals is scarce. However, lots of efforts have been made to overcome the difficulties in filtering photoplethysmography waves (PPG), that share many properties with REG signals since they both record a similar waveform resulting from the circulation of the blood through the vessels, also known as pulse waves.

Several publications provide indications on how to remove respiration interference with adaptive filters or wavelet based filters [138]–[141]. However, the most commonly used solution relies on bandpass filters, even though they are not always able to get rid of noise preserving the pulse wave intact [142]. Stuban and Niwayama published their work [143] analyzing the optimal filter bandwidth for pulse oximetry, concluding that the best cut-off frequency to be chosen was the one closest to the fundamental frequency of the signal, obtaining a sinusoidal wave that contained enough information to estimate the O_2 concentration in arterial blood, despite the fact that the dicrotic notch was filtered out as well.

One of the most commonly used filters is the Butterworth filter [144]–[146]. Elgendi et al. [144] used in their work a zero-phase second order Butterworth filter with bandpass from 0.5 to 15 Hz. In other publications, a Butterworth filter of order 2 and phase zero was used but with different bandwidths (0.5 to 8 Hz in [145] and 0.5 to 7Hz in [146]). Even though the selection of the cut-off frequencies was detailed, the order of the filter was not supported by any justification.

Chebyshev filters have also been used to filter PPG signals. A Chebyshev Type I, zero-phase, of order 6 with cut-off frequencies of 0.3 and 12 Hz was used in [147], while Chebyshev Type II filters were used by Kubicek et al.[148]:

PPG waves were filtered with a 5th order Chebyshev Type II with 90 dB of attenuation in the stop band. Moreover, elliptic filters[149], median filters [149], [150], and Hamming-based Finite Impulse Response filters [149], [151] were also applied to PPG signals in several publications.

Liang et al. [149] systematically tested the signal quality obtained by using nine types of filters to analyze which filter and parameters optimized the recovered PPG signal. They concluded that the best signal quality was obtained with a Chebyshev Type II 4th order filter, which outperformed all other filtering options tested.

Analogously, the objective of this chapter is to find the best filter for REG signal processing, which cancels out noise while preserving the pattern of the REG waves. This will be done comparing two different methods: (1) in the linear domain, selecting the best classical filter (Butterworth, Chebyshev or elliptic) for this dataset and (2) in the nonlinear domain, using local geometric projections of REG signals. This method is based on the one originally published by Cawley and Hsu [152] and later applied by other authors in RR signals [153].

4.2 Methods

Physiological signals need to be filtered to remove noise related to non-physiological sources or to physiological signals that are not desired in a specific application. Unwanted signals shall be cancelled while preserving an undistorted representation of the targeted signal. Aiming at identifying the optimal filter for REG signals, linear and nonlinear noise reduction algorithms were compared. In this section, all filters tested are described, followed by the methodology applied to generate the reference signals used to evaluate the filters and the assessment of the performance of each algorithm.

4.2.1 Classical time domain filters

Typically, time domain classical filters are used for noise removal. In this chapter, Butterworth, Chebyshev (Type I and Type II) and elliptic filters were evaluated, searching, in each case, the optimal set of parameters for REG signals: filter order (n), cut-off frequency (ω_c) and attenuation (Rs and/or Rp).

A review of the main characteristics and analytic expressions [154] is provided in this section.

The Butterworth filter is characterized by a flat response in the passband followed by a monotonic decrease for frequencies above the cut-off frequency. The squared transfer function of a low pass filter is shown in **Figure 4-1**(a) and its analytic formula can be written as:

$$|H(j\omega)|^2 = \frac{1}{1 + \left(\frac{j\omega}{j\omega_c}\right)^{2n}} \tag{4.1}$$

where n is the order of the filter and the cut-off frequency is ω_c. It is worth noting that higher orders provide sharper transitions between the passband and stopband.

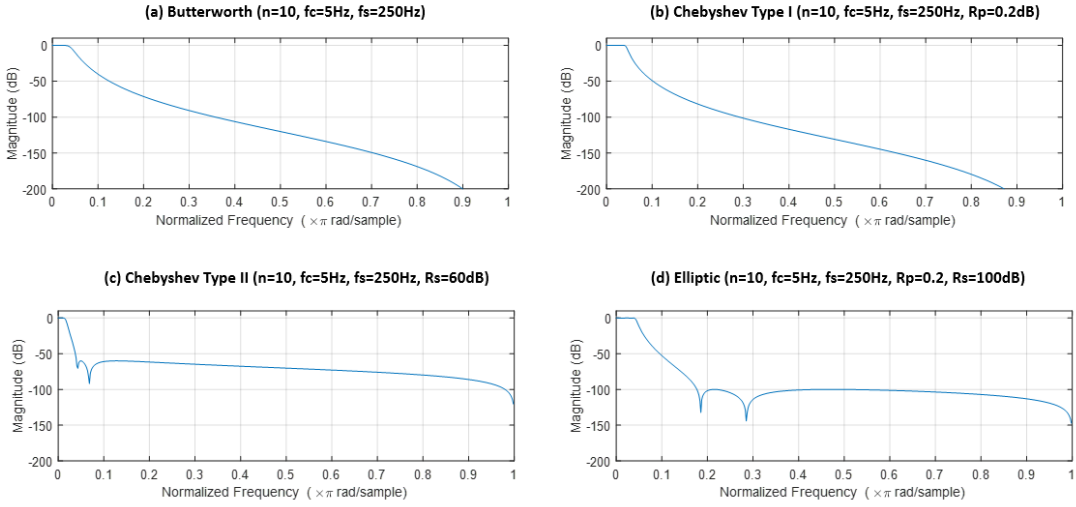

Figure 4-1 Example of magnitude responses for the digital low pass filters (a) Butterworth, (b) Chebyshev Type I, (c) Chebyshev Type II and (d) Elliptic.

Chebyshev filters, when compared to Butterworth, provide sharper responses given the filter order. Since Butterworth filters provide a monotonical response, they concentrate accuracy errors in the lowest frequencies of the passband and above the cut-off frequency. To avoid this, Chebyshev filters distribute the accuracy error uniformly in the passband or the stopband (or both).

Chebyshev type I shows a ripple in the passband and monotonic stop band (**Figure 4-1** (b)), with a magnitude response of the type:

$$|H(j\omega)|^2 = \frac{1}{1 + \varepsilon^2 V_n^2\left(\frac{\omega}{\omega_c}\right)} \tag{4.2}$$

where ε represents the passband ripple, ω_c the cut-off frequency and $V_n(x)$ is a Chebyshev polynomial of order n:

$$V_n(x) = \cos(n \cos^{-1} x) \tag{4.3}$$

Typically, those filters are designed by providing the required peak to peak passband ripple (Rp), which relates to the value of ε in equation (4.2) as:

$$\varepsilon = \sqrt{10^{0.1Rp(dB)} - 1} \tag{4.4}$$

In contrast, Chebyshev Type II filters show the ripple in the stopband and are monotonic in the passband (**Figure 4-1** (c)). Their transfer function for low pass filters can be defined by means of the same parameters used for the Type I filters and it is of the form:

$$|H(j\omega)|^2 = \frac{1}{1 + \left(\varepsilon^2 V_N^2\left(\frac{\omega_c}{\omega}\right)\right)^{-1}} \tag{4.5}$$

where the ripple in the stop band attenuation (Rs) is a function of ε:

$$Rs(dB) = 10 \log\left(1 + {}^{1}/_{\varepsilon^2}\right) \tag{4.6}$$

Elliptic filters distribute the error through all the frequency band, showing ripple in both the passband and the stopband. This results in the optimal type of filter given a filter order n, since it provides the smallest transition band of the four types of filters herein presented (**Figure 4-1** (d)). Their magnitude function can be determined as:

$$|H(j\omega)|^2 = \frac{1}{1 + \varepsilon^2 U_N^2(\omega)} \tag{4.7}$$

where ε is the allowable ripple as specified in equation 4.4 and U_n is a Jacobian elliptic function of the form:

$$U_N^2(\omega) = sn\left[k\, sn^{-1}\left({}^{\omega}/_{\omega_p}, {}^{\omega_p}/_{\omega_s}\right) + cX_1, \varepsilon_p \varepsilon_s\right] \qquad (4.8)$$

where sn is the Jacobian elliptic sine function, ω_p and ω_s the frequency of the passband and stopband respectively, c depends on the filter order, X_1 is the elliptic integral and ε_p and ε_s a function of the ripple in the passband and stopband frequencies.

4.2.2 The nonlinear filter

Poincaré plot analysis has been extensively used for physiological signals processing, to evaluate changes or disease conditions (see Chapter 6). Moreover, Cawley and Hsu [152] first published an algorithm for a nonlinear filter to be applied to the state-space representation of a signal, the attractor. In their work, the noise reduction algorithm is designed with controlled time series and applied to the signal resulting from a magnetoelastic ribbon experiment. The same algorithm was later on applied to RR time series [153], providing successful results.

This algorithm is iterative and consists on a set of steps herein detailed. For clarity, an example with a sinusoidal wave with additive white noise is provided. The algorithm is applied to a signal y(t) of the form

$$y(t) = s(t) + n(t) \qquad (4.9)$$

where s(t) is the sinusoidal signal and n(t) the white noise component.

The steps of the algorithm are illustrated in **Figure 4-2** and are as follows:

Step 1 - Given the time series y(t) (**Figure 4-2** (a)), containing N samples, the attractor Y(t) is reconstructed with time lag τ and in a m dimension phase space (equation 4.10). The values τ=1 and m=2 have been chosen to allow its graphical representation and interpretation. Due to the low signal-to-noise (SNR) ratio of the input signal y(t), the attractor is a cloud of points around the identity line (**Figure 4-2**(b)).

$$Y(t) = [y(t) \quad y(t+\tau) \quad y(t+2\tau) \quad \dots \quad y(t+(m-1)\tau)] \qquad (4.10)$$

Step 2 - All the points in the attractor are clustered in neighborhoods. A first reference point x_{01} is randomly selected and its neighborhood is defined as the subset of points in the attractor containing the v-1 nearest neighbors. Iteratively, further reference points of the form $x_{0\alpha}$ are randomly selected under the condition that the reference point does not belong to any previously established neighborhood. This process is repeated until all points are associated to at least one neighborhood. As an example, **Figure 4-2**(c) illustrates the first three neighborhoods identified in the attractor of the input signal y(t) containing v=120 points each.

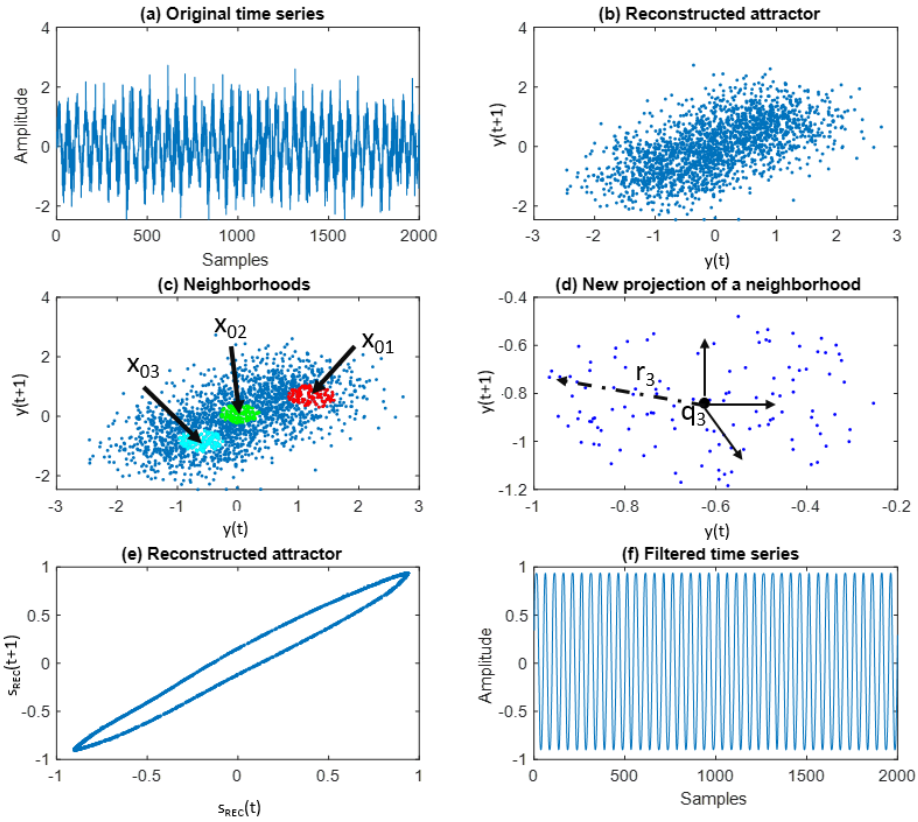

Figure 4-2 Nonlinear filter algorithm description: (a) original time series, (b) reconstructed attractor, (c) identification of neighborhoods, (d) new projection of neighborhoods, (e) final attractor after 8 iterations, (f) filtered time series.

Step 3 - Neighborhood projection: for each neighborhood, the center of gravity q_α and radius r_α, defined as the maximum distance between any neighbor and its center of gravity, are computed. Neighborhoods are sorted according to decreasing values of r_a and for each neighborhood, starting with the one with higher radius value, the local covariance matrix is calculated (equation 4.11). Using a singular value decomposition approach, points in each neighborhood are projected into a new subspace of lower dimension, keeping the largest variance for each neighborhood (quantified in the parameter k) while suppressing small variations since those are likely to be caused by noise. All points shall be projected only once: if a data point belongs to more than one neighborhood, it will only be projected within the neighborhood with highest r_a value.

$$C = \frac{1}{v}\sum_{i=0}^{v-1}[x_i \quad q]\,[x_i \quad q]^T \tag{4.11}$$

Step 4 - Return to time series: once all points have been projected on a new subspace, time series are reconstructed while minimizing the overall error. The time series minimizing the error is of the form [152]:

$$s_{REC}(t) = \begin{cases} \frac{1}{z}\sum_{j=1}^{z} y(t-(j-1)\tau), & 1+(z-1)\tau \le t \le z\tau, \quad z = 1,\dots,m-1 \\ \frac{1}{m}\sum_{j=1}^{d} y(t-(j-1)\tau), & 1+(m-1)\tau \le t \le N-(m-1)\tau \\ \frac{1}{z}\sum_{j=d-z+1}^{d} y(t-(j-1)\tau), & 1+N-z\tau \le t \le N-(z-1)\tau, \quad z = m-1,\dots,1 \end{cases} \tag{4.12}$$

Step 5 - Steps 1-4 are repeated until a predefined condition on the time series is satisfied, such as a SNR target or signal variance. **Figure 4-2**(e) shows the reconstructed attractor after eight iterations (arbitrarily fixed in this example) and **Figure 4-2**(f) illustrates the recovered time series using the formula presented in equation 4.12.

The application of this algorithm requires the a priori definition of a set of parameters. Given a time series y(t), with N samples, the following parameters need to be fixed:

- τ: time lag for attractor reconstruction

- m: embedding dimension of the attractor
- v: number of points to be considered in each neighborhood
- k: percentage of variance to be preserved after the projection of each neighborhood

The values assigned to those parameters depend on the characteristics of the dataset to be processed. Typically, τ is chosen to be 1 sample, and k takes values close to 1 (e.g. k=0.95) to avoid filtering out too much variance of the system. The embedding dimension m must fulfill the condition $m \geq 2d+1$, where d is the real dimension of the attractor and can be estimated by means of the correlation dimension [153]. REG signals show a sinusoidal waveform and therefore their correlation dimension is expected to be close to 1. Nonetheless, the existing noise in the collected signal would increase the correlation dimension significantly. For that reason, in this analysis, the value of the embedding dimension was obtained empirically, together with the number of points (v) to be included in each neighborhood.

Moreover, a strategy to evaluate the effects of the filter and the need of an additional iteration shall be defined. In this work, the parameters providing a lowest error in the reconstructed REG signal $s_{REC}(t)$ were analyzed, followed by the definition of a method to assess the number of iterations needed to recover the original signal s(t).

4.2.3 Experimental dataset

REG data from patients under general anesthesia were used to validate the proposed nonlinear filter based on the signal attractor. Twenty patients were randomly selected from the General Anesthesia Dataset1 and REG segments of 4000 samples (i.e. 16 seconds) free from artefacts were extracted. Those segments belonged to different anesthetic states, including awake periods, light anesthesia and deep anesthesia. The dataset was randomly divided in two subsets of 10 patients each, one to be used for training and a second one for validation.

In order to provide an objective measurement of the error of each filter applied to the dataset, known reference signals are needed. For that purpose, the original signals REG(t) were filtered in a first step to create the reference signals s(t) to which white noise n(t) should be added. Low frequency

components were removed by means of a Butterworth high pass filter with cut-off frequency 0.1 Hz, and subsequently the nonlinear filter herein presented was applied with input parameters m=400 for the embedding dimension, τ=1 for the attractor reconstruction, v=300 neighbors, k=0.95 percentage of variance preserved and 100 iterations. Once the filtered signals s(t) were obtained, white noise n(t) was added to build up a signal y(t) under the form in equation 4.9, with SNR = 0dB, in which both s(t) and n(t) were known. These steps, followed to create the synthetic signals, are summarized in **Figure 4-3**. The filtered datasets were used for training and validation of the filter as described in the data analysis subsection.

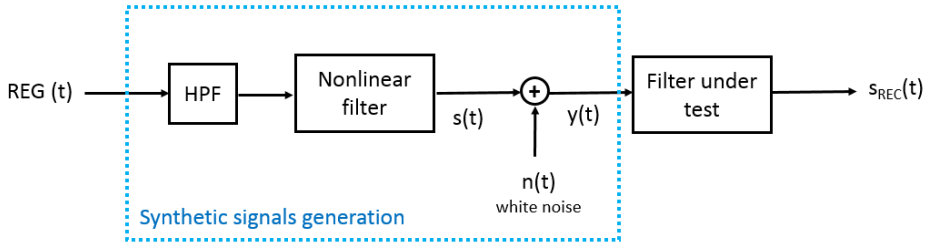

Figure 4-3 Processing applied to the recorded REG signals to obtain the input dataset y(t), consisting on a high pass filter (HPF) with cut-off frequency 0.1 Hz, the application of the nonlinear filter with parameters m=400, τ=1, v=300, k=0.95 and 100 iterations, and the addition of white noise.

4.2.4 Evaluation of the performance of the filters under test

To evaluate and compare the performance of the filters under test, the input dataset y(t) was filtered with all the classical filters herein presented as well as with the proposed nonlinear algorithm, to obtain the filtered signal $s_{REC}(t)$. The parameters needed to design the filters under test were optimized for the training dataset using as a reference the percentage root-mean-square difference error (PRD). PRD has been selected due to its low computational time and its ability to assess distortion, for instance in compressed electrocardiographic signals [155]. Different formulas for PRD calculation are available in the literature, proposing different denominators to compute the final error [156]. The one selected for this application is of the form:

$$\mathrm{PRD}\ (\%) = \sqrt{\frac{\sum_{i=1}^{N}(s_i - \hat{s}_{REC\,i})^2}{\sum_{i=1}^{N}(s_i)^2}} . 100 \qquad (4.13)$$

where s_i is the original signal before the addition of white noise, $S_{REC\,i}$ the recovered signal and N the length of both time series.

Regarding the classical filters under test, signals were filtered forward and backward to avoid phase changes. **Table 4-1** provides the range of parameters tested for every type of filter. The average error obtained with each kind of filter was established as the reference threshold to evaluate the performance of the nonlinear filter.

Table 4-1 Time domain filters tested for REG signals in the training set.

FILTER	ORDER	CUT-OFF FREQUENCY	RP	RS
Butterworth	2 to 10	2 to 20 Hz	-	-
Chebyshev Type I	2 to 10	2 to 20 Hz	0.1 to 1 dB	-
Chebyshev Type II	2 to 10	2 to 20 Hz	-	20 to 100 dB
Elliptic	2 to 10	2 to 20 Hz	0.1 to 1 dB	20 to 100 dB

Rp: peak to peak passband ripple(dB)
Rs: stopband attenuation (dB)

Analogously, the a priori values of the parameters needed to design the nonlinear filter were optimized as well to minimize the PRD in the training set. The time lag for the attractor reconstruction was set to τ=1 sample and the percentage of variance to be preserved in each projection of the neighborhoods was fixed to k=0.95, to make sure the signal was recovered without significant information loss. Since all segments in the dataset were N= 4000 samples long, the parameters to be optimized were the embedding dimension m the number of neighbors v, and the number of iterations needed, as well as the criteria to be used to decide upon the need of a new iteration.

The determination of those values was done empirically, in two steps. Initially, the number of iterations was fixed to a sufficiently high number to guarantee the existence of a PRD minimum. A value of 40 iterations was chosen for each m and v combination, in order to detect the combination minimizing the PRD. Secondly, once filtered signals were analyzed and the best v and m parameters selected, characteristics of the signals along the iterations were extracted to be able to define a mechanism to automatically stop the iterations.

As reflected in the introduction, biomedical signals acquired in operating rooms are often affected by noise. In the case of REG signals, the expected waveform has as main frequency the heart rate, which under resting conditions is between 48 and 98 beats per minute [157] (i.e. 0.8 and 1.6 Hz) and during general anesthesia is known to decrease[158]. Artifacts affecting this signal are typically of higher frequencies, as for example electromyography and electrooculograms. Therefore, the energy distribution along the frequency domain was used to evaluate the filter performance after each iteration and stop it when an adequate energy ratio is reached.

Three energy bands were tested, E5 (Energy from 0 to 5Hz), E2 (Energy from 0 to 2Hz) and E1 (Energy from 0 to 1Hz). All three values were divided by the total energy of the signal, such that energy values from all patients were comparable. Among the three resulting energy ratios, the one providing the highest correlation with the number of iterations was chosen as the criteria to stop the iterative algorithm.

Afterwards, the performance of the nonlinear filter compared to the classical time domain filters was analyzed both in the training and validation sets. The PRD error was used for comparisons through statistical hypothesis testing. Paired t-student tests or Wilcoxon tests were used, depending on the assessment of normality of the samples through a Kolmogorov-Smirnov test. Statistical significance was set to $p<0.025$ (including Bonferroni correction).

The use of the nonlinear filter in the steps followed to create the synthetic signals (**Figure 4-3**) should be considered as a confounding factor, resulting in an advantageous situation for the results of the nonlinear filter. Therefore, the analysis of the results was repeated placing a Butterworth filter before the addition of white noise (**Figure 4-4**), with the same parameters that optimized the PRD error with the first set of synthetic signals.

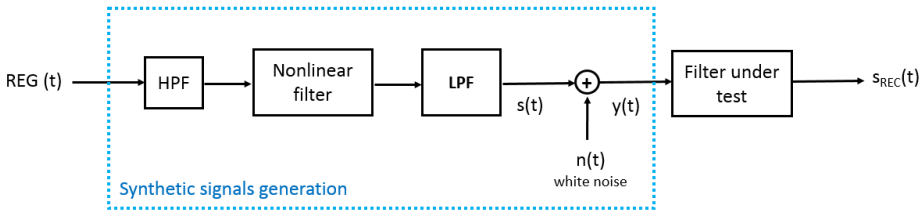

Figure 4-4 Inclusion of a Butterworth second order low pass filter (LPF) with cut-off frequency at 4Hz in the steps followed to create the set of synthetic signals.

Moreover, the effects of different SNR levels (simulated by modifying n(t)) and time series length N on the performance of the filters were evaluated. Additionally, execution times of each filter were considered for further comparison, to assess the limitations of each filter strategy for real time applications. Execution times were obtained by applying the filters implemented in MATLAB 2018a (Mathworks, Inc., Natick, MA) in a 64-bit operating system, i5 Intel® Core™ processor at 1.9 GHz and 8GB RAM.

4.3 Results

The Butterworth filter minimizing the PRD error was the second order low pass filter with cut-off frequency at 4Hz, showing an average PRD of 4.1%. The cut-off frequency for the optimal Chebyshev Type I filter, which was also a second other filter, was smaller due to its sharper transition and was placed at 2Hz for a maximum Ripple of 0.2dB in the bandpass, providing also a PRD of 4.1%. Type II Chebyshev best filter showed a slightly higher PRD, 4.2%, requiring a fourth order filter with cut-off frequency at 16Hz and a minimal attenuation of 70dB in the stopband. Finally, the best elliptic filter was a second order filter with an average PRD of 4.1%, cut-off frequency of 2Hz, maximum bandpass ripple of 0.2dB and minimum attenuation of 100dB in the stopband. The magnitude response of each filter is presented in **Figure 4-5**.

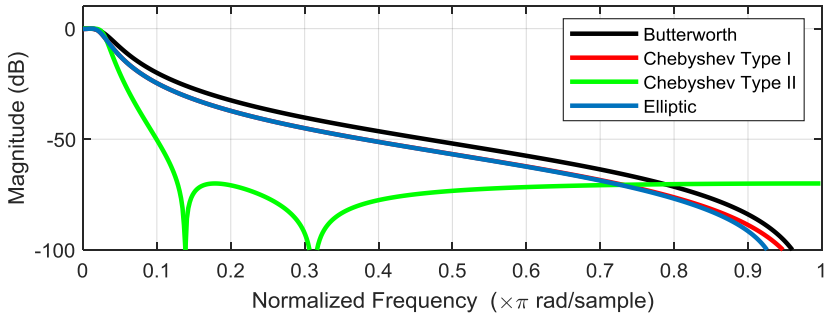

Figure 4-5 Frequency responses of the optimal time domain filters.

Regarding the nonlinear filter on the state-space domain, all the combinations for the number of neighbors v and the dimensions m were computed and the PRD error calculated in each case. **Figure 4-6** shows the evolution of the PRD error with the number of iterations, the number of neighbors and the number of dimensions, suggesting an asymptotic decrease of PRD as a function of the number of iterations, a local minimum for the number of neighbors at v=120 and a monotonic decrease of PRD with the embedding dimension.

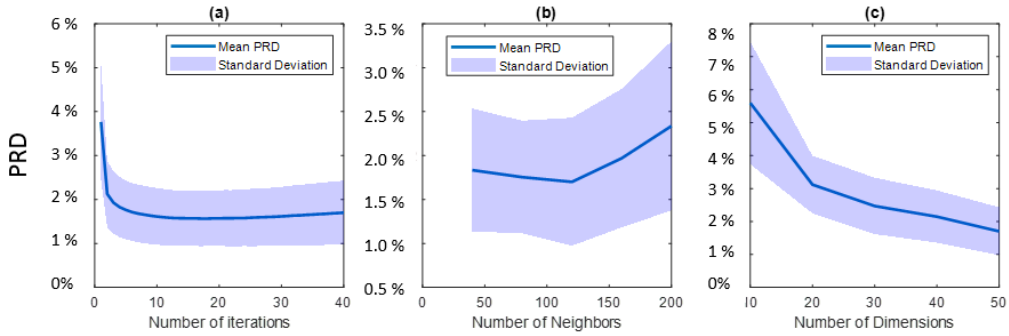

Figure 4-6 PRD of the filtered signal as a function of: (a) the number of iterations (with v=120 and m=50), (b) the number of neighbors (with m=150 and 40 iterations) and (c) the number of embedded dimensions (with v=120 and 40 iterations).

In order to choose the optimal nonlinear filter, the lowest PRD among all the v and m parameter combinations was identified, as well as the number of iterations needed to reach the minimum. **Figure 4-7**a shows the number of iterations needed for each v and m combination to reach the minimum PRD value (**Figure 4-7**b) and the corresponding PRD error in each case. It can be observed that the higher the dimension, the lowest the error, with m=50 providing the lowest errors, and the combination m=50 and v=120 resulting in the optimal filter. The number of iterations required decreases as the number of neighbors increases for the set of filters with m=50. Even though v=200 provides the lowest number of iterations, v=120 is the chosen result since it optimizes the PRD error.

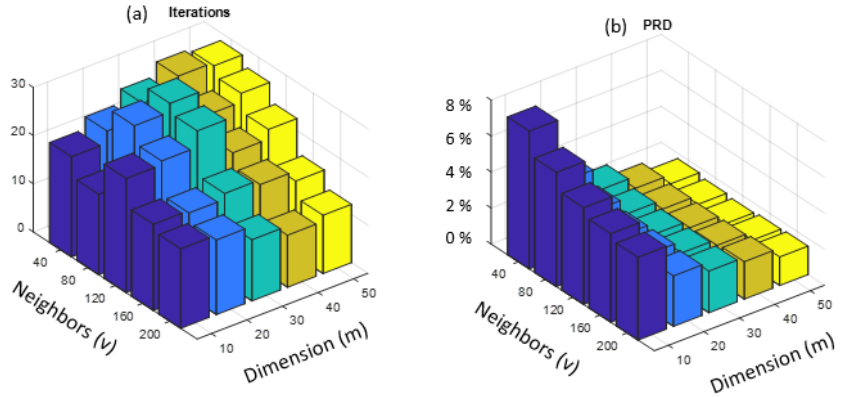

Figure 4-7 Number of iterations needed (a) and PRD error (b) obtained for each v and m combination.

Once the number of neighbors and dimensions optimizing the filter performance was set, an automatic condition was sought so that the filter used the minimum number of iterations while recovering the signal free from artifacts. Three energy ratios E5 (energy from 0 to 5Hz), E2 (energy from 0 to 2Hz) and E1 (energy from 0 to 1Hz) were tested, all three values divided by the total energy of the signal.

In the training dataset, the energy ratio showing the highest correlation (ρ) with the PRD error was E2, with ρ=0.998, and was therefore the one selected to be used to stop the iterations of the nonlinear filter. To establish a threshold for the E2 ratio parameter, E2 values before and after the number of iterations minimizing the PRD were calculated and compared. Before the absolute PRD minimum was reached, average differences among consecutive iterations were E2 = 0.038 ± 0.065 (mean ± standard deviation) while those differences got down to E2 = 0.00005 ± 0.0033 in the following iterations. Therefore, the criteria to stop the iterations was chosen to be a decay of less than 0.005 (n.u.) in the parameter E2.

Data on the training and validation set were filtered through the nonlinear filter algorithm, stopping automatically as a function of the parameter E2. The PRD errors were computed in each case and the results were compared with those obtained with the classical filters. Results are shown in **Figure 4-8**.

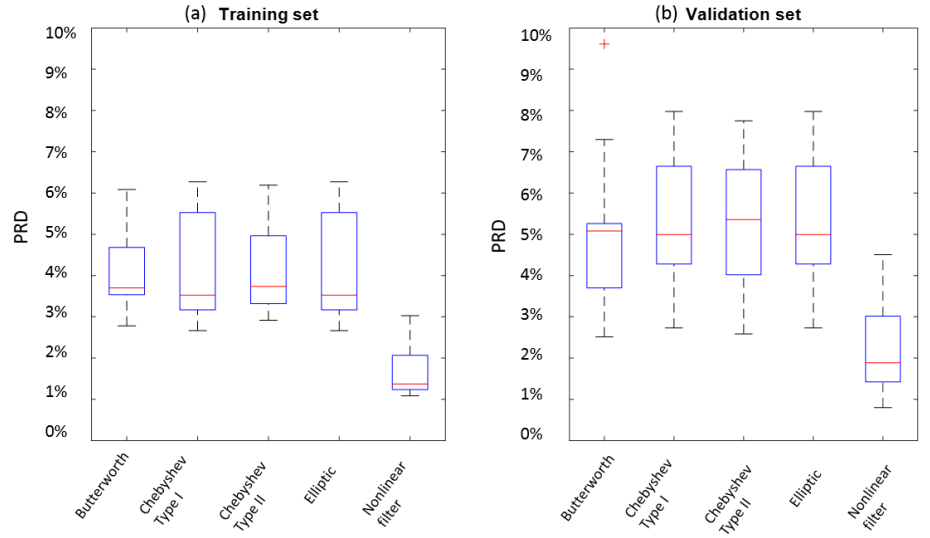

Figure 4-8 PRD errors of the signals filtered with each filter under test in the training set (a) and the validation set (b).

The four classical filters provide similar performances in terms of PDR, while the nonlinear filter provides lower error values both in the training and the validation sets. To assess the statistical significance of those differences observed in the graphical representation, paired hypothesis testing was applied to the errors of each filter. **Table 4-2** summarizes the p-values obtained from the comparison between the nonlinear filter and all other filters, showing that the nonlinear option provides statistically significant lower errors. No differences were detected among PRD errors of classical filters.

Table 4-2 Statistical significance p-value of the paired t-student test comparing the PRD errors of the nonlinear filter with the one obtained with each classical filter.

P-VALUE	BUTTER-WORTH	CHEBYSHEV TYPE I	CHEBYSHEV TYPE II	ELLIPTIC
Training set	<0.0001	<0.0001	<0.0001	<0.0001
Validation set	0.0024	0.0106	0.0131	0.0106

The effect of using either a classical or the nonlinear filter is illustrated through an example in **Figure 4-9**. Given one of the signals in the validation set, white noise was added and results for the Butterworth filter and the

nonlinear filter are presented. When using the nonlinear filter, the recovered signal $s_{REC}(t)$ preserves the same waveform without any visible interference. In contrast, the time series $s_{REC}(t)$ obtained after applying the Butterworth filter, shows some distortions that were not present in the original waveform.

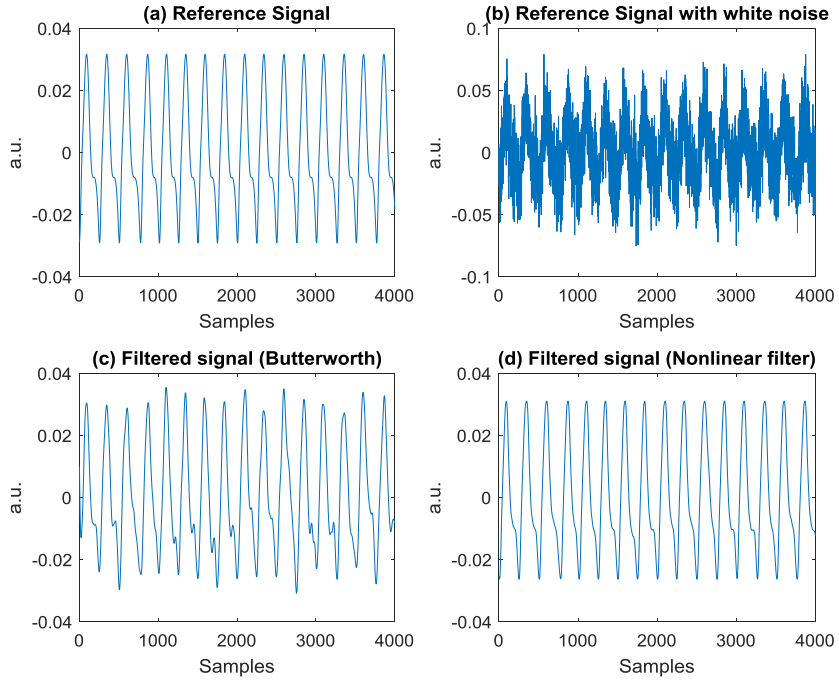

Figure 4-9 Example of a reference signal REG(t) (a), signal y(t) with white noise (b), sREC(t) result after applying a Butterworth filter (c) and sREC(t) result obtained with the nonlinear filter (d).

As previously stated, the filter used in the generation of the synthetic dataset was the nonlinear filter and this might have biased the obtained results. In order to discern the effect of this bias, a Butterworth filter was added in the generation of synthetic signals as indicated in **Figure 4-4**. Under these new conditions, optimal classical filters were coincident with the ones previously identified except for the Chebyshev Type II, that provided the lowest PRD error for a 3rd order lowpass filter, with cut-off frequency at 20Hz and an attenuation in the stopband of 60dB. Regarding the nonlinear filter, the number of embedding dimensions was coincident while the number of neighbors minimizing the error was either v=120 or v=160 (with no statistical

differences among both solutions). Therefore, v=120 was taken as the parameter to be used in the optimal filter.

PRD errors obtained with this new set of synthetic signals are shown in **Figure 4-10**. The nonlinear filter preserves its superiority when compared to all other options in both datasets, suggesting that the filter used to generate the synthetic signals does not translate into a biased result. Moreover, **Table 4-3** includes the p-values obtained from the hypothesis testing applied to the PRD errors resulting of the application of the different filter options. The nonlinear filter outperforms all other four options, providing even lower p-values than the ones showed for the originally generated synthetic dataset (see **Table 4-2** for comparison). This result suggests that a coarse filtering applied before the use of the nonlinear filter might improve the PRD error of the recovered time series.

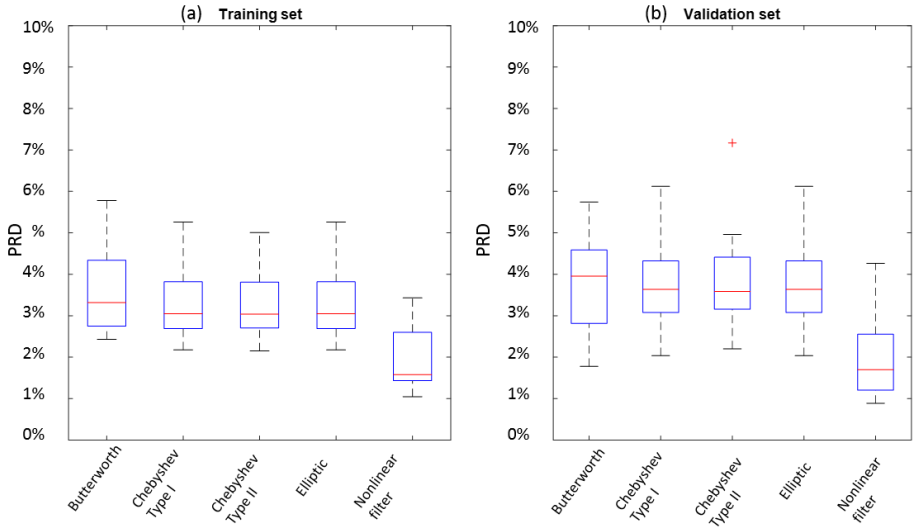

Figure 4-10 PRD errors of the signals filtered with each filter under test in the training set (a) and the validation (b) set, after the inclusion of a Butterworth filter in the generation of the synthetic signals dataset.

Table 4-3 Statistical significance p-value of the paired t-student test comparing the PRD errors of the nonlinear filter with the one obtained with each classical filter.

P-VALUE	BUTTER-WORTH	CHEBYSHEV TYPE I	CHEBYSHEV TYPE II	ELLIPTIC
Training set	<0.0001	<0.0001	<0.0001	<0.0001
Validation set	0.0001	0.0008	0.0026	0.0008

The five filters have been evaluated using an input signal y(t) with SNR=0dB, with the nonlinear filter showing the best performance. In order to assess the effect of different input signal SNR levels in the comparison of the proposed filters, SNR was set to 0, 5, 10, 15, 20 and 25 dB. Results from this analysis are shown in **Figure 4-11**. For all filters, the PRD error decreases when SNR of y(t) increases, with the nonlinear filter providing a significantly lower error for any of the SNR values tested. Moreover, the lower the SNR of the input signal y(t), the bigger the improvement obtained by using the nonlinear filter.

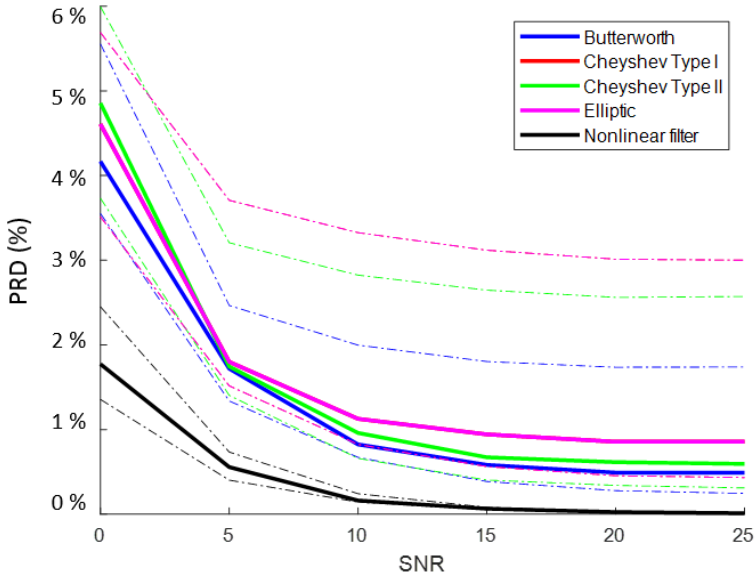

Figure 4-11 Effect of different SNR levels in the performance of the filters, by comparing median and interquartile values of the PRD error (curves from Chebyshev type I and elliptic filters are overlapped).

Intuitively, low SNR scenarios would require a higher number of iterations in the nonlinear filter, thus affecting the execution time of this algorithm. **Figure 4-12** shows a boxplot comparing the execution time of each filter as a function of the SNR value of the input signal y(t). Classical filters have very low execution times (a few milliseconds maximum) while the execution time for the nonlinear filter clearly depends on the SNR of the input signal, with median values slightly above 0.5 seconds in case of a SNR = 25dB and up to more than 2s for SNR=0dB. Those differences in execution times are statistically significant ($p<0.0001$).

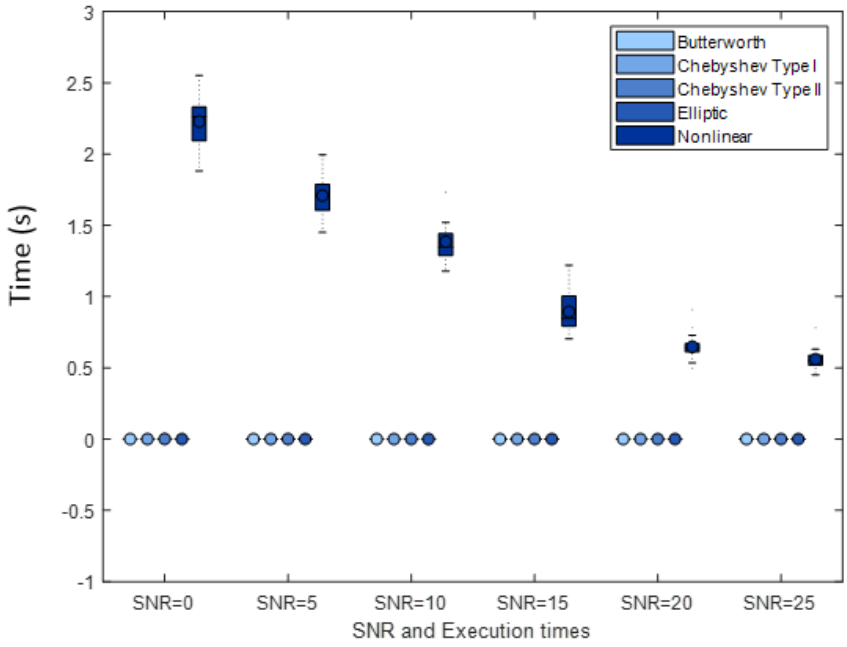

Figure 4-12 Execution time of each filter as a function of the SNR value.

Finally, the effects of the length of the input signal y(t) in the performance of the filters was assessed by reducing the length of the time series used. Signal lengths of y(t) were increased from 500 to 4000 samples in steps of 500 samples, and SNR was fixed to 5 dB. All the classical filters showed increasing PRD errors (and higher dispersion of those errors) for increasing signal length (**Figure 4-13**). However, for the nonlinear filter, PRD decreased with increasing signal length, as well as the dispersion of the PRD values. For input y(t) signals below 1000 samples length, classical filters provided the most accurate filtered signal, while around 1000 samples all five filters showed comparable performance. Finally, for input signals longer than 1000 samples, using the nonlinear filter improved the PRD error of the filtered signals, providing results with a PRD below 1%.

The length of the input signals y(t) is again one factor influencing the execution time of the filters. For all filters, execution times increased with signal length. As illustrated in **Figure 4-14**, for the nonlinear filter this increase exponentially grows with increasing signal length, while the increase in the classical filters appears to be negligible. Results from this analysis suggest that even though there is an increased accuracy of the recovered signal when using

the nonlinear filter, there is a tradeoff between filter performance and execution times that might compromise the use of the nonlinear filter for real time applications.

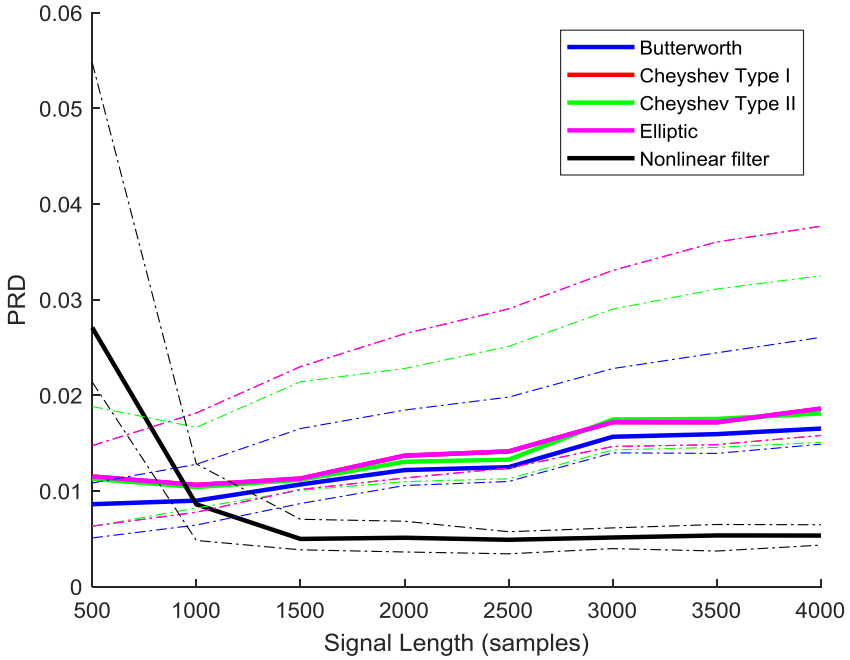

Figure 4-13 Effects of the input signal length on the performance of the filters, by comparing median and interquartile values of the PRD error (curves from Chebyshev type I and elliptic filters are overlapped).

4.4 Conclusions

Among all the filters under test herein proposed, the nonlinear filter provided better performance than standard digital filters (Butterworth, Chebyshev and Elliptic filters), showing a higher improvement for decreasing signal-to-noise ratios. Furthermore, results suggest that a two-step filtering process, composed by a coarse filtering process with classical filters followed by the application of the nonlinear filter, enhances the accuracy of the recovered signals.

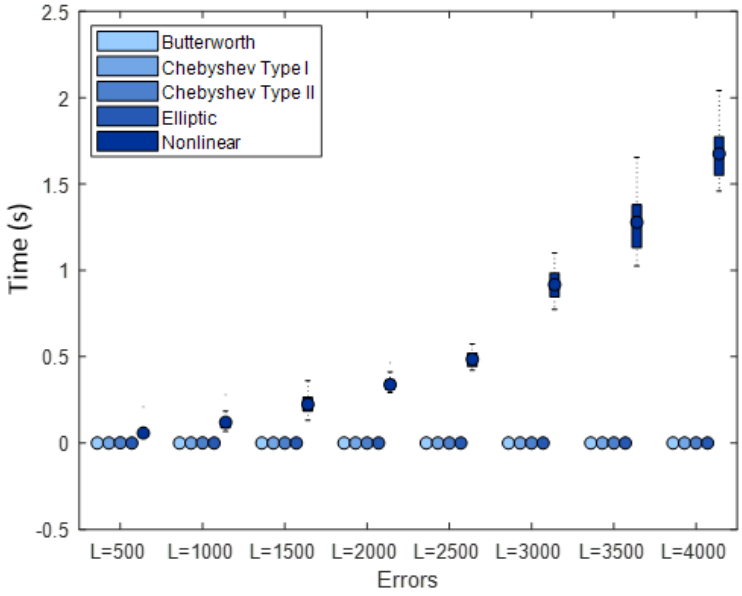

Figure 4-14 Execution time of each filter as a function of the input signal length N.

However, there is a tradeoff between the performance of the filters under test and the execution times required to obtain the filtered time series. Moreover, for short sequences, standard filters outperform the nonlinear filter. For those reasons, the use of the nonlinear filter seems adequate for post-hoc analysis of long REG recordings (at least 1500 samples at 250 samples/s), while other alternative filters should be considered for real time applications.

Considering these results, the use of the nonlinear filter will be restricted to retrospective data analysis in this Doctoral Thesis, while real time studies will benefit from the use of classical filters. Due to the equivalent performance among the classical linear filters, the Butterworth filter was selected to be the one used along this for linear filtering.

Chapter 5

Geometric features extraction from REG signals

Abstract

This chapter contains the analysis of REG waves, during an apnea challenge and during an anesthetic procedure, by means of the classical approach based on the extraction of geometric features from the pulse waves. Results of this chapter aim at providing a reference for the evaluation of other techniques proposed in this Thesis for REG signals processing.

5.1 Introduction

REG signals have traditionally been analyzed by assessing the geometrical properties of the blood pulse waves in the time domain, such as the duration of the anacrotic phase of the pulse, the maximum and minimum amplitudes, the slope and the area under the curve [53], [159]. For example, Traczewski et al. [61] analyzed the number of inflection points in the REG curve, concluding that REG was a useful technique for the diagnosis of normal pressure hydrocephalus. In a REG study with animals, linear correlations of sliding windows, aiming at identifying differences in the waveform patterns, were used to detect the lower limit of CAR [62]. Moreover, Bodo et al. [63] calculated the amplitude and integral of the pulse wave in rats to assess cerebrovascular reactivity.

Those studies based in the pulse waveform analysis are consistent with the ones used for other physiological signals reflecting pulse waves or their surrogates, such as intracranial pressure (ICP), photoplethysmography (PPG) and impedance cardiography (ICG). For example, the waveform analysis of ICP signals allows to identify several physiological and pathological changes, through the amplitude of the wave and the detection of its main peaks [160]. The extraction of geometric features of ICP signals was useful to predict the early and 12-months outcome after aneurismal subarachnoid hemorrhage [161]. Moreover, the amplitude of the pulses in the time domain has been considered as an indicator of intracranial compliance [162], [163]. Despite of these evidences, Di Ieva et al.[131] published a review on the analysis of ICP signals in which they called for new methods of ICP signals processing, mainly nonlinear ones, to consider not only the waveform changes but other underlying physiological mechanisms affecting ICP.

In the same sense, efforts are continuously being made to enhance PPG feature detection algorithms for personal health monitoring applications [164] and the use of PPG for diagnostic purposes. For instance, Mahri et al. used features extracted from the second derivative of the PPG signal to identify patients with myocardial infarction [165] and Solosenko et al. developed a method to detect premature ventricular contractions trough PPG extracted features [166]. A thorough review of clinical applications based on PPG contour analysis was published by Millasseau et al., highlighting the usefulness of PPG signals in studying the endothelial function, as well as arterial stiffness and aging [166].

Nonetheless, the closest technology to REG is ICG, since they both share the same working principle based on the electrical bioimpedance. ICG measures the electrical impedance of the thoracic cavity and allows the assessment of several hemodynamic variables, such as cardiac output (CO), stroke volume (SV), left ventricular ejection time (LVET) and systemic vascular resistance (SVR), among others [167]. This technology has been used to predict the short term risk of clinical decompensation in patients with chronic heart failure [168] as well as the effects of cardiac rehabilitation on the same type of patients [169]. Furthermore, ICG proved to be useful for hypertension management [170] and the evaluation of antihypertensive therapies [171].

Due to the similarities between REG and ICG, and the positive clinical outcome of the use of ICG, the rationale behind the analysis of ICG waves will be applied to REG recordings for CBF estimation in this chapter, together with the main geometric features extracted from the signals.

One strategy used to evaluate CBF measurements consists of continuous assessment of blood flow during the execution of respiratory challenges known to modify the CBF. For example, episodes of apnea or breath holding reduce the amount of oxygen in blood and therefore partial CO_2 pressure increases provoking increases in CBF. Kastrup et al. [17] quantified the effect of an apnea procedure in regional CBF measured with magnetic resonance imaging and found an average regional CBF increase of 47-87%, dependent on apnea duration. Increasing inhaled CO_2 [19] is an alternative method that can be used to provoke changes in CBF that has also been widely used though its implementation is far more complex since it requires controlled CO2 inhalation.

This chapter aims at evaluating the ability of the geometric features extracted from REG signals to reflect CBF changes. Two scenarios are studied: the first one uses a simple breath holding challenge to trigger cerebral perfusion changes while the second is based on the analysis of REG recordings during surgical procedures under general anesthesia.

5.2 Methods

5.2.1 Geometric features extraction

The classical methods used to assess CBF by means of REG signals rely on the analysis of the geometry of the pulse waves. In this way, for REG recordings, minimums and maximums of each pulse wave and their respective derivatives were automatically detected, and the following features were calculated for each signal to be processed: amplitude range of the pulse (Range), time between two consecutive maximums (Δtmax), time between two consecutive minimums (Δtmin), time between each minimum and the following maximum (Δtmin-max), the slope of the pulse during this interval (α), the area under the curve (Area), the systolic Area (AreaSyst) – area delimited by a minimum and its consecutive maximum - the maximum derivative (δmax) and the range of the derivative (δrange). A graphical representation of the extracted features is provided in **Figure 5-1**.

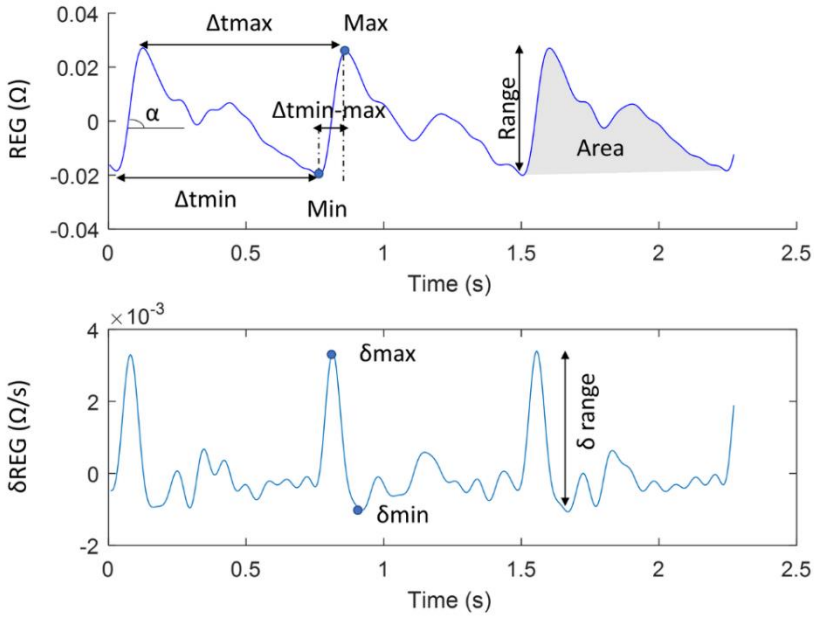

Figure 5-1 Features extracted from REG wave and its derivative.

In addition to the use of direct geometrical features extracted from the time domain time series, blood volume and blood flow estimations were also considered. For that purpose, ICG principles were applied to REG waves, linking the brain blood volume to the SV and the CBF to the cardiac output.

Several methods have been proposed to calculate the stroke volume by means of the analysis of ICG signals, but two of them are the most broadly used: the Kubicek and the Bernstein equation. The Kubicek [172] method is described by equation 5.1, assuming a cylindrical model for the thorax:

$$SV = \rho \frac{L^2}{Z_0^2} \left(dZ/dt\right)_{max} LVET \quad (5.1)$$

where L is the distance between the sensing electrodes in cm, Z_0 is the basic thoracic impedance in Ω, $\left(dZ/dt\right)_{max}$ is the maximum derivative of the impedance in each heart cycle (Ω/s), LVET is the left ventricular ejection time (s) and ρ is the resistivity of blood (Ωcm). The estimation of ρ is controversial. Some studies concluded that calculating it using patient's hematocrit enhances the SV accuracy [173], [174]. However, it has also been published after in vivo and in vitro investigations that it could be assumed to be constant [175].

An alternative methodology was proposed by Sramek and slightly modified by Berstein [115], [176], assuming a truncated cone model for the thorax, resulting in an SV calculation of the form

$$SV = \delta \frac{(0.17H)^3}{4.25} \frac{\left(dZ/dt\right)_{max}}{Z_0} LVET \quad (5.2)$$

where H is the patient height. This equation does not depend on the blood resistivity but includes instead a correcting factor δ that has not been validated [177].

Even though the Sramek-Bernstein equation is more frequently used, Kubicek equation lead to higher correlations with reference methods used for validation when direct comparisons were performed for the same set of patients [174], [177], [178]. For that reason, the Kubicek equation was the one selected for the analysis of REG waves.

Since REG aims at providing a relative CBF measurement, ρ, L and Z_0 were considered constant. The maximal impedance change reflected by the term $\left(dZ/dt\right)_{max}$ corresponds to the δmax parameter represented in **Figure 5-1**. Finally, the value for LVET needs to be estimated. In ICG recordings, LVET is deducted from the tracing of the first derivative of the impedance, as shown in **Figure 5-2**. Willems et al. [179] published their work on the

relationship between HR and LVET, concluding that there is a very weak influence of parameters other than HR in the LVET value. **Figure 5-3** shows the regression curves of LVET as a function on HR, showing certain dependence with gender and age but clearly influenced by HR values.

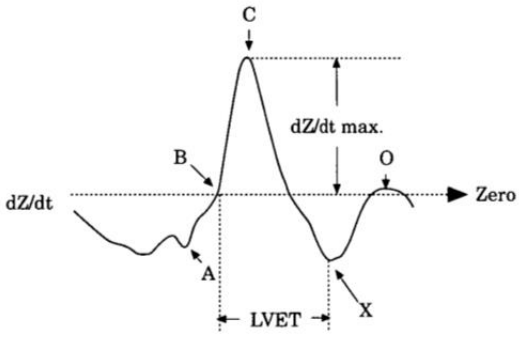

Figure 5-2 Graphical representation of LVET in the derivative of the ICG curve (from [177]).

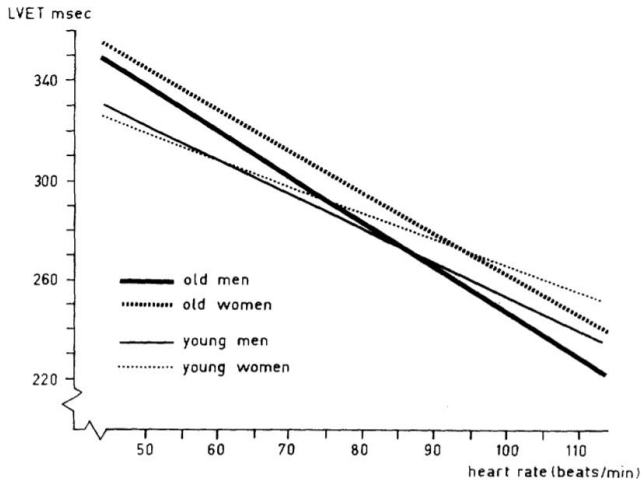

Figure 5-3 Regression curves for the relationship between HR and LVET (from [179]).

In their work, Willems [179] et al. provided several regression curves for different population groups, concluding that for the general population the following expression could be used:

$$\mathrm{LVET} = 416 - 1.56\,\mathrm{HR} \tag{5.3}$$

In this chapter, LVET was considered as a function of HR as indicated in equation 5.3, where HR is computed as the difference between two consecutive maximums of the REG curve. Brain blood volume and brain blood flow were estimated analogously to SV and cardiac output. Therefore, the relative cerebral blood volume (CBVrel) was calculated as

$$\mathrm{CBVrel} = \delta\max \mathrm{LVET} \tag{5.4}$$

and the CBF estimation as

$$\mathrm{CBFest} = \mathrm{CBVrel}\,\mathrm{HR} \tag{5.5}$$

Those two parameters, as well as the geometric features previously listed, were tested for their ability to track CBF changes in REG signals, both during an apnea challenge and when applied to REG curves collected during anesthetic procedures.

5.2.2 Experimental datasets

The geometric feature extraction of REG signals was applied to two different datasets. Firstly, the ability of the extracted features to assess CBF changes in REG recordings was analyzed in the Apnea-Baseline dataset. As described in Chapter 3, this dataset includes data of 16 young healthy volunteers undergoing breath holding challenges.

Secondly, the same set of features was extracted from REG signals collected during surgical procedures under general anesthesia, from the dataset General Anesthesia Dataset 1 presented in Chapter 3. REG data of 40 female patients under TIVA with propofol and remifentanil are included in this database, as well as other clinical signs typically monitored during anesthetic procedures.

For both datasets, two filtering strategies will be performed, one based on the optimal linear filter for REG signals and the other on the optimal nonlinear filter, both identified in Chapter 4. Figure 5-4 shows a schematic overview of the datasets to be processed.

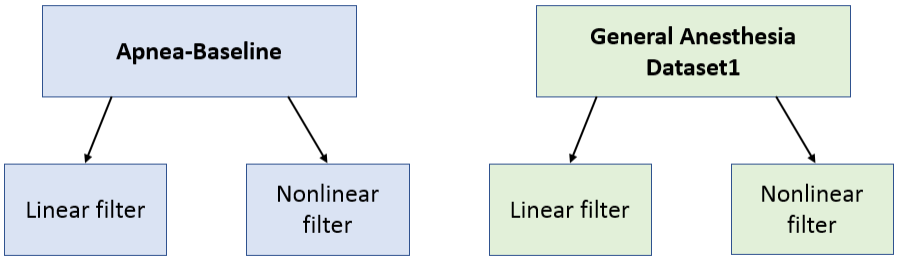

Figure 5-4 Experimental datasets to be processed.

5.2.3 Data analysis for apnea detection

REG segments free from artifacts were identified in the Apnea-Baseline dataset, each of them containing 4000 samples (16s). Finally, 53 sequences were selected, 29 belonging to apnea recordings and 24 from baseline periods. The average main frequency of the recorded signals was 1.10 ± 0.47 Hz (mean ± standard deviation), resulting in a cardiac cycle of 227 ± 57 samples. The dynamic range of the recorded REG waves was 0.089 ± 0.028 Ω (95% confidence interval). No differences were observed between groups in terms of amplitudes or heart cycle duration.

Prior to the extraction of the geometric features, recorded REG signals were preprocessed in order to remove interferences caused by other electrical sources and undesired physiological signals. For that purpose, REG segments were high-pass filtered using a 4th-order Chebyshev type II, with 0.1 Hz stop band frequency to eliminate DC fluctuations, followed by either the optimal linear filter or the optimal nonlinear filter as indicated in **Figure 5-4**.

For each selected segment, the geometrical features under study were extracted: Range, Δtmax, Δtmin, Δtmin-max, α, Area, AreaSyst, δmax, δrange, CBVrel and CBFest. To reduce the effect of possible outliers, the median values for all the pulses belonging to each recording was used as the associated value for the REG signal under analysis.

Results obtained for both apnea and baseline segments were tested for their ability to detect apneas, by means of hypothesis testing, considering significance for p-values<0.05. Normality was assessed through a Kolmogorov-Smirnov test and subsequently, a student t-test was performed

for Gaussian distributions and a Mann-Whitney test otherwise. The Area Under the Curve (AUC) of the Receiver Operating Characteristic, the sensitivity, the specificity and the accuracy of parameters showing significant differences between groups were also computed.

5.2.4 Data analysis for general anesthesia recordings

REG data from the General Anesthesia Dataset1 were filtered with a 4th-order Chebyshev type II, with 0.1 Hz stop band frequency, and the linear and nonlinear filters presented in Chapter 4. REG segments free from artifacts, of 4000 samples each, were identified and labeled in 5 different categories based on the clinical state of the patient in each situation:

- Awake: data recorded before the anesthesia induction
- LOC: data recorded immediately after the loss of eyelash reflex
- Anes: data recorded during steady state anesthesia with constant propofol dosages
- BSR: data recorded during the detection of suppression patterns in the EEG, as indicated by the Conox device
- ROC: data recorded after patient extubation.

The main characteristics of the selected segments as well as the number of signals available for each state are summarized in **Table 5-1**. It should be noted that statistical differences were detected between the 5 states prior to the extraction of the geometrical features. Namely, REG signals at LOC presented a higher range than those in the Anes state, and the cardiac cycle for LOC was longer than for the awake state.

For each segment, the geometrical features selected for analysis were extracted, using the median value of each segment as the reference. Hypothesis testing was used to asses the ability of each extracted feature to distinguish between different anesthetic states. Paired Student t-test or Wilcoxon test were used depending on the distribution of the samples, previously assessed by the Kolmogorov-Smirnov test. A significance level of

$p<0.01$ was used, applying the Bonferroni correction for the 5 groups of signals.

Table 5-1 Description of the signals belonging to General Anesthesia Dataset 1: sample size, dynamic range (95% confidence interval), cardiac cycle duration and p-value obtained from the comparison with values in the following clinical state.

ANESTHESIA STATE	SAMPLE SIZE (N.U.)	DYNAMIC RANGE (Ω) MEAN±STD	CARDIAC CYCLE (SAMPLES) MEAN±STD
Awake	34	0.053 ± 0.036	230 ± 64^{+}
LOC	35	0.059 ± 0.038*	286 ± 116^{+}
Anes.	33	0.032 ± 0.013*	249 ± 39
BSR	22	0.037 ± 0.015	248 ± 49
ROC	40	0.043 ± 0.026	242 ± 52

*p<0.01

$^{+}$p<0.001

Furthermore, correlations between the extracted features and patient demographics were calculated to infer the influence of confounding factors in the parameters under study. Additionally, other clinical data recorded during surgery such as HR, the effect site concentration of propofol (CePropo), the effect site concentration of remifentanil (CeRemi), MAP and qCON values, were also included in this analysis.

5.3 Results for apnea detection

5.3.1 With linear filter

Results obtained for the features extracted from the REG pulse waves and their derivatives are summarized in **Table 5-2**. Even though some differences can be found between apnea and baseline recordings, only one of the selected parameters showed the ability to distinguish between both with statistical significance, the systolic area (AreaSyst). However, it can be observed that this parameter presented a high standard deviation in both groups, mainly for the apnea recordings, in which it is more than twice the

mean value. The parameter AreaSyst presented an AUC of 0.69, with a sensitivity of 75.8 % and a specificity of 58.3 %, resulting in an accuracy of 67.9%.

Table 5-2 Results of geometric features using classical filters: average values (mean ± standard deviation) for apnea and baseline recordings and statistical significance of their difference (p-value).

PARAMETER	APNEA MEAN±STD	BASELINE MEAN±STD	P-VALUE
Range (Ω)	0.092 ± 0.028	0.099 ± 0.033	0.376
Δtmax (samples)	238.7 ± 22.1	254.9 ± 43.3	0.084
Δtmin (samples)	242.1 ± 23.2	248.6 ± 38.8	0.455
Δtmin-max (samples)	52.9 ± 27.4	60.6 ± 24.8	0.217
α (n.u.)	0.002 ± 0.001	0.002 ± 0.001	0.406
Area (Ω.s)	12.4 ± 4.8	13.5 ± 4.9	0.446
AreaSyst (Ω.s)	0.212 ± 0.569	0.516 ± 0.419	0.014
δmax (Ω/s)	0.006 ± 0.002	0.005 ± 0.002	0.272
δrange (Ω/s)	0.007 ± 0.002	0.007 ± 0.002	0.145
CBVrel (Ω)	2.32 ± 0.65	2.11 ± 0.74	0.195
CBFest (Ω/s)	154.5 ± 37.7	125.8 ± 44.4	0.229

5.3.2 With nonlinear filter

The results obtained for the nonlinear filtered REG data processing are provided in **Table 5-3**. The only parameter providing statistically significant differences between the apnea and baseline groups was the systolic area (AreaSyst), with a p-value of 0.004.

Table 5-3 Results of geometric features using the nonlinear filter: average values (mean ± standard deviation) for apnea and baseline recordings and statistical significance of their difference (p-value).

PARAMETER	APNEA MEAN±STD	BASELINE MEAN±STD	P-VALUE
Range (Ω)	0.087 ± 0.027	0.096 ± 0.032	0.264
Δtmax (samples)	240.9 ± 23.2	252.2 ± 40.3	0.209
Δtmin (samples)	241.6 ± 23.6	249.2 ± 39.2	0.385
Δtmin-max (samples)	54.3 ± 33.5	60.3 ± 27.0	0.249
α (n.u.)	0.002 ± 0.001	0.002 ± 0.001	0.649
Area (Ω.s)	11.8 ± 4.6	13.2 ± 4.7	0.282
AreaSyst (Ω.s)	0.184 ± 0.559	0.582 ± 0.531	0.004
δmax (Ω/s)	0.006 ± 0.002	0.005 ± 0.002	0.483
δrange (Ω/s)	0.007 ± 0.002	0.006 ± 0.002	0.183
CBVrel (Ω)	2.075 ± 0.639	1.896 ± 0.732	0.189
CBFest (Ω/s)	128.6 ± 36.7	114.4 ± 44.7	0.105

The parameter AreaSyst presented an AUC of 0.73, with a sensitivity of 75.8% and a specificity of 54.2%, resulting in an accuracy of 66.0%. Compared to the outcome of the linear filter analysis, the use of the nonlinear filter resulted in lower p-value and higher AUC, while sensitivity was maintained, and specificity and accuracy provided lower rates (**Table 5-4**). The graphical representation of the Receiver Operating Characteristic curves from both analyses is provided in **Figure 5-5**.

Table 5-4 Comparison of the performance of AreaSyst with the linear and nonlinear filter.

	LINEAR FILTER	NONLINEAR FILTER
p-value	0.014	0.004
AUC	0.69	0.73
Sensitivity	75.8%	75.8%
Specificity	58.3%	54.2%
Accuracy	67.9%	66.0%

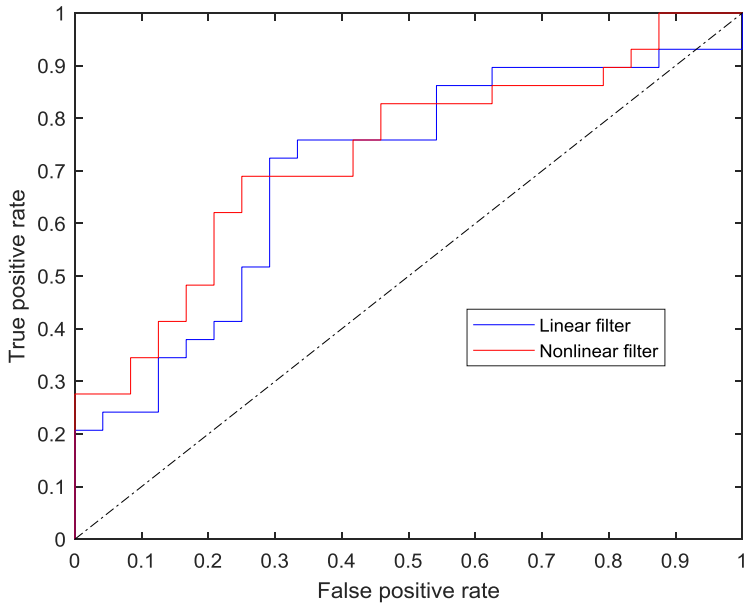

Figure 5-5 Receiver Operating Characteristic curves of AreaSyst in the linearly and nonlinearly filtered dataset.

5.4 Results for general anesthesia

5.4.1 With linear filter

The results obtained for all the extracted features under anesthesia using the optimal linear filter are summarized in **Table 5-5**, characterized by their mean values and standard deviation. Even though some differences can be observed among the anesthetic states, high standard deviations were obtained for almost all the parameters under test.

Table 5-5 Average values (mean, standard deviation) of all the extracted geometric features in each anesthesia state for REG data preprocessed with the linear filter.

	AWAKE MEAN (STD)	**LOC** MEAN (STD)	**ANES** MEAN (STD)	**BSR** MEAN (STD)	**ROC** MEAN (STD)
Range	0.103 (0.061)	0.130 (0.094)	0.062 (0.025)	0.071 (0.031)	0.082 (0.049)
Δtmax	379.2 (222.2)	361.4 (154.4)	277.0 (93.3)	272.9 (45.8)	357.5 (179.9)
Δtmin	383.0 (227.2)	352.1 (150.2)	275.4 (80.5)	285.8 (69.4)	359.0 (186.0)
Δtmin-max	182.7 (145.0)	162.7 (107.1)	107.4 (75.8)	114.6 (36.3)	179.5 (133.0)
α	0.0009 (0.0006)	0.0011 (0.0009)	0.0008 (0.0003)	0.0008 (0.0004)	0.0007 (0.0004)
Area	417.6 (257.8)	393.9 (184.4)	287.8 (83.2)	301.0 (72.0)	387.6 (210.1)
AreaSyst	198.7 (159.8)	181.5 (123.3)	112.2 (77.7)	120.7 (37.6)	194.8 (150.1)
Δmax	0.0019 (0.0012)	0.0023 (0.0017)	0.0012 (0.0004)	0.0013 (0.0006)	0.0014 (0.0008)
Δrange	0.0030 (0.0020)	0.0033 (0.0022)	0.0018 (0.0006)	0.0020 (0.0009)	0.0022 (0.0012)
CBVrel	1.015 (0.669)	1.128 (0.822)	0.593 (0.194)	0.660 (0.295)	0.747 (0.412)
CBFest	51.91 (40.34)	48.76 (31.14)	33.99 (12.42)	37.51 (18.86)	34.87 (19.90)

The evolution of the parameters across the 5 anesthesia states is depicted in Figure 5-6. The REG Range showed its maximum value for LOC, and its minimum for steady state anesthesia. The same trend was shared by δrange, δmax and CBVrel. Regarding the systolic area (AreaSyst), its value in Awake and ROC was comparable, a slightly decrease was observed for LOC and the lowest values took place in Anes and BSR states. A similar behavior was detected for CBFest, with the only difference that Awake values were not recovered at ROC.

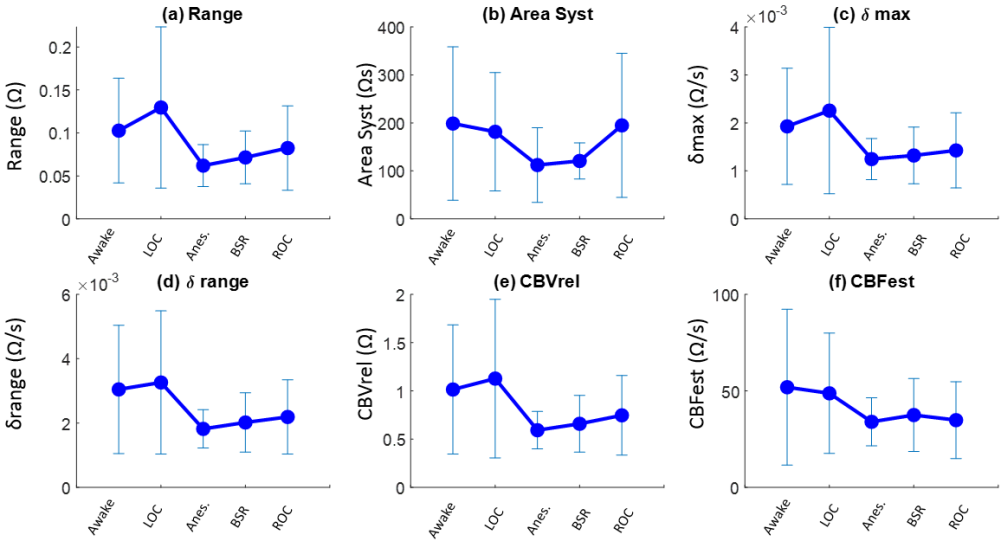

Figure 5-6 Trends (mean and standard deviation) of the parameters showing statistically significant differences for the transitions between the defined anesthetic states: (a) Range, (b) AreaSyst, (c) δmax, (d) δrange, (e) CBVrel and (f) CBFest.

In order to highlight which extracted features present statistically significant differences among consecutive anesthesia states, Table 5-6 presents the results for the hypothesis testing. The REG range, the relative cerebral blood volume CBVrel, the CBF estimation CBFest and the maximum and range of the derivatives presented significant differences between the states of LOC and Anes, while AreaSyst was the only feature able to track differences between BSR and ROC.

Table 5-6 Statistical significance (p-value) of the differences in every transition of anesthetic states. Significant values ($p<0.01$) are indicated in bold type.

FROM TO	AWAKE LOC	LOC ANES	ANES BSR	BSR ROC
Range	0.280	**1.78E-04**	0.568	0.661
Δtmax	0.990	0.027	0.330	0.062
Δtmin	0.328	0.220	0.341	0.149
Δtmin-max	0.248	0.021	0.139	0.011
α	0.238	0.024	0.921	0.650
Area	0.409	0.097	0.362	0.149
AreaSyst	0.328	0.013	0.141	**0.006**
δmax	0.316	**1.78E-04**	0.768	0.833
δrange	0.424	**1.43E-04**	0.925	0.733
CBVrel	0.354	**7.37E-05**	0.837	0.615
CBFest	0.829	**0.004**	0.330	0.783

5.4.2 With nonlinear filter

Similar values to those presented for the linear filter were obtained with the nonlinear filter (Table 5-7). The extracted features presented as well high standard deviations when compared to the average values, suggesting considerable dispersions of their distributions.

Table 5-7 Average values (mean, standard deviation) of all the extracted geometric features in each anesthesia state for REG data preprocessed with the nonlinear filter.

	AWAKE MEAN (STD)	**LOC** MEAN (STD)	**ANES** MEAN (STD)	**BSR** MEAN (STD)	**ROC** MEAN (STD)
Range	0.095 (0.054)	0.130 (0.093)	0.064 (0.026)	0.070 (0.030)	0.079 (0.047)
Δtmax	359.5 (200.3)	363.2 (160.3)	268.5 (75.0)	260.7 (52.3)	341.0 (164.5)
Δtmin	365.6 (214.1)	358.6 (162.6)	272.8 (78.7)	267.9 (55.8)	340.3 (164.3)
Δtmin-max	175.5 (135.7)	154.6 (103.5)	85.9 (49.6)	96.5 (39.7)	155.9 (119.8)
α	0.0010 (0.0007)	0.0011 (0.0010)	0.0010 (0.0006)	0.0010 (0.0006)	0.0008 (0.0005)
Area	392.0 (239.1)	396.6 (196.8)	282.9 (80.8)	279.3 (57.6)	363.2 (187.9)
AreaSyst	188.3 (149.5)	170.4 (117.4)	89.2 (51.2)	100.8 (41.3)	167.7 (135.4)
δmax	0.0018 (0.0010)	0.0023 (0.0018)	0.0014 (0.0005)	0.0014 (0.0007)	0.0014 (0.0007)
δrange	0.0028 (0.0018)	0.0034 (0.0024)	0.0020 (0.0007)	0.0021 (0.0009)	0.0021 (0.0011)
CBVrel	0.923 (0.569)	1.159 (0.885)	0.632 (0.221)	0.669 (0.282)	0.718 (0.386)
CBFest	50.39 (40.08)	50.30 (33.50)	36.94 (14.28)	40.76 (21.33)	35.17 (21.16)

The trends of those parameters are graphed in Figure 5-7. The parameters Δtmin-max and AreaSyst presented analogous trends, characterized by higher values at Awake and ROC, a small decrease for LOC and a minimum in Anes. All other parameters presenting statistical significant differences (Range, δrange, δmax and CBVrel) showed an absolute maximum at LOC and the minimum in anesthesia, with ROC values slightly lower than the ones recorded in the Awake state.

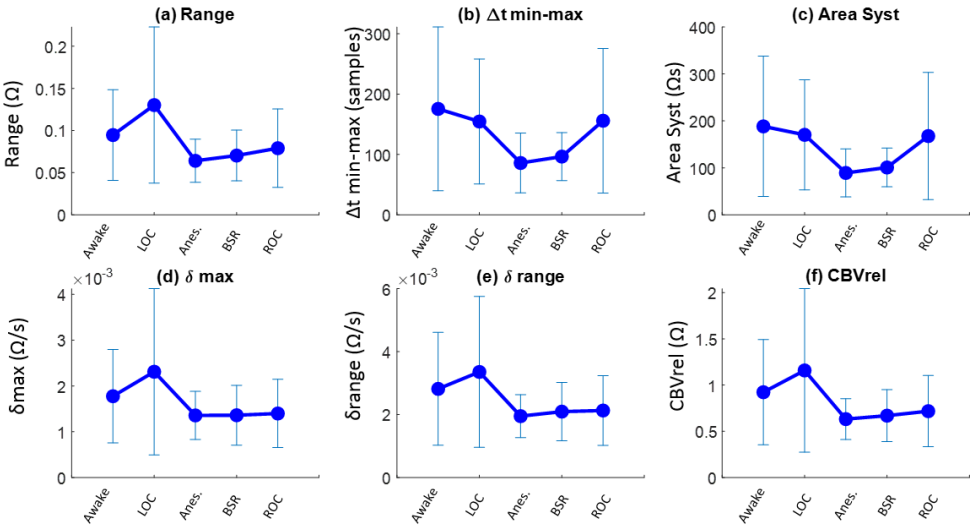

Figure 5-7 Trends (mean and standard deviation) of the parameters showing statistically significant differences for the transitions between the defined anesthetic states when using the nonlinear filter for data preprocessing: (a) Range, (b) Δtmin-max, (c) AreaSyst, (d) δmax, (e) δrange and (f) CBVrel.

The statistical significance of the results obtained from the hypothesis testing are summarized in Table 5-8. The only transition identifiable with the selected set of geometrical features was the one from LOC to Anes, that was detected by the REG Range, the time difference between a minimum and its consecutive maximum (Δtmin-max), the systolic area (AreaSyst), the maximum of the derivative and its dynamic range (δmax and δrange) and the relative blood volume (CBVrel).

Table 5-8 Statistical significance (p-value) of the differences in every transition of anesthetic states when preprocessing with the nonlinear filter. Significant values ($p<0.01$) are indicated in bold type.

FROM TO	AWAKE LOC	LOC ANES	ANES BSR	BSR ROC
Range	0.0880	**0.0001**	0.4430	0.7578
Δtmax	0.9044	0.0476	0.3894	0.1579
Δtmin	0.6480	0.2022	0.7141	0.2234
Δtmin-max	0.2205	**0.0013**	0.8155	0.0119
α	0.1428	0.8913	0.0855	0.2490
Area	0.9617	0.0964	0.7162	0.1677
AreaSyst	0.2488	**0.0008**	0.8257	0.0119
δmax	0.1184	**0.0006**	0.5354	0.4909
δrange	0.1128	**0.0001**	0.4543	0.9612
CBVrel	0.0716	**0.0001**	0.2804	0.8076
CBFest	0.4711	0.0404	0.5995	0.7089

5.4.3 Confounding factors

Patient demographics (age, height, weight and BMI) were tested for their influence in the REG features extracted in each clinical state (**Table 5-9**). A few significant correlations were found between patient characteristics and REG parameters in the awake state, but most of them were identified in the Anes state. No significant correlations were found for LOC, BSR and ROC.

In the Awake state, age showed a low but significant correlation with Range and CBVrel in the linear filter group, not detected in the nonlinear approach. However, weight and BMI had a moderate significant correlation with Range, that remained significant in the nonlinear group even though the correlation values calculated were lower. Moreover, CBVrel was also correlated with both weight and BMI in the linear filter group, the latest being reproduced as well in the nonlinear analysis.

Table 5-9 Spearman correlation of each geometric feature with patient demographics for every clinical state, either using the linear filter or the nonlinear filter. Cells are colored as indicated in **Figure 5-8** and statistical significance ($p<0.05$) is indicated in bold.

	Linear filter				Nonlinear filter			
Awake	Age	Height	Weight	BMI	Age	Height	Weight	BMI
Range	**0.369**	0.107	**0.459**	**0.447**	0.239	0.042	**0.390**	**0.397**
Δtmax	0.244	0.170	0.291	0.258	0.123	0.100	0.249	0.226
Δtmin	0.043	0.144	0.191	0.161	-0.070	0.086	0.121	0.112
Δtmin-max	0.289	0.159	0.224	0.182	0.122	0.147	0.169	0.117
α	0.115	-0.061	0.204	0.230	0.132	-0.112	0.076	0.141
Area	0.092	0.166	0.238	0.196	-0.080	0.107	0.142	0.123
AreaSyst	0.306	0.174	0.245	0.192	0.133	0.161	0.163	0.106
δmax	0.302	-0.018	0.348	**0.376**	0.219	-0.094	0.254	0.317
δrange	0.339	0.002	0.308	0.331	0.296	-0.021	0.244	0.288
CBVrel	**0.369**	0.033	**0.382**	**0.395**	0.343	-0.005	0.308	**0.346**
CBFest	0.101	-0.090	0.096	0.123	0.184	-0.071	0.053	0.092
LOC								
Range	-0.058	0.085	0.199	0.140	-0.101	0.022	0.120	0.094
Δtmax	-0.261	0.087	0.004	-0.052	-0.313	0.059	-0.041	-0.078
Δtmin	-0.279	0.104	-0.102	-0.162	-0.251	0.006	-0.008	-0.025
Δtmin-max	-0.216	0.151	0.114	0.047	-0.249	0.029	0.017	-0.003
α	0.173	-0.045	0.130	0.124	0.173	0.026	0.089	0.069
Area	-0.264	0.111	-0.093	-0.155	-0.250	0.000	-0.013	-0.026
AreaSyst	-0.202	0.143	0.088	0.024	-0.218	0.026	0.026	0.004
δmax	0.068	0.028	0.187	0.164	-0.009	0.002	0.113	0.106
δrange	0.104	0.045	0.271	0.244	0.038	0.003	0.194	0.189
CBVrel	0.048	0.081	0.271	0.232	-0.003	0.022	0.195	0.182
CBFest	0.238	-0.021	0.278	0.273	0.225	0.001	0.245	0.241
Anes								
Range	0.329	-0.034	**0.548**	**0.605**	0.261	-0.101	**0.454**	**0.527**
Δtmax	0.262	0.307	0.235	0.150	0.289	0.310	0.261	0.189
Δtmin	0.254	0.282	0.185	0.118	0.161	0.328	0.307	0.225
Δtmin-max	0.130	0.195	**0.397**	0.320	0.161	0.243	**0.467**	**0.385**
α	0.013	-0.070	0.110	0.151	-0.041	-0.234	-0.190	-0.088
Area	0.268	0.275	0.203	0.140	0.178	0.305	0.320	0.248
AreaSyst	0.148	0.212	**0.425**	**0.348**	0.177	0.240	**0.483**	**0.405**
δmax	0.071	-0.125	0.133	0.200	0.008	-0.201	0.016	0.112
δrange	0.178	-0.034	0.329	**0.369**	0.037	-0.128	0.154	0.220

Table 5-9 (continued)

CBVrel	0.232	-0.001	**0.408**	**0.435**	0.062	-0.091	0.194	0.250
CBFest	0.100	-0.118	0.285	**0.353**	0.030	-0.239	0.129	0.237
BSR								
Range	0.227	-0.190	0.317	0.411	0.211	-0.172	0.319	0.418
Δtmax	0.251	0.100	0.361	0.399	0.089	0.134	0.371	0.373
Δtmin	0.101	0.213	0.195	0.185	-0.077	0.193	0.270	0.260
Δtmin-max	0.024	0.232	0.175	0.028	-0.140	0.238	0.347	0.178
α	0.109	-0.160	0.054	0.162	0.182	-0.264	-0.086	0.112
Area	0.161	0.159	0.177	0.187	-0.075	0.190	0.287	0.276
AreaSyst	0.047	0.205	0.166	0.033	-0.112	0.187	0.336	0.189
δmax	0.230	-0.244	0.083	0.231	0.187	-0.259	0.044	0.208
δrange	0.189	-0.268	0.214	0.348	0.260	-0.335	0.050	0.213
CBVrel	0.226	-0.276	0.223	0.364	0.200	-0.253	0.153	0.291
CBFest	0.180	-0.359	0.070	0.199	0.172	-0.352	-0.115	0.036
ROC								
Range	0.022	-0.071	0.220	0.269	-0.022	-0.055	0.185	0.225
Δtmax	-0.048	0.178	0.036	0.003	-0.144	0.233	-0.002	-0.058
Δtmin	-0.035	0.089	-0.021	-0.043	-0.094	0.163	-0.042	-0.082
Δtmin-max	0.055	0.116	0.188	0.167	0.068	0.121	0.222	0.191
α	-0.143	-0.041	0.075	0.081	-0.175	-0.062	-0.077	-0.047
Area	-0.011	0.075	0.027	0.017	-0.090	0.183	0.012	-0.032
AreaSyst	0.052	0.092	0.182	0.170	0.073	0.123	0.219	0.189
δmax	-0.129	-0.061	0.086	0.140	-0.158	-0.009	0.067	0.103
δrange	-0.032	-0.102	0.176	0.239	-0.128	-0.013	0.160	0.196
CBVrel	-0.027	-0.093	0.169	0.231	-0.099	0.013	0.149	0.182
CBFest	-0.053	-0.059	0.239	0.258	-0.042	-0.091	0.186	0.224

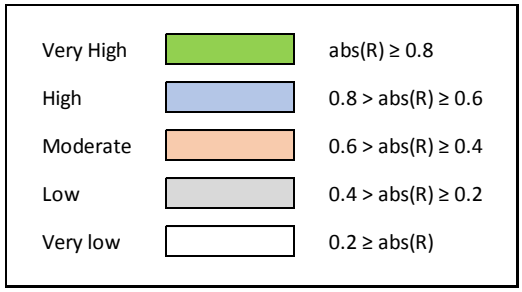

Figure 5-8 Spearman correlation values matching with colors and qualitative level.

Correlation values in the Anes state were higher, limited to weight and BMI. In the linear group, weight showed a moderate significant correlation with Range, AreaSyst and CBVrel, and a low significant correlation with Δtmin-max. The BMI presented a high and significant correlation with Range, a moderate one with CBVrel, and low but significant with AreaSyst, δrange and CBFest. Those correlations were in general lower in the nonlinear analysis, the highest value being also the one obtained for the pair Range and BMI.

Together with the correlations between demographics and the absolute values of the extracted features, the correlations of the relative values in each transition between anesthetic states and patient demographics were also assessed. The results are presented in **Table 5-10**. The only transitions associated with statistically significant correlations were the ones from Awake to LOC and from LOC to Anes.

Age was the most relevant factor in the transition between Awake and LOC, presenting negative significant correlation with Δtmax, Δtminmax and AreaSyst. The correlation with Δtmax was the only one coincident with the results in the nonlinear group, where a negative significant correlation between the patient weight and total area under the curve was also identified.

In the transition between LOC and Anes, age was again the most relevant factor, showing a moderate significant correlation with the REG range in both the linear and nonlinear approaches. Moreover, in the nonlinear group, age presented a low but significant correlation with Area as well.

The correlation analysis between the extracted REG features and other clinical variables is summarized in **Table 5-11**. The larger coefficients were the ones involving the BSR state, where several high and very high correlations were detected. Considering the transition between Awake and LOC, Δtmin and MAP had a moderate significant correlation in the linear analysis, and the effect site concentration of remifentanil presented moderate significant correlations with Δtmax, Δtmin, Δtmin-max, α and AreaSyst in the nonlinear approach.

Table 5-10 Spearman correlation between patient demographics and differences in geometric features for every transition between consecutive clinical states analyzed, either using the linear filter (left side) or the nonlinear filter (right side). Cells are colored as a function of the correlation value (see **Figure 5-8**) and statistical significance ($p<0.05$) of the correlations is indicated in bold type.

	Linear filter				**Nonlinear filter**			
Awake-LOC	Age	Height	Weight	BMI	Age	Height	Weight	BMI
Range	-0.233	0.014	-0.181	-0.240	-0.212	-0.044	-0.107	-0.161
Δtmax	**-0.399**	-0.212	-0.217	-0.136	**-0.401**	-0.064	-0.256	-0.217
Δtmin	-0.341	-0.263	-0.256	-0.172	-0.218	-0.161	-0.336	-0.284
Δtmin-max	**-0.407**	-0.124	-0.052	-0.009	-0.311	-0.120	-0.116	-0.069
α	0.089	0.104	-0.022	-0.110	0.037	0.077	-0.010	-0.082
Area	-0.277	-0.195	-0.384	-0.325	-0.208	-0.127	**-0.403**	-0.372
AreaSyst	**-0.389**	-0.155	-0.064	-0.009	-0.352	-0.130	-0.133	-0.083
δmax	-0.126	0.038	-0.052	-0.106	-0.122	0.026	0.003	-0.059
δrange	-0.145	0.072	-0.024	-0.112	-0.166	0.037	0.073	-0.027
CBVrel	-0.240	0.098	-0.060	-0.147	-0.257	0.053	0.057	-0.033
CBFest	0.138	0.140	0.124	0.037	0.104	0.050	0.129	0.049
LOC-Anes								
Range	**0.403**	-0.061	0.148	0.248	**0.439**	-0.023	0.167	0.245
Δtmax	0.287	0.156	0.184	0.181	0.362	0.159	0.172	0.160
Δtmin	0.317	0.149	0.283	0.258	0.359	0.227	0.259	0.215
Δtmin-max	0.056	0.164	0.110	0.026	0.254	0.164	0.198	0.148
α	0.100	-0.065	0.002	0.111	-0.074	-0.274	-0.235	-0.091
Area	0.363	0.070	0.236	0.248	**0.390**	0.209	0.266	0.232
AreaSyst	0.035	0.141	0.091	0.018	0.241	0.147	0.185	0.140
δmax	0.300	-0.141	0.016	0.143	0.297	-0.080	-0.016	0.068
δrange	0.281	-0.138	-0.036	0.085	0.273	-0.148	-0.052	0.056
CBVrel	0.291	-0.116	0.004	0.119	0.352	-0.113	0.002	0.099
CBFest	0.024	-0.182	-0.124	0.004	-0.167	-0.265	-0.192	-0.045
Anes-BSR								
Range	-0.045	0.248	0.056	-0.107	-0.070	0.276	0.050	-0.096
Δtmax	-0.259	-0.219	0.158	0.357	0.018	-0.079	-0.240	-0.171
Δtmin	-0.063	0.172	0.025	0.025	-0.052	0.117	-0.009	0.004
Δtmin-max	0.018	-0.192	0.278	0.404	-0.032	0.023	0.188	0.057
α	-0.084	0.278	-0.034	-0.243	0.130	-0.099	-0.145	-0.007
Area	-0.057	0.192	0.054	0.036	-0.052	0.117	-0.009	0.004

Table 5-10 (Continued)								
AreaSyst	0.039	-0.199	0.272	0.400	-0.032	0.023	0.188	0.057
δmax	-0.030	0.133	0.077	0.011	-0.136	0.231	0.269	0.168
δrange	0.007	0.022	-0.107	-0.107	-0.102	0.068	-0.061	-0.104
CBVrel	-0.014	0.063	-0.086	-0.118	-0.023	0.072	-0.068	-0.104
CBFest	0.220	-0.068	-0.163	-0.111	0.036	0.014	-0.032	-0.025
BSR-Awake								
Range	-0.238	0.202	-0.185	-0.258	-0.141	0.141	-0.120	-0.165
Δtmax	-0.235	0.219	-0.034	-0.127	-0.122	0.124	-0.001	-0.008
Δtmin	-0.172	0.198	-0.071	-0.189	-0.096	0.096	-0.134	-0.172
Δtmin-max	-0.124	0.248	0.172	0.091	0.022	0.153	0.154	0.117
α	-0.271	0.181	-0.015	-0.091	-0.287	0.233	0.090	-0.033
Area	-0.203	0.167	-0.112	-0.216	-0.130	0.092	-0.170	-0.205
AreaSyst	-0.164	0.231	0.106	0.027	0.005	0.167	0.142	0.104
δmax	-0.279	0.170	-0.052	-0.086	-0.277	0.203	0.012	-0.036
δrange	-0.274	0.279	-0.034	-0.083	-0.220	0.211	0.022	-0.013
CBVrel	-0.282	0.233	-0.015	-0.058	-0.193	0.195	-0.023	-0.041
CBFest	-0.280	0.291	0.011	-0.068	-0.237	0.266	0.037	-0.033

In the transition between LOC and Anes, HR and the propofol dosage were the clinical variables concentrating most significant correlations. In the linear analysis, HR correlated moderately with Δtmax, Δtmin and Area, and the propofol dosage with Range, Δtmax, Δtmin-max, AreaSyst, δrange and CBVrel. Moreover, the depth of anesthesia index qCON did also provide a significant moderate correlation with Δtmax. The results for the nonlinear analysis are consistent with those obtained with the linear one, with HR presenting significant and moderate correlations with Δtmax and Δtmin, and the propofol dosage with Range, Δtmax, Δtmin-max, Area, AreaSyst and CBVrel. In this case, MAP also showed a significant correlation with CBFest.

Regarding the transition from Anes to BSR, high correlations with statistical significance were detected between HR and Δtmin, HR and Area, MAP and α, MAP and AreaSyst, and between the qCON index and Range, δmax and CBFest. Additionally, very high correlations between the depth of anesthesia index and δrange and CBVrel were obtained. In the nonlinear analysis, correlations were in general lower, except for those related to HR. The transition between BSR and Awake was characterized by a very high significant correlation between MAP and Range for the nonlinearly filtered data. Overall, HR, MAP and qCON are the most relevant clinical variables

presenting significant correlations with REG features. Details on all pairs of correlations can be found in **Table 5-11**.

Table 5-11 Spearman correlation between clinical variables related to depth of anesthesia and hemodynamics and differences in geometric features for every transition between consecutive clinical states analyzed, either using the linear filter (left side) or the nonlinear filter (right side). Cells are colored as a function of the correlation value (see **Figure 5-8**) and statistical significance ($p<0.05$) of the correlations is indicated in bold type.

	Linear filter					**Nonlinear filter**				
Awake - LOC	HR	Propo	Remi	MAP	qCON	HR	Propo	Remi	MAP	qCON
Range	0.002	0.254	-0.133	0.317	-0.097	0.065	0.212	0.122	0.107	-0.020
Δtmax	-0.200	-0.240	-0.372	0.515	-0.306	-0.323	-0.274	**-0.483**	0.405	-0.230
Δtmin	-0.207	-0.275	-0.351	**0.567**	-0.275	-0.328	-0.215	**-0.487**	0.295	-0.184
Δtmin-max	-0.025	-0.347	-0.389	0.499	-0.313	-0.125	-0.414	**-0.553**	0.482	-0.305
α	-0.049	0.244	0.358	-0.215	0.208	0.018	0.426	**0.456**	-0.309	0.238
Area	-0.267	-0.118	-0.330	0.394	-0.288	-0.277	-0.072	-0.439	0.336	-0.186
AreaSyst	-0.035	-0.337	-0.430	0.515	-0.328	-0.128	-0.418	**-0.525**	0.529	-0.295
δmax	0.167	0.104	-0.065	-0.019	-0.085	0.198	0.180	0.039	-0.135	-0.015
δrange	0.181	0.191	-0.014	0.033	-0.048	0.132	0.268	0.102	-0.096	0.012
CBVrel	0.072	0.202	-0.144	0.129	-0.073	0.084	0.245	-0.047	-0.072	-0.083
CBFest	0.198	0.312	0.165	-0.275	0.171	0.232	0.308	0.298	-0.248	0.138
LOC-Anes										
Range	-0.139	**0.407**	0.015	-0.015	-0.143	-0.050	**0.432**	-0.003	0.006	-0.091
Δtmax	**-0.462**	**0.447**	-0.087	0.208	**-0.424**	**-0.421**	**0.427**	-0.049	0.175	-0.307
Δtmin	**-0.562**	0.325	-0.068	0.100	-0.305	**-0.409**	**0.380**	-0.099	0.043	-0.211
Δtmin-max	-0.158	**0.503**	-0.163	0.163	-0.359	-0.207	**0.588**	-0.186	0.181	-0.306
α	0.054	0.038	0.215	-0.394	0.022	0.136	-0.138	0.253	-0.285	0.133
Area	**-0.568**	0.364	-0.031	0.152	-0.284	**-0.400**	**0.419**	-0.073	0.119	-0.221
AreaSyst	-0.142	**0.498**	-0.156	0.147	-0.341	-0.195	**0.582**	-0.196	0.181	-0.307
δmax	0.073	0.357	0.053	-0.041	-0.080	0.141	0.337	0.076	-0.059	-0.002
δrange	0.077	**0.408**	0.005	-0.107	-0.032	0.140	0.373	0.066	-0.081	0.043
CBVrel	0.020	**0.453**	-0.007	-0.060	-0.097	0.076	**0.432**	0.008	-0.024	0.007
CBFest	0.236	0.081	0.224	-0.393	0.111	0.163	-0.118	0.263	**-0.481**	0.154
Anes-BSR										
Range	0.005	0.461	0.250	0.384	**0.683**	0.141	0.511	0.311	0.443	**0.634**
Δtmax	-0.395	-0.329	0.014	-0.100	0.054	**-0.581**	-0.300	0.043	-0.151	-0.036

Table 5-11 (Continued)

Δtmin	**-0.697**	-0.218	0.475	0.205	0.245	**-0.715**	-0.371	**0.571**	0.269	0.186
Δtmin-max	-0.315	-0.164	-0.250	-0.584	-0.030	-0.213	0.064	-0.379	-0.315	-0.084
α	0.368	**0.579**	0.271	**0.616**	**0.525**	0.372	0.193	0.125	0.297	0.481
Area	**-0.686**	-0.182	0.514	0.274	0.279	**-0.715**	-0.371	**0.571**	0.269	0.186
AreaSyst	-0.340	-0.171	-0.268	**-0.630**	-0.077	-0.213	0.064	-0.379	-0.315	-0.084
δmax	-0.034	0.411	0.300	0.434	**0.717**	0.181	0.336	0.354	0.461	**0.581**
δrange	0.245	0.357	0.386	0.511	**0.826**	0.324	0.439	0.425	**0.603**	**0.799**
CBVrel	0.177	0.396	0.346	0.511	**0.817**	0.157	0.429	0.418	**0.626**	**0.774**
CBFest	0.359	0.411	0.207	0.452	**0.665**	**0.515**	0.464	0.304	0.575	**0.651**
BSR-Awake										
Range	0.155	0.416	-0.320	0.633	0.277	0.170	0.403	-0.284	**0.817**	0.392
Δtmax	-0.338	0.250	0.020	-0.183	-0.181	-0.377	0.313	-0.074	-0.183	-0.050
Δtmin	-0.292	0.219	-0.069	-0.300	-0.112	-0.371	0.295	-0.098	-0.317	-0.152
Δtmin-max	-0.114	0.058	0.171	-0.283	-0.208	-0.138	0.091	0.251	-0.333	-0.330
α	0.301	0.266	-0.347	**0.750**	**0.531**	0.239	0.134	-0.273	0.633	**0.556**
Area	-0.264	0.261	-0.130	-0.217	-0.046	-0.356	0.350	-0.119	-0.233	-0.098
AreaSyst	-0.158	0.170	0.108	-0.333	-0.212	-0.144	0.115	0.247	-0.333	-0.303
δmax	0.201	0.390	-0.293	**0.733**	0.377	0.231	0.289	-0.301	**0.700**	**0.435**
δrange	0.248	0.330	-0.315	0.683	0.260	0.262	0.292	-0.268	**0.750**	0.424
CBVrel	0.187	0.397	-0.273	0.567	0.278	0.216	0.319	-0.234	0.617	0.399
CBFest	0.362	0.168	-0.290	**0.817**	0.417	0.378	0.123	-0.250	**0.817**	**0.455**

5.5 Discussion of the results obtained in apnea detection

The area of the systolic part of the cerebral pulse wave was the only feature among the ones under test that showed statistically significant differences between apnea and baseline REG recordings. Those results could suggest that either REG curves do not reflect CBF changes or that the geometrical features of the pulse wave do not contain enough information for CBF assessment under an apnea challenge.

Previous studies have assessed the influence of breath holding in CBF, using other monitoring techniques. For instance, Kastrup et al. used magnetic resonance to track rCBF changes during apnea, concluding that the detected

changes in cerebral hemodynamics were dependent on the apnea duration [17]. Vestergaard et al. [180] compared the changes in CBF in a group of freedivers with those from a control group. In both cases, they observed that CBF changes were time dependent as well, reaching an increase of CBF of 107% in freedivers and 25.6% in the control group. Moreover, before the expected increase of CBF, a small decrease was detected during the first seconds. Considering those evidences, one of the reasons for the lack of detection of CBF differences in this study might be the limited duration of the apnea challenge, as well as the selection of the segments to be analyzed: those were chosen to avoid artifacts without considering the time elapsed since the start of the breath holding challenge. However, the estimation of CBF (CBFest) showed higher values for the apnea group even though those were not statistically significant, which is consistent with the expected behavior of CBF during a breath holding challenge.

Only one of the selected features, AreaSyst, presented statistically significant higher values in the baseline periods. Several studies analyzing the aortic pulse wave [181][182] have reported that stroke volume is proportional to the area under the systolic portion of the arterial blood pressure curve. Considering the analogy with cerebral blood flow, AreaSyst might provide information on the blood volume reaching the brain in every heart beat. When compared to the cerebral blood volume estimation herein proposed, CBVrel, both parameters show opposite behaviors, with CBVrel increasing in apnea recordings. Therefore, results are not conclusive on which estimation of CBV better reflects the brain blood volume, needing further evidences and the validation with other technologies to reach a conclusion.

Overall, the extracted geometric features for REG provided limited information on CBF changes during the apnea challenge, requiring further validation and selecting REG segments during apnea with equivalent elapsed time since the start of the respiratory challenge. Moreover, the use of the nonlinear filter did not enhance the performance of the parameters under test, providing equivalent results in both processing strategies.

5.6 Discussion of the results obtained in anesthesia

The geometric features extracted from REG waves collected during general anesthesia provided a larger amount of statistically significant results when compared to the detection of apnea. Using the linear filter as the preprocessing technique, several geometric descriptors were able to detect differences between the LOC and Anes states: Range, δrange, δmax, CBVrel and CBFest. The evolution of those values suggest a generally decreased CBF and instantaneous blood flow velocity during anesthesia, as previously reported by Conti et al [78] and Fodale et al.[50].

CBFest and CBVrel decreased during general anesthesia. This phenomenon has been related with the vasoconstriction associated to the propofol administration [183][184]. It should be noted that values for those two features are not recovered after extubation. This is probably caused by the effects of propofol in hemodynamics, since at the time of extubation it has not been eliminated from the body [185].

The reduction of CBF and related parameters in the anesthetic state might seem inconsistent with the slight increases detected during BSR. Intuitively, the lower the anesthetic depth, the lower the brain metabolism, CBV and CBF. However, it has been proved in rats that hemodynamic fluctuations at the brain level occur during general anesthesia: cortical electrical activity is accompanied by oscillations in cerebral hemodynamics [186][187]. This might explain the small (and non-significant) increase of the CBF related parameters during BSR.

When comparing the results obtained with the two preprocessing techniques, the use of the nonlinear filter provided slightly different results but confirmed that the geometric features tested were capable of distinguishing between LOC and Anes states only. The main differences between the results obtained with the two preprocessing techniques were the inclusion of Δtminmax and AreaSyst in the list of parameters reflecting differences between LOC and anesthesia under the nonlinear filter hypothesis, while CBFest did not. A plausible explanation for this is that the algorithm of the nonlinear filter equalizes repeated patterns even in non-steady state conditions, based on a random selection of the first pattern. However, the extraction of the median value of each feature in every time window after linear filtering, preserves information on the distribution of the features within

the processed REG segment, providing more consistent values for the selected metrics.

The analysis of confounding factors revealed that weight and BMI have an influence on the baseline values of CBF. However, those correlations were moderate. In contrast, high and very high correlation scores were detected in the transitions from Anes to BSR, and from BSR to ROC. The presence of BSR in the two transitions suggests that under adequate general anesthesia CBF is decreased but without any major alterations, while in very deep anesthesia more changes occur. Analyzing the correlations calculated, those changes appear at the brain activity level, assessed with the qCON index, and at the hemodynamic level, indicated by MAP.

The correlation between MAP and REG extracted features suggests a possible coupling between MAP and CBF that deserves further attention since it could imply the impairment of the autoregulation mechanism. However, there is consensus in the scientific community around the fact that propofol, unlike some inhaled agents, preserves CAR [75]. Since propofol reduces both CBF and MAP, a correlation between both clinical variables might take place without the need of a causal relationship between them.

Finally, correlations with the qCON index reveal a relationship between the depth of anesthesia level and CBF, as previously reported by other authors [188][189]. This link is demonstrated by the high correlations with REG range, δmax and CBFest and the very high correlation with δrange and CBVrel.

5.7 Conclusions

Even though the use of geometrical features to track CBF changes from REG signals was not successful during the breath holding challenge, the analysis of signals recorded during general anesthesia provided relevant results.

The transition between LOC and Anes was characterized by significant changes in REG parameters reflecting a decrease in the signal Range, CBVrel and the parameters extracted from the REG derivative, consistent with the expected behavior. Moreover, correlations with other clinical variables such as MAP and the qCON index, reflected that those CBF changes were also

related to the brain activity (EEG) and the global hemodynamic state of the patient (MAP). Further studies are needed with larger datasets to analyze the influence of patient demographics in CBF as well as possible causal relationships among EEG, hemodynamics and CBF parameters.

Chapter 6

Poincaré Plot Analysis of REG Signals

Abstract

Nonlinear analysis of physiological signals is often used to detect underlying structures in the time series. This chapter explores the hypothesis that one of those techniques, Poincaré plot analysis, provides further information on CBF changes when applied to REG signals than the traditional approach based on the detection of geometric features of pulse waves.

6.1 Introduction

Biological signals are known to be controlled by central nervous system oscillators that make them complex, causing some irregular patterns [190]. Nonetheless, some underlying well determined behavior exists. Therefore, physiological signals might be better characterized by dynamic nonlinear analysis instead of using standard linear time series signal processing techniques, as the ones presented in Chapter 5.

One nonlinear technique used to study beat to beat intervals is the method of delayed coordinates for state-space analysis, the so-called Poincaré plot. Dimitriev et al. [191] analyzed by means of nonlinear dynamics based on Poincaré plots how the state of anxiety affected heart rate variability. Voss et al. [192] have previously published on the effects of age and gender in short-term heart rate variability analyzed with Poincaré plots among other features and Ebrahimzadeh [193] explored the prediction of sudden cardiac death based on complexity analysis. Other biological signals have been studied by means of Poincaré plots. Hayashi [194] related the delayed coordinates map to changes provoked by anesthesia in the electroencephalograph (EEG). Xiong et al. [195] explored the ability of Poincaré plots from electromyogram (EMG) to reflect facial paralysis and Son et al. [196] studied regularity in respiratory signals using this same technique.

Hoshi et al. [197] used standard descriptors of Poincaré plot analysis to distinguish between healthy subjects and patients suffering coronary disease, concluding that the SD1/SD2 index provided useful information for that purpose. Even though some features extracted from Poincaré plots are known to be highly correlated to linear time domain information [198], some others reflect nonlinear behaviors, complementing the diagnosis capabilities of heart rate variability signals, such as the SD1/SD2 parameter or the Complex Correlation Measure [199].

Poincaré plot Analysis is typically applied with a time lag of 1 sample, therefore plotting the original signal versus its 1 sample delayed version. Several publications have explored the possibility of using different time lags to build the Poincaré plot. Since consecutive samples are highly correlated, when a lag of 1 sample is used, data are concentrated on the identity line. Increasing time lags would spread the data points over the Poincaré plot, because there is less correlation between lagged samples [200], [201].

Brennan et al. [198] discussed the effects of lagging the Poincaré plots, showing that those lagged plots characterize the autocovariance function, yet there is no consensus on which lags should be used [202]. Lerma et al. [203] determined that a lag of 4 heart beats would optimize the detection of changes in heart rate variability due to hemodialysis in chronic renal failure patients, while Thakre and Smith [201] stated that a heartbeat can only influence up to the next 6 to 8 beats and therefore higher lags would not be suitable for those applications. Therefore, lags lower than 10 are typically used for RR intervals [202].

Contreras et al. [204] used lagged Poincaré plots and assessed the correlation between the spectral features (HF and LF) and the SD1 parameter, concluding that the value of those correlations was different in healthy and pathological heart rate variability signals. Lagged plots were also used by Goshvarpour [200] to analyze heart rate during mediation, detecting an increase in the SD1 parameter for increasing lags up to 6 beats which reflects the transition between cigar-shaped plots for the smallest lag to a cloud of points with the largest ones.

This chapter focuses on the analysis of the dynamics of REG signals through lagged Poincaré plots aiming at understanding underlying nonlinear behavior and identifying how those dynamics can assess physiological changes affecting the system. Since CBF is modulated by several physiological conditions, applying nonlinear analysis could be a very promising tool for improving clinical information extracted from REG. The analysis herein proposed is therefore based on the method of delayed coordinates for state-space analysis since, to the extent of the knowledge of the author, it has not been used for REG data processing. A simple respiratory challenge, apnea, was initially used to explore REG capability to reflect CBF changes and to analyze nonlinear dynamics in REG signals. Results obtained from this analysis were afterwards applied to REG data collected during surgeries under general anesthesia, to assess the ability of REG to reflect changes in CBF under those circumstances.

6.2 Methods

6.2.1 Poincaré plot analysis

Taken's theorem [205] states that the attractor of a dynamical system can be reconstructed as a state-space representation for a specific time delay (τ) and embedding dimension (m). This attractor, X(t), can therefore be specified as:

$$X(t) = [x(t) \quad x(t+\tau) \quad x(t+2\tau) \quad \dots \quad x(t+(m-1)\tau)] \qquad (6.1)$$

Even though the attractor of a given system might have a high embedding dimension, the analysis of reconstructed attractors on two dimensions has been extensively used to characterize biomedical signals, such as heart rate variability, and has proven to provide relevant information [203], [206], [207]. In this case, equation 6.1 can be simplified as:

$$X(t) = [x(t) \quad x(t+\tau)] \qquad (6.2)$$

Two-dimensional Poincare plots were constructed from REG sequences. Each Poincaré plot is generated with the x-axis representing the REG signal (REG(t)) and the y-axis representing the REG signal after a specified time delay τ (REG(t + τ)), where the length of the series is N and t moves from 1 to N-τ. The time lag τ to be applied to the signal samples to build the Poincare attractor is commonly defined by these criteria:

- 1/4 or 1/5 of the dominant cycle period (T) of the signal [208]
- First local minimum of the auto-mutual information function (AMIF) [209]
- First zero crossing of the autocorrelation function (ACF) [210]

- First value for which the normalized autocorrelation function has a decay of $1/e$ [210].
- First sign change of the second derivative of the autocorrelation function [211]
- 1/10 to 1/20 of the first local minimum of the autocorrelation function [212]

The choice of the time lag τ is critical, since very low values would not allow the attractor to expand, with a majority of points laying on the diagonal line [213], while very large values of τ would cause deformations of the attractor due to the fact that pairs of samples would be uncorrelated [209][211] . Since no previous work has been done on the analysis of REG attractors, a wide range of τ values was used, from 1 up to the maximum of the above listed criteria, to provide the maximum possible information relating to the dynamics hidden in REG signals.

To generate quantitative information on the distribution of REG signals in the Poincare plots, several features were extracted from the reconstructed attractor characterization. Two of these features are considered the standard descriptors of Poincaré plots, being named SD1 and SD2. They are obtained by defining a new set of perpendicular axis (x1 and x2 in **Figure 6-1**), x2 following the identity line and therefore rotating the axis 45º and fitting an ellipse to the plot as shown in **Figure 6-1**. Features SD1 and SD2 are defined as the standard deviation of the distance along the axis x1 and x2 respectively, and lay on the axis of the fitted ellipse having half its size [198], [208], [214]–[216]. They are computed following the equations 6.3 and 6.4, where var is the variance.

$$SD1 = \sqrt{\mathrm{var}\left(\frac{REG(t) - REG(t+\tau)}{\sqrt{2}}\right)} \tag{6.3}$$

$$SD2 = \sqrt{\mathrm{var}\left(\frac{REG(t) + REG(t+\tau)}{\sqrt{2}}\right)} \tag{6.4}$$

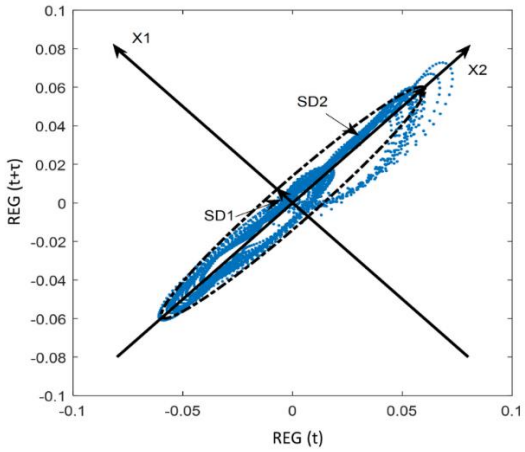

Figure 6-1 SD1, SD2 and ellipse fitting of a REG signal.

Short term variability is reflected by SD1 while SD2 reflects both, long and short-term variability. Moreover, the area (A) of the ellipse (equation 6.5) has also been considered since it provides a measure of the total variability of the attractor [215].

$$A = \pi \, SD1 \, SD2 \tag{6.5}$$

The ratio of SD1/SD2 was also used as a parameter (SDratio) to measure the changes in the scatter patterns. Hayashi et al. [208] proposed this technique as a useful tool for depth of anesthesia assessment by means of Poincaré plots as this ratio reflects the degree of linearity included in the processed signal.

Correlation measures are also proposed to characterize the shape of the Poincaré plots. Equation 6.6 shows the correlation measure (R)[198], in which E [ ] is the expected value of the time series and $\overline{REG}$ the average value of the REG(t) time series.

$$R = \frac{\mathrm{E}[(REG(\mathrm{t}) - \overline{REG})(REG(\mathrm{t}+\tau) - \overline{REG})]}{\sqrt{\mathrm{E}[(REG(\mathrm{t}) - \overline{REG})^2]\mathrm{E}[(REG(\mathrm{t}+\tau) - \overline{REG})^2]}} \quad (6.6)$$

Another correlation descriptor considered is the Complex Correlation Measure (CCM) [217]. Its computation identifies all possible sets of three consecutive attractor points of the Poincaré plot and the area of the triangle they define is calculated (**Figure 6-2**). In cases where all three points are aligned, the area is considered to be zero. The purpose of analyzing sets of three points in this way is that the descriptor will integrate information from different time lags and instead of reflecting just the overall variance as with SD1 and SD2, it will integrate temporal information as well. CCM is computed as indicated in equation 6.7, where N is the number of points in the Poincaré plot, A_n is a normalization constant equivalent to the ellipse area ($A_n = \pi*SD1*SD2$), τ is the time lag of the Poincaré plot and M(i) is the matrix including the coordinates of the three points from each subset whose determinant is the area of the triangle formed by them.

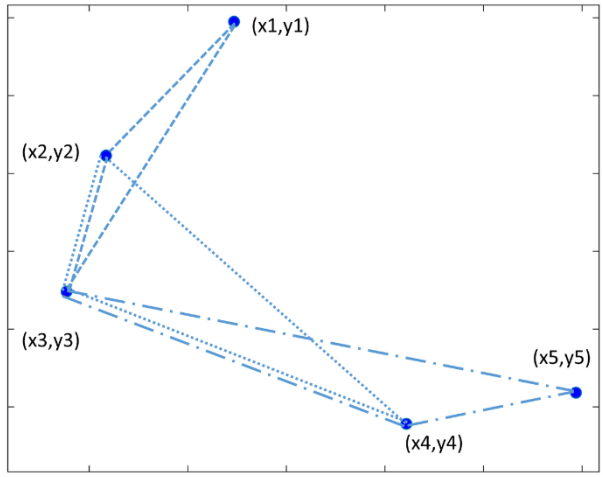

Figure 6-2 Example of the application of the Complex Correlation Measure (CCM) algorithm in a subset of 5 data points.

$$\mathrm{CCM}(\tau) = \frac{1}{\mathrm{A_n}(\mathrm{N}-2)} \sum_{\mathrm{i}=1}^{\mathrm{N}-2} \|\mathrm{M(i)}\| \quad (6.7)$$

6.2.2 Experimental datasets

The Poincaré plot analysis was applied to two datasets, Apnea-Baseline and General Anesthesia Dataset 1. The first of them contains REG signals recorded on 16 healthy volunteers under apnea and baseline periods while the second one is composed of REG waves collected from 40 patients undergoing surgical procedures requiring general anesthesia. Details on both datasets were provided in Chapter 3.

In a first analysis, the Apnea-Baseline dataset was used to determine the range of lags τ to be considered for analysis, by means of applying the set of criteria described in section 6.2.1. Moreover, the ability of the Poincaré plot descriptors to detect apnea periods was assessed through hypothesis testing and a final set of τ was chosen for further analysis. In a second step, results from the Apnea-Baseline dataset were applied in the calculation of the Poincaré plot descriptors of REG signals during general anesthesia.

6.2.3 Data analysis for apnea detection

A total of 53 sequences free from artifacts, with 4000 samples length, were obtained from the Apnea-Baseline dataset analysis. From those signals, 29 were recorded during apneas while 24 belonged to baseline periods. All signals were filtered with a 4th order high-pass filter with a stop band frequency of 0.1Hz to remove baseline drift.

Moreover, a classical linear filter was applied to all the REG recordings to remove high frequency noise while preserving the pulse wave pattern. The 2D-Poincaré plot of the attractor of each signal in the dataset was reconstructed for varying time lags, and the following features were extracted: SD1, SD2, SDratio, SDarea, R and CCM. A statistical analysis was performed to select τ values that allowed 2D-Poincaré plot features to statistically distinguish between signals belonging to apneas and resting periods. Hypothesis testing was applied using student t-test for normal distributions and Mann-Whitney test for non-normal distributions verified by the Kolmogorov–Smirnov test. Significant statistical level was set at $p\text{-value}<0.05$ and Bonferroni correction ($p\text{-value}<0.025$) was applied. The ability of the extracted features to distinguish between apnea and baseline periods was

further assessed by means of sensitivity, specificity, area under the curve (AUC) of the Receiver Operating Characteristic and accuracy. Finally, this analysis was repeated for REG signals preprocessed with the nonlinear filter algorithm, to assess the influence of the filtering technique in the obtained results.

6.2.4 Data analysis for general anesthesia recordings

REG signals in the General Anesthesia Dataset 1 were classified in 5 different categories depending on the clinical state of the patients during general anesthesia:

- Awake – corresponding to the data recorded prior to anesthesia induction.
- Loss of Consciousness (LOC) – data recorded right after LOC is detected and while intubation is being prepared
- Steady state anesthesia – data recorded during anesthesia, without burst suppression episodes and after intubation has been achieved and patient positioned for surgery.
- Burst Suppression Rate (BSR) - data belonging to periods in which the Conox BSR index provides values higher than 10.
- Recovery of consciousness (ROC) – data belonging to the end of the procedure, once drug infusion has been stopped and patent is ready to be extubated.

After artifact rejection, recordings of 4000 samples were classified obtaining 34 REG signals for the Awake state, 35 for LOC, 33 for Anesthesia. 22 for BSR and 40 for ROC. As in the Apnea-Baseline dataset, all segments were high pass filtered to eliminate slow fluctuations and low pass filtered using either the optimal classical filter or the nonlinear algorithm.

The Poincaré plot descriptors SD1, SD2, SDratio, SDarea, CCM and R, were calculated for each segment, using the τ range optimizing apnea detection in the previous analysis. The ability of those parameters to

distinguish between the different stages of anesthesia was assessed by means of hypothesis testing. A paired student t-test was used for normal distributions and Wilcoxon test for non-normal distributions, verified by the Kolmogorov–Smirnov test. Considering the number of categories defined and the application of Bonferroni correction, the statistical significance threshold was set to $p<0.01$.

The influence of patient demographics and variations in the clinical condition of the patient other than the ones provoked by the anesthetic state were considered as confounding factors. Therefore, Spearman correlation of heart rate (HR), mean arterial pressure (MAP), propofol effect site concentration (CePropo), remifentanil effect site concentration (CeRemi) and the depth of anesthesia index (qCON) with the Poincaré plot descriptors was computed, considering statistical significance of the resulting correlations for p-value<0.05.

6.3 Results for apnea detection

6.3.1 With linear filter

The dominant cycle period of the REG recorded signals, the auto-mutual information and autocorrelation were computed to determine the range of τ values to be used in the reconstruction of the attractors following the criteria previously listed. The average period of REG signals was 0.99 ± 0.12s (mean $\pm$ standard deviation), equivalent to 246.9 ± 30.8 samples. No differences were detected between periods of apnea and baseline signals (p-value = 0.345). All values presented for each criterion used for τ calculation are presented in **Table 6-1**. On average, the highest τ is provided by the recommendation based on ¼ of the period (61.7 ± 7.7 samples) and therefore the range of τ values used was from 1 to 70 samples (from 0.004 to 0.28 s).

Table 6-1 Tau values (in samples) calculated from the REG signals following the criteria recommended in literature.

	1/4 of the period	1/5 of the period	1st Relative min of AMIF	1st zero of ACF	1/e decay of ACF	2nd derivative of ACF sign change	1/10 of 1st local min ACF	1/20 of 1st local min ACF	1/4 of the period	1/5 of the period	1st Relative min of AMIF	1st zero of ACF
Mean	61.7	49.4	34.2	58.4	36.5	19.0	12.0	5.98	61.7	49.4	34.2	58.4
Std	7.70	6.16	11.6	14.3	9.73	9.63	3.15	1.57	7.70	6.16	11.6	14.3
Min	38.5	30.8	16.0	20.0	14.0	10.0	3.40	1.70	38.5	30.8	16.0	20.0
Max	76.9	61.5	70.0	91.0	56.0	49.0	17.5	8.75	76.9	61.5	70.0	91.0

Mean, standard deviation (std) min and max values are provided for each criterion

Attractors were reconstructed for every signal and τ value. The two-dimensional Poincaré plots for a baseline and apnea REG signal built for τ=5, τ=10 and τ=70 samples are shown in **Figure 6-3**. While low τ values seem to preserve the attractor shape, for τ=70 samples the attractor looks deformed.

From the reconstructed attractors, the defined Poincaré plot features (SD1, SD2, SDratio, SDarea, CCM and R) were calculated for every selected segment and every time lag, and their ability to separate apnea from baseline signals was assessed through hypothesis testing. The evolution of all parameters, as a function of the chosen time lag τ, for both apneas and baseline can be observed in **Figure 6-4**.

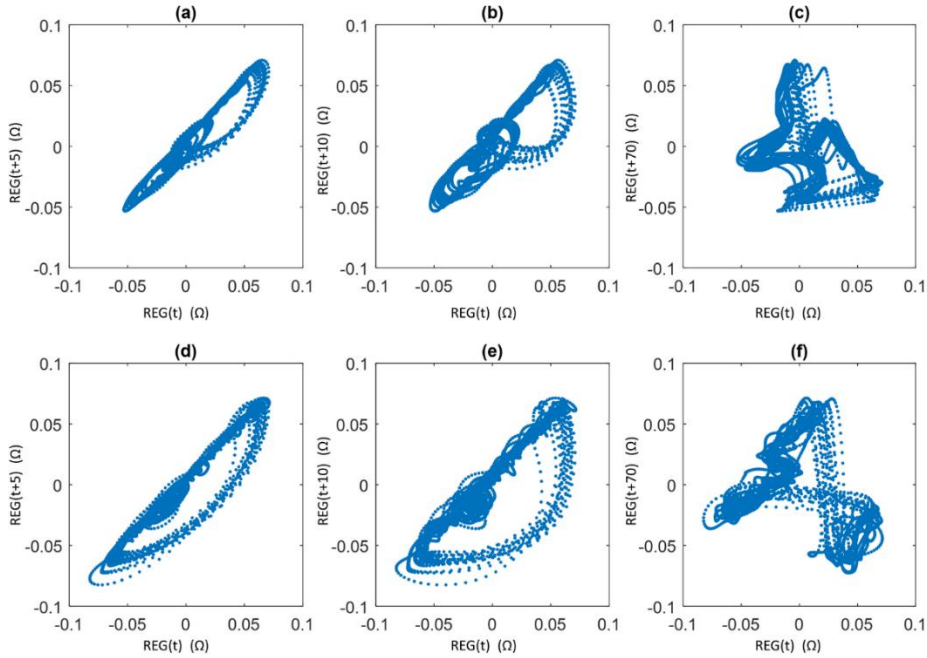

Figure 6-3 Poincaré plot reconstruction of apnea and baseline signals. Apnea signal (a,b,c) and baseline signal (d,e,f) for different time lags: τ=5 samples (a,d), τ=10 samples (b,e) and τ=70 samples (c and f).

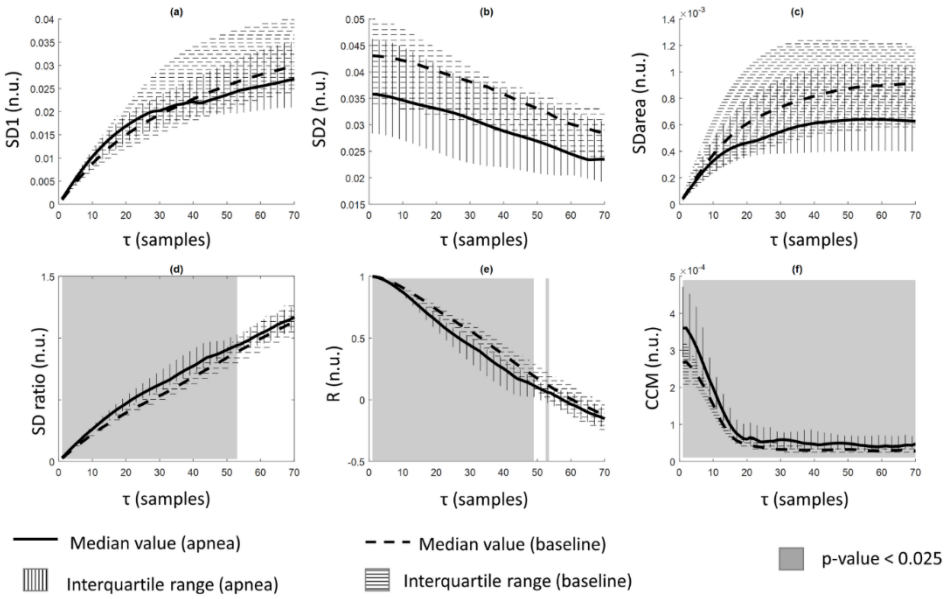

Figure 6-4 Comparison of the results obtained for apnea and baseline periods (median values, interquartile range and statistical significance) of all tested features in function of the time lag τ. (a) SD1; (b) SD2; (c) SDarea; (d) SDratio; (e) R; (f) CCM. Grey solid color corresponds to statistical significance level of p-value<0.025.

SD1 shows a curvilinear increase as τ increases (**Figure 6-4**a) for both apneas and baseline periods, presenting higher values in apneas for low τ values and reversing this behavior for τ values above 40 samples. The behavior of SD2 is the opposite (**Figure 6-4**b), decreasing as τ increases, providing higher values for baseline periods for all tested τ values. None of those features show significant differences between the apnea and baseline groups.

SDarea, which is a composite measure of SD1 and SD2 (**Figure 6-4**c), increases with an exponential pattern while τ increases and provides higher values for the baseline group, even though differences are not significant. However, SDratio (**Figure 6-4**d) is also a composite feature and shows significant differences between apnea and baseline periods for τ up to 53 samples, resulting in higher values for the apnea group.

The values of parameter R have an opposite behavior when compared to SDratio (**Figure 6-4**e), decreasing as τ increases, with the baseline group showing higher values than the apnea group. These differences were

significant for all τ lower than 49 and τ=53. Finally, observing the evolution of the values of the parameter CCM, it can be stated that they are higher in apnea group than baseline group with p-value <0.025 for all range of the analyzed time lags.

Among all tested features, three have shown to be capable of distinguishing between apneas and baseline data for several τ values: SDratio, R and CCM. The features R and SDratio showed statistically significant differences between groups for τ values below 50 samples, showing the lowest p-value for τ equal 2 and 3 samples (p-value=$7.01*10^{-5}$). CCM showed significant differences between groups for all τ values, presenting its minimum value for τ =13 samples (p-value =0.00012).

Figure 6-5 illustrates the comparison between the τ values for which the extracted features were significant (**Figure 6-4**) with those theoretical τ values presented in **Table 6-1**. It can be observed that R and SDratio are statistically different for τ values lower than 50 samples, while CCM is significant for all range with lower values between 10 and 20. It should be noted that for the first six proposed theoretical criteria (1/20 and 1/10 of the first local minimum of the autocorrelation function, the first sign change in its second derivative, the first local minimum of the automutual information, a decay of 1/e of the autocorrelation and 1/5 of the signal dominant period) the three extracted features remain significant, since when using the criterion of 1/5 of the period all p-values are below 0.025.

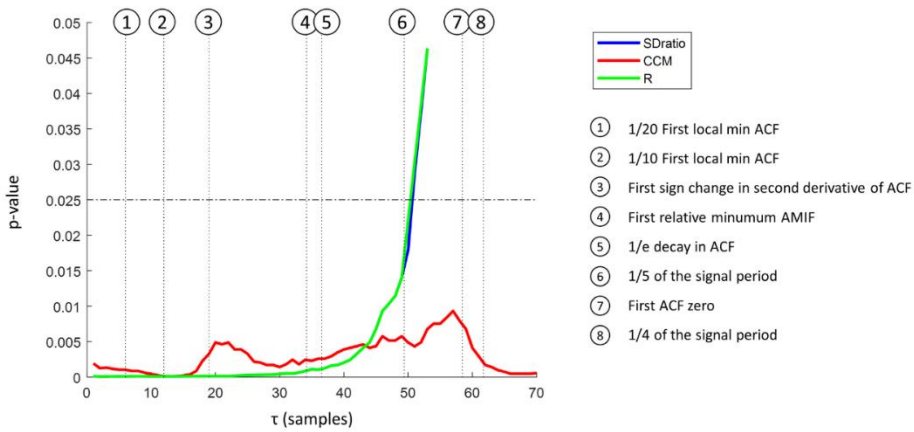

Figure 6-5 Statistical significance levels (p-value) for SDratio, CCM and R, as a function of the time lag τ when comparing apnea and baseline segments. R and SDratio curves are overlapped for almost all values. The dotted horizontal black line shows significance when applying Bonferroni correction. Vertical lines indicate the different criteria commonly used to determine τ.

Correlations were performed between features that were statistically significant (**Figure 6-6**). Pearson's correlation was applied to the full dataset including SDratio, CCM and R values from all subjects and all time lags (i.e. resulting in 3710 data points in each case). Since their definitions are quite similar both SDratio and R showed a high correlation (ρ=0.965, p-value<0.001) although not linear. As can be observed in **Figure 6-6**c, CCM showed lower correlations with both SDratio and R.

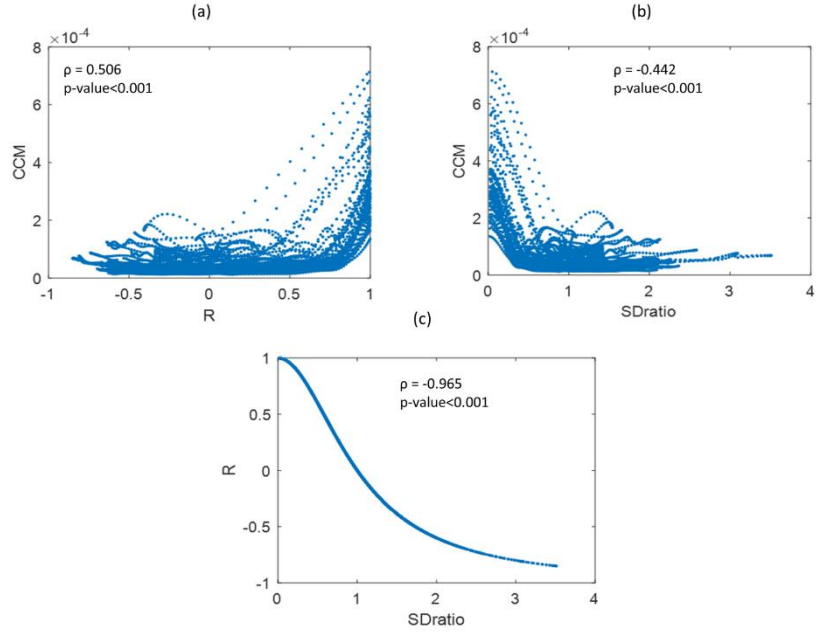

Figure 6-6 Correlations between R, CCM and SDratio. (a) R and CCM, (b) SDratio and CCM, and (c) CCM and R.

The parameters that showed positive results were analyzed by means of computing their sensitivity, specificity and AUC. **Figure 6-7** shows the sensitivity and specificity for SDratio, R and CCM features in the time lag values for which they showed statistically significant levels. Both SDratio and R provide a high specificity but very low sensitivities, typically below 60% and with higher values for low τ, for which it can be observed that SDratio shows better performance. CCM shows better sensitivity and specificity, showing a

peak of 90% specificity for τ between 10 and 20, and maximal sensitivity for τ lower than 10.

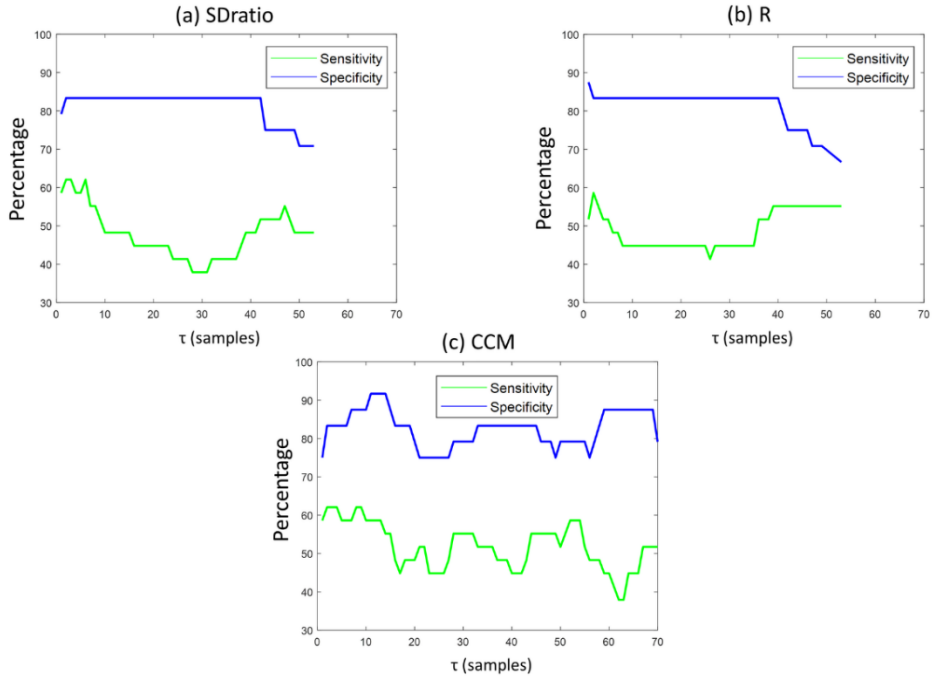

Figure 6-7 Sensitivity and specificity of apnea and baseline classification as a function of the time lag values (τ). (a) SDratio, (b) R and (c) CCM.

For all three, the best performances are detected for very small τ values (lower than 5 samples), lower than the ones proposed in the literature for other physiological signals shown in **Table 6-1**, the closest approximation being a time lag corresponding to 1/20 of the first local minimum of the autocorrelation function.

Figure 6-8 presents the AUC computed for each parameter and each time lag τ. Both SDratio and R provide the best results, with values higher than 0.8 for low τ values ($\tau < 5$ samples) and decreasing when τ increases. Even though CCM also offers its best AUC values for low time lags, it does not show such a monotonic decreasing behavior. As previously seen in the analysis of the obtained p-values, SDratio (**Figure 6-4**d) and R (**Figure 6-4**e) provide optimal results for τ values lower than the ones recommended in the literature (**Table 6-1**) while the best performance of CCM takes place for τ

values consistent with 1/10 of the first local minimum of the autocorrelation function and the first sign change in its second derivative.

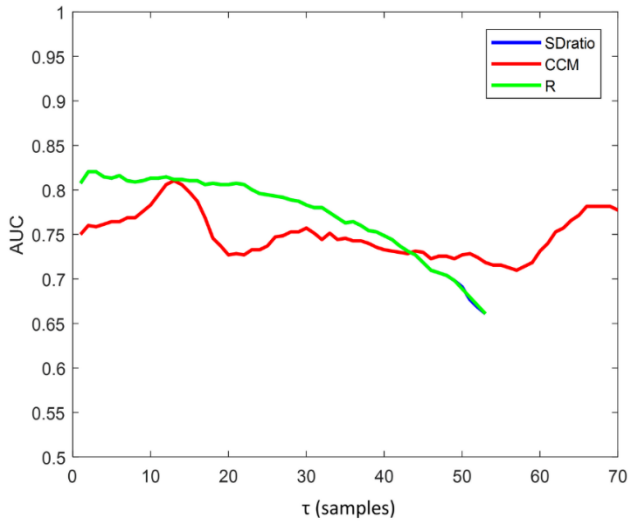

Figure 6-8 AUC of the Receiver Operating Characteristic for SDratio, CCM and R, as a function of the time lag. AUC for R and SDratio are overlapped.

Finally, **Figure 6-9** depicts the accuracy of SDratio, CCM and R. It can be observed that CCM provides the highest accuracy for τ values around 10 samples, while SDratio and R reach their maximum accuracy for τ<5samples.

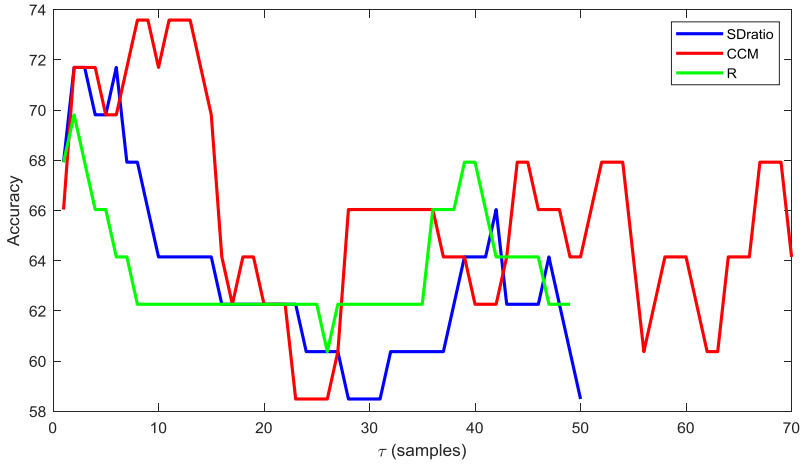

Figure 6-9 Accuracy of SDratio, CCM and R, as a function of the time lag τ.

6.3.2 With nonlinear filter

The results for the Poincaré descriptors in REG signals preprocessed with the nonlinear filter are shown in **Figure 6-10**. The evolution of each parameter as a function of τ is equivalent to the one identified with linearly filtered signals, providing similar range of values for all features. This suggests that Poincaré plot descriptors are not affected by the filter choice. However, intervals of τ with statistically significant differences between apnea and baseline recordings are slightly shorter in this case, as shown in **Figure 6-11**.

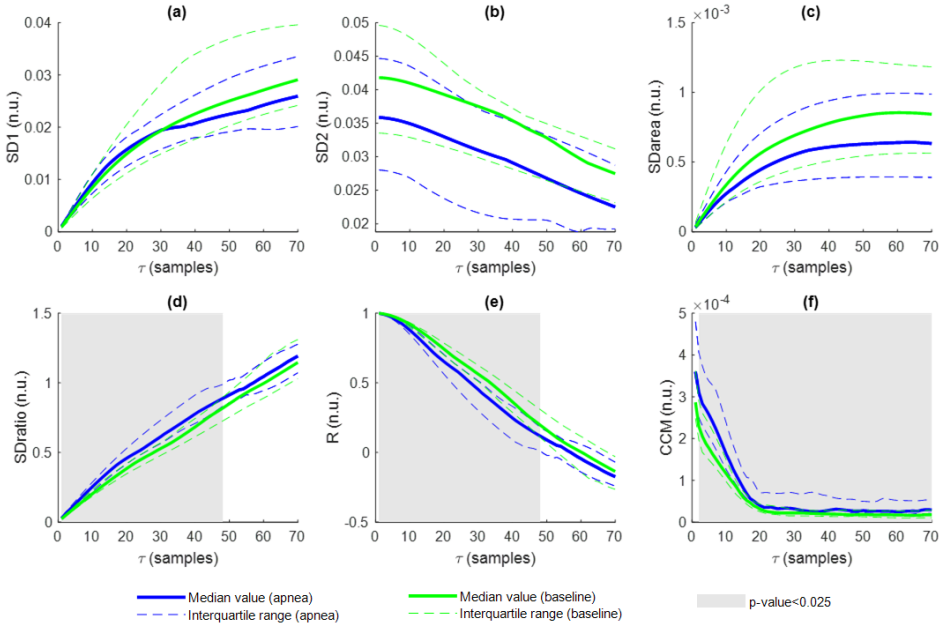

Figure 6-10 Comparison of the results obtained for apnea and baseline periods after nonlinear filtering (median values, interquartile range and statistical significance) of all tested features in function of the time lag τ. (a) SD1; (b) SD2; (c) SDarea; (d) SDratio; (e) R; (f) CCM. Grey solid color corresponds to statistical significance level of p-value<0.025.

The p-values obtained as a result of the hypothesis testing comparing the apnea and baseline groups are graphed in **Figure 6-11**. While the p-values obtained for SDratio and R provide trends, as a function of τ, like those

observed for linearly filtered signals, CCM shows a different pattern, providing lower values and loosing statistical significance for τ=1.

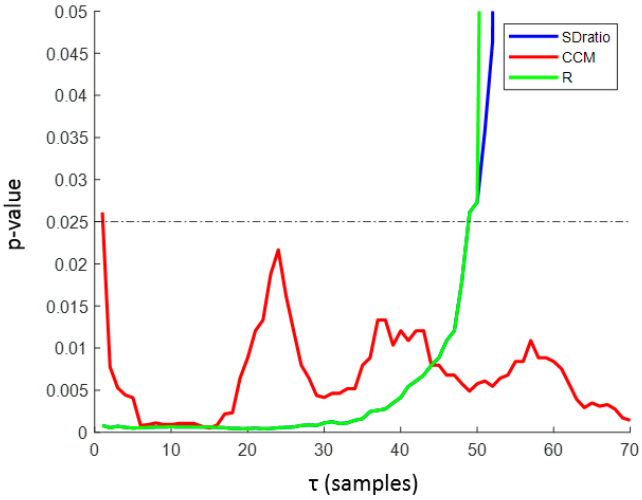

Figure 6-11 Statistical significance levels (p-value) for SDratio, CCM and R, as a function of the time lag τ when comparing apnea and baseline segments extracted from REG signals nonlinearly filtered. R and SDratio curves are overlapped for almost all values. The dotted horizontal black line shows significance when applying Bonferroni correction.

Besides the analysis of the p-values obtained for the comparison of both groups, specificity and sensitivity were also computed (**Figure 6-12**). Specificity provides higher values than sensitivity for all features, with CCM showing the highest specificity for τ values around 10 samples. Regarding the sensitivity, it is maximized for low τ values in all cases, with a clear drop as a function of τ for SDratio, while R preserved higher sensitivity levels. Overall, the trends for all three descriptors show a similar behavior when compared to the results obtained for the REG signals after linear filtering.

The AUC of the Receiver Operating Characteristic for SDratio, CCM and R is depicted in **Figure 6-13**. SDratio and R are fully overlapped and provide higher values than CCM for almost all the range of τ under analysis. Comparing to the curves obtained when using the linear filter, AUC values

are slightly lower in the nonlinear option but preserve the same trends previously identified.

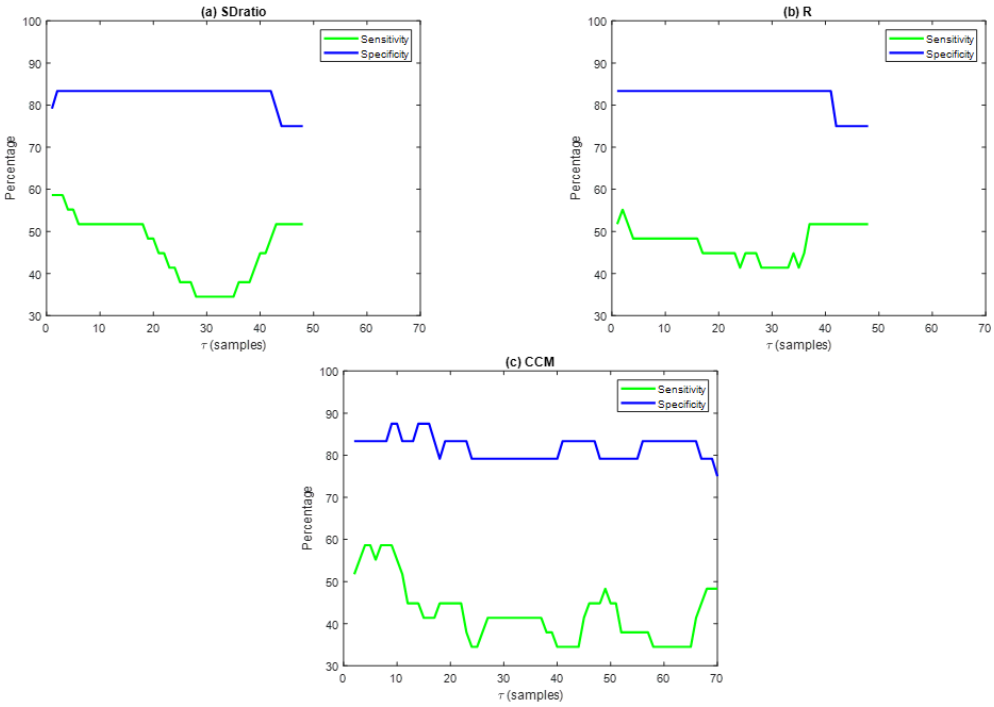

Figure 6-12 Sensitivity and specificity of apnea and baseline classification as a function of the time lag values (τ) for signals processed with the nonlinear filter. (a) SDratio, (b) R and (c) CCM.

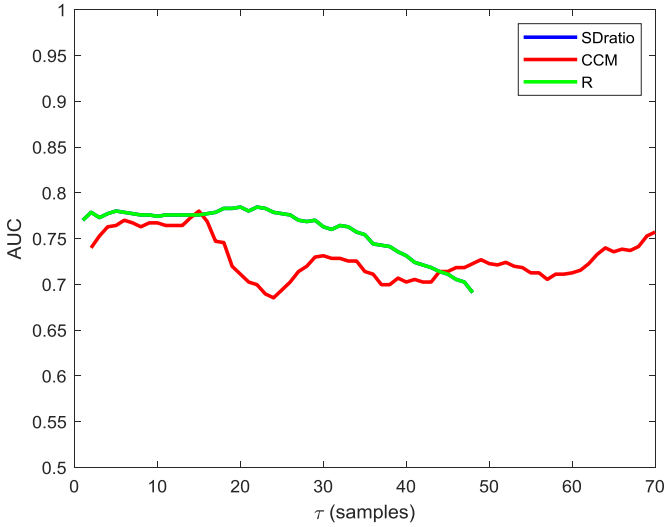

Figure 6-13 AUC of the Receiver Operating Characteristic for SDratio, CCM and R, when computed from nonlinearly filtered data, as a function of the time lag τ. AUC for R and SDratio are overlapped.

Finally, **Figure 6-14** shows the accuracy of the three parameters providing statistically significant results as a function of τ. Once again, differences between the two sets of data (linearly and nonlinearly filtered) are negligible, with CCM providing again the highest accuracy, followed by SDratio and R.

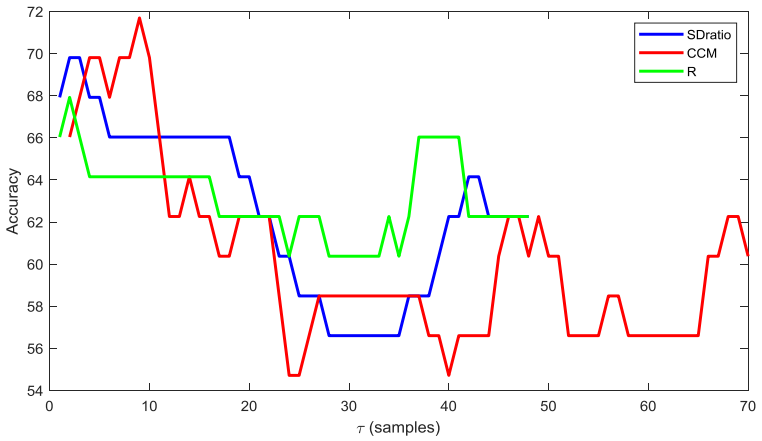

Figure 6-14 Accuracy of SDratio, CCM and R, after preprocessing with the nonlinear filter.

6.3.3 Selection of τ ranges optimizing apnea detection

The analysis of the linear and nonlinear filtered datasets showed equivalent results regarding which Poincaré plot descriptors presented the ability to detect apneas: SDratio, R and CCM. The values obtained for statistical significance, AUC and accuracy (acc) were dependent on the time lag τ used for the reconstruction of the attractor. In order to select the best interval of τ values for apnea detection, the performance of each of the three metrics providing statistically significant results was analyzed by means of the graphical representation of p-values, AUC and accuracy. **Figure 6-15** summarizes the results for SDratio. It can be observed that AUC has a plateau for τ<20 for both filtering options and an almost monotonical decrease for higher values of τ. The minimal p-values from the hypothesis testing are reached for very low τ values (2 and 3 samples) for the linear filter option while the absolute minimum goes up to τ=20 for the nonlinear filtered data. Finally, accuracy was optimal for very low τ values (τ<10) in both cases.

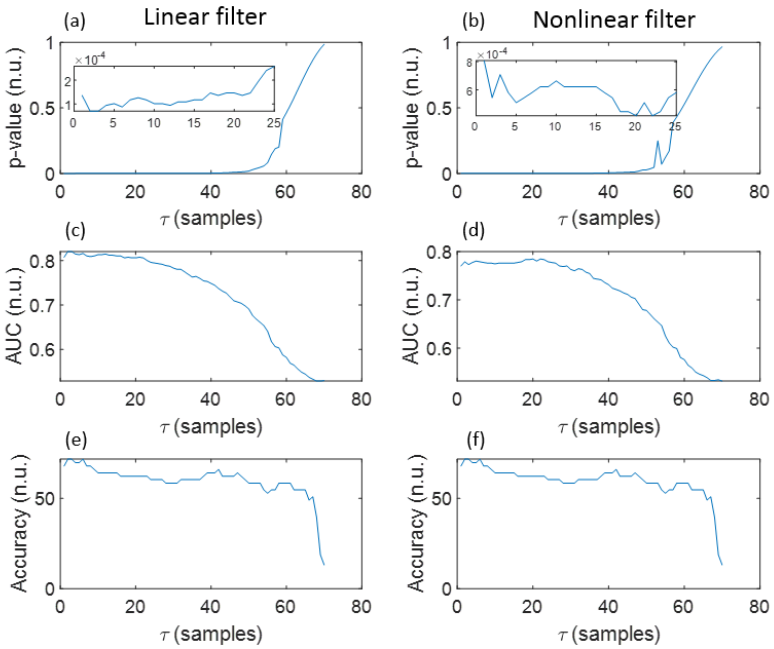

Figure 6-15 Summary of SDratio performance assessed by means of p-value (a,b), AUC (c,d) and accuracy (e,f) as a function of τ, when data were filtered with the linear filter (a,c,e) and the nonlinear filter (b,d,f).

Results for R (**Figure 6-16**) are analogous to those obtained for SDratio due to their high correlation. The minimum p-values were obtained for τ=2

samples in the linear filter dataset, while the absolute minimum for the nonlinear filtered data is obtained for τ=20 samples. AUC provides a similar trend, with a plateau providing the highest values from τ=1 to τ=20 samples, and accuracy showing its maximum values for very low τ values (below 5 samples) and for τ values around 40 samples.

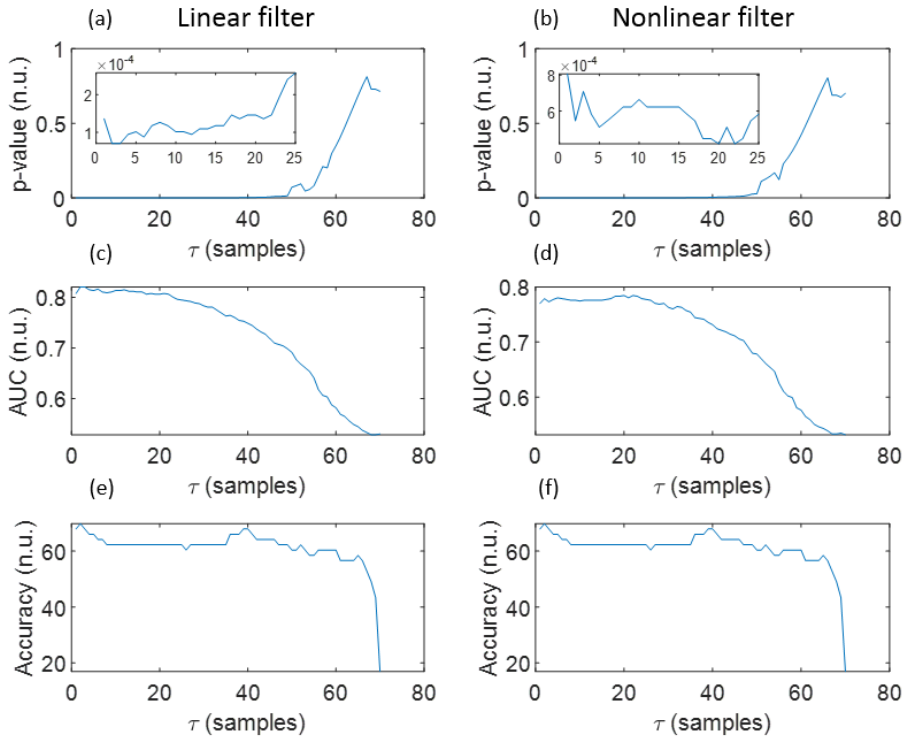

Figure 6-16 Summary of R performance assessed by means of p-value (a,b), AUC (c,d) and accuracy (e,f) as a function of τ, when data were filtered with the linear filter (a,c,e) and the nonlinear filter (b,d,f).

The CCM descriptor also showed that τ values below 20 samples would optimize p-values, AUC and accuracy (**Figure 6-17**). The minimum p-values are obtained for τ=13 samples and τ=15 samples under the linear and nonlinear filter assumptions, respectively. Moreover, a maximum AUC is reached in both cases for τ=15 samples, while maximum accuracy also occurs in this same range of τ values. However, it should be noted that when the

nonlinear filter is used, the CCM values obtained for apnea and baseline signals do not provide statistically significant differences for τ=1.

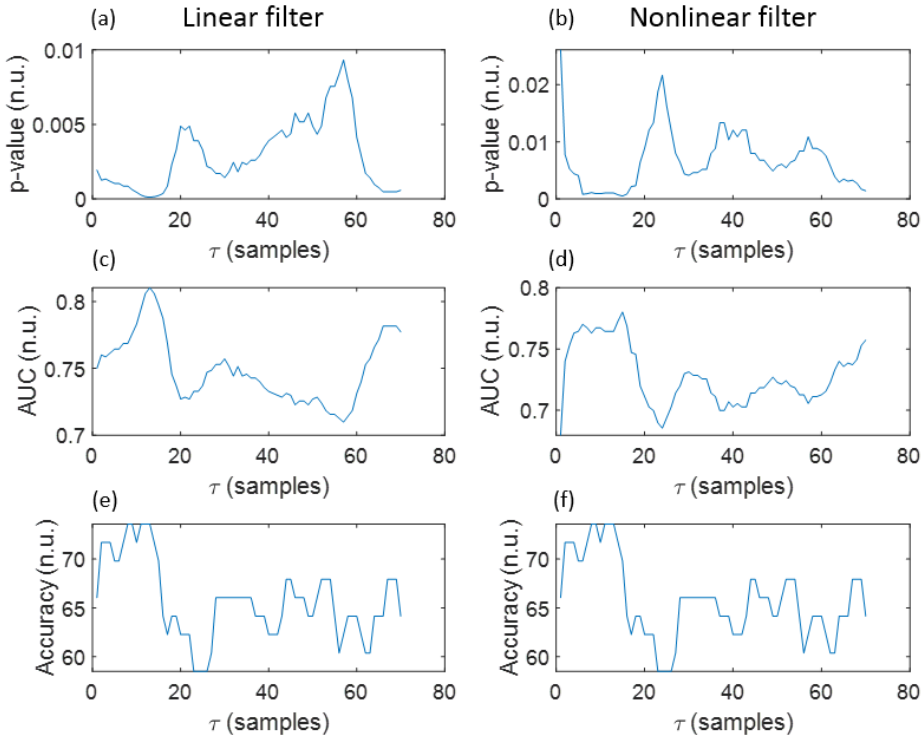

Figure 6-17 Summary of CCM performance assessed by means of p-value (a,b), AUC (c,d) and accuracy (e,f) as a function of τ, when data were filtered with the linear filter (a,c,e) and the nonlinear filter (b,d,f).

Considering the τ ranges optimizing apnea detection for all features and both filtering techniques, the interval of τ values from 1 to 20 samples would include successful results across all options. Therefore, this was the τ interval chosen for analysis of REG signals recorded during general anesthesia procedures. Final results for p-values, AUC and accuracy for this interval are provided in **Table 6-3**.

Table 6-2 Performance of SDratio, CCM and R in apnea detection for τ values between 1 and 20 samples.

	P-VALUE	AUC (MEAN ± STD)	ACC (%) (MEAN ± STD)
Linear filter			
SDratio	<0.0005	0.812 ± 0.004	66.0 ± 3.5
CCM	<0.005	0.772 ± 0.023	69.5 ± 4.1
R	<0.0005	0.812 ± 0.004	63.8 ± 2.4
Nonlinear filter			
SDratio	<0.001	0.777 ± 0.003	66.5 ± 1.5
CCM*	<0.01	0.758 ± 0.018	65.6 ± 3.8
R	<0.001	0.777 ± 0.003	64.2 ± 1.4

*The interval of τ goes from 2 to 20 samples.

6.4 Results for general anesthesia

The General Anesthesia Dataset 1 was processed using the set of Poincaré features listed in the methods section, for an interval of τ values between 1 and 20 samples. This interval is deducted from the results obtained for the Apnea-Baseline dataset.

6.4.1 With linear filter

The evolution of each Poincaré plot descriptor as a function of the time lag τ for each anesthesia phase is depicted in **Figure 6-18**. SD1 increases as τ increases in all states, reaching higher values for awake and LOC, which are also characterized by a wider interquartile range. In contrast, SD2 remains stable for all τ values, providing a highest score in the LOC state and presenting also higher dispersion for awake and LOC. Subsequently, their ratio increases as τ increases, with similar interquartile ranges among the various anesthesia stages, while the ellipse area (SDarea) shows again higher values for awake and LOC, with a significantly bigger dispersion in those two

states and decreasing values as τ increases across all states. The behavior of the correlation R is the opposite of SDratio, due to their high negative correlation: it decreases for increasing τ values in all anesthesia phases with the LOC state showing the lowest values and similar interquartile ranges across states. Finally, CCM is the only feature showing a local maximum, identified in low τ values (τ≤5) and provides its highest values in the anesthesia state followed by ROC.

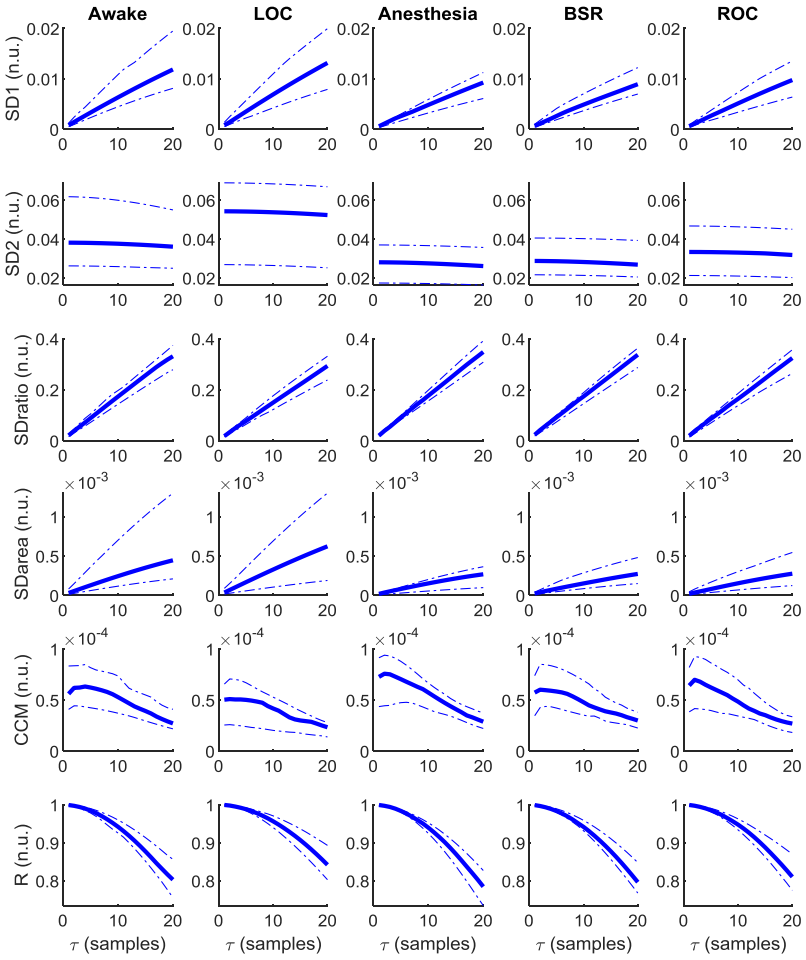

Figure 6-18 Evolution of SD1, SD2, SDratio, SDarea, CCM and R as a function of τ for the set of anesthesia states under analysis: awake, LOC, anesthesia, BSR and LOC. Median values are graphed, together with the 25th and 75th quartiles represented with dashed lines.

All the extracted features present differences between the targeted set of anesthetic states. The statistical significance of those differences is assessed in **Figure 6-19**. SD1 and SD2 showed the ability to differentiate between LOC and anesthesia for all τ values, while they failed in reflecting differences among all other transitions between consecutive states. Regarding SDratio, significant differences were detected in both the transitions between awake and LOC and LOC and anesthesia. Nonetheless, the τ range in which p-values were under the significance threshold was reduced to the intervals 8 to 20 samples and 12 to 20 samples, respectively. The correlation R provided a similar performance but with narrower τ ranges for significance: 10 to 20 samples for the transition between awake and LOC and 17 to 20 samples for LOC and anesthesia. The ability of SDarea to distinguish between consecutive states was limited to the transition between LOC and anesthesia, preserving the statistical significance for all τ values tested. CCM is the only feature that does not distinguish between LOC and anesthesia, but it provides positive results in the transition between anesthesia and BSR for τ from 18 to 20. Moreover, it also reflects differences between awake and LOC states for $\tau > 10$.

Considering the selection of the optimal τ values to assess differences between consecutive anesthesia states using the set of features extracted from the Poincaré plot, low τ values have proved to fail in reflecting changes while the highest range of the tested interval showed a better performance considering all features and anesthesia states. Therefore, the value $\tau=20$ samples was chosen to be the optimal to detect changes in anesthesia states. Average values for each feature and state for $\tau = 20$ samples are summarized in **Table 6-3**.

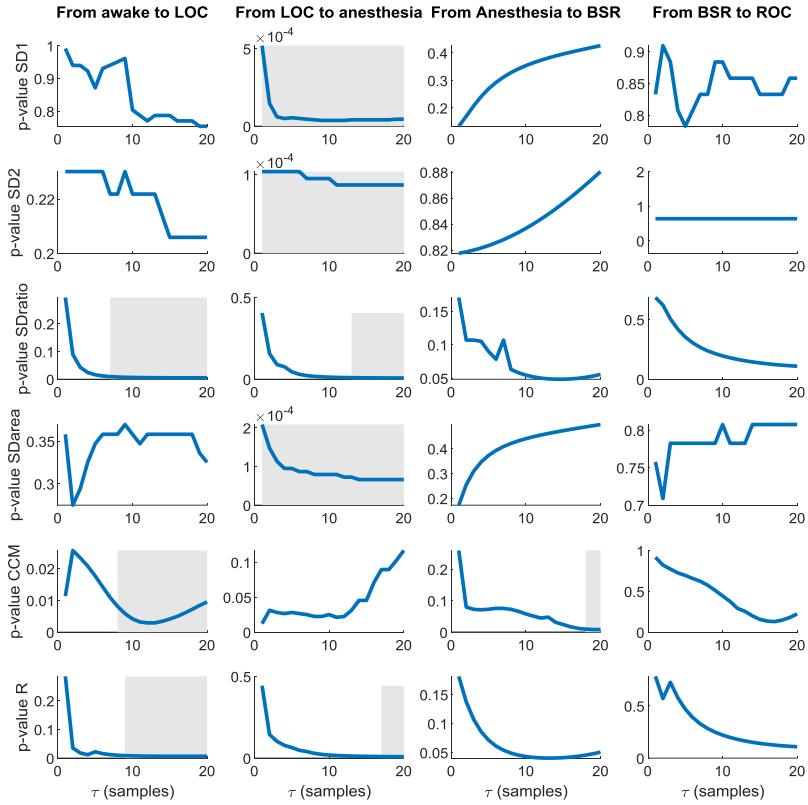

Figure 6-19 Statistical significance (p-values) obtained for the comparison of the median values of each Poincaré feature among consecutive anesthesia states. Grey areas represent intervals in which the graphed parameter shows statistical significance of p-value<0.01.

.

Table 6-3 Average values (mean ± standard deviation) of each Poincaré plot feature in the selected anesthesia states considering $\tau = 20$ samples.

	AWAKE	LOC	ANES.	BSR	ROC
SD1	0.015 ± 0.009	0.015 ± 0.009	0.009 ± 0.003	0.010 ± 0.004	0.011 ± 0.006
SD2	0.045 ± 0.027	0.058 ± 0.043	0.027 ± 0.011	0.031 ± 0.014	0.036 ± 0.022
SDratio	0.339 ± 0.074	0.295 ± 0.074	0.345 ± 0.054	0.329 ± 0.053	0.316 ± 0.060
SDarea	0.00089 ± 0.00109	0.00122 ± 0.00162	0.00027 ± 0.00018	0.00037 ± 0.00031	0.00051 ± 0.00059
CCM	0.000034 ± 0.000020	0.000028 ± 0.000032	0.000031 ± 0.000013	0.000030 ± 0.000011	0.000030 ± 0.000017
R	0.789 ± 0.084	0.834 ± 0.073	0.785 ± 0.059	0.802 ± 0.056	0.814 ± 0.063

The graphical representation of the values reported in **Table 6-3** is provided in **Figure 6-20**. As previously mentioned, all the features except SDratio and SDarea showed a high dispersion for Awake and LOC states that was reduced from anesthesia to ROC. SD1 presented similar values, in average, in awake and LOC, decreasing during anesthesia and slightly increasing for BSR and ROC, but without recovering the initial values at LOC. SD2 had a similar performance, except for the transition between awake and LOC, where SD1 showed similar values while SD2 increased. Since SDarea is proportional to the product of SD1 and SD2, it followed the same behavior described for those two features. Regarding SDratio and R, they presented opposite trends as expected, with similar variances for all patient states: SDratio showed an absolute minimum for LOC, while R had its maximum in this same state. Finally, CCM presented a maximum for the awake state and a minimum for LOC, presenting similar values for all states except for LOC.

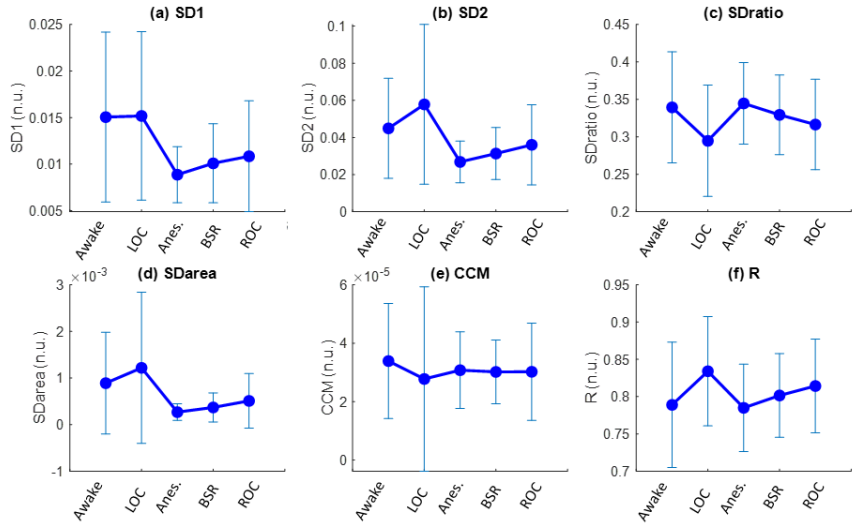

Figure 6-20 Trends for (a) SD1, (b) SD2, (c) SDratio, (d) SDarea, (e) CCM and (f) R across the different anesthesia states for τ=20 samples, represented as mean ± standard deviation.

The trends of all the extracted features present changes along the anesthetic procedure for τ=20 samples, mainly during LOC. However, only some of those changes are statistically significant. The p-values obtained after hypothesis testing are compiled in **Table 6-4**. All the features except CCM were able to detect changes in the transition between LOC and anesthesia, providing p-values as low as $5*10^{-5}$ for SD1. Regarding the differences between the awake and LOC states, SDratio, CCM and R provided statistically significant results while none of the features lead to positive results for the transitions among other anesthesia states.

Table 6-4 Statistical significance (p-value) of the differences between consecutive anesthesia states for the Poincaré plot extracted features, considering τ=20 samples.

FROM TO	AWAKE LOC	LOC ANES.	ANES. BSR	BSR ROC
SD1	0.75387	**0.00005**	0.42648	0.85828
SD2	0.20589	**0.00009**	0.88039	0.63782
SDratio	**0.00530**	**0.00756**	0.05565	0.10933
SDarea	0.32519	**0.00007**	0.49686	0.80762
CCM	**0.00950**	0.11696	0.00834	0.22312
R	**0.00651**	**0.00873**	0.05071	0.10879

6.4.2 With nonlinear filter

This section describes the results obtained for the General Anesthesia Dataset1 when using the nonlinear filter as the preprocessing strategy. The evolution of the median values of each Poincaré parameter as a function of τ for all anesthesia states is represented in **Figure 6-21**. SD1, SD2, SDratio, SDarea and R present the same trends observed for the linearly filtered dataset. However, CCM shows a different behavior: instead of presenting a local maximum among the smallest τ values as previously reported (**Figure 6-18**), it decreased monotonically presenting an inflection point in the same position and an asymptotic trend towards τ=20 samples. Moreover, CCM provided higher values for all τ and anesthesia states, suggesting a higher correlation among consecutive set of points in the attractor.

The ability to differentiate between consecutive anesthesia states of the features extracted from the Poincaré plot analysis is presented in **Figure 6-22**. When the nonlinear filter is applied, the only state that can be identified with Poincaré plot indicators is the transition between LOC and anesthesia, for which almost all τ provide statistically significant results.

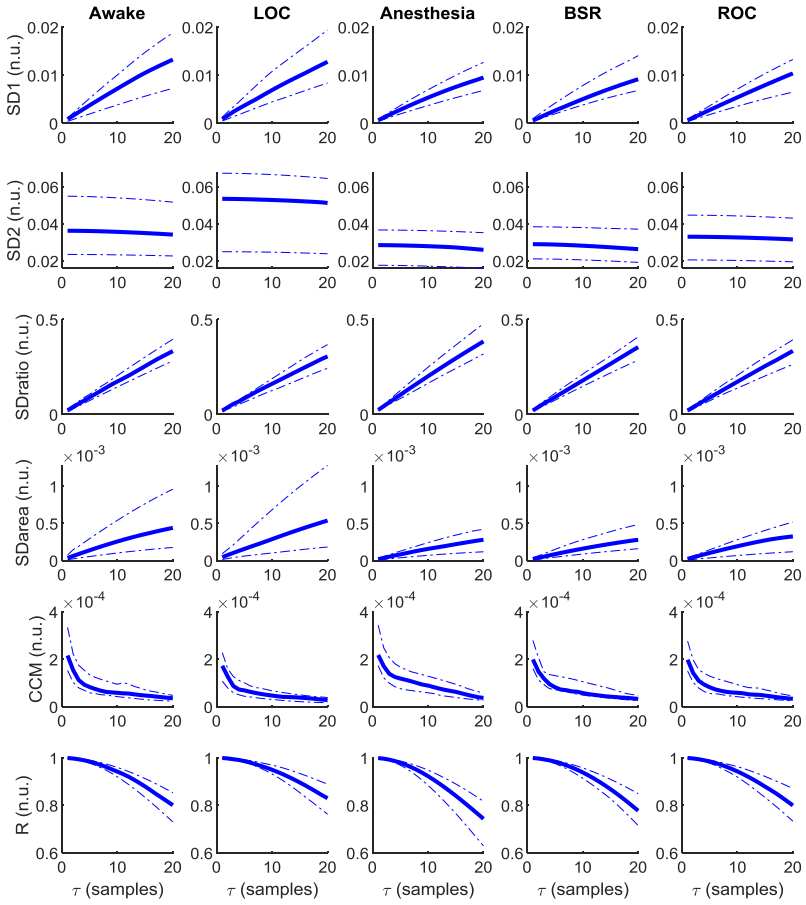

Figure 6-21 Evolution of SD1, SD2, SDratio, SDarea, CCM and R as a function of τ for the nonlinearly filtered REG signals collected in the anesthesia states under analysis: awake, LOC, anesthesia, BSR and LOC. Median values are graphed, together with the 25th and 75th quartiles represented with dashed lines.

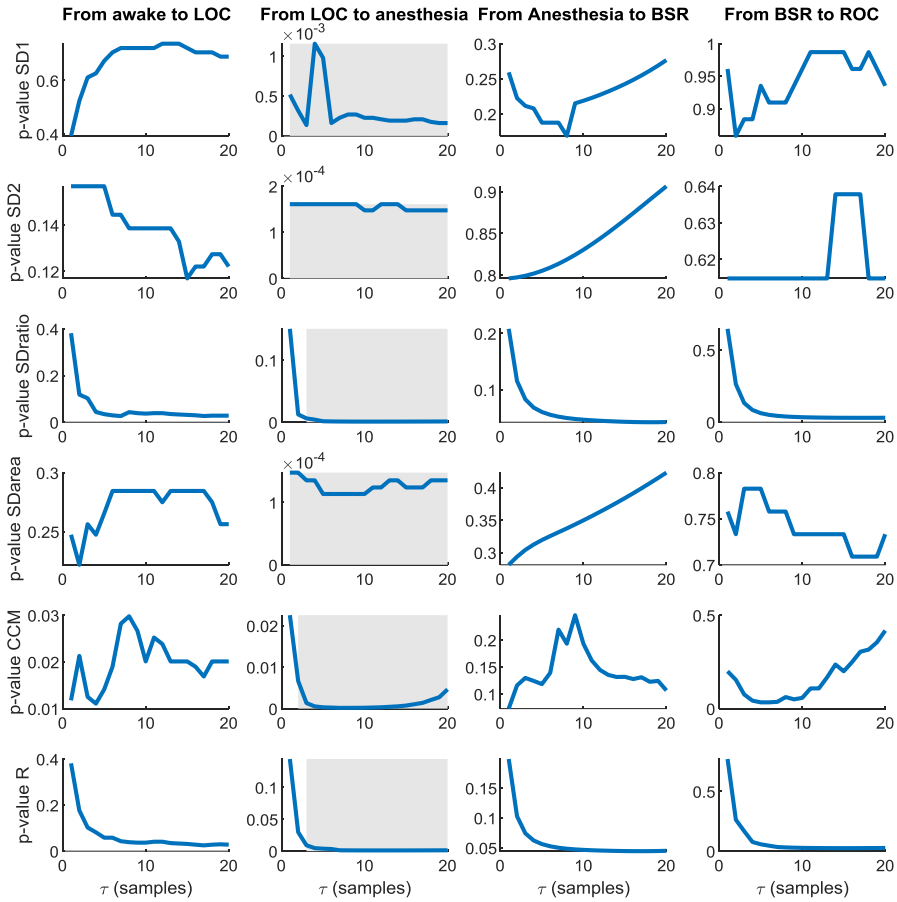

Figure 6-22 Statistical significance (p-values) obtained for the comparison of the median values of each Poincaré feature among consecutive anesthesia states, computed on the nonlinearly filtered dataset. Grey areas represent intervals in which the graphed parameter shows statistical significance of p-value<0.01.

Even though there is a wide range of τ values providing successful results for the transition between LOC and anesthesia, the final value of τ = 20 samples was used to be consistent with the results on the linearly filtered dataset. The values obtained with this time lag are summarized in **Table 6-5**.

A graphical representation of the values presented in **Table 6-5** is provided in **Figure 6-23**. The trends of all the Poincaré plot descriptors are consistent with the ones obtained when signals were preprocessed with a linear filter. The only noticeable difference is the standard deviation of CCM values at LOC, that is significantly smaller with the nonlinear filter approach.

Table 6-5 Average values (mean ± standard deviation) of each Poincaré plot feature in the selected anesthesia states considering τ = 20 samples.

	AWAKE	LOC	ANES	BSR	ROC
SD1	0.015 ± 0.010	0.015 ± 0.009	0.010 ± 0.003	0.010 ± 0.004	0.011 ± 0.005
SD2	0.042 ± 0.025	0.056 ± 0.043	0.026 ± 0.011	0.030 ± 0.014	0.034 ± 0.020
SDratio	0.360 ± 0.115	0.309 ± 0.091	0.395 ± 0.091	0.358 ± 0.084	0.335 ± 0.087
SDarea	0.00080 ± 0.00097	0.00117 ± 0.00159	0.00029 ± 0.00018	0.00036 ± 0.00030	0.00046 ± 0.00049
CCM	0.00004 ± 0.00003	0.00003 ± 0.00001	0.00004 ± 0.00002	0.00004 ± 0.00001	0.00004 ± 0.00002
R	0.763 ± 0.135	0.817 ± 0.094	0.724 ± 0.107	0.768 ± 0.095	0.792 ± 0.095

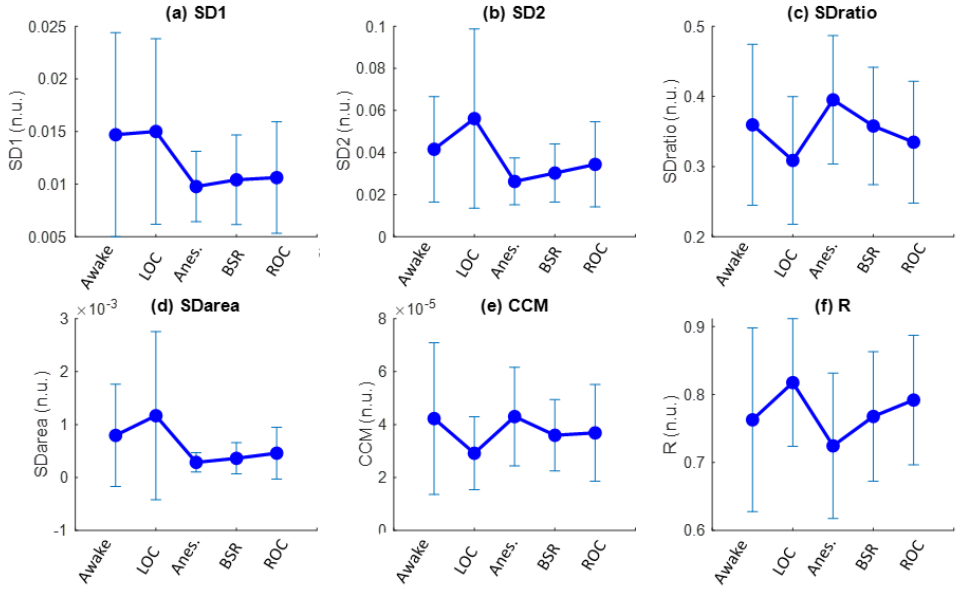

Figure 6-23 Trends for (a) SD1, (b) SD2, (c) SDratio, (d) SDarea, (e) CCM and (f) R across the different anesthesia states for τ=20 samples, represented as mean ± standard deviation.

Regarding the statistical significance of the differences between consecutive anesthesia states, when using the nonlinear filter p-values lower than the established threshold for significance were only achieved for the transition from LOC to anesthesia. The lowest p-value was provided by SDarea, closely followed by SD2 and SD1 (**Table 6-6**).

Table 6-6 Statistical significance (p-value) of the differences between consecutive anesthesia states for the Poincaré plot extracted features, considering τ=20 samples.

From / **To**	**Awake** / **LOC**	**LOC** / **Anes**	**Anes** / **BSR**	**BSR** / **ROC**
SD1	0.68913	**0.00016**	0.27666	0.93531
SD2	0.12209	**0.00015**	0.90650	0.61481
SDratio	0.02818	**0.00127**	0.04259	0.03095
SDarea	0.25628	**0.00014**	0.42332	0.73319
CCM	0.02010	**0.00465**	0.10659	0.41761
R	0.02818	**0.00138**	0.04500	0.02687

6.4.3 Confounding factors

The interpretation of the results provided in the previous section shall be done together will the analysis of confounding factors that might play a role in CBF changes. The correlations between the Poincaré plot descriptors and the main characteristics of the patients are presented in **Table 6-7**. Patient weight and BMI present moderate correlations with the features extracted from Poincaré plot analysis, either using the linear or nonlinear filter for preprocessing. SDratio and R present the highest correlations, while SD1 the lowest. During LOC those correlations are low or very low, and after the transition to the anesthesia period they raise again, providing even higher values than for the awake state, with SD2 and CCM showing the highest values with statistical significance. Moreover, in the anesthesia period, patient age also correlates with SDratio, R and CCM, with higher ages associated to higher values of R and lower values for SDratio and CCM. Regarding BSR and awake, correlations are in general lower, with only a statistically significant moderate correlation detected in BSR between BMI and SD2.

Table 6-7 Spearman correlation of each Poincaré feature with patient demographics for every clinical state, either using the linear filter or the nonlinear filter. Cells are colored as indicated in **Figure 6-24** and statistical significance is indicated in bold.

	Linear filter				Nonlinear filter			
Awake	**Age**	**Height**	**Weight**	**BMI**	**Age**	**Height**	**Weight**	**BMI**
SD1	0.246	-0.064	0.269	0.309	0.241	-0.060	0.249	0.287
SD2	**0.346**	-0.028	**0.477**	**0.500**	0.337	-0.018	**0.482**	**0.502**
SDratio	-0.165	-0.223	**-0.589**	**-0.505**	-0.113	-0.215	**-0.597**	**-0.511**
SDarea	0.316	-0.034	**0.393**	**0.421**	0.282	-0.026	**0.347**	**0.372**
CCM	-0.104	-0.170	**-0.552**	**-0.487**	-0.101	-0.147	**-0.563**	**-0.486**
R	0.165	0.223	**0.589**	**0.505**	0.113	0.215	**0.597**	**0.511**
LOC								
SD1	0.040	-0.006	0.110	0.092	-0.004	-0.003	0.053	0.027
SD2	-0.098	0.021	0.107	0.075	-0.083	-0.004	0.085	0.057
SDratio	0.215	-0.082	-0.124	-0.067	0.142	-0.064	-0.208	-0.167
SDarea	-0.001	0.018	0.127	0.099	-0.027	0.013	0.079	0.050
CCM	0.074	-0.058	-0.150	-0.099	-0.039	-0.057	-0.165	-0.120
R	-0.215	0.082	0.124	0.067	-0.142	0.064	0.208	0.167

Table 6-7 (Continuation)

Anes								
SD1	0.106	-0.083	**0.373**	**0.436**	0.019	-0.166	0.232	0.320
SD2	**0.371**	-0.113	**0.538**	**0.625**	**0.363**	-0.125	**0.523**	**0.612**
SDratio	**-0.571**	0.035	**-0.550**	**-0.600**	**-0.590**	-0.024	**-0.577**	**-0.598**
SDarea	0.266	-0.104	**0.458**	**0.533**	0.192	-0.153	**0.372**	**0.462**
CCM	**-0.540**	0.117	**-0.512**	**-0.589**	**-0.615**	-0.023	**-0.601**	**-0.627**
R	**0.571**	-0.035	**0.550**	**0.600**	**0.590**	0.024	**0.577**	**0.598**
BSR								
SD1	0.214	-0.210	0.237	0.336	0.178	-0.222	0.153	0.278
SD2	0.236	-0.202	0.357	**0.448**	0.244	-0.260	0.302	**0.441**
SDratio	-0.149	0.127	-0.267	-0.387	-0.125	0.119	-0.270	-0.338
SDarea	0.209	-0.182	0.315	0.414	0.176	-0.201	0.245	0.365
CCM	-0.172	0.173	-0.134	-0.276	-0.141	0.172	-0.109	-0.202
R	0.149	-0.127	0.267	0.387	0.125	-0.119	0.270	0.338
ROC								
SD1	-0.031	-0.037	0.210	0.242	-0.113	-0.019	0.154	0.183
SD2	0.047	-0.031	0.228	0.264	0.014	-0.035	0.209	0.240
SDratio	-0.192	-0.036	-0.167	-0.171	-0.206	0.005	-0.192	-0.205
SDarea	0.012	-0.031	0.234	0.264	-0.017	-0.035	0.205	0.238
CCM	-0.139	-0.022	-0.211	-0.216	-0.163	0.190	-0.010	-0.078
R	0.192	0.036	0.167	0.171	0.206	-0.005	0.192	0.205

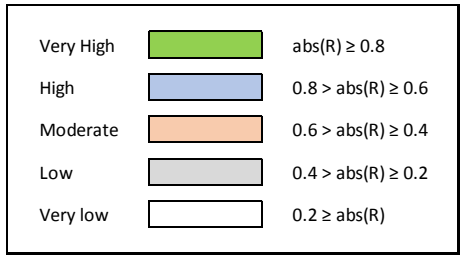

Figure 6-24 Spearman correlation values matching with colors and qualitative level.

Patient demographics have proved to be correlated with the Poincaré plot descriptors in Awake, anesthesia (Anes) and, to a lower extent, BSR. Furthermore, the analysis of the transitions between consecutive states and patient characteristics also provided significant correlations to be considered (**Table 6-8**). For instance, weight and BMI are correlated with SDratio, CCM and R in the transition between awake and LOC periods, while in the transition from LOC to anesthesia age plays a more significant role showing significant moderate correlations with SD2, SDratio, CCM and R. In all other transitions, correlations were either low or very low.

Besides patient demographics, other clinical variables are susceptible to provoke changes in Poincaré plot descriptors, such as HR, propofol effect site concentrations (CePropo), remifentanil effect site concentrations (CeRemi), MAP and the depth of anesthesia index, qCON. Those variables were also analyzed looking for synergies between their evolution and the information extracted from the signal attractor through Poincaré plot analysis (**Table 6-9**). Both MAP and CePropo provide moderate correlations with the variables under study in the transition between awake and LOC, but only the pair SD2 and CePropo provides statistically significant results when using the nonlinear filter. However, between the states of LOC and anesthesia (Anes), CePropo presents significant correlations with SD1, SD2 and SDarea for linear filter processing, and with SD1, SD2, SDarea and CCM under the nonlinear filter assumption. The higher the propofol dosage, the higher the SD1 and SD2 values, suggesting enhanced complexity under higher anesthetic dosage changes. Additionally, HR presents significative moderate correlations with SDratio, CCM and R when using the linear filter and with CCM when preprocessing is performed with the nonlinear algorithm.

Table 6-8 Spearman correlation between patient demographics and differences in Poincaré plot descriptors for every transition between consecutive clinical states analyzed, either using the linear filter (left side) or the nonlinear filter (right side). Cells are colored as a function of the correlation value (see **Figure 6-24**) and statistical significance of the correlations is indicated in bold type.

	Linear filter				**Nonlinear filter**			
Awake – LOC	**Age**	**Height**	**Weight**	**BMI**	**Age**	**Height**	**Weight**	**BMI**
SD1	-0.147	0.028	-0.091	-0.169	-0.113	0.046	-0.048	-0.126
SD2	-0.289	-0.002	-0.221	-0.285	-0.278	-0.021	-0.245	-0.305
SDratio	0.298	0.271	**0.490**	**0.415**	0.253	0.259	**0.498**	**0.434**
SDarea	-0.240	0.046	-0.091	-0.167	-0.184	0.007	-0.058	-0.124
CCM	0.096	0.335	**0.434**	**0.375**	0.084	0.215	**0.465**	**0.429**
R	-0.309	-0.307	**-0.489**	**-0.402**	-0.255	-0.244	**-0.493**	**-0.437**
LOC – Anes								
SD1	0.288	-0.072	0.204	0.294	0.278	-0.091	0.173	0.281
SD2	**0.421**	-0.024	0.245	0.322	**0.425**	-0.061	0.234	0.326
SDratio	**-0.520**	-0.009	-0.259	-0.303	**-0.523**	-0.121	-0.354	-0.346
SDarea	0.309	-0.097	0.159	0.252	0.300	-0.090	0.166	0.252
CCM	**-0.398**	0.148	-0.182	-0.288	**-0.509**	-0.037	**-0.403**	**-0.436**
R	**0.495**	0.015	0.240	0.280	**0.550**	0.138	**0.389**	0.367
Anes-BSR								
SD1	-0.075	0.231	0.023	-0.129	-0.252	0.222	0.041	-0.100
SD2	0.073	0.152	-0.002	-0.100	0.077	0.135	-0.045	-0.114
SDratio	-0.122	-0.025	-0.059	-0.100	-0.102	0.002	-0.235	-0.261
SDarea	0.066	0.172	-0.018	-0.139	-0.107	0.181	0.077	-0.029
CCM	-0.182	0.224	-0.106	-0.300	0.005	0.386	0.199	0.021
R	0.164	0.007	0.059	0.107	0.114	-0.030	0.240	0.289
BSR-ROC								
SD1	-0.217	0.178	-0.059	-0.083	-0.209	0.165	-0.036	-0.077
SD2	-0.184	0.177	-0.137	-0.191	-0.211	0.204	-0.103	-0.176
SDratio	0.100	-0.354	-0.005	0.189	0.115	-0.297	0.057	0.177
SDarea	-0.196	0.206	-0.115	-0.156	-0.260	0.259	-0.045	-0.138
CCM	0.189	-0.259	-0.055	0.111	0.021	0.074	0.274	0.282
R	-0.109	0.357	0.025	-0.164	-0.136	0.297	-0.069	-0.184

The transition between anesthesia and BSR shows many interactions among the variables being analyzed. While most of them did not show statistical significance, the qCON index shows high and significative correlations with SD1, SD2 and SDarea, despite of the technique used for signal preprocessing, suggesting a correlation between the anesthetic depth and the features extracted from REG signals. Moreover, to further support this relationship, when using the nonlinear filter, the correlations between CePropo and SD1, SD2 and SDarea presented moderate correlations with statistical significance.

Finally, when considering the existing changes between BSR and ROC periods, the clinical variable that provides the most relevant correlations with the Poincaré plot descriptors is the MAP. Under the nonlinear filter assumptions, its correlation with SD1 and SDarea is very high, followed by a high correlation with SD2. For the linear filter analysis, correlations are high but not statistically significant, except for the pair CCM-MAP. Those results are a sign of the important role of MAP in the regulation of CBF, analyzed through the complexity of REG signals.

Table 6-9 Spearman correlation between clinical variables related to depth of anesthesia and hemodynamics and differences in Poincaré plot descriptors for every transition between consecutive clinical states analyzed, either using the linear filter (left side) or the nonlinear filter (right side). Cells are colored as a function of the correlation value (see **Figure 6-24**) and statistical significance of the correlations is indicated in bold type.

	Linear filter					**Nonlinear filter**				
Awake - LOC	**HR**	**Ce Propo**	**Ce Remi**	**MAP**	**qCON**	**HR**	**Ce Propo**	**Ce Remi**	**MAP**	**qCON**
SD1	0.128	0.257	0.199	-0.069	-0.132	0.162	0.247	0.287	-0.077	-0.050
SD2	-0.068	0.447	0.135	0.267	-0.178	-0.060	**0.455**	0.173	0.275	-0.151
SDratio	0.209	-0.266	-0.018	-0.507	0.190	0.114	-0.177	0.061	-0.482	0.151
SDarea	0.102	0.299	0.110	0.011	-0.210	0.135	0.252	0.173	-0.044	-0.152
CCM	0.114	-0.187	-0.040	-0.518	-0.107	0.131	-0.214	0.027	-0.380	-0.024
R	-0.203	0.195	0.018	0.559	-0.187	-0.134	0.166	-0.048	0.482	-0.134
LOC-Anes										
SD1	0.105	**0.548**	0.065	0.012	-0.095	0.040	**0.454**	0.146	-0.110	-0.105
SD2	-0.132	**0.471**	0.018	0.020	-0.129	-0.115	**0.489**	0.053	0.022	-0.138
SDratio	**0.426**	-0.330	0.011	-0.028	0.135	0.340	-0.350	0.116	-0.138	0.121
SDarea	0.031	**0.522**	0.057	0.039	-0.085	0.019	**0.471**	0.055	0.024	-0.069

Table 6-9 (Continuation)										
CCM	**0.509**	-0.202	-0.210	0.092	0.167	**0.417**	**-0.451**	-0.020	0.010	0.198
R	**-0.420**	0.323	-0.010	0.047	-0.144	-0.343	**0.371**	-0.073	0.132	-0.124
Anes-BSR										
SD1	0.097	0.557	0.368	0.511	**0.681**	0.329	**0.604**	0.300	0.566	**0.672**
SD2	-0.039	0.564	0.175	0.384	**0.651**	0.054	**0.532**	0.261	0.402	**0.704**
SDratio	0.509	0.250	0.068	0.178	0.147	0.409	0.075	0.221	0.283	-0.034
SDarea	0.059	0.561	0.239	0.466	**0.626**	0.241	**0.575**	0.318	0.452	**0.608**
CCM	0.132	0.414	-0.036	0.041	0.041	0.138	0.075	-0.032	-0.160	-0.397
R	-0.502	-0.204	-0.096	-0.219	-0.150	-0.433	-0.032	-0.229	-0.283	0.009
BSR-ROC										
SD1	0.331	0.415	-0.383	0.683	0.379	0.338	0.337	-0.368	**0.833**	**0.462**
SD2	0.171	0.434	-0.365	0.667	0.326	0.155	0.413	-0.368	**0.733**	0.309
SDratio	0.362	-0.160	0.154	-0.600	0.158	0.270	-0.235	0.187	-0.583	0.164
SDarea	0.338	0.346	-0.365	0.750	0.352	0.296	0.369	-0.395	**0.817**	0.390
CCM	0.339	-0.145	0.208	**-0.767**	-0.097	0.343	0.073	0.006	0.117	0.154
R	-0.368	0.144	-0.158	0.600	-0.184	-0.258	0.228	-0.197	0.533	-0.178

6.5 Discussion of the results obtained in apnea detection

In this work, it has been shown that several features extracted from Poincaré plots differ from REG signals extracted from baseline and apnea periods (SDarea, R and CCM). When compared to the performance of the classical parameters based on REG pulse wave geometry, Poincaré related features outperformed the former ones since only one of the geometric time domain features, the systolic area AreaSyst, showed the ability to detect apneas (see Chapter 5).

Different time lags (τ) have been tested in Poincaré plot analysis; lower values optimized the detection of apnea periods both when either using a linear filter or a nonlinear filter for data preprocessing. No previous work has been found on the delayed coordinates state-space representation for REG signals therefore results have been compared to the ones provided in

publications based on other biological signals, namely heart rate variability. As published by Lerma et al. [203], increasing the time lag should increase SD1, decrease SD2 and therefore increase SDratio. Our findings support these trends for the three descriptors of the reconstructed attractor, showing a curvilinear increase for SD1, a curvilinear decrease for SD2 and a linear increase for their ratio (SDratio). Although SD1 and SD2 did not show any statistically significant differences among apnea and baseline groups, their ratio (SDratio) was able to distinguish between both for τ lower than 53 samples (0.21s) for linearly filtered data and for τ lower than 48 samples (0.19s) under the nonlinear filter assumption. It is noticeable that the SDarea descriptor, which integrates SD1 and SD2 information, evolves in an exponential fashion as τ increases but shows no significant differences between groups. The correlation parameter R, having a definition very close to SDratio and showing a negative correlation close to -1, has the opposite behavior when τ increases, keeping the statistical significance for almost the same τ range.

The CCM feature was also computed for all the reconstructed attractors, showing a monotonic decrease for τ up to 20 samples and a stable value for higher time lags. It demonstrated the ability to distinguish (with statistical significance) between groups for all tested τ values, except for τ=1 sample when the nonlinear filter was used. Karmakar et al. [217] showed that CCM outperformed SD1 and SD2 when applied to heart rate variability signals used to identify arrythmia and congestive heart failures, due to the fact that CCM quantifies the underlying temporal dynamics of the system which are not considered in the definition of the standard Poincaré features. They concluded that a decrease in CCM indicates increased regularity and decreased variability in the signal. In this work, CCM provides better results than SD1 and SD2 when used as a predictor for apneas, but SDratio offers even lower p-values in the hypothesis testing. Therefore, short term (SD1) and long term (SD2) variability are not affected by apneas in a significant manner, but their ratio and CCM value are, which could be interpreted, following Karmakar's conclusions, as an increased regularity and less variability present in baseline signals.

The significance level of SDratio, R and CCM depends on the time lag used for the attractor reconstruction as shown in **Figure 6-5** and **Figure 6-11**. The τ values for which the differences among apnea and baseline groups were optimized were compared to the criteria traditionally used for the time lag determination (summarized in **Table 6-1**). All those criteria aim at defining a time lag for which the signal samples are still correlated or, in other words,

the correlation width [211]. The results from this work show that low τ values provide the best ability to differentiate between apneas and baselines and that for high values, as illustrated in **Figure 6-3** and discussed in other publications [209], the attractor deformation occurs. This suggests that the τ range used (1 to 70 samples) is too wide and that higher τ, instead of further unfolding the attractor, result in a deformation of its underlying structure.

The time lags for which SDratio and R are optimal are included in the set of τ values recommended in the literature when using 1/20 of the first relative minimum of the correlation as the reference criteria. For CCM, the best performance is achieved for τ values closer to 1/10 of the period. Other methods usually applied in literature for other physiological signals propose a set of τ values that would not be suitable for this application. This suggests that those criteria might need to be reviewed for REG signals since the work herein presented indicates that they contain useful clinical information, but it is not available, or maximized, by the same time lags commonly accepted for other applications.

Besides the possibility of using 1/10 or 1/20 of the first minimum of autocorrelation function as the range of τ values to be investigated, the evolution of the CCM parameter over the different time lags suggests that CCM could be a useful reference to determine the maximum τ value for which the system should be tested. The trends of CCM as a function of τ (**Figure 6-4**f and **Figure 6-10**f) clearly show a first stage in which CCM decreases monotonically until a plateau is reached in both apnea and baseline signals. This inflection point in CCM could be interpreted as the loss of correlation between the signal and its delayed version, presenting CCM as a suitable criterion to identify the range of τ values useful for this application. Furthermore, the inflection point in the CCM trend is consistent with the second derivative sign criteria presented in **Table 6-1** (τ=19), indicating that optimal range within the 1 to 70 samples interval for all studies parameters is delimited by this upper threshold. Instead of targeting a specific τ value for Poincaré plot analysis, this work suggests that an interval of time lags should be used, which confirms Lerma's findings [203], and that this interval could be limited by the inflection point observed in the CCM parameter.

An important limitation of this study is related to the inexistence of previous results, which does not allow the comparison between the presented findings with other research outcomes of REG signals. However, since

information related to REG changes has been obtained by means of feature extraction from the Poincaré plot analysis, the findings indicate that this topic deserves a deeper look with an extended and independent database to validate the results herein presented. Furthermore, since REG signals for apnea and baseline periods have shown to present statistical differences in the features extracted, this suggests that CBF changes provoked by apneas are traceable by means of REG recordings.

6.6 Discussion of the results obtained in anesthesia

The Poincaré plot descriptors of the General Anesthesia Dataset1 were computed for a range of τ values from 1 to 20 samples, after the preprocessing stage with either the linear filter or the nonlinear filter. Very few differences were detected when comparing the evolution of the Poincaré extracted features for the linearly filtered and nonlinearly filtered datasets. The most relevant one affected CCM only, which presented a local maximum for low τ in the data preprocessed with the linear filtered that was not detected in the results from the nonlinear filter.

When the linear filter was used for preprocessing, statistical differences were found between Awake-LOC and LOC-Anes transitions, with a wide range of parameters showing statistically significant differences (SDratio, CCM and R in the Awake-LOC transition and all features but CCM in the LOC-Anes transition). Within the 1 to 20 samples interval of τ tested, the upper values concentrated the highest amount of statistically singificant differences among anesthetic states. It is therefore concluded that a value of $\tau = 20$ samples is the most appropriate one for the analysis of REG signals during anesthesia.

The nonlinearly filtered dataset provided a weaker performance in terms of identifying different anesthetic states, since only the transition from LOC to Anes was supported with statistically meaningful results. However, it should be noted that all Poincaré descriptors and all $\tau > 4$ values were able to identify this transition. The enhanced performance associated to the linearly filtered data might be due to the reduced variability of REG signals preprocessed with the nonlinear filter, as a result of the reduction of the dimension of attractor neighborhoods as presented in Chapter 4.

Several confounding factors were considered to study the dependence of Poincaré plot descriptors with patient characteristics. Age, weight and BMI showed moderate to high correlations with Poincaré based features in the Awake, Anes and BSR states, as well as in the transitions from Awake to LOC and from LOC to Anes. Older patients show higher SD2 while this trend is not followed in SD1, resulting in lower SDratio scores. Age seems therefore to increase long term variability but not short term variabilty of Poincaré plots reconstructed from REG time series under general anesthesia. A higher weight (and BMI) was also related to an increase in SD2 and a decrease in SDratio, suggesting that differences in weight are related to a higher long term variability but less related to the short term variability. Those results are consistent with previously published data, suggesting that age and BMI are important factors when analyzing CBF measurements [218]–[220].

Correlations between global hemodynamic variables (HR and MAP) and Poincaré plot descriptors were also identified. HR showed moderate correlations in the transition between LOC and Anes, with SDratio, CCM and R providing statistically significative results for the linear filter option but limited to CCM for the nonlinear filter. MAP provided high and very high correlations in the transition between BSR and ROC. Nonetheless, most of them, mainly when using the linear filter, lacked statistical significance. This might be due to a lower sample size in the BSR group when compared to other anesthesia states. Moreover, in this particular case, CCM seems to be highly affected by the pre-procesing filter choice. The nonlinear filtered data show higher correlations with MAP, the significant ones being with SD1, SD2 and SDarea, suggesting increasing complexity while MAP increases. MAP does not show singifcant correlations in any other transition. This could be interpreted as an interaction between MAP and REG features limited to very deep anesthesia scenarios, which could be associated with clinical conditions close to the lower limit of CBF autoregulation.

Regarding the influence of drug dosages on the Poincaré plot extracted features, CeRemi did not show statistically significant results for any correlation, even though it is well know that remifentanil has deep effects in global hemodynamics [221]. However, CePropo and qCON values did, probably due to their relationship with cerebral metabolsim [222], [223]. Those results suggest that CBF autoregulation is preserved and therefore CBF is not directly dependent on hemodynamic effects of remifentanil and in the case of propofol correlations, significant results are not due to the

hemodynamic depression but to its effects in the brain activity, also reflected by the qCON correlations.

Two limitations on the correlation analysis should be considered. The sample size in this dataset is limited to 40 female patients, going down to 22 for BSR episodes, therefore the results cannot be extrapolated to other populations. Moreover, correlation provides an overview on how each pair of variables evolves but does not allow to infer causal relationships between those physiological signals. Other techniques, such as the analysis of causal interactions (see Chapter 9), are needed to interpret how anesthesia, general hemodynamics and CBF evolve during general anesthesia under propofol and remifentanil.

6.7 Conclusions

The information extracted from the Poincaré plot descriptors of REG signals during an apnea challenge and under anesthesia suggests that this analysis might be able to reflect CBF changes in REG waves. The performance of those parameters is dependent on the time lag τ used to reconstruct the signal attractor. Considering all the results previously discussed, a time lag of 20 samples (0.08s) seems the most appropriate for this application.

SDratio, R and CCM proved their ability to detect apneas, despite the preprocessing filter used for data preparation. However, in REG data collected under general aneshesia, the linear filter provided better performance with a larger set of statistically significant results: all the Poincaré plot descriptors under analysis detected differences either in the transition from Awake to LOC or in the transtion from LOC to Anes, with SDratio and R proving to be effective in both cases.

Finally, Poincaré plot descriptors were correlated to patient characteristics (age, weight and BMI), as well as to global hemodynamic changes (HR and MAP) and anesthetic depth (CePropo and qCON). This suggests an interaction between the anesthetic dosage, depth of anesthesia and global hemodynamics that will be further analyzed in Chapter 9.

Chapter 7

Entropy Analysis of REG Signals

Abstract

This chapter explores different entropy-based algorithms in order to assess their ability to extract CBF information from REG signals. The selected algorithms were applied to REG signals during apnea and anesthesia, providing successful results in the characterization of cerebral hemodynamic changes in both scenarios.

7.1 Introduction

One of the most relevant problems that arise from REG signals is the interferences provoked by movements, respiration and contamination with extracranial blood flow [54], [57], [58]. Consequently, REG recordings suitable for processing are often short and noisy, and statistics adapted to those conditions are needed to be able to extract relevant clinical information from REG. Based on the hypothesis that apnea would provoke changes in REG signals under the form of increased complexity, several entropy metrics robust in noisy environments are assessed for REG analysis during breath holding.

Pincus et al. [224] presented the Approximate Entropy (ApEn), as a relative entropy metric suitable for short and noisy datasets, applicable to biomedical signals. ApEn approximates the exact regularity statistic Kolmogorov-Sinai Entropy and reflects the predictability of a time series by exploring repetitive patterns in the data. It has been extensively used in heart rate variability (HRV) analysis as for example to detect heart failure [225] or to identify differences in HRV in diabetic patients [226]. Moreover, ApEn has also been used to study the electroencephalograph (EEG) regularity during sleep [227], [228] and under sevoflurane anesthesia [229]. Even though those clinical applications have shown the ability of ApEn to correlate with physiological conditions, there is lots of controversy on its use. It has been reported to be inconsistent, lower than expected for short records and thus dependent on the length of the time series [230]. Furthermore, to compute the ApEn value of a time series, three parameters need to be defined: the segment length (N), the embedded dimension (m) and the noise threshold (r). The choice of those three parameters influences the ApEn result, therefore limiting its use to relative measurements.

In order to compensate for the limitations of ApEn, Richman and Moorman [230] proposed a new entropy metric, called SampEn. The main difference between the computation of ApEn and SampEn is that SampEn does not count self matches. However, it still requires the a priori definition of the same parameters (N, m and r).

SampEn has been used in different type of biomedical signals, as for example to characterize human gait signals [231], as a detector of driving fatigue in HRV signals [232] or to study EEG brain maturation in newborns [233]. Advantages of SampEn over the use of ApEn have also been reported, indicating that ApEn presents inconsistencies that are avoided by using SampEn instead [234] and that it is a better choice for short datasets [235].

Both ApEn and SampEn rely on the Heaviside function to define the similarity between two patterns. Due to its binary output, pairs of patterns are either included or rejected before the entropy calculation. In contrast, FuzzyEn was defined as a new entropy metric [213], in which the Heaviside function classifying the patterns as similar or not is replaced by a fuzzy function that computes a membership coefficient ranging from 0 to 1, where 1 maximizes the membership likelihood. Consequently, in addition to the selection of N, m and r, FuzzyEn requires a fourth parameter, n, which is the gradient of the boundary of the exponential function used to assess similarity. When compared to ApEn and SampEn, FuzzyEn outperformed the other measures in electromyogram (EMG) signals characterization [213], as well as in Alzheimer's disease detection in electrocardiographic signals (ECG) [236].

Those three Entropy metrics rely on the selection of several parameters and there is lots of controversy around how they should be selected and the bias they introduce in the final entropy values. Even though some methods have been proposed to determine those values [237]–[240], no consensus has been reached so far. For that reason, in this chapter, other metrics will be used not requiring the definition of so many parameters: Shannon Entropy (SE) and Corrected Conditional Entropy (CCE).

Shannon Entropy (SE) was introduced by Shannon to be applied in the Information Theory domain [241] and reflects the regularity of the information generated by a defined source. For its use in biomedical applications, at a sample level, the parameters to be defined are the signal length N to be considered, and the number of quantization levels (ε) used for signal discretization. Additionally, in some cases, SE is applied to sequences of symbols rather than at a sample level and requires therefore an extra parameter, the embedding dimension (m). SE has provided successful results when applied to EEG signals for person identification [242] and monitoring of intrapartum fetal heart rate dynamics [243].

Corrected Conditional Entropy (CCE) is an entropy measure introduced by Porta [244] that reduces the bias of regularity existing in Conditional Entropy. It is based on the definition of SE and has been used mainly on HRV signals, in some cases showing the expected trends but without statistical significance [245], [246], and in others providing successful results, such as the ones obtained by Viola et al. [247], describing a reduction in complexity of HRV signals during Rapid Eye Movement (REM) sleep with aging.

The entropy measures herein presented have not been previously applied to REG signals to the extent of the knowledge of the author, but they have been extensively used for diagnosis purposes in other biomedical signals, such as the previously mentioned examples, mainly on electromyography (EMG) and HRV. Nonetheless, entropy measures have been applied to the study of plethysmography signals, which also reflect a pulse wave and are therefore closer to REG signals than EMG and HRV. For instance, Pham et al.[248] proved that SampEn of plethysmography records is a good predictor of mental disorder detection, therefore proving the usefulness of entropy assessment in pulse waves.

The main goal of this work is to study if entropy metrics applied to REG signals can detect changes in CBF during breath holding -apnea- and analyze which parameters would optimize the results. The underlying hypothesis is that entropy would increase during apneas, since under those circumstances CBF changes take place, altering the regular baseline pattern of REG signals and thus reducing regularity and increasing entropy. Following this preliminary analysis, the second goal is to apply the entropy metrics identified for apnea detection to REG signals collected during anesthesia, to study which entropy metrics would be suitable for CBF monitoring during surgeries requiring general anesthesia, which are known to provoke CBF changes.

7.2 Methods

7.2.1 Entropy definitions

This section provides information on the algorithms used for entropy calculations. Different entropy metrics will be calculated and tested: ApEn, SampEn, FuzzyEn, SE and CCE. The parameters involved in the entropy evaluation will be a priori identified: the embedding dimension (m), the signal length (N), the multiplicand of the standard deviation to define the noise level (r), the gradient of the fuzzy membership function (n) and the number of quantization levels (ε).

7.2.1.1 Shannon Entropy

The Shannon Entropy (SE) [35] assesses the amount of information generated by a system. It can be used either locally or globally [249] and, for consistency with the other entropy metrics evaluated in this work, SE will be applied to consecutive patterns of length m. Hence, from a time series x(n) of length N, quantized in ε levels, a phase space reconstruction with dimension

m is built, resulting in a set of vectors $x_m^\varepsilon(i) = (x^\varepsilon(i), x^\varepsilon(i-1), \ldots, x^\varepsilon(i-m+1))$. The SE of the time series is then computed as

$$SE(m, \varepsilon) = -\sum_{x_m^\varepsilon} p(x_m^\varepsilon) \log\, p(x_m^\varepsilon) \tag{7.1}$$

where $p(x_m^\varepsilon)$ corresponds to the joint probability of the x_m^ε pattern and the sum is performed across all the different patterns. This entropy metric requires the definition of the number of quantization levels (ε), the embedding dimension (m) and the length of the input signal (N). Thus, in this work, SE for apnea detection will be computed for a set of quantization levels ε ranging from 10 to 50, in steps of 10, with dimensions m from 2 to 4 and a set of signal lengths N = {1000, 2000, 3000, 4000} samples. The set of parameters optimizing apnea detection will be applied to REG signals under general anesthesia.

7.2.1.2 Corrected Conditional Entropy

Corrected Conditional Entropy[244] is based on the correction applied to the Conditional Entropy (CE) definition. CE is calculated as the variation of SE in two consecutive values for the embedding dimension, m:

$$CE\,(m, \varepsilon) = -\sum_{x_{m-1}^\varepsilon} p(x_{m-1}^\varepsilon) \sum_{x_m^\varepsilon} p\left(\frac{x_m^\varepsilon}{x_{m-1}^\varepsilon}\right) \log p\left(\frac{x_m^\varepsilon}{x_{m-1}^\varepsilon}\right) \tag{7.2}$$

where the first term sums across all the different x_{m-1}^ε patterns, $p(x_{m-1}^\varepsilon)$ corresponds to the joint probability of the x_{m-1}^ε pattern and the second term covers all m samples in the pattern, with $p(x_i^\varepsilon / x_{m-1}^\varepsilon)$ representing the joint probability of the m-th pattern conditioned to the preceding m-1 patterns. Therefore, CE can be formulated as a function of SE:

$$CE(m, \varepsilon) = SE(m, \varepsilon) - SE(m-1, \varepsilon) \tag{7.3}$$

Porta et al. proposed in [244] a correction to CE in order to compensate for unique patterns that should theoretically increase entropy but reduce it when using the CE definition. The proposed correction consists in adding a corrective term and defining CCE as:

$$CCE(m, \varepsilon) = CE(m, \varepsilon) + SE(1, \varepsilon)\, perc(m, \varepsilon) \tag{7.4}$$

where $\mathrm{perc}(m, \varepsilon)$ is the percentage of single points in the m-dimensional space. Moreover, the same authors propose the use of the minimum of the CCE entropy, CCEmin, as an approximation to the entropy of the signal, avoiding having to define the value for m in advance for the entropy calculation [250] [251]. Additionally, they introduced the regularity index ρ, computed as:

$$\rho = 1 - \min\big(\mathrm{NCCE}(m, \varepsilon)\big) \tag{7.5}$$

to estimate the overall regularity of a time series. In equation 7.5, NCCE refers to the normalized CCE by SE(1,ε), resulting in a regularity index providing values between 0 and 1, representing maximum and minimum complexity, respectively.

CCE and the regularity index ρ were computed for all the signals in the Apnea-Baseline experimental dataset. Analogous to the parameter set chosen for SE, CCE was computed with embedding dimension m from 2 to 4, quantization levels ε of 10, 20, 30, 40 and 50 while the length N of the segments used ranged from 1000 to 4000, in steps of 1000 samples. Results obtained with this dataset were afterwards applied to REG signals in General Anesthesia Dataset 1.

7.2.1.3 Approximate Entropy

ApEn [224] allows to quantify the regularity of a time series without the need of previous knowledge of the dynamics of the system [249], resulting in larger values for increasing complexity in the data. ApEn reflects the likelihood that patterns that are close, within a defined distance r, in a m-dimensional space remain close within the same tolerance when defined in a m+1 dimensional space.

Given a digital signal u(n), with length of N samples, values for the embedded dimension m and the filtering level r are fixed a priori. A set of vectors, x, in the R^m dimensional space are then created:

$$x_i = [u(i), \quad \cdots, \quad u(i + m - 1)] \tag{7.6}$$

For each i, $1 \leq i \leq N\text{-}m+1$, an estimation of the correlation integral $C_i^m(r)$ is computed as:

$$C_i^m(r) = \frac{\text{number of j such that } d[x(i), x(j)] \leq r}{N - m + 1} \tag{7.7}$$

where the distance between x(i) and x(j) is defined as:

$$d[x^m(i), x^m(j)] = \max_{k=1,2,..,m}\left(\left|u(t_{i+k-1}) - u(t_{j+k-1})\right|\right) \quad (7.8)$$

Finally, ApEn is calculated as:

$$ApEn(m, r, N) = \phi^m(r) - \phi^{m+1}(r) \quad (7.9)$$

where

$$\phi^m(r) = (N - m + 1)^{-1} \sum_{i=1}^{N-m+1} \log C_i^m(r) \quad (7.10)$$

The performance of ApEn depends on the choice for the input parameters r and m, as well as the length of the time series to be compared. Since noise smaller than r is filtered out, ideally r should be small enough to preserve the information of the dynamics of the system, but very small values would compromise the calculation of conditional probabilities [252]. Regarding the choice for m, larger values are preferred but it shall be considered that its selection is limited by the length of the time series (N), since N should be between 10^m and 30^m points [253] [254].

ApEn values can vary significantly for r and m values, therefore it shall be used for systems comparison. Typical values for m are m=2 and m=3, while selected values for r depend on the type of signals to which this technique is applied [224]. The most commonly used combination is m=2 and r=0.2 (20% of the standard deviation) [249]. Pincus et al. [224] obtained significant results on the comparison of HRV signals of healthy and sick infants using r values ranging from 0.1 to 0.25 while Chen at al. used r=0.3 to successfully distinguish EMG signals originated by four different movements [213].

Even though several algorithms have been published to overcome the difficulties in the choice of r [239], [240], when comparing ApEn values for two or more groups the optimal r value could be different in each group and

lead to inconsistent results [255]. Therefore, experimental analysis is recommended to identify the best r for each application.

It should also be taken into account that ApEn is a biased statistic, strongly dependent on the signal length and lacking of consistency [230], providing unexpected ApEn variations for different pairs of m and r values [254]. The bias is due to the concavity of the logarithmic function, as well as to the fact that ApEn counts self matches when computing the correlation integral [252].

For the analysis of REG signals in apnea and baseline recordings, considering that data sequences available were 4000 samples length, N values of the analyzed time series ranged from 1000 to 4000, in steps of 1000. For the parameter m, it was limited to m=2, m=3 and m=4, the last one exceeding the $N \leq 10^m$ criteria. Finally, chosen r values covered the range of 0.05 to 0.3 times the standard deviation of the input signal. The parameters optimizing apnea detection were applied to REG signals during surgeries under general anesthesia.

7.2.1.4 Sample Entropy

The entropy metric SampEn [230] intends to surpass the constraints presented in ApEn by excluding self matches in the entropy calculation and therefore reducing computation times. The algorithm follows the same initial steps presented for ApEn, but when computing the correlation integral self-matches are excluded, as shown in equation 7.11.

$$C_i^m(r) = \frac{\text{number of j such that } d[x(i), x(j)] \leq r \text{ and } i \neq j}{N - m + 1} \tag{7.11}$$

Lastly, $\phi^m(r)$ is defined as

$$\phi^m(r) = (N - m)^{-1} \sum_{i=1}^{N-m} \log C_i^m(r) \tag{7.12}$$

and SampEn is calculated as the difference between the logarithms of $\phi^m(r)$ and $\phi^{m+1}(r)$:

$$\text{SampEn}(m, r, N) = \log \phi^m(r) - \log \phi^{m+1}(r) \tag{7.13}$$

SampEn requires the a priori definition of the same parameters listed for ApEn - N, m and r – and those are typically coincident with the ones used for ApEn (i.e. m=2, r=0.2). However, even though some authors consider the same criteria can be used for both SampEn and ApEn [256], other publications suggest that they should be explored independently since algorithms proposed for the choice of r in ApEn are not applicable for SampEn [257]. Moreover, appropriate values for m and r depend of the type of signal under analysis [256].

For instance, Lake et al. [258] studied the selection of m and r parameters for neonatal HRV analysis, concluding that the best pair of values was m=3 and r=0.2. In contrast, while applying SampEn algorithm to characterize the effects of exercise in RR and QT intervals, Lewis et al. [259] explored different combinations of r and m values to finally chose m=2 and r between 0.1 and 0.15. Higher r values have also been considered as optimal, as for example in the atrial fibrillation organization analysis presented by Alcaraz et al. [256], in which after identifying several combinations providing good classification results, the best values were considered to be m=3 and r between 0.3 and 0.4.

SampEn overcomes the bias problem detected in ApEn as well as its inconsistencies, such that if SampEn of one signal (x_1) is higher than the value obtained with another signal (x_2) for a pair of m and r values, a new m-r pair would still provide higher SampEn values for the signal x_1 [258]. Nonetheless, Castiglioni et al. [257] detected inconsistencies in SampEn calculations when studying mechanomyographic signals for certain m values, and Yentes et al. [235] published similar findings for some r choices, suggesting that under certain conditions SampEn can also be affected by inconsistencies.

Controversy around adequate m and r values and the existence of inconsistencies in SampEn calculations requires that, for a new type of signals such as REG signals, an analysis of the effect of m, r and N is performed. Therefore, in this work, the same values suggested for ApEn were used to explore the ability of SampEn to detect apnea periods in REG signals: a range of m (from 2 to 4), r (from 0.1 to 0.3) and N (from 1000 to 4000). Moreover, the selected set of parameters optimizing apnea detection was used for entropy analysis of REG signals during general anesthesia.

7.2.1.5 Fuzzy Entropy

ApEn and SampEn share a definition of similarity in which data segments with distances lower than the threshold value r are considered as positive matches, while others are rejected and not considered for the calculation. Even though ApEn includes self-matches and SampEn does not, in both cases a Heaviside function is used to assess similarity. In contrast, the definition of FuzzyEn [213] relies on a degree of similarity between 0 and 1. This similarity is based on the concept of fuzzy membership as defined by Zadeh [260] and results in a weaker influence of the choice of r in the final entropy calculations [249].

Besides the use of fuzzy membership calculations, FuzzyEn algorithm also differs from ApEn and SampEn in the way it creates the set of m-dimensional vectors. Given a time series N-samples length u(n), vector sequences are defined as:

$$x_i^m = \{u(i), u(i+1), \cdots, u(i+m-1)\} - u0(i), \tag{7.14}$$

where $u0(i)$ represents the baseline trend and is computed as

$$u0(i) = \frac{1}{m}\sum_{j=0}^{m-1} u(i+j) \tag{7.15}$$

The distance between two vectors, x_i^m and x_j^m, is defined as the maximum distance among all the scalar components of the vector d_{ij}^m. A matrix, D_{ij}^m is built, containing the similarity degrees for all pairs of r and n (width and gradient of the boundary of the exponential function, respectively)

$$D_{i,j}^m = \mu\left(d\left(\bar{x}_i^m, \bar{x}_j^m\right), n, r\right) \tag{7.16}$$

where μ is the exponential fuzzy function:

$$\mu(x, n, r) = e^{-\left(\frac{x}{r}\right)^n} \tag{7.17}$$

Finally, the function ϕ^m is calculated as

$$\phi^m = \frac{1}{N-m}\sum_{i=1}^{N-m}\sum_{j=1, j\neq i}^{N-m}\frac{D_{i,j}^m}{N-m-1} \tag{7.18}$$

and the fuzzy entropy is computed as:

$$\mathrm{FuzzyEn}(m, r, n, N) = \ln \phi^{m} - \ln \phi^{m+1} \ . \qquad (7.19)$$

FuzzyEn needs therefore four parameters to be computed: N, m, r and n values. Typical values for N, m and r are coincident with the ones used for SampEn and ApEn, even though dependence on r is less critical due to the substitution of the Heaviside function by the fuzzy membership calculation. Regarding the values for n, only small values guarantee a good approximation of entropy [249], being n=2 the most frequently used [213], [261], [262].

For this application on apnea REG signals, N, m and r ranges tested were the same ones proposed for ApEn and SampEn, while n values ranged from 2 to 10. The set of parameters optimizing apnea detection were used for the study of this entropy metric in the general anesthesia dataset.

7.2.2 Experimental protocols

Two datasets were used to explore the ability of entropy metrics to detect CBF alterations when applied to REG signals. In a first step, the Apnea-Baseline Dataset was used to study the best parameters to be used to calculate each entropy metric and to identify the ones capable of identifying CBF changes. In a second step, the selected set of entropy metrics optimizing apnea detection were applied to the General Anesthesia Dataset 1, to assess their ability to detect changes during general anesthesia.

Details on both datasets were provided in Chapter 3. The Apnea-Baseline Dataset included REG data from 16 young healthy volunteers during two successive breath holding challenges. In contrast, the General Anesthesia Dataset 1 contained REG data from 40 female patients undergoing surgical procedures in which general anesthesia was applied.

7.2.3 Data analysis for apnea detection

Even though entropy measures are known to be robust in presence of limited amounts of noise, the recorded signals were filtered to reduce the influence of powerline interferences in the computed parameters and to filter out slow drifts provoked by respiration as well as other direct current fluctuations.

Two different algorithms were used to filter the input dataset: one based on classical linear filters and the other one relying on the nonlinear approach applied to the signal attractor, as presented in Chapter 4. For both options, signals were filtered in advance with a 4th order high-pass filter with a stop band frequency of 0.1Hz. The set of filtered signals was screened, and detected artefacts were rejected to finally select data segments of 4000 samples. A total of 53 sequences were obtained, 29 belonging to apnea recordings and 24 from baseline periods. The main characteristics of those signals were previously presented in Chapter 5.

All entropy metrics were computed for each input parameter combination indicated in **Table 7-1**, and their ability to distinguish baseline and apnea sequences was assessed by hypothesis testing, using either T-student tests or Mann-Whitney tests, for normal and non-normal distributions, respectively. Normality was determined using a Kolmogorov-Smirnov test. The statistical significance threshold was set at $p<0.05$, and Bonferroni corrections were applied resulting in a final threshold of $p<0.025$. Additionally, the area under the curve (AUC) of the Receiver Operating Characteristic and the classification accuracy (acc) were also computed. Results obtained with linear and nonlinear preprocessing algorithms were compared in order to assess the potential advantages of the use of nonlinear algorithms to filter REG recordings.

Table 7-1 Parameter combinations used to calculate each entropy metric.

	SIGNAL LENGTH (N) (SAMPLES)	EMBEDDING DIMENSION (m)	FILTERING LEVEL (r)	QUANTIZATION LEVELS (ε)	FUZZY FUNCTION GRADIENT (n)
SE	1000 to 4000	2 to 4	-	10 to 50	-
CCE	1000 to 4000	2 to 4*	-	10 to 50	-
ApEn	1000 to 4000	2 to 4	0.05 to 0.3	-	-
SampEn	1000 to 4000	2 to 4	0.05 to 0.3	-	-
FuzzyEn	1000 to 4000	2 to 4	0.05 to 0.3	-	2 to 10

* Only used in CCE calculation, not applicable for ρ

7.2.4 Data analysis for general anesthesia recordings

General Anesthesia Dataset 1 was preprocessed to analyze changes in the entropy of REG signals during anesthetic procedures. All collected REG waves were filtered following the same steps as for the Apnea-Baseline Dataset. Using the guidance provided by clinical annotations recorded during the data collection process, 5 artefact free segments 4000 samples long were selected form each recording:

- Awake – corresponding to the data recorded prior to induction of anesthesia.
- Loss of Consciousness (LOC) – data recorded right after LOC is detected and while intubation is being prepared.
- Steady state anesthesia (Anes)– data recording during anesthesia, without burst suppression episodes and after intubation has been achieved and patient positioned for surgery.
- Burst Suppression Rate (BSR) - data belonging to periods in which the Conox BSR index provides values higher than 10.

- Recovery of consciousness (ROC) – data belonging to the end of the procedure, once drug infusion has been stopped and patient is ready to be extubated.

Once artefacts were rejected and segments selected, 34 recordings were available for the Awake state, 35 for LOC, 33 for steady state anesthesia, 22 for BSR and 40 for ROC. All entropy algorithms described in this section were applied to the selected segments, using for their computation the set of parameters (N, r, m, n, ε) deducted from the analysis of the Apnea-Baseline Dataset.

Differences in entropy were analyzed by means of hypothesis testing, using paired T-student tests or Wilcoxon tests depending on the distribution of the samples. The Kolmogorov-Smirnov test was used for normality assessment. Statistical significance was considered for $p\text{-value}<0.05$ and, provided that 5 groups were compared, Bonferroni correction was applied resulting in a significance threshold for $p\text{-value}<0.01$.

It should be noted that in the Apnea-Baseline Dataset, all participants were young healthy volunteers, with comparable age and physical conditions. However, this is not applicable to the General Anesthesia Dataset 1. For this reason, correlations between the entropy values in each clinical state and demographic data of the patients were assessed, as well as correlations between those demographics and the entropy changes identified between consecutive states. Moreover, other clinical information was studied as well, to analyze its relationship with entropy values and changes. Heart rate (HR), mean arterial pressure (MAP), propofol effect site concentration (CePropo), remifentanil effect site concentration (CeRemi) and the depth of anesthesia index (qCON) were considered for this analysis. Spearman correlation was used, considering statistical significance of the resulting correlations for $p\text{-value}<0.05$.

7.3 Results for apnea detection

7.3.1 With linear filter

The evolution of the entropy metrics ApEn(m,r,N), SampEn(m,r,N), FuzzyEn(m,n,r,N), SE(N,m,ε), CCE(N,m,ε) and ρ(N,ε), after being preprocessed with the linear filter, as a function of the parameters selection is

herein presented, as well as their ability to differentiate between apnea and baseline signals.

The CCE and the regularity index ρ resulted in statistically significant results for apnea detection, while none of the parameter combinations tested for SE was able to identify apneas. Results for CCE as a function of ε, m and N are provided in **Figure 7-1**, together with the corresponding p-value illustrating the ability of CCE to distinguish between apnea and baseline recordings. As the number of quantization levels ε increases, CCE increases for both apnea and baseline periods (**Figure 7-1** (a)), but the p-value decreases (**Figure 7-1** (d)), showing a minimum for ε = 10 and ε =20 levels. Regarding the embedding dimension m, CCE decreases as m increases, providing the best statistical significance for m=2 (**Figure 7-1** (b) and (e)), while CCE remains almost stable for increasing segments length (N) (**Figure 7-1** (c)). Segments with lengths of 2000 and 3000 samples provide the lowest p-value.

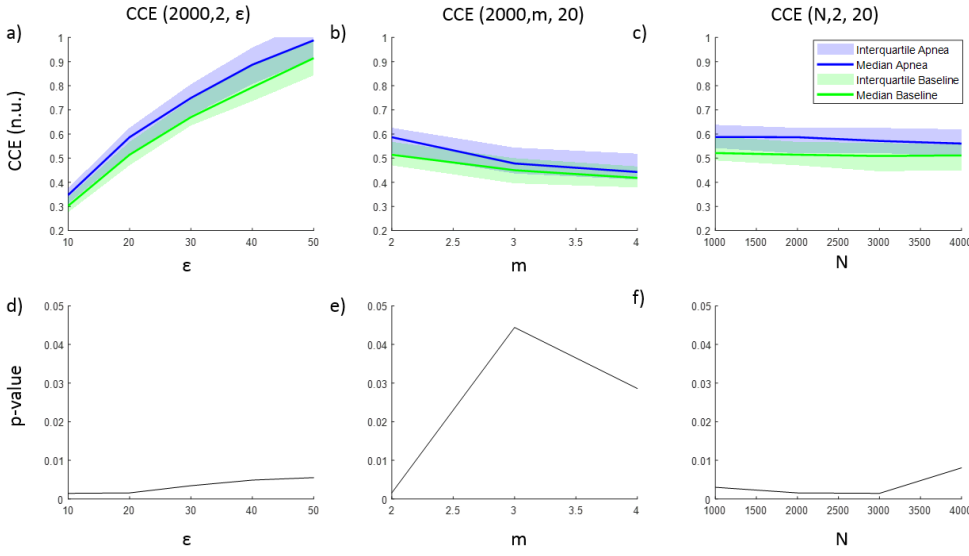

Figure 7-1 Corrected Conditional Entropy (CCE(N, m, ε)) values of apnea and baseline recordings as a function of a) the quantification intervals (ε), b) the embedding dimension (m) and c) the signal length (N). The corresponding statistical significance (p-value) of the differences between apnea and baseline recordings is presented in d), e) and f), respectively.

In addition to the analysis of CCE values, **Figure 7-2** illustrates the results for the regularity index ρ. A monotonic decrease in regularity was observed for increasing number of quantification intervals (ε), showing higher regularity for baseline recordings (**Figure 7-2** (a)). The effect of increasing the signal length (N) is depicted in **Figure 7-2** (b), showing an increase of regularity as N increases. Regarding the influence of the number of the quantification intervals in the statistical significance of the results, using ε ≤50 intervals kept p-value lower than the significance threshold ($p<0.025$) for signal lengths of N=2000 samples, as shown in **Figure 7-2** (c). However, for a fixed number of quantification intervals ε=20, the regularity index ρ is statistically significant for signal lengths N≥2000 samples (**Figure 7-2** (d)). Therefore, optimal parameters for ρ calculation to detect apneas are ε =20 quantification steps for signals of N=2000 samples.

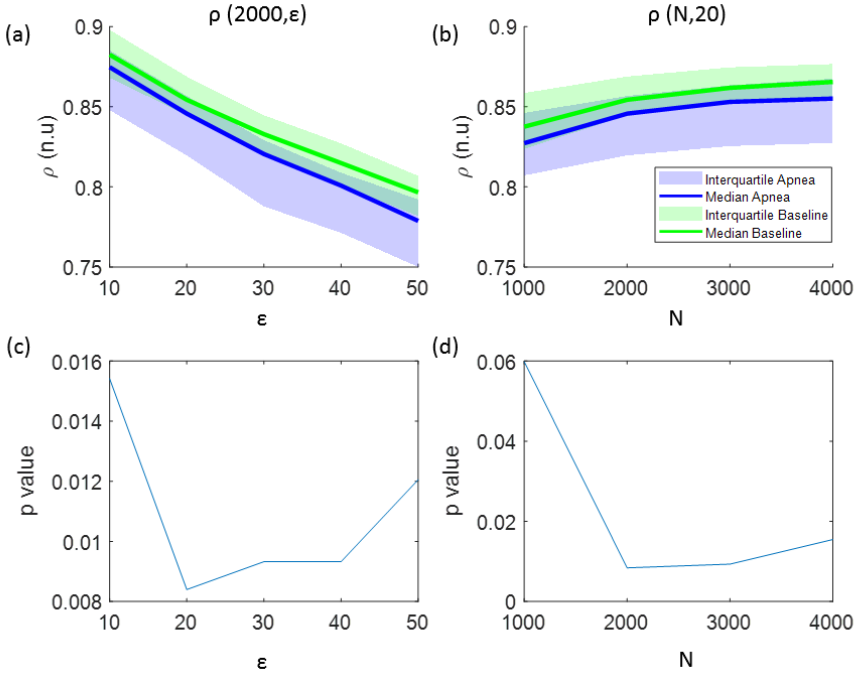

Figure 7-2 The influence of the signal length and the number of quantization levels in the Regularity index (ρ(N, ε)) is analyzed in: (a) values of ρ as a function of the number of quantification intervals (ε) and (b) values of ρ as a function of the signal length (N). The results of the statistical analysis (p-value) comparing apnea and baseline signals using this entropy indexes are shown in: (c) p-values versus the number of quantification intervals and (d) p-values versus the signal length.

The results in **Figure 7-2** were obtained considering an embedded dimension m=10, assuming that the minimum value CCEmin of the CCE would fall into this m range. To prove this assumption, a study of the entropy CCE varying the values of the embedded dimension m is presented in **Figure 7-3**. Each plotted CCE curve in **Figure 7-3** (a) belongs to an apnea recording and each one in **Figure 7-3** (b) to a baseline recording. It can be observed that the minimum entropy takes place for m<10 in both apnea and baseline signals. Furthermore, the location of the minimum CCE is not affected by the type of signal (apnea or baseline), as shown in **Figure 7-3**, and the median CCE values of the apnea signals are higher than the median values obtained from the baseline recordings.

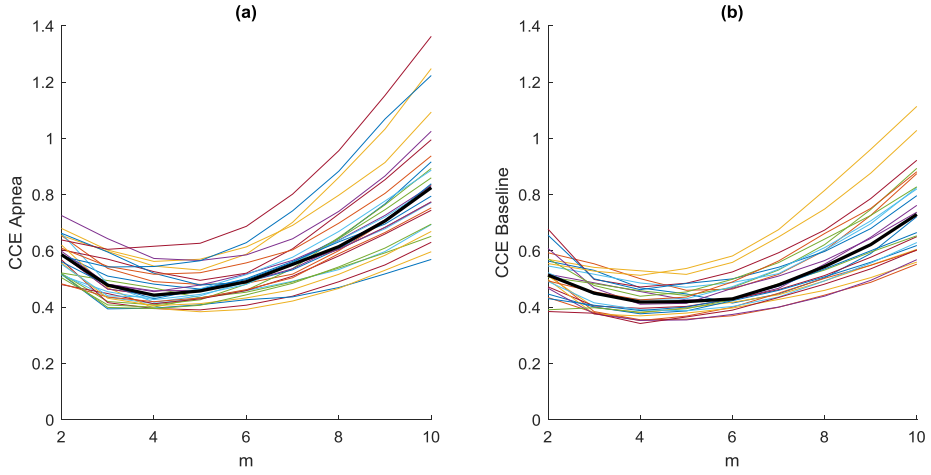

Figure 7-3 Values of the entropy CCE(N,m,ε) with ε=20 and N=2000 as a function of the embedding dimension m for all apnea (a) and baseline (b) recordings, including their median values (thick black line).

Results referred to the study of ApEn, SampEn and FuzzyEn entropies are shown in **Figure 7-4**. In order to explore the effects of m and N, the parameter r was initially fixed to 0.3 as recommended in [213]. Entropy values were higher for apneas when compared to baseline for all entropy metrics and parameter combinations. ApEn provided the highest entropy values, followed by SampEn and FuzzyEn, respectively. Both ApEn and SampEn provided lower values for recordings of N=1000 samples and remained approximately stable for recordings of N= 2000 samples or larger.

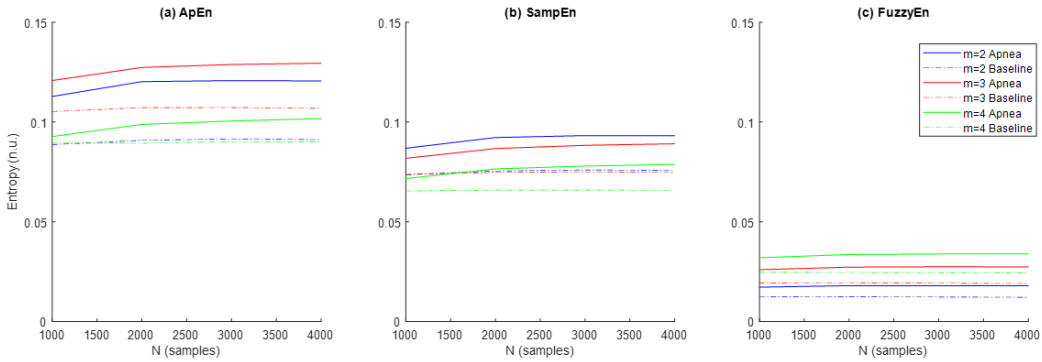

Figure 7-4 Values of the entropies ApEn, SampEn and FuzzyEn as a function of the number of samples (N) and the dimension (m), with r=0.3 and n=2 for FuzzyEn, for apnea (solid line) and baseline segments (dashed line).

The ability of the three entropy metrics to distinguish between apnea and baseline segments was assessed by the p-value resulting from the hypothesis testing (**Table 7-2**). FuzzyEn provided statistically significant differences between both types of signals in all parameter combinations tested for m and N, while statistical significance for ApEn was limited to m=2 and m=3 for any sequence length and for SampEn was limited to m= 2 for a signal length of N≥2000 samples. Therefore, parameter values m=2 and N=2000 were selected as the most appropriate across all entropy metrics for apnea detection in REG signals.

Table 7-2 Parameter combination used to calculate each entropy metric.

	N=1000	**N=2000**	**N=3000**	**N=4000**
ApEn				
m=2	0.0044	0.0006	0.0006	0.0004
m=3	0.0131	0.0014	0.0013	0.0004
m=4	0.6379	0.4915	0.5376	0.3391
SampEn				
m=2	0.048	0.014	0.017	0.017
m=3	0.166	0.195	0.145	0.136
m=4	0.387	0.280	0.183	0.172
FuzzyEn				
m=2	0.00076	0.00013	0.00014	0.00012
m=3	0.00086	0.00018	0.00016	0.00014
m=4	0.00329	0.00042	0.00022	0.00021

Regarding the parameter r, all entropies showed lower values as r increased and this behavior was common for both apnea and baseline signals (**Figure 7-5**, a-c). In the case of FuzzyEn, p-values decreased monotonically with r, proving a better differentiation between apnea and baseline as r grows, even though FuzzyEn provided p-value< 0.025 for all r (**Figure 7-5**, f). Instead, ApEn and SampEn needed at least r=0.2 and r=0.25, respectively, to provide significant results, showing both a minimum for r=0.25 (**Figure 7-5**, d-e). For that reason, r=0.25 was considered a suitable value for apnea detection in REG signals.

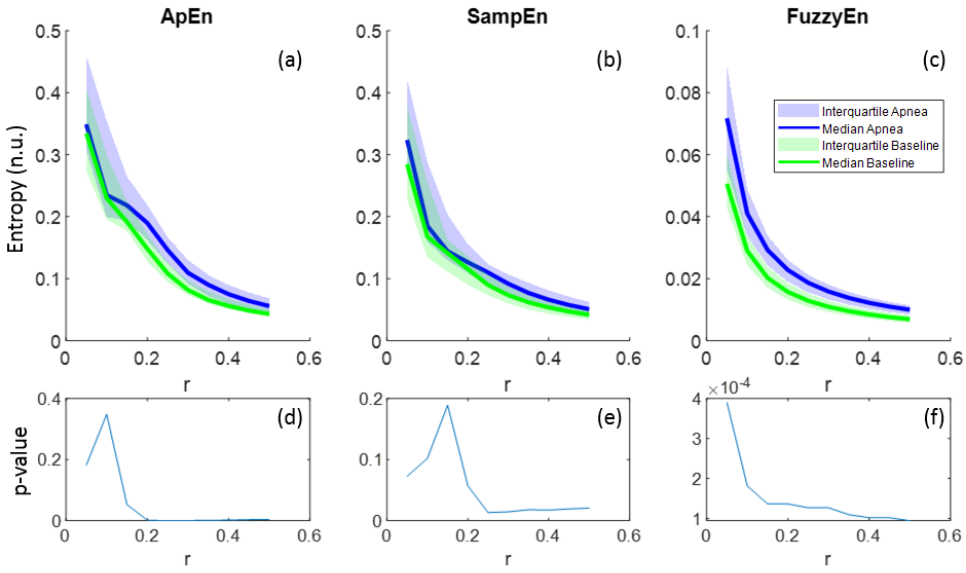

Figure 7-5 Entropy values of ApEn(m,r,N), SampEn(m,r,N) and FuzzyEn(m,r,,n,N) as a function of r with m=2, n=2 and N=2000 for apnea and baseline recordings (a-c) and the corresponding p-values (d-f).

The entropies ApEn and SampEn are fully characterized with values for N, r and m. However, for FuzzyEn, a fourth parameter (n) needs to be considered. FuzzyEn showed decreasing values for increasing n values, as shown in **Figure 7-6**a, and the standard deviation of computed entropies only tended to 0 for values of n higher than 6 (**Figure 7-6**b). In order to select the best n value for apnea detection, the statistically significant level was calculated comparing the FuzzyEn values of apnea from baseline group. FuzzyEn had

the minimum p-value at n=2 and hence this was considered the best choice (**Figure 7-6**c).

The standard deviation of the entropy metrics provides an assessment of their stability. Moreover, its evolution of r is used to determine their consistency [213]. Therefore, the evolution of the standard deviation of the three entropy metrics (ApEn, SampEn and FuzzyEn) as a function of the parameter r is depicted in **Figure 7-7**. All of them decrease with increasing r, showing a higher standard deviation value for apneas than baselines. FuzzyEn showed the lowest standard deviation, followed by SampEn. It is worth noting that both FuzzyEn and SampEn decreased monotonically while ApEn showed an almost flat behavior for r values around 0.3 in the apnea signals. This phenomenon was less pronounced in baseline recordings, but an inflection point can be observed in the same r range.

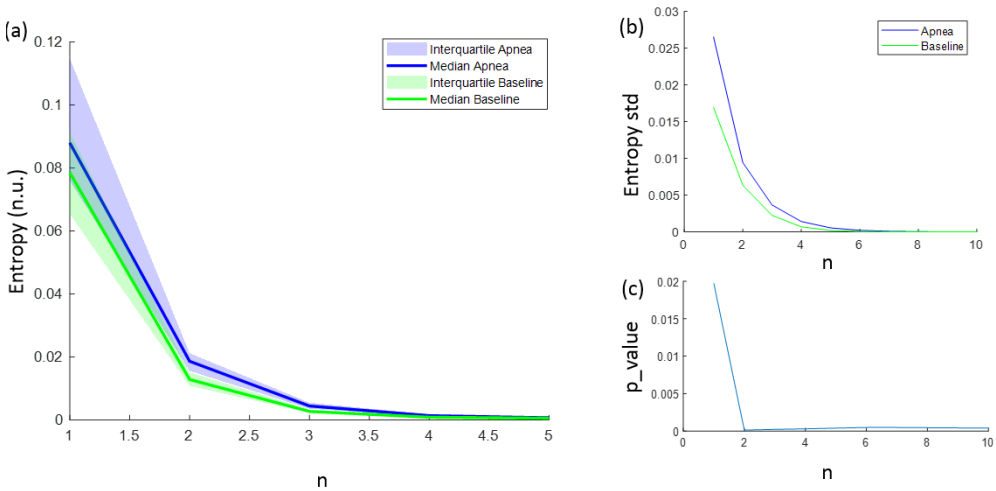

Figure 7-6 Fuzzy entropy (FuzzyEn(m,r, n,N)) (a) FuzzyEn(2,0.25, n, 2000) values as a function of n, including the 25-75 interquartile range (colored area); (b) standard deviation of FuzzyEn(2,0.25, n, 2000) as a function of n; (c) p-value obtained comparing FuzzyEn(2,0.25, n, 2000) values in apnea and baseline groups as a function of n.

Results for all tested entropy metrics are included in **Table 7-3.** The values of the parameters that best describe these entropies when comparing apnea and baseline recordings are included. All these entropy metrics show increased values for apnea recordings, indicating an increased signal

complexity. It should be noted that the index ρ presents the opposite behavior, since it reflects regularity instead of complexity.

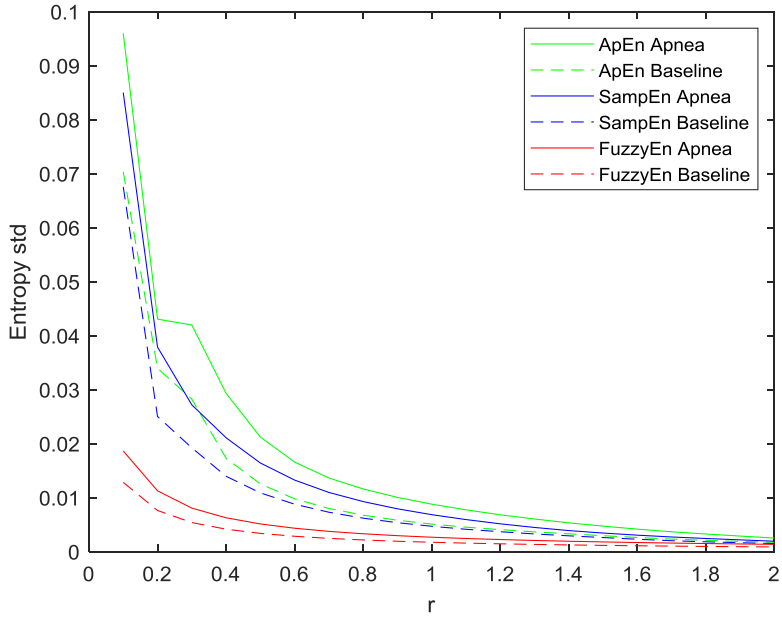

Figure 7-7 Standard deviation of ApEn(m, r, N), SampEn(m, r, N) and FuzzyEn(m, r, n, N) as a function of r comparing baseline and apnea segments, with m=2, n=2, N=2000.

Since Shannon entropy did not provide significant results for any parameter (N, m, ε) combination it has not been included in this table. In addition to the p-value computed for each metric, **Table 7-3** contains the values of area under the curve (AUC) and accuracy (acc), in which FuzzyEn outperforms other entropy metrics. Moreover, **Figure 7-8** depicts the Receiver Operating Characteristic curves for all the entropy metrics summarized in the table.

Table 7-3 Mean values and standard deviation of all entropy metrics when comparing apnea and baseline recordings. The values of the set of parameters that best describe these entropies are included. Statistics as p-value, AUC and accuracy (acc) are provided to assess the ability of the entropy metrics to distinguish between apnea and baseline.

ENTROPY MEASURE	PARAMETERS	APNEA MEAN ± STD	BASELINE MEAN ± STD	P-VALUE	AUC	ACC (%)
ApEn	r=0.25 m=2 N=2000	0.155 ± 0.045	0.118 ± 0.035	0.0003	0.789	69.8
SampEn	r=0.25 m=2 N=2000	0.111 ± 0.031	0.092 ± 0.022	0.0132	0.698	60.4
FuzzyEn	r=0.25 m=2 N=2000 n=2	0.021 ± 0.009	0.015 ± 0.006	0.0001	0.809	69.8
CCE	ε=20 m=2 N=2000	0.581 ± 0.063	0.518 ± 0.075	0.0016	0.744	67.9
ρ	ε =20 N=2000	0.838 ± 0.024	0.854 ± 0.017	0.0084	0.713	62.3

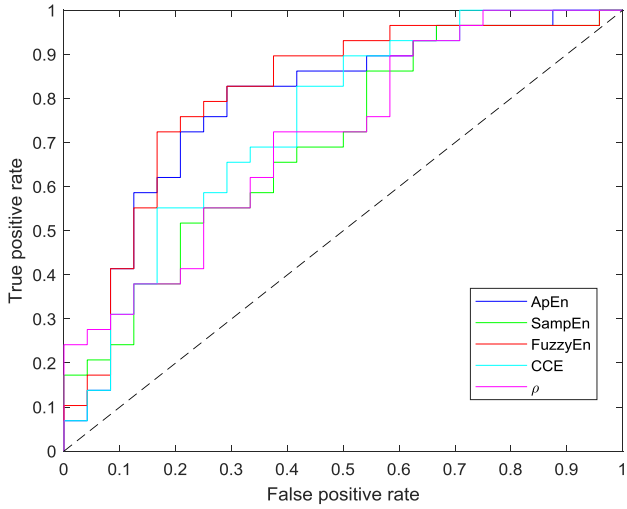

Figure 7-8 Receiver Operating Characteristic curves of all entropy metrics providing statistically significant differences between apnea and baseline recordings.

Additionally, **Figure 7-9** shows the distribution of each entropy metric for baseline and apnea groups. CCE and ρ present the highest dispersion of values, while ApEn, SampEn and FuzzyEn have less dispersed distributions but with many outliers, especially ApEn and FuzzyEn. Those results suggest that even though the selected metrics provide statistically significant differences in apnea and baseline recordings, individual differences should be noted.

7.3.2 With nonlinear filter

The entropy metrics proposed for REG analysis were also applied to the Apnea-Baseline Dataset preprocessed with the nonlinear filter, and the results were compared to those obtained when using classical linear filters. SE was excluded from the analysis since it failed to detect apneas for all N and ε combinations in the linearly filtered dataset. Moreover, signals with $N \leq 1000$ samples were discarded due to their inability to provide successful results for any of the entropy metrics evaluation.

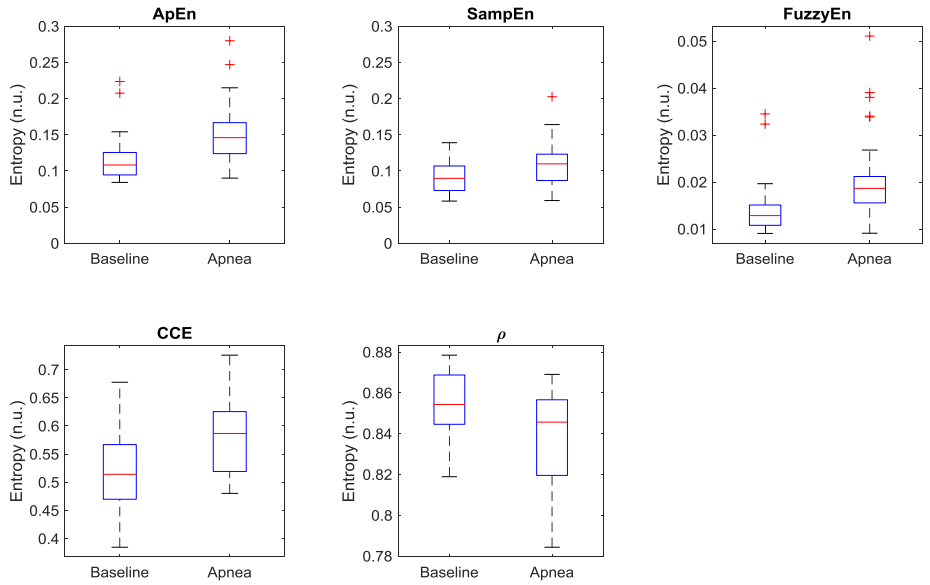

Figure 7-9 Boxplot of all selected entropy metrics, showing the median values (horizontal red lines) and outliers (red crosses): ApEn (m, r, N), SampEn (m, r, N), FuzzyEn(m, r, n, N), CCE (N, m, ε) and ϱ (N, ε), with m=2, r=0.25, N=2000, n=2 and ε=20.

In **Figure 7-10**, results for CCE, the regularity index ρ and the position of the minimum of CCE are provided. CCE showed higher entropy values for apnea signals, decreasing for higher m values (**Figure 7-10**(a)), remaining stable along N values (**Figure 7-10** (b)), and increasing with ε (**Figure 7-10** (e)). In contrast, ρ shows higher regularity for baseline signals for N≥3000 with ε=20 (**Figure 7-10** (c)), and for ε≥30 when N=2000 (**Figure 7-10** (f)), while for smaller values of N and ε, respectively, it reflects the opposite behavior. This suggests that ρ presents some inconsistencies when applied to this dataset and might not be a reliable indicator for apnea detection. However, its trend when compared to results in **Figure 7-2** is preserved, decreasing when ε increases and increasing with N.

Even though the position of the CCE minimum in the linearly filtered dataset did not show differences between apnea and baseline groups, **Figure 7-10** (g) shows relevant differences for ε=10 when N=2000 in this dataset: CCEmin is obtained at m=9 for apneas and at m=7 for baseline signals.

Moreover, the location of the minimum shows a slight increase with increasing N values and a significant decrease while ε increases.

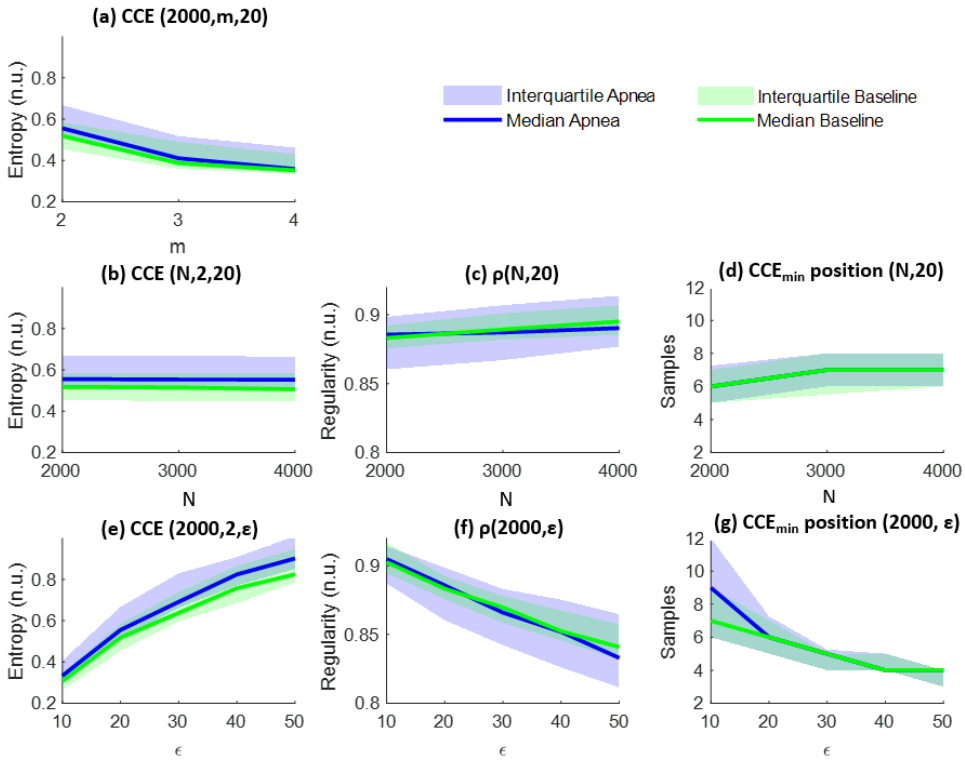

Figure 7-10 Values of CCE(N,m,ε), ϱ(N,ε) and CCEmin(N,ε) position median and interquartile values as a function of N, m and ε for apnea and baseline signals: (a) CCE(2000,m,20), (b)CCE(N,2,20), (c) ρ(N,20), (d) CCEmin(N,20), (e) CCE(2000, 2,ε), (f) ρ(2000,ε), (g) CCEmin(2000,ε).

The statistical significance of the ability of those metrics to distinguish between apnea and baseline segments is depicted in **Figure 7-11**. As expected, the regularity index did not provide significant results for any N and ε combination, while the location of the minimum of CCE was significantly different between groups for ε=10 and N=2000. Moreover, CCE provided acceptable results for the same set of parameters identified in the linearly filtered dataset (i.e. m=2, N=2000, ε=20).

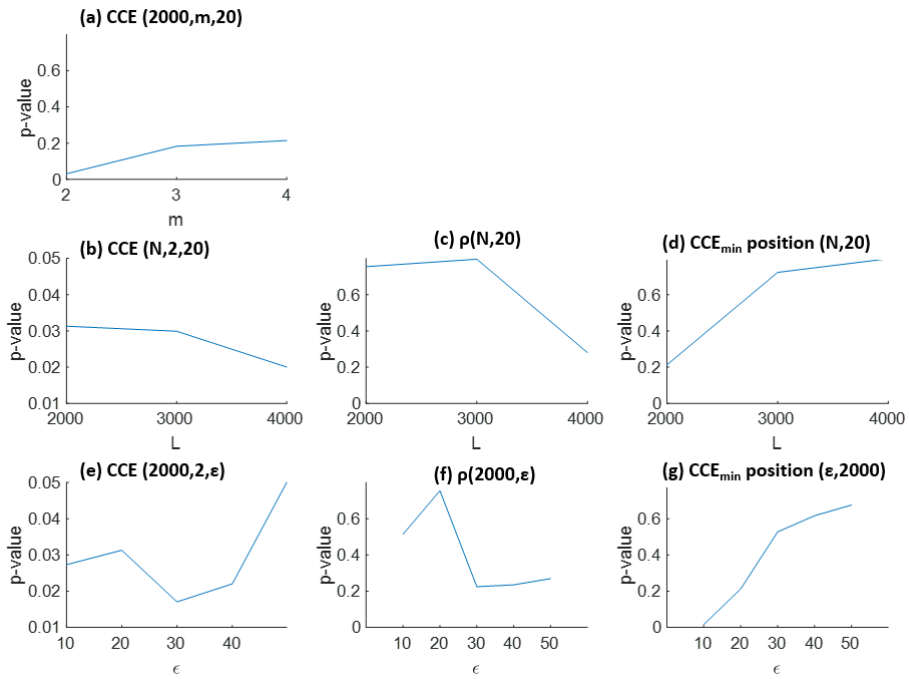

Figure 7-11 Analysis of the statistical significance (p-value) for apnea detection of CCE(N,m,ε), ρ(N,ε) and CCEmin(N,ε) as a function of N, m and ε: (a) CCE(2000,m,20), (b)CCE(N,2,20), (c) ρ(N,20), (d) CCEmin(N,20), (e) CCE(2000, 2,ε), (f) ρ(2000,ε), (g) CCEmin(2000,ε).

The comparison of the results obtained for linearly and nonlinearly filtered data is provided in **Figure 7-12**. In both cases, the CCE of apnea segments showed higher entropy values than baseline recordings, with the linearly filtered data showing enhanced statistical significance. It should also be noted that dispersion is bigger when the nonlinear filter is used, affecting mainly the apnea recordings. Regarding the regularity index ρ, data processed with the nonlinear filter show higher regularity than those processed with linear filters. Moreover, both sets of data provide an opposite assessment comparing the performance in apnea and baseline signals.

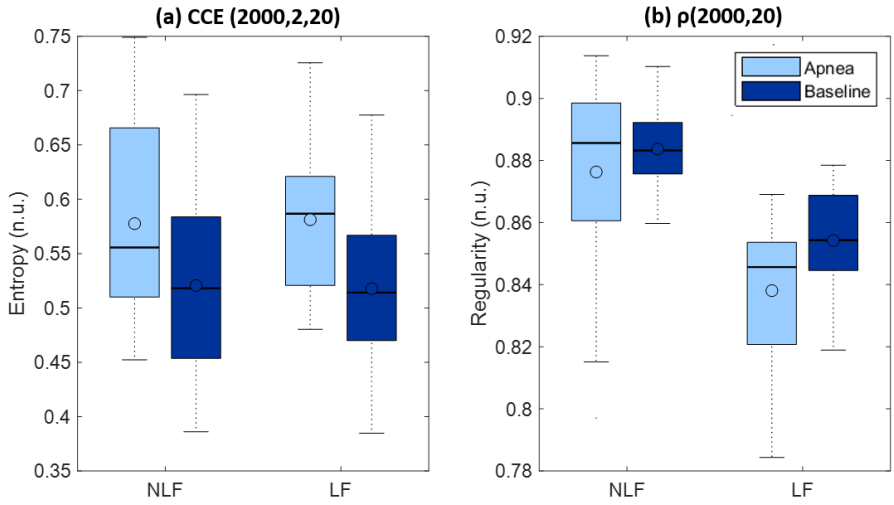

Figure 7-12 Boxplot showing the distribution of CCE(N,m,ε) and ρ(N,ε) when N=2000, m=2 and ε=20 for data preprocessed with linear filters (LF) and nonlinear filters (NLF). Median values are indicated with horizontal lines, and mean values with circles.

The results obtained for ApEn, SampEn and FuzzyEn are summarized in **Figure 7-13**. The three metrics provide higher entropy values for apnea recordings despite of the parameters used for their calculation, which is consistent with the previous findings in the analysis of the dataset filtered with linear algorithms. ApEn showed a stable behavior along the different signal lengths N, a monotonic decrease with m for apnea recordings but a maximum entropy for m=3 in baseline signals. Regarding the noise threshold r, ApEn decreases while r increases for r≥0.2, showing an absolute maximum at r=0.15 for both apnea and baseline recordings. SampEn results are also consistent with those presented in the linearly filtered dataset, showing an entropy decrease for larger embedding dimensions, stable results for different signal lengths and a monotonic decrease with r. Finally, FuzzyEn increases with higher m values, remains relatively stable with signal length and decreases with the noise threshold r. It should be noted that all FuzzyEn calculations in this section were performed with n=2, since all n values showed successful results in the previous analysis.

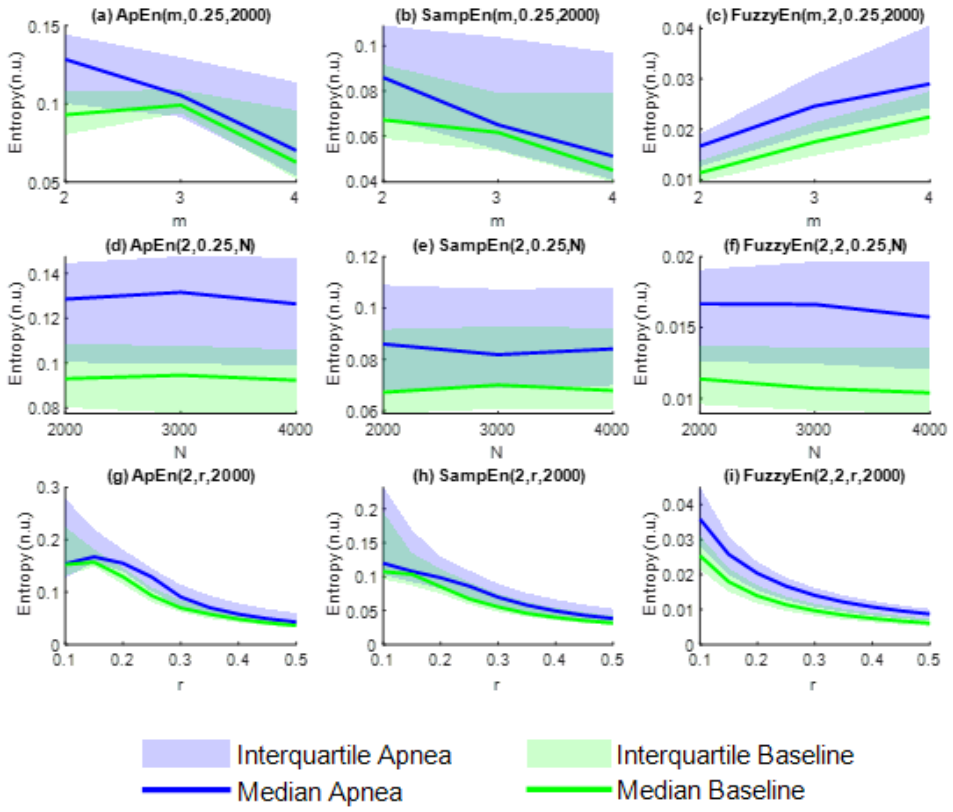

Figure 7-13 ApEn(m,r,N), SampEn(m,r,N) and FuzzyEn(m,n,r,N) values as a function of the embedding dimension (m) (a,b,c,), the signal length (N) (d,e,f) and the threshold r (g,h,i).

Even though the behavior of all three metrics is like the one presented in section 7.3.1, results for the hypothesis testing provide a different output (**Figure 7-14**). None of the parameter combinations for SampEn presents p-value<0.025, hence SampEn is not suitable for apnea detection when preprocessing is performed through the nonlinear algorithm. The statistical significance of ApEn is enhanced for lower m, higher N and higher r values. However, for FuzzyEn, the optimal significance is reached for m=3 (when r=0.25, n=2 and N=2000), showing better significance as N increases and r decreases.

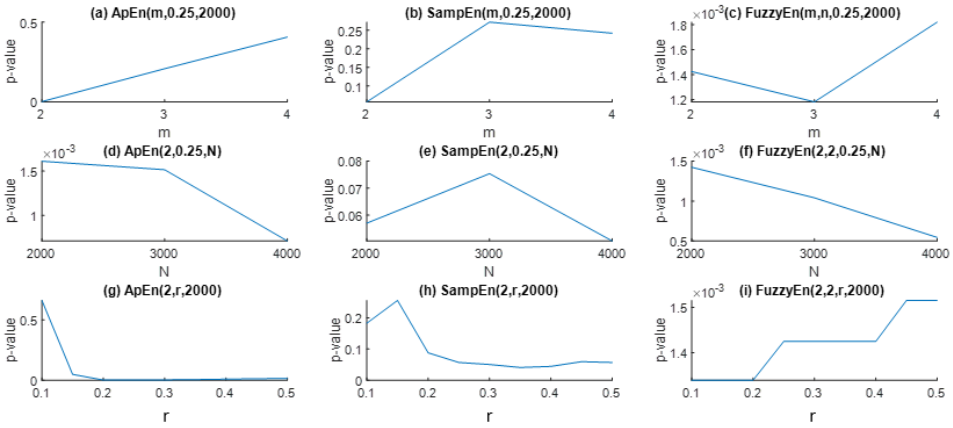

Figure 7-14 Analysis of the statistical significance (p-value) for apnea detection of ApEn(m,r,N), SampEn(m,r,N) and FuzzyEn(m,n,r,N) as a function of m, N and r.

A comparison between the results obtained using the linear and nonlinear filters for data preprocessing is provided in **Figure 7-15**. Using the nonlinear filter results in slightly smaller entropy values in all cases but with similar distributions for every group. Except for SampEn, the same parameters used with the linear filter preserve the ability to distinguish apnea from baseline signals, showing similar results despite of the technique used for data preprocessing.

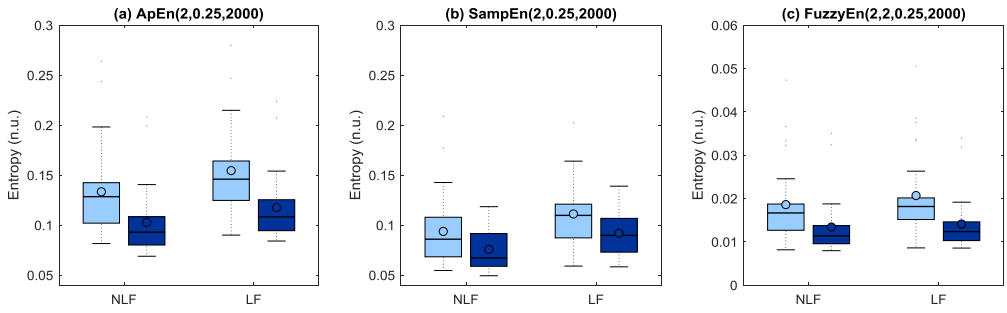

Figure 7-15 Boxplot of the distribution of ApEn(m,r,N), SampEn(m,r,N) and FuzzyEn(m,r,n,N) when m=2, r=0.25, n=2, and N=2000 and for data preprocessed with linear filters (LF) and nonlinear filters (NLF). Median values are indicated with horizontal lines, and mean values with circles.

All the entropy metrics herein tested providing statistically significant results for apnea detection are summarized in **Table 7-4**. SampEn and ρ are not included in the table since they did not provide significant results for any parameter combination. As in section 7.3.1, FuzzyEn outperformed all other entropy metrics, followed by ApEn, which provides very close AUC, acc and p-value. CCE and CCEmin position, although they provided statistically significant differences between apnea and baseline signals, showed higher p-value and lower AUC and acc. In order to illustrate those differences, **Figure 7-16** depicts the Receiver Operating Characteristic curves for those four entropy metrics and reassures the superiority of FuzzyEn and ApEn for apnea detection.

Table 7-4 Mean values and standard deviation of all entropy metrics when comparing apnea and baseline recordings using the nonlinear filter. The values of the set of parameters that best describe these entropies are included. Statistics as p-value, AUC and accuracy (acc) are provided to assess the ability of the entropy metrics to distinguish between apnea and baseline.

ENTROPY MEASURE	PARAMETERS	APNEA MEAN ± STD	BASELINE MEAN ± STD	P-VALUE	AUC	ACC (%)
ApEn	r=0.25 m=2 N=2000	0.133 ± 0.046	0.103 ± 0.036	0.0016	0.754	67.9
FuzzyEn	r=0.25 m=2 N=2000 n=2	0.019 ± 0.009	0.013 ± 0.007	0.0014	0.757	67. 9
CCE	ε=20 m=2 N=2000	0.732 ± 0.103	0.665 ± 0.089	0.0171	0.692	54.7
CCEmin position	ε =20 N=2000	9.10 ± 3.32	7.21 ± 1.86	0.0162	0.666	62.5

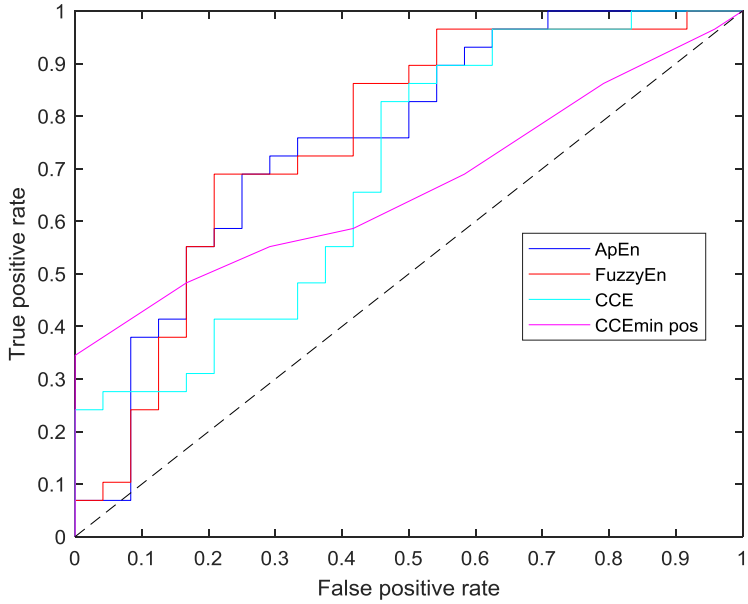

Figure 7-16 Receiver Operating Characteristic curves of all entropy metrics providing statistically significant differences between apnea and baseline recordings in the nonlinear filter dataset.

7.4 Results for general anesthesia

7.4.1 With linear filter

Results obtained for the apnea analysis regarding the parameters to be used for the calculation of each entropy metric were applied for the study of the entropy of REG signals during general anesthesia. Therefore, ApEn, SampEn, FuzzyEn, CCE and ρ were computed with m=2, r=0.25, N=2000, n=2 and ε=20, for the five states identified during general anesthesia, labeled as (1) Awake, (2) LOC, (3) Anes, (4) BSR and (5) ROC. The average values (mean ± standard deviation) of the entropy metrics in each group are summarized in **Table 7-5**, and their graphical representation is provided in **Figure 7-17**. ApEn, SampEn and FuzzyEn show similar trends, with a significant decrease of their values at LOC and similar values in all other states. It should also be noted that the range of values for each metric is wide, as assessed by the standard deviation values provided. The entropy CCE also

showed a decrease in LOC, followed by an increase during steady state anesthesia (Anes) where its maximum value takes place. The regularity index ρ represents the opposite concept and is consistent with the output of all other metrics since a maximum is observed at LOC.

Table 7-5 Average entropy values for each clinical state and each entropy metric.

	ApEn MEAN±STD	SampEn MEAN±STD	FuzzyEn MEAN±STD	CCE MEAN±STD	ρ MEAN±STD
Awake	0.083±0.022	0.077±0.021	0.008±0.003	0.388±0.066	0.859±0.021
LOC	0.071±0.024	0.065±0.024	0.006±0.003	0.361±0.056	0.870±0.020
Anes.	0.084±0.017	0.078±0.017	0.008±0.003	0.394±0.045	0.861±0.016
BSR	0.080±0.015	0.076±0.014	0.007±0.002	0.384±0.042	0.863±0.014
ROC	0.081±0.019	0.075±0.016	0.007±0.003	0.388±0.044	0.861±0.016

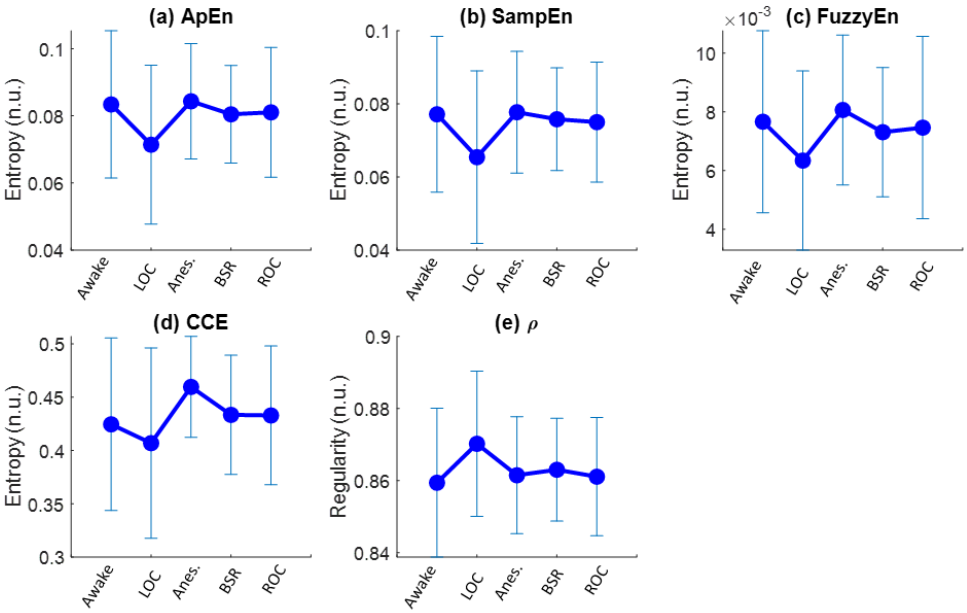

Figure 7-17 Mean and standard deviation values in each clinical state of the anesthetic process for the entropies (a) ApEn, (b) SampEn, (c) FuzzyEn, (d) CCE and (e) ρ.

Considering the ability of the entropy metrics to reflect differences between consecutive anesthesia stages, paired hypothesis tests were performed. Results from this analysis are summarized in **Table 7-6**. ApEn was the only entropy algorithm showing statistically significant differences

between Awake and LOC states (p-value=0.0074), while SampEn and CCE were the ones able to distinguish between LOC and steady state anesthesia. Transitions from anesthesia to BSR and from BSR to ROC were not detected by any of the metrics proposed.

Table 7-6 Statistical significance (p-value) of each entropy metric reflecting the ability to distinguish between consecutive anesthesia stages.

From To	AWAKE LOC	LOC ANES	ANES BSR	BSR ROC
ApEn	**0.0074**	0.0102	0.0250	0.3211
SampEn	0.0106	**0.0094**	0.0712	0.2294
FuzzyEn	0.0332	0.0134	0.0386	0.3489
CCE	0.3476	**0.0010**	0.7606	0.6911
ρ	0.0211	0.0329	0.5592	0.4768

7.4.2 With nonlinear filter

A second analysis on the General Anesthesia Dataset 1 was performed, preprocessing the recorded signals with the nonlinear filter. The N, m, r, n and ε parameters needed to compute the entropy metrics were the same ones applied to the linearly filtered signals for the sake of comparison. The trends followed by ApEn, SampEn, FuzzyEn, CCE and ρ are depicted in **Figure 7-18**. As observed when using the linear filter, a minimum is reached by all the entropy definitions at LOC, except for ρ, which presents the opposite behavior and therefore has an absolute maximum at this stage. The maximum entropy values are found for the steady state anesthesia stage (Anes), but the regularity index does not show a clear minimum in this position. All values present a high standard deviation as detected under the linear filter assumption. Descriptive statistics of all the entropy metrics (mean and standard deviation) are summarized in **Table 7-7**.

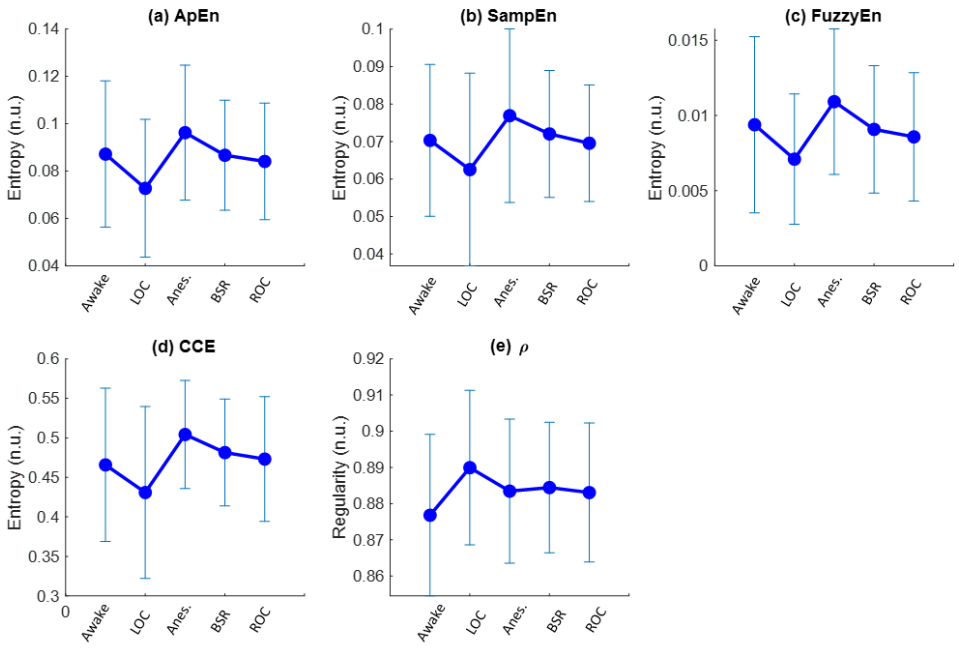

Figure 7-18 Mean values in each clinical state for (a) ApEn, (b) SampEn, (c) FuzzyEn, (d) CCE and (e) ρ.

Table 7-7 Average values (mean ± standard deviation) for all entropy metrics in each anesthetic states when preprocessing signals with the nonlinear filter.

	ApEn MEAN±STD	SampEn MEAN±STD	FuzzyEn MEAN±STD	CCE MEAN±STD	ρ MEAN±STD
Awake	0.087±0.031	0.070±0.020	0.009±0.006	0.343±0.065	0.877±0.022
LOC	0.073±0.029	0.063±0.026	0.007±0.004	0.308±0.061	0.890±0.021
Anes.	0.096±0.028	0.077±0.023	0.011±0.005	0.331±0.057	0.883±0.020
BSR	0.087±0.023	0.072±0.017	0.009±0.004	0.328±0.051	0.884±0.018
ROC	0.084±0.025	0.070±0.016	0.009±0.004	0.330±0.055	0.883±0.019

The statistical significance obtained from the hypothesis tests is presented in **Table 7-8**. Differences between the Awake state and LOC are detected by both ApEn and ρ, the latest providing the lowest p-value. The transition from LOC to steady state anesthesia (Anes) showed statistically significant differences for ApEn, FuzzyEn and CCE, with FuzzyEn showing the best results. As observed in the linearly filtered dataset, none of the metrics is able to assess differences between Anesthesia and BSR, nor between BSR and ROC.

Table 7-8 Statistical significance (p-value) of each entropy metric reflecting the ability to distinguish between consecutive anesthesia stages.

From To	AWAKE LOC	LOC ANES	ANES BSR	BSR ROC
ApEn	**0.0090**	**0.0022**	0.0350	0.0266
SampEn	0.0272	0.0105	0.1329	0.0898
FuzzyEn	0.0455	**0.0015**	0.0313	0.0264
CCE	0.1268	**0.0017**	0.2047	0.2261
ρ	**0.0069**	0.1908	0.1538	0.5517

The use of the nonlinear filter lead to a wider group of entropy metrics providing statistically significant results. However, with both filter options, only transitions involving LOC showed changes in signal entropy.

7.4.3 Confounding factors

The entropy metrics analyzed as possible indicators of different anesthetic states could be influenced by other factors other than the anesthetic state. In order to assess possible confounding factors, correlations of the entropy metrics with patient demographics and other clinical signs were computed.

The correlations between patient demographics as age, height, weight and body mass index (BMI) are illustrated in **Table 7-9**. In general, correlations are either low or very low and lack statistical significance. However, the states of Awake and Anes deserve a deeper look. In the Awake state, all entropy metrics show a moderate or high correlation with weight and BMI, all of them with statistical significance except for the regularity index when the nonlinear filter is used. This suggests that patients with higher weight or higher BMI present lower entropy in their REG signals for the Awake state. Those correlations turn into low or moderate during steady state Anes, most of them losing statistical significance. However, in the Anes state, age showed a moderate or high correlation with signal entropy for all metrics without exception, suggesting that the inherent entropy of the recordings is related to

patient demographics, reducing its complexity when age increases (negative correlation).

Table 7-9 Spearman correlation of each entropy metric with patient demographics for every clinical state analyzed, either using the linear filter (left side) or the nonlinear filter (right side). Cells are colored (see **Figure 7-19** for its meaning) as a function of the correlation value and statistical significance of the correlations is indicated in bold type.

	Linear Filter				Nonlinear Filter			
Awake	**Age**	**Height**	**Weight**	**BMI**	**Age**	**Height**	**Weight**	**BMI**
ApEn	-0.109	0.001	**-0.647**	**-0.633**	-0.060	-0.035	**-0.646**	**-0.598**
SampEn	-0.058	0.052	**-0.605**	**-0.623**	0.060	0.004	**-0.521**	**-0.522**
FuzzyEn	-0.094	-0.071	**-0.639**	**-0.580**	-0.037	-0.097	**-0.667**	**-0.586**
CCE	-0.162	0.002	**-0.465**	**-0.470**	0.003	-0.045	**-0.498**	**-0.478**
ρ	0.002	-0.115	**0.491**	**0.558**	0.016	-0.080	0.326	0.324
LOC								
ApEn	0.155	-0.054	-0.053	-0.011	0.066	-0.072	-0.087	-0.042
SampEn	0.178	-0.049	0.040	0.079	0.112	-0.103	-0.017	0.043
FuzzyEn	0.140	-0.090	-0.113	-0.052	0.064	-0.072	-0.154	-0.112
CCE	0.110	-0.024	0.081	0.076	0.158	-0.004	0.034	0.032
ρ	-0.251	-0.052	-0.176	-0.157	-0.178	-0.076	-0.244	-0.260
Anes								
ApEn	**-0.579**	0.153	-0.386	**-0.483**	**-0.615**	0.014	**-0.524**	**-0.564**
SampEn	**-0.547**	0.220	-0.233	-0.359	**-0.562**	0.164	-0.342	**-0.455**
FuzzyEn	**-0.553**	0.023	**-0.536**	**-0.581**	**-0.573**	-0.063	**-0.565**	**-0.567**
CCE	**-0.524**	0.065	-0.257	-0.332	**-0.597**	0.008	-0.293	-0.340
ρ	**0.405**	-0.265	0.058	0.179	**0.460**	-0.154	0.015	0.099
BSR								
ApEn	-0.312	0.335	-0.167	-0.388	-0.248	0.229	-0.276	-0.404
SampEn	-0.347	0.299	-0.185	-0.421	-0.228	0.219	-0.185	-0.329
FuzzyEn	-0.292	0.206	-0.260	-0.406	-0.186	0.159	-0.228	-0.293
CCE	-0.199	0.067	-0.133	-0.181	-0.244	0.036	-0.149	-0.205
ρ	0.171	-0.265	0.086	0.292	0.045	-0.285	0.042	0.195
ROC								
ApEn	-0.159	-0.049	-0.144	-0.150	-0.250	0.006	-0.193	-0.211
SampEn	-0.078	-0.064	-0.108	-0.111	-0.147	-0.007	-0.069	-0.078
FuzzyEn	-0.194	-0.056	-0.214	-0.218	-0.241	0.014	-0.202	-0.222
CCE	-0.047	-0.078	-0.031	-0.025	-0.133	-0.075	-0.071	-0.085
ρ	0.124	-0.037	0.078	0.112	0.150	-0.227	0.055	0.121

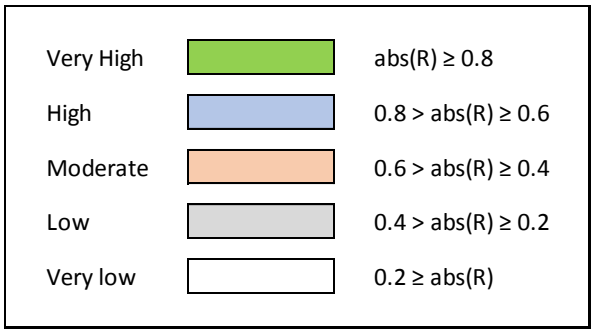

Figure 7-19 Spearman correlation values matching with colors and qualitative level.

Once the relationship between patient characteristics and the entropy in each state was assessed, a second analysis was performed (**Table 7-10**) based on the correlations of patient demographics and the differences in entropy between consecutive anesthesia states (obtained from **Table 7-7**). Consistently with observations in **Table 7-9**, BMI and weight showed a moderate to high correlation with entropy values in the transition between Awake and LOC states, with statistical significance, suggesting that the higher the weight the smaller the absolute entropy differences between both states. The next transition, to steady state anesthesia, showed a clear dependency with age, indicating that the higher the age the lower the increase in entropy between LOC and Anes. Those correlations however are only significant when using the nonlinear filter for signal preprocessing. The two other transitions provide very few correlations to be pointed out, the most relevant one being a significant correlation of -0.72 between age and the transition between Anes and BSR for the nonlinear filtered data. Moreover, patient height showed a moderate significant correlation with ApEn and SampEn when moving from BSR to ROC, which was found to be low for the nonlinear filter group.

Table 7-10 Spearman correlation between patient demographics and differences in entropy metrics for every transition between consecutive clinical states analyzed, either using the linear filter (left side) or the nonlinear filter (right side). Cells are colored (see **Figure 7-19** for its meaning) as a function of the correlation value and statistical significance of the correlations is indicated in bold type.

	Linear Filter				**Nonlinear Filter**			
Awake – LOC	**Age**	**Height**	**Weight**	**BMI**	**Age**	**Height**	**Weight**	**BMI**
ApEn	0.147	0.189	**0.599**	**0.563**	0.149	0.138	**0.534**	**0.511**
SampEn	0.132	0.101	**0.611**	**0.611**	0.087	0.079	**0.524**	**0.526**
FuzzyEn	0.183	0.208	**0.573**	**0.528**	0.197	0.165	**0.520**	**0.495**
CCE	0.174	-0.061	**0.448**	**0.437**	0.138	0.064	**0.511**	**0.487**
P	-0.002	-0.157	**-0.628**	**-0.622**	-0.007	-0.064	**-0.499**	**-0.526**
LOC – Anes								
ApEn	-0.540	0.041	-0.289	-0.357	**-0.485**	-0.014	-0.314	-0.346
SampEn	-0.496	0.098	-0.274	**-0.378**	**-0.442**	0.107	-0.265	**-0.374**
FuzzyEn	-0.528	0.003	-0.333	**-0.384**	**-0.504**	-0.058	-0.339	-0.349
CCE	-0.442	0.021	-0.242	-0.293	**-0.543**	-0.044	-0.262	-0.280
ρ	0.530	-0.044	0.200	0.269	**0.477**	-0.083	0.290	0.366
Anes-BSR								
ApEn	-0.014	-0.122	-0.235	-0.246	-0.061	-0.072	-0.240	-0.239
SampEn	0.011	-0.176	-0.109	-0.107	0.113	-0.242	-0.145	-0.046
FuzzyEn	-0.086	0.007	-0.161	-0.239	-0.055	0.111	-0.326	-0.421
CCE	0.073	-0.210	-0.249	-0.100	0.293	-0.386	-0.363	-0.171
ρ	0.075	0.032	0.057	0.143	**-0.720**	0.129	0.106	0.004
BSR-ROC								
ApEn	0.196	**-0.463**	-0.046	0.182	0.248	-0.263	0.010	0.153
SampEn	0.314	**-0.481**	-0.061	0.179	0.237	-0.361	0.058	0.254
FuzzyEn	0.202	-0.385	0.038	0.221	0.201	-0.212	0.133	0.228
CCE	0.029	-0.086	0.053	0.102	0.049	-0.129	-0.002	0.063
ρ	-0.040	0.416	0.015	-0.196	-0.044	0.164	-0.091	-0.199

Finally, the correlation between the entropy changes in consecutive states and other collected clinical data was assessed (**Table 7-11**), to better identify the factors influencing those changes in signal complexity. HR was the clinical sign with highest correlation with entropy changes, particularly in the LOC-

Anes transition. Furthermore, in this same transition, the correlation between CCE and CePropo was also moderate and significant. Even though all other correlations did not show statistical significance, MAP provides high and moderate correlations in the BSR to ROC transition that should be taken into account since the lack of statistical significance might be due to the limited number of patients that presented BSR states.

Table 7-11 Spearman correlation between clinical variables related to depth of anesthesia and hemodynamics and differences in entropy metrics for every transition between consecutive clinical states analyzed, either using the linear filter (left side) or the nonlinear filter (right side). Cells are colored (see **Figure 7-19** for its meaning) as a function of the correlation value and statistical significance of the correlations is indicated in bold type.

	Linear filter					Nonlinear Filter				
Awake - LOC	**HR**	**Propo**	**Remi**	**MAP**	**qCON**	**HR**	**Propo**	**Remi**	**MAP**	**qCON**
ApEn	0.137	-0.375	-0.105	-0.262	0.027	0.179	-0.294	-0.040	-0.292	0.057
SampEn	0.122	-0.364	-0.236	-0.309	0.104	0.062	-0.364	-0.240	-0.168	0.044
FuzzyEn	0.159	-0.331	-0.084	-0.347	0.032	0.182	-0.275	-0.023	-0.413	0.077
CCE	0.126	-0.181	0.206	-0.107	0.277	0.192	-0.151	0.047	-0.168	0.166
ρ	-0.005	0.273	0.242	0.298	0.131	-0.089	0.406	0.373	0.146	0.162
LOC - Anes										
ApEn	**0.459**	-0.269	-0.101	-0.019	0.135	**0.430**	-0.348	0.000	-0.053	0.176
SampEn	**0.556**	-0.290	-0.192	-0.061	0.228	**0.563**	-0.316	-0.158	0.023	0.358
FuzzyEn	**0.445**	-0.258	-0.081	0.036	0.105	0.408	-0.352	0.014	-0.098	0.153
CCE	**0.441**	**-0.420**	-0.013	-0.070	0.269	**0.421**	-0.403	0.084	-0.146	0.232
ρ	-0.348	0.331	0.178	-0.070	-0.046	-0.132	0.176	0.191	-0.245	-0.124
Anesth-BSR										
ApEn	0.139	0.218	0.114	0.114	0.071	0.449	-0.157	0.164	0.037	-0.248
SampEn	0.052	0.229	-0.118	-0.046	0.000	0.349	-0.136	-0.086	-0.324	-0.488
FuzzyEn	0.366	0.057	0.132	0.169	0.016	0.247	-0.107	0.307	0.260	-0.207
CCE	0.107	-0.146	-0.029	-0.201	-0.209	0.195	-0.014	-0.132	-0.219	-0.290
ρ	-0.109	-0.414	0.021	-0.228	-0.145	-0.415	-0.307	0.343	0.447	0.163
BSR-ROC										
ApEn	0.351	-0.174	0.153	-0.517	0.184	0.262	-0.426	0.285	-0.650	0.047
SampEn	0.395	-0.222	0.200	-0.600	0.173	0.191	-0.224	0.342	-0.517	0.167
FuzzyEn	0.312	-0.229	0.232	-0.533	0.234	0.240	-0.396	0.291	-0.550	0.124
CCE	-0.006	0.014	-0.063	0.383	0.101	0.062	-0.136	0.082	0.033	0.124
ρ	-0.114	-0.108	-0.222	0.467	0.022	-0.249	-0.065	-0.216	0.367	-0.168

7.5 Discussion of the results obtained in apnea detection

All entropy metrics proposed, except for SE, provided evidence regarding the increased irregularity in apnea signals when compared to baseline recordings. However, those results showed to be dependent on the choice of the parameters needed for each entropy metric calculation and the selection of the filter used for preprocessing. For instance, CCE values increased with an increasing number of quantization intervals ε, and decreased with increasing m, while remained stable with increasing sequence length N for both filter options. The regularity index (ρ) decreased with the number of quantization levels ε, in accordance with the evolution of CCE since ρ reflects regularity instead of entropy. However, ρ increased with increasing signal length N indicating that a fewer number of new patterns were detected when signal length was extended. Those results are also coincident for both filters and are consistent with those published by Porta et al.[244], since REG waves show a quasi-periodic pattern. However, it should be noted that when using REG signals, the optimal number of quantization levels providing a better differentiation between apnea and baseline recordings, ε=20, is higher than the one proposed by Porta in his work, ε=6.

Considering the performances of CCE and the regularity index ρ, the latter provided the lowest p-value when tested for differences between apnea and baseline recordings with linearly filtered data. However, this parameter showed inconsistencies when the nonlinear algorithm for noise removal was used, identifying baseline recordings as more regular than apneas depending on the pair of N and ε values used. CCE showed to be less sensitive to the selected filter, providing statistically significant results for both filter options, using the same signal length but a different number of quantization levels. (ε=20 for the linear filter, ε=30 for the nonlinear).

Even though SE and CCE are both derived from the original definition of the Shannon Entropy, CCE provides significant results while SE does not. This different performance of SE and CCE exists because SE reflects the distribution of the patterns in a given sequence while CCE assesses differences between consecutive patterns. This phenomenon has been analyzed previously in other publications [251], referring to SE as an entropy measure and conditional entropy as an entropy rate.

Regarding the results for ApEn, SampEn and FuzzyEn using the linear filter approach, they all decrease with increasing r threshold. Nonetheless, their behavior with increasing time series length N and embedding dimension m differs. **Figure 7-4** (a) shows increasing ApEn values for longer signals in apneas while effects of signal length in baseline recordings are negligible. The same trend can be observed for SampEn in **Figure 7-4** (b), while FuzzyEn (**Figure 7-4** (c)) shows stable entropy values for all signal lengths. SampEn was reported to be independent of signal length while ApEn is known to provide lower entropy estimates for short recordings [230]. Considering that the effect of signal length is only present in apneas, results could be interpreted as an increasing complexity in REG signals proportional to apnea duration, rather than just a weakness of the entropy estimators.

The influence of the nonlinear filtering algorithm is assessed in **Figure 7-13**. The dependence of those entropy metrics with signal length is reduced and does not show any clear trend, while the variation as a function of the threshold r is consistent with the one observed with the linear filter except for ApEn. A maximum of ApEn is identified at r=0.15, followed by a monotonic decrease of entropy as r grows. This is a consequence of the different noise patterns embedded in the REG signals after the preprocessing stage.

One of the main differences between ApEn, SampEn and FuzzyEn is their evolution as a function of the embedding dimension m. SampEn (**Figure 7-4** (b) and **Figure 7-13** (b)) provides lower entropies for increasing m, while FuzzyEn (**Figure 7-4** (c) and **Figure 7-13** (c)) shows the opposite behavior and ApEn does not show a consistent behavior, since the highest entropy is obtained for m=3, followed by m=2 and m=4 (**Figure 7-4** (a) and **Figure 7-13** (a)). Those results are common for both linearly and nonlinearly filtered data. This inconsistency in ApEn might be due to the bias inherent in this estimation. Moreover, the use of the Heaviside function might be influencing the results in such a way that softening the similarity boundary with fuzzy membership functions provides the most consistent results in terms of entropy rates as a function of the embedding dimension for a fixed r value.

No other inconsistencies were detected in ApEn, SampEn or FuzzyEn. Some authors have reported a flip-flop effect in entropy estimations [263] [264]. They observed that, given two groups of signals to be compared, some r values resulted in higher entropy for signals in one group, while other r

selections provided the opposite results. No flip-flop episodes were detected in this Apnea-Baseline Dataset. Moreover, considering the definition of Aktaruzzaman [265] of practical consistency, one can conclude that the three metrics were consistent since always identified higher entropies in the apnea group for a broad range of input parameters. However, looking at the evolution of the standard deviation of each entropy (**Figure 7-7**), FuzzyEn provides the lowest values, followed by SampEn. For ApEn, the Entropy standard deviation is not decreasing monotonically, since it shows a plateau around r=0.3. This suggests a higher variability of ApEn calculations when compared to the other estimators.

Among ApEn, SampEn and FuzzyEn, ApEn provides the highest entropy values (see **Table 7-3** for linear filter results and **Table 7-4** for nonlinear filter) and FuzzyEn the lowest, but they both provide significantly different results for apnea and baseline recordings, for one or more sets of N, m, r and n parameters. Optimal values for apnea detection were common to ApEn, SampEn and FuzzyEn – using n=2 for fuzzy membership functions- even though FuzzyEn showed to be less sensitive to parameter selection, providing significant results for all the parameter combinations tested. Nonetheless, it should also be noted that SampEn did not provide significant results in the analysis of REG signals nonlinearly filtered, while ApEn and FuzzyEn succeeded in both scenarios.

Recommended values for r, m and N are slightly different from the ones reported by other authors with different types of signals. The embedding dimension, m=2, is coincident with most of the analysis published, but different from the one provided for plethysmograms [248], m=7. However, due to the limited length of the recording, using embedding dimensions m higher than 3 or 4 would require the use of very large r values, loosing information of the patterns in the time series. Values for the r threshold optimizing apnea detection are higher than the ones reported in other applications, usually ranging from 0.15 to 0.2 [258], [259]. Regarding the value of n in the FuzzyEn algorithm, recommendations of using the smallest possible value are consistent with the results herein presented, where n=2 provided the better statistical significance for apnea detection with the linear filter option and was maintained for the analysis of the effects of using the nonlinear filter.

For the first analysis, based on linear filters, FuzzyEn provided the best statistical significance and AUC for apnea detection in REG signals, followed by ApEn, CCE and SampEn, all of them identifying higher complexity in

apnea when compared to baseline signals (**Table 7-3**). When REG signals were preprocessed by means of the nonlinear algorithm, FuzzyEn remained as the best choice for apnea detection, followed again by ApEn and CCE. SampEn did not show the ability to distinguish apnea and baseline signals, while the regularity index ρ did. Previous publications have also compared the performance of different entropy metrics. For instance, Chen et al. [213] compared ApEn, SampEn and FuzzyEn in their ability to characterize surface EMG signals, where FuzzyEn outperformed the other metrics, both in terms of classification and by providing a lower standard deviation of the entropy metrics, as it is also observed in the present study. Xie et al. [261] also compared the same three entropy definitions with the objective of detecting muscular fatigue in EMG signals. FuzzyEn provided the best results while ApEn failed to detect muscular fatigue. Furthermore, while analyzing EEG in patients with Alzheimer's disease compared to healthy subjects, FuzzyEn was also the best predictor when compared to ApEn and SampEn [236], and ApEn was again considered the poorest estimator. Even though SampEn is known to outperform ApEn [230], in this study ApEn provided a better discrimination between apnea and baseline signals. Analogously, Cuesta-Frau et al. [266] reached the same conclusion when studying body temperature records of critical patients as a predictor of survival.

All time series processed in this study were sampled as 250 Hz. It is well known that sampling frequency affects the selection of the optimal parameters for entropy calculation [256], as well as signal to noise ratio [235]. However, due to the artefacts present in the recording because of movements, reducing the sampling frequency would have limited the length of the time series and therefore the range of dimensions m tested for each entropy definition. Therefore, sampling frequency was not included as an input variable in the estimation of entropy in the recorded dataset.

The use of entropy metrics applied to physiological signals often aims at detecting a disease, as for example heart failure [225] or sick newborns [258] by means of the analysis of HRV signals. In those cases, lower entropies are associated to the disease condition. No previous studies on the regularity of REG signals have been published to the extent of the knowledge of the author. However, Pham et al. [248] analyzed plethysmograms, which share many properties with REG signals, and used the information for diagnosis purposes, aiming at detecting mental disorders. In the present study, participants were healthy volunteers performing a simple respiratory challenge to provoke CBF

changes. Therefore, rather than detecting a disease, entropy metrics were used to detect alterations in CBF reflected in REG waves. The results suggest that during apneas, in order to preserve a fixed amount of oxygen supplied to the brain, compensation mechanisms are activated that modify the REG pulse waves adding complexity to the signal. During baseline, oxygen and blood supply to the brain do not suffer alterations and REG signals are therefore more regular.

Further studies are needed to confirm those findings, but results suggest that entropy analysis is suitable for CBF changes detection in REG signals produced by breath holding. Moreover, this analysis outperforms the classical approach used for REG signals, based in geometric features detection in the pulse waves, which provided a very limited performance in apnea detection.

7.6 Discussion of the results obtained in anesthesia

The analysis of the General Anesthesia Dataset1 was focused on the ability of the entropy metrics proposed to distinguish among different anesthesia stages. The parameters used to compute entropies were limited to those identified in the Apnea-Baseline Dataset. No previous studies have been found regarding the analysis of regularity of CBF during anesthesia. Therefore, results should be interpreted with caution since they cannot be compared to existing literature.

All entropy metrics showed the same pattern, providing similar results in all the anesthesia stages proposed except for LOC, where entropy was lower (ApEn, SampEn, FuzzyEn and CCE) and the regularity index ρ showed its highest value. However, only a few set of metrics presented significative differences between the state of LOC and the preceding and subsequent states. When using the linear filter in the preprocessing of the dataset, ApEn was the only metric providing statistically significant differences between the awake and LOC states, while SampEn and CCE showed differences between LOC and anesthesia with CCE presenting the lowest p-value. In contrast, when using the nonlinear filter, both ApEn and ρ provided significant differences between Awake and LOC, while LOC and anesthesia were distinguished by ApEn, FuzzyEn and CCE. Among those, FuzzyEn showed the lowest p-value.

Those results allow to conclude that there is a dependency of the results on the type of filter used in the preprocessing stage, but it should be

highlighted that ApEn preserves its ability to distinguish between Awake and LOC states despite the filter chosen as well as CCE maintains its capabilities to detect changes between LOC and Anes.

All statistically significant differences of entropy metrics between anesthesia states involve the state of LOC. Once patients received the anesthetic dosages and LOC was assessed by the loss of eyelash reflex, patients were pre-oxygenated in preparation for the intubation. This oxygenation period is therefore associated with a lower entropy (and higher regularity) across all metrics proposed. Those results are consistent with the ones obtained for the Apnea-Baseline Dataset. Apneas were characterized by a higher entropy due to the lack of oxygen producing an increase in cerebral blood flow, translated into a higher complexity in REG signals. In this case, the increase of oxygen in the inspired air would provoke a decrease in cerebral blood flow, enhancing its regularity. After intubation, once mechanical ventilation started, patients recovered the same average entropy rates detected in the Awake state. This suggests that entropy metrics can track REG alterations due to differences in oxygen supply but remain unchanged under the effects of anesthetics, for the clinical states analyzed

Furthermore, patient characteristics have demonstrated to play an important role in the complexity of REG signals during anesthesia. Entropy values in the Awake state are reduced in patients with higher weight or body mass index (BMI). This is consistent for instance with the reduction detected in the HRV for obese patients[267]. In the transition from Awake to LOC, weight and BMI also show a significant correlation with the change in entropy rate, indicating that higher weight is associated to a higher difference in entropy between both anesthesia stages. In contrast, during the process in which patients are intubated and put under steady-state anesthesia, both weight and BMI have a lower correlation with the entropy rates, while age appears to be more relevant: older patients present smaller changes in REG entropy.

Besides the relationship between patient characteristics and entropy metrics, in this chapter entropy metrics and their correlations with other clinical variables collected during surgery were also analyzed. Among HR, CePropo, CeRemi, MAP and qCON values, the only variable providing significative correlations with entropy rates was HR. In the transition between LOC and steady state Anesthesia, ApEn, SampEn, FuzzyEn and CCE

showed a positive correlation with the differences in entropy of the linearly filtered signals. The higher the change in HR, the higher the change in entropy, suggesting once again that entropy metrics of REG signals are closely related to hemodynamic changes. An exception would be CCE, that is also moderately correlated to the propofol concentration in this transition, however this correlation is not significant anymore when the nonlinear filter is used. In contrast, ApEn, SampEn and CCE remain correlated with HR despite of the filter choice.

Entropy algorithms applied to REG signals during anesthesia have proved to be useful to track hemodynamic changes during the procedure and influenced by patient demographics. However, due to the lack of significant differences between Awake and Anes states, results suggest that their ability to assess anesthetics stages is limited to the oxygenation and intubation period.

7.7 Conclusions

The findings presented in this study suggest that FuzzyEn is the entropy metric providing the best ability to distinguish between apnea and baseline in REG signals among the set of entropy metrics proposed, followed by ApEn and CCE. Nonetheless, a careful selection of the input parameters needed to compute those entropy metrics should be performed in advance, since values recommended for other applications are not suitable for REG signals. Moreover, the filter strategy used for preprocessing influences the obtained results, with ApEn being the metric showing less dependence on the filter selected.

Entropy metrics also showed statistically significant differences when applied to REG signals during anesthesia. However, those differences were more related to hemodynamic changes rather than to anesthetic states and were correlated to the weight, BMI and age of the patients. Overall, the results presented in this chapter suggest that REG signals seem to be carrying CBF information that can be assessed by means of complexity analysis.

.

Chapter 8

Classification of REG signals during general anesthesia

Abstract

REG signals have shown to present differences between different anesthetic states. This chapter aims at combining the information extracted through time domain analysis and Poincaré plot descriptors to classify REG signals as belonging to awake or anesthetized patients.

8.1 Introduction

The study of REG waves presented in Chapters 5, 6 and 7 suggests that they contain information related to cerebral hemodynamics, as for example CBF, both during respiratory challenges and general anesthesia procedures. This chapter aims at using the extracted REG features previously analyzed to predict the anesthetic state of a patient, to be used for general anesthesia monitoring.

The elevated computational effort needed to execute some of the presented algorithms makes it unfeasible to include them in real time monitors. For instance, the nonlinear filter presents high execution times, mainly in noisy data, which would compromise CBF monitoring in real time. Moreover, even though entropy metrics provided interesting results in the post-hoc analysis of Chapter 7, their calculations are often cumbersome. For those reasons, all REG signals used in this chapter were preprocessed with the linear filter, and the set of parameters to be used as inputs for depth of anesthesia prediction were limited to those obtained from geometrical features extraction and Poincaré plot analysis.

The combination of time domain and complexity features has often been used to build classifiers for diagnostic purposes. Begg et al. [268] developed an automatic gait classification algorithm combining linear features extracted from gait recordings with Poincaré plot descriptors. Both sets of parameters were used as inputs for a classifier aiming at differentiating gait signals recorded from young or elderly patients.

Several authors have focused on the combination of linear and nonlinear parameters in HRV analysis. For instance, Melillo et al. [269] worked on the identification of possible fallers among hypertensive subjects. For that purpose, they used standard HRV processing together with Poincaré plot extracted features. The combination of geometric, nonlinear and frequency domain parameters lead to a better accuracy when compared to previous attempts to classify fallers among hypertensive subjects. Moreover, Nardelli et al. [270] also combined frequency domain, time domain and nonlinear HRV features in an emotions recognition system while Isler and colleagues [271] used a similar approach to detect congestive heart failure.

In this chapter, the optimal classifier predicting the anesthetic state of patients under general anesthesia by means of REG extracted features was developed. After signals preprocessing and the calculation of the descriptors, a feature selection method was used to identify the input parameters

optimizing the classifier. Subsequently, several classifiers were tested and their performance compared to finally select the optimal classification algorithm for depth of anesthesia prediction.

8.2 Methods

8.2.1 Features selection

One of the challenges in the process of building a classifier is the feature selection step. Several options are available to achieve it, focusing on reducing the computational time while exploring the interactions between the set of features under analysis.

The features selection algorithms are typically classified in filter, wrapper and embedded methods [272]. The former methods are characterized by using an evaluation metric independent of the type of classifier to be applied and are therefore compatible with all classification algorithms. The wrapper methods are iterative and complex methods, requiring a modeling algorithm, that select a set of input features under a leave one out strategy. Finally, the embedded methods are part of the classifier itself and are therefore algorithm dependent.

For this application, the use of a filter method applied individually to all features under test was chosen: the Relief algorithm [273]. This method has the ability to provide a weighting score for each feature while taking into account feature dependencies, with relatively low computational cost and compatible to any classifier to be used subsequently. It was originally developed for binary classification and some extensions were published afterwards to deal with multiclass problems as well. However, in this work, the basic Relief algorithm was used since the number of classess is limited to two: the awake and anesthetized states.

The Relief algorithm uses as input a set of attribute vectors (input candidates) associated to their classification. It is composed by k iterations, selected by the user. In each of those iterations, an array of attributes of an instance is randomly chosen (A), and two other instances are identified: (a) the closest one belonging to the same class (near hit, NH) and (b) the closest

belonging to the other class (near miss, NM). The weight of each attribute (W_a) is updated after every iteration following the equation [272]:

$$W_a = W_a - (A - NH)^2 + (A - NM)^2 \quad (8.1)$$

Therefore, the weight of a given input is decreased when the distance to the nearest neighbor of the same class is longer than the distance to the nearest neighbor in the alternative class. Once the k iterations have been performed, all weights are divided by the number of iterations used.

In the initial algorithm provided by Kira and Rendell [273], the selection of parameters after the application of Relief was done by chosing all the parameters with weights over a certain threshold. However, other applications have suggested to choose a subset of the most relevant parameters to optimize the classification and limit the computational load of the classifier.

8.2.2 Classification algorithms

The performance of three different classifiers was compared in this study: logistic regression, naïve Bayes and classification trees. While logistic regression aims at estimating the probability of belonging to a defined class, based on the values of one or more predictors, naïve Bayes maximizes the a posteriori probability by applying the Bayes' theorem, assuming independence among predictors [274]. The logistic regression classifier used in this work is based on a binomial distribution while naïve Bayes was implemented using a Gaussian kernel.

Both classifiers have been often used in medical applications. Chhatwal et al. [275] developed a risk estimation model based in a logistic regression classifier that allowed to identify the malignancy of breast cancer. Moreover, this classifier was used by Combes et al. [276] to predict the length of stay of pediatric patients in the emergency departments with successful results.

Naïve Bayes showed a similar accuracy compared to logistic regression in the study published by Wang et al. [277], in which both classifiers were used to predict brain metastasis from lung cancer. In another application, Morales at al. [278] developed a naïve Bayes classifier to predict dimentia in patients diagnosed of Parkinson's disease, concluding that the most relevant factors

for dementia were cerebral white matter, volume of the lateral ventricle and volume of the hippocampus.

Decision trees have also been used in clinical environments and are based on the classification and regression trees (CART) algorithm [279]. In those algorithms a prediction tree model is built in which each internal node evaluates conditions on predictors, branches represent the output of those evaluations and leaves indicate the class to be assigned to a set of attribute values.

Decision trees were applied by Sims et al. [280] for cesarean delivery prediction due to the inexistence of a single factor indicating this risk. Comparable performance was obtained for decision trees and logistic regression algorithms, with the former needing a smaller number of inputs to reach the same performance.

Tsien et al. also compared logistic regression and decision trees classifiers for the diagnosis of miocardial infarction [281]. Even though both provided similar outcomes in terms of AUC of the Receiver Operating Characteristic curve, outperforming classical methods used for infarction prediction, the authors considered that a decision tree was the best choice since it is easier to follow in rutine clinical practice.

In this chapter, logistic regression, naïve Bayes and classification trees will be tested and compared for their ability to classify REG signals as belonging to an awake or anesthetized patient, using linear and nonlinear extracted features as inputs.

8.2.3 Experimental dataset

The use of REG features as inputs for a classifier to predict the anesthetic state of patients under propofol general anesthesia was developed on the General Anesthesia Dataset 2. This dataset is composed by data of 90 patients undergoing elective surgeries in Hospital CLÍNIC de Barcelona. Patients were continously monitored and REG signals from a few minutes before anesthesia induction until patient extubation were collected. Other clinical variables were collected simultaneously as described in Chapter 3, the most relevant one for this study being the depth of anesthesia index qCON.

8.2.4 Data processing

An automatic artefact rejection algorithm was applied to the recorded signals, in order to avoid processing noisy data resulting from patient movements or the use of other devices, mainly the surgical knife. Subsequently, time series were processed in moving time windows of 2000 samples length with 1750 samples overlap, thus providing new results every second.

REG data were linearly filtered, and geometric features and Poincaré plot descriptors listed in **Table 8-1** were calculated as previously detailed in Chapter 5 and Chapter 6, respectively. Since REG signals only provide relative values, all data were normalized to cancel out the interindividual variabilities.

Table 8-1 Geometric and Poincaré parameters extracted from REG signals to be used as inputs for the classifier.

GEOMETRIC FEATURES	POINCARÉ PLOT DESCRIPTORS
Range	SD1
Δtmax	SD2
Δtmin	SDratio
Δtmin-max	SDarea
A	CCM
AreaSyst	R
Δmax	
Δrange	
CBVrel	
CBFest	

Before feature selection, an equalization of the input observations was performed to train and validate the classifiers with a similar number of events belonging to the awake and anesthetized classes. Since awake periods are siginificantly shorter, all awake events were selected for the classifier development and an equivalent number of events under anesthesia were randomly selected for each patient. Subjects for which only one class was identified or for which a class was represented by less than 10 observations were rejected.

The Relief algorithm was applied to the database and all inputs were storted from highest to lowest weights. The three developed classifiers were validated using a leave-one-out strategy, using a growing number of inputs form the sorted list. The metrics used to assess the performance of each classifier and compare the results among them were sensitivity, specificity and accuracy.

Additionally, a second training and crossvalidation process was performed including the demographic data of the patients (age, weight and height), to analyze their role, if relevant, in the classifier. Results from both classifiers were then compared in terms of accuracy and number of inputs needed to reach the same accuracy level.

8.3 Classification results

The study was finally performed on data from 59 subjects, resulting in 8996 datapoints, from which 4498 were recorded during the awake periods and another 4498 under general anesthesia.

The Relief algorithm was applied to the full dataset with 5, 10, 15, 20 and 25 nearest neighbors to assess the stability of the weights provided by the algorithm as a function of the number of neighbors chosen. The order of the first set of 10 parameters remained unchanged for 15, 20 and 25 neighbors and therefore the Relief output with 25 neighbors was used as the reference to build the classifiers. The weights obtained for each feature are illustrated in **Figure 8-1**, where each parameter is color coded depending on the linear or nonlinear origin of each feature.

The first two parameters with higher weights were extracted from the geometric analysis of REG waves, with CCM being the most relevant input within the Poincaré descriptors set. Differences between consecutive minimums (Δtmin) and maximums (Δtmax) presented the highest weights, while the Range of the impedance signal appeared in the last position.

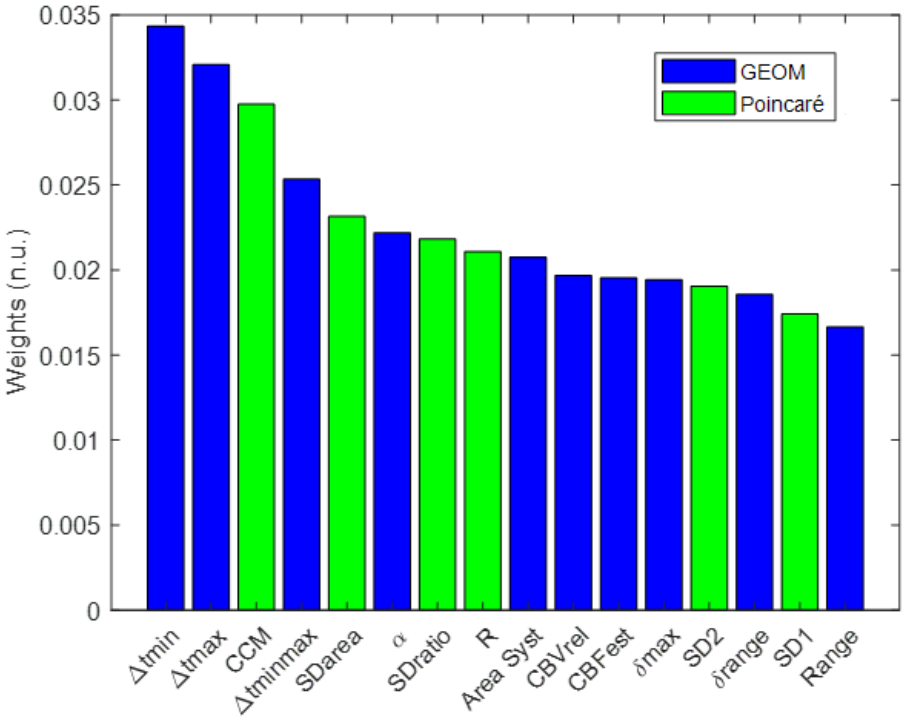

Figure 8-1 Weights calculated with the Relief algorithm for the geometric features (GEOM) and the Poincaré plot descriptors (Poincaré).

A set of classifiers were trained using the Relief results to select the inputs. For each type of algorithm (logistic regression, naïve Bayes or classification tree), 16 different classifiers were built, with increasing number of input variables, from 1 up to the total number of available features, 16.

The sensitivity, specificity and accuracy of all the classifiers measured across a leave-one-subject-out cross-validation strategy are shown in **Figure 8-2.** The classification tree presents the lowest sensitivity, followed by the naïve Bayes and the logistic regression. In terms of specificity, naïve Bayes presents a stable trend, with values reaching almost 90%, followed by the classification tree and the logistic regression classifiers, which provide higher sensitivity when the number of inputs is increased. Overall, the accuracy of the logistic regression and the naïve Bayes classifiers is comparable, with values between 65% and 75% for all inputs, while the classification tree provides values on the 55 to 65% range.

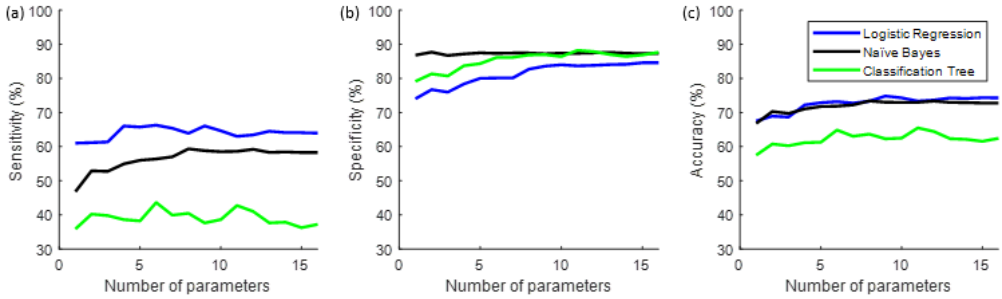

Figure 8-2 Sensitivity (a), specificity (b) and accuracy (c) of the logistic regression, naïve Bayes and classification tree, as a function of the number of parameters used as inputs in the classifier, following the order provided by the Relief algorithm.

All accuracies presented an increasing trend as the number of inputs increased. Analyzing the values obtained for accuracies across all the classifiers, a threshold of 70% could be considered as the best possible performance. Using this criterion, **Table 8-2** summarizes the number of input parameters needed for each classifier to achieve a 70% of accuracy. The best results were obtained with the naïve Bayes algorithm, which needed only 2 parameters to present an accuracy of 70.31%. None of the input parameters combinations provided accuracies higher than 70% for the classification tree.

Table 8-2 Number of input parameters needed for each classifier to reach at least an accuracy of 70%.

CLASSIFIER	NUMBER OF INPUTS	ACCURACY
Logistic Regression	4	72.22%
Naïve Bayes	2	70.31%
Classification tree	-	-

The feature selection process was reformulated to include the main demographic data of the patients, provided that in previous chapters the extracted features showed significant correlations with patient characteristics. Age, height and weight were added to the list of input variables and the results obtained are depicted in **Figure 8-3**. The Relief algorithm associated the highest weights to demographic variables, followed by geometric features and

Poincaré plot descriptors. The CCM parameter was again the most relevant Poincaré descriptor while Range was identified as the less relevant feature.

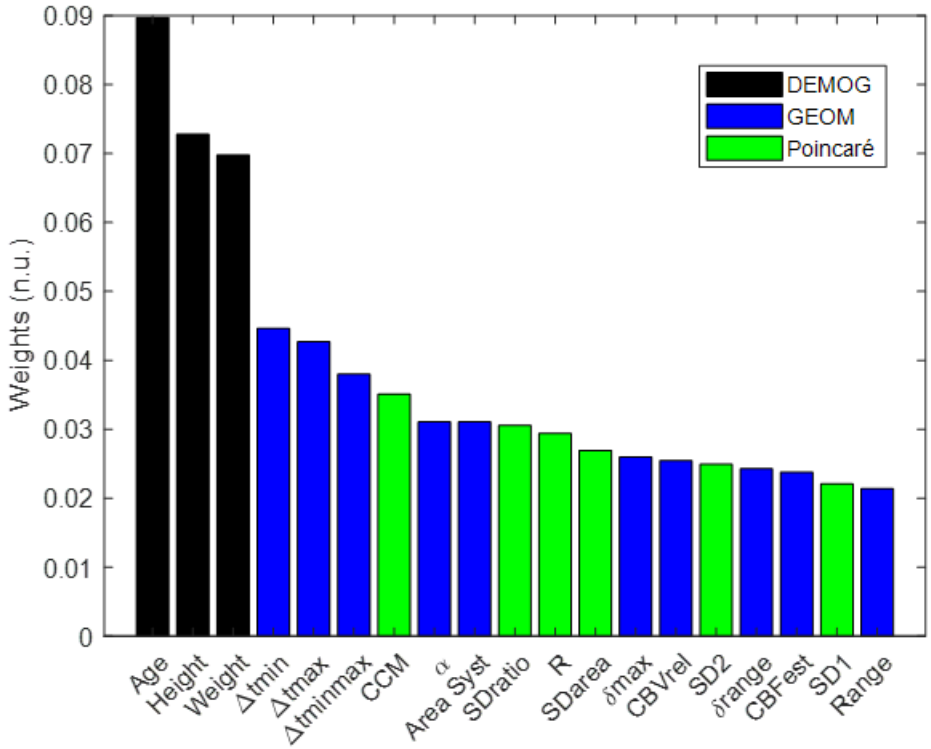

Figure 8-3 Weights calculated with the Relief algorithm for the demographic variables (DEMOG), the geometric features (GEOM) and the Poincaré plot descriptors (Poincaré).

Even though demographic data on their own were not considered likely to provide a successful classifier, the same steps previously presented were taken, building in this case 19 classifiers of each type with increasing number of inputs. The performance of the classifiers is presented in **Figure 8-4**. The sensitivity, specificity and accuracy values for 1 to 3 inputs clearly showed that the demographic features were considered relevant by the feature extraction algorithm due to the interindividual differences in REG signals, but as expected, they were not capable of providing an accuracy better than 50%.

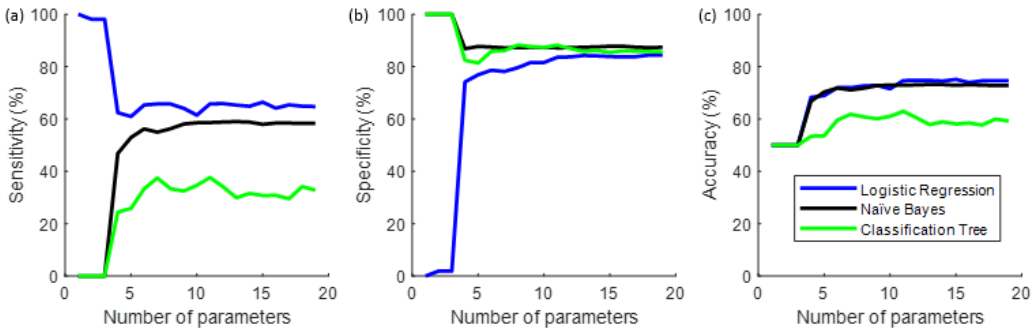

Figure 8-4 Sensitivity (a), specificity (b) and accuracy (c) of the logistic regression, naïve Bayes and classification tree, as a function of the number of parameters used as inputs in the classifier, following the order provided by the Relief algorithm when demographic variables were included.

Regarding the use of higher number of parameters, the trends for all classifiers were similar to those previously presented in **Figure 8-2**, providing similar values for accuracies, and with naïve Bayes and logistic regression providing similar accuracies.

Considering a threshold of 70% in accuracy, the best option was again the naïve Bayes algorithm, which needed in this case 5 inputs to reach an accuracy of 70.31%. The second best classifier was the one based in logistic regression, needing just one more input, while the classification tree did not achieve a 70% of accuracy with any set of inputs (**Table 8-3**).

Table 8-3 Number of input parameters needed for each classifier to reach at least an accuracy of 70% when including the demographic variables as inputs of the classifier.

CLASSIFIER	NUMBER OF INPUTS	ACCURACY
Logistic Regression	6	71.98%
Naïve Bayes	5	70.31%
Classification tree	-	-

8.4 Discussion of the results

In this study, the naïve Bayes algorithm proved to be the best option among the classifiers under test to identify REG signals recorded in awake and anesthetized states. Nonetheless, the accuracies presented by naïve Bayes, and logistic regression were very similar to each other, the main difference being the number of input parameters needed to obtain a similar accuracy. Naïve Bayes needed only 2 inputs to reach a 70% accuracy, compared to the 4 needed by the logistic regression. The classification tree did not reach the 70% threshold.

In previous studies in which different classifiers were compared, similar accuracies were also found among the algorithms under test[280], often chosing as the final solution the most comprehensive one for healthcare professionals [281]. In this case, the classifier is not designed to be used as a diagnostic tool and therefore this concept is not applicable. Moreover, the classification tree provided the lowest accuracy while values for the other two classifiers were comparable.

The input variables providing the best naïve Bayes classifier were: Δtmin and Δtmax. They are both related to temporal features extracted from REG signals and more specifically to heart rate. The relationship between heart rate and depth of anesthesia is well-know and supported by those findings. For instance, one of the clinical scales used for anesthesia before the appearance of depth of anesthesia monitors was the PRST scale [282], that gathered information on blood pressure, heart rate, sweating and tears to evaluate the adequecy of anesthesia.

In addition to the two time-related features, CCM was the third input used for the Naïve Bayes classifier and was included in the smallest set of parameters to reach a 70% accuracy with logistic regression. This suggests that geometric features are the most useful indicators extracted from REG signals for depth of anesthesia monitoring, but the contribution of nonlinear features should also be taken into account.

Finally, it should be noted that the inclusion of demograhic data did not improve the accuracy of any of the classifiers under test, even though the dependence of both geometric and Poincaré features on those variables was assessed in previous chapters. The Relief algorithm identified demographic

data as relevant features, probably due to the existence of this dependence together with the limited size of the dataset.

8.5 Conclusions

The geometric features combined in a naïve Bayes classifier were able to predict the anesthetic state of the patient with a 70% accuracy. Those results indicate that CBF related features extracted from REG signals are not enough sensitive to be used for depth of anesthesia monitoring. However, the aim of using CBF features in anesthesia is not to replace existing depth of anesthesia monitors but to enhance the available information on cerebral activity and hemodynamics, to provide anesthesiologists with an extra source of information that allows the best equilibrium between unconsciousness, low brain activity and brain hemodynamics stability. In this way, in Chapter 9 the causal interactions between EEG and REG were analyzed, in order to identify the relevant CBF features providing additional information to the one currently available with depth of anesthesia monitors.

Chapter 9

Causality analysis between EEG, REG and hemodynamics during anesthesia

Abstract

In this chapter, causal interactions between general hemodynamics, cerebral hemodynamics and brain activity are studied. A first analysis along complete surgical procedures is provided, followed by a breakdown of specific events such as patient positioning or drug infusion. Brain activity, represented by EEG related variables, showed a causal relationship with hemodynamics, suggesting that clinical decisions related to anesthesia should integrate CBF measurements to preserve hemodynamic stability at a general and cerebral level.

9.1 Introduction

As previously mentioned in Chapter 2, during propofol general anesthesia, both CBF and EEG signals suffer changes due to the induced loss of consciousness and depressed hemodynamic activity. This chapter aims at analyzing the causal relationships between both physiological signals during anesthetic procedures.

Causal interaction techniques are based on Granger's econometric models [283]. Given two signals, R and S, n being the present time with current samples Rn and Sn, and p past samples such that $R_n^p = [R_{n-1} \cdots R_{n-p}]^T$ and $S_n^p = [S_{n-1} \cdots S_{n-p}]^T$, under the time domain analysis, the parametric representation of a restricted regression (meaning that time series only depend on their own past samples) is presented in Equations 9.1 and 9.2:

$$R_n = \tilde{A} \cdot R_n^p + \tilde{U}_n \quad (9.1)$$

$$S_n = \tilde{B} \cdot S_n^p + \tilde{W}_n \quad (9.2)$$

in which Ã, and $\tilde{B}$ have dimension p and $\tilde{U}_n, \tilde{W}_n$ are prediction errors. The assumption of causality between Rn and Sn leads to an unrestricted regression model, allowing each time series to depend on the past samples of both signals, as represented in Equations 9.3 and 9.4:

$$R_n = A \cdot S_n^p + B \cdot R_n^p + U_n \quad (9.3)$$

$$S_n = C \cdot S_n^p + D \cdot R_n^p + W_n \quad (9.4)$$

where A, B, C and D are the parametrization matrices and have dimension p, while U_n, W_n are the new prediction errors.

Time domain causality can be expressed as in Equations 9.5 and 9.6, where σ^2 indicates residual variance. $C_{S\to R}$ indicates how past samples of the time series S are able to improve prediction of R: a 0 value implies that past samples of S do not provide any additional information for the prediction of R, while a value of 1 indicates that using values of S for Rn prediction results in a perfect prediction. The analogous reasoning should be performed for $C_{R\to S}$ [284].

$$C_{S\to R} = \frac{\sigma^2_{\tilde{U}} - \sigma^2_{U}}{\sigma^2_{\tilde{U}}} \tag{9.5}$$

$$C_{R\to S} = \frac{\sigma^2_{\tilde{W}} - \sigma^2_{W}}{\sigma^2_{\tilde{W}}} \tag{9.6}$$

In the equations provided to illustrate causality linear regressions have been used for simplicity. However, several publications in the field suggest that non-linear models, such as non-linear autoregressive models (NAR) or non-linear autoregressive exogenous models (NARX) show a better performance [285] [286], and that model free approaches could improve causality systems results [287]. The analysis herein presented will be based in AR models built from the time series under analysis, as discussed in the Methods section. Furthermore, even though causality analysis can be performed either in time domain, frequency domain or information domain, this chapter will focus on the time domain causality.

The causality analysis of different phyisiological signals has gained popularity in the last decade. Several publications are centered in the interactions between RR intervals and systolic blood pressure, for instance for baroreflex assessment [284][246]. It has been reported that classical approaches such as cross-spectral interactions are not enough for understanding the underlying mechanisms and methods for interaction analysis need to account for causality [288].

Even though most of the causality studies of biomedical signals have been published with two variables, some of them are using more complex systems, for example by analyzing causal relationships between heart period, systolic arterial pressure (SAP) and respiration [287] [289]. Relevant clinical results have arisen from those publications: for example, Rield et al. [290] explored short term couplings between respiration, systolic and diastolic blood pressure and heart, in order to have a deeper understanding on pre-eclampsia, which is responsible for significant neonatal and maternal mortality; they concluded that respiration might have a key role in pre-eclampsia, as affected patients showed increased respiratory influence on the diastolic blood pressure.

Additionally, Porta et al. [291] studied the causal interactions between heart period, respiration and systolic arterial pressure at rest and after the

administration of different drugs, concluding that Granger causality is a suitable tool to describe cardiovascular control and describe the effects of the administered drugs.

Besides interactions in the hemodynamics system, several publications have focused on the application of Granger Causality in EEG signals. For example, Juan et al. [292] studied the connectivity across EEG bands in patients with Alzheimer's disease, detecting increments of connectivity in the δ band, together with decremental connectivities in other EEG bands. They concluded that Granger Causality (GC) was suitable for Alzheimer diagnosis, since the disconnection among different brain regions is a well-known effect of the disease. Another application of GC in EEG signals was presented by Coben et al. [293], who analyzed pre and post-ictal periods of epileptic seizures to study the connectivity between brain regions in epileptic patients. Additionnally, Lee et al. [294] analyzed the neural connectivity during NREM sleep and detected a decreased local connectivity at low frequencies (4Hz) during consciouss periods when compared to unconsciousness.

The GC principles have also been applied to EEG signals during anesthesia. Nicolaou et al. [295] developed a system capable of classifying EEG signals as belonging to awake or anesthetized patients with a 96% accuracy, using as inputs the interactions between EEG signals from different brain areas. Moreover, in another study [296], an accuracy of 98% was obatined for loss of consciousness detection, suggesting that GC could be used as an awareness detection system.

Barrett et al. [297] analyzed steady state EEG signals during propofol induced anesthesia recorded from the anterior and posterior brain areas, detecting a bilateral increase in GC for the power spectral density in the β and γ bands during loss of consciousness.

The interactions between the brain and the hemodynamic system have also been the target of many research projects. Duggento et al. [298] analyzed functional MRI data, respiration and heart beat recordings, concluding that GC is a suitable tool to assess causality among brain and heart activity. In [299], Greco et al. studied the causality between hemodynamics and EEG activity during the exposure to pleasant or unpleasant visual stimulation, to relate the reaction to emotions with the changes at the cardiovascular and brain level. Pleasant images increased the coupling from the left hemisphere to the heart, while unpleasant images increased the coupling with the right one, when compared to GC indices at rest.

Faes et al. [285] analyzed causal relationships brain-heart and brain-brain during sleep, and concluded that both kind of interactions were effectively taking place. Moreover, brain-heart interactions were also studied by Wo et al. [300] for different sedation levels in anesthetic procedures. EEG spectral power and heart rate signals were analyzed, showing a higher connectivty from brain to heart when compared with the opposite direction for all sedation levels, finding as well a higher coupling in deeper sedation states.

Those findings support the hypothesis that interactions between EEG and REG signals should exist during general anesthesia, and that this connectivity could be assessed by means of GC. For this reason, causal relations between EEG spectral energy and the geometric and Poincaré REG descriptors were studied through data recorded during surgical procedures under propofol anesthesia.

9.2 Methods

9.2.1 Granger Causality

Granger Causality (GC) is a probabilistic tool to assess causality between pairs of variables. It relies on a hypothesis test in which the null hypothesis is that, given two variables x(t) and y(t), y(t) does not cause x(t). In order to assess the causality between the signals, two autoregression models (AR) are built: the restricted and the unrestricted model. The restricted model (equation 9.7) uses only past values from the signal x(t) to predict its future values, while the unrestricted model uses past values from both x(t) and y(t) to predict values of x(t).

$$x(t) = \sum_{i=1}^{\infty} \alpha_i x(t-i) + c_1 + v_1(t) \tag{9.7}$$

$$x(t) = \sum_{i=1}^{\infty} \alpha_i x(t-i) + \sum_{j=1}^{\infty} \beta_j y(t-j) + c_2 + v_2(t) \tag{9.8}$$

The GC principle states that if the prediction of the unrestricted model is more accurate than the one provided by the restricted model, there is a causal relationship from y(t) to x(t).

Equations 9.7 and 9.8 consider infinite AR models. In practice, the optimal lags for the models must be computed as a prior step to assess causality. For that purpose, an empirical approach was used, testing all possible lags up to 10 samples (i.e. 10 seconds) for each model, and evaluating its goodness of fit.

Several algorithms are available to evaluate the adequacy of proposed AR models, the most commonly used being the Bayesian Information Criterion (BIC) [301] and the Akaike Information Criterion (AIC)[302], whose analytic expression is provided in equations 9.9 and 9.10:

$$\mathrm{AIC} = -2\log \mathrm{L}(\hat{\theta}) + 2k \tag{9.9}$$

$$\mathrm{BIC} = -2\log \mathrm{L}(\hat{\theta}) + k\log(n) \tag{9.10}$$

where θ represents the set of parameters in the model, $\mathrm{L}(\hat{\theta})$ the likelihood of the model under evaluation, k the number of parameters in the model and n the number of observations.

For the study herein presented, BIC was chosen over AIC since it has been published to be more consistent [303] and it demonstrated, in previous studies, to provide reliable values for EEG models under general anesthesia[304].

In the comparison of several models, the absolute minimum among the computed BIC values indicates the model that fits best the data, while differences between BIC values (dBIC) should be interpreted as the strength of the evidence supporting the superiority of a model over another, following a short set of rules of thumb [305]:

- dBIC<2: poor evidence
- 2 ≤ dBIC < 6: positive evidence
- 6 ≤ dBIC < 10: strong evidence
- dBIC > 10: very strong evidence

In this study, both the restricted and unrestricted AR models are optimized using the BIC algorithm and the variances of the prediction errors of both models are compared through an F test. Statistical significance is then corrected as a function of the comparison among multiple groups derived from the number of lags tested, resulting in a corrected F probability that should be lower than 0.05 to consider statistical significance.

In case differences with statistical significance are detected between the restricted and unrestricted models, the causality index is computed as:

$$C_{Y \to X} = \frac{\sigma_R^2 - \sigma_U^2}{\sigma_R^2} \tag{9.11}$$

where σ_R^2 is the variance of the restricted model and σ_U^2 the variance of the unrestricted model. This index allows to quantify the strength of the causality from one signal to another, and together with the occurrence of causalities provides a way to characterize the interactions between sets of selected signals.

To further detail the steps followed to assess causality among pairs of signals belonging to the selected database, a step-by-step example is herein illustrated. Let x(t) be the depth of anesthesia index qCON (**Figure 9-1**a), and y(t) the propofol effect site concentration CePropo (**Figure 9-1**b), both recorded simultaneously from a patient undergoing general anesthesia. The qCON index should decrease because of increased drug dosages and vice versa, hypothesizing that a causal relationship should exist from CePropo to qCON. To prove this assumption, Granger Causality was applied following the steps herein listed:

Step 1 - An AR model is built, called the restricted model, in which the signal x(t) is predicted using samples from its own past by means of a least squares linear regression . To obtain the AR model optimizing the variance of the residuals, an AR model is generated for each possible time lag and the metric BIC is assessed for all models. In this case, the maximum allowable time lag for x(t) was set to 10 samples.

Step 2 - Among the set of restricted AR models calculated, the one minimizing the metric BIC is selected. In this particular case, as illustrated in

Figure 9-2, the minimum BIC was obtained for xlag=1 sample, resulting in an AR model with an associated BIC of -1.313*10^4 and total error variance of $\sigma_R^2 = 0.003$.

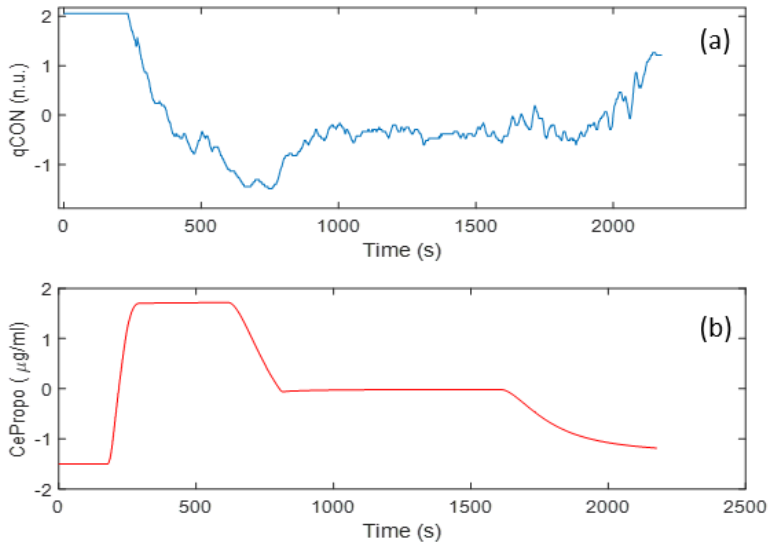

Figure 9-1 (a) Normalized qCON data and (b) normalized propofol effect site concentration recorded during a general anesthesia procedure.

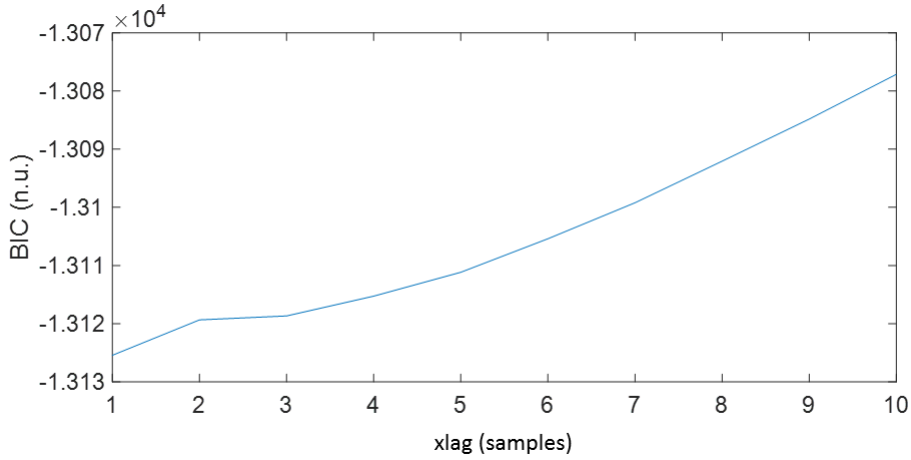

Figure 9-2 BIC values as a function of the selected xlag for the restricted AR model.

Step 3 - A second AR model is searched, called the unrestricted model, allowing samples from y(t) to be used in the prediction of x(t). The maximum ylag considered was 10 samples and the algorithm used to compute the AR model was the same as previously used for the restricted model. One model candidate was defined for each possible time lag to be considered.

Step 4 - The best unrestricted model (i.e. the one minimizing BIC) is chosen among the set of unrestricted AR models. In this example, the minimum BIC was obtained for ylag=1 sample (**Figure 9-3**). This resulted in an unrestricted AR model with an associated BIC of -1.315*10^4, and a total error variance of $\sigma_U^2 = 0.002$.

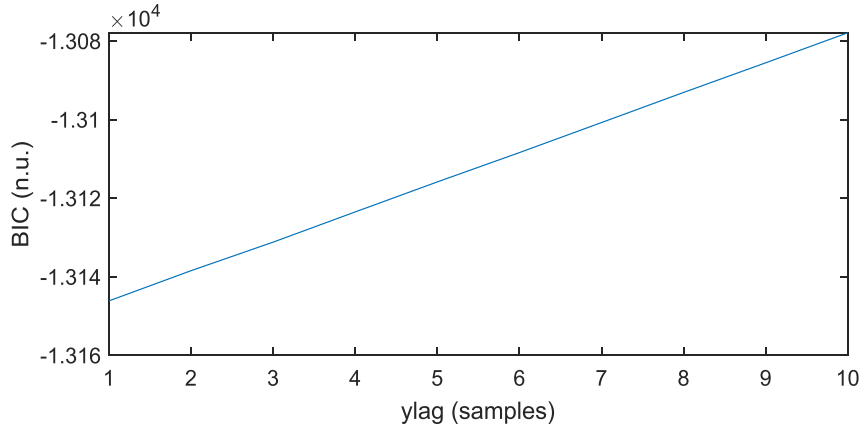

Figure 9-3 BIC values as a function of the selected ylag for the unrestricted AR model.

Step 5 - Causality is assessed by comparing the BIC values and computing the F-statistic and the causality index ($C_{Y\rightarrow X}$). The differences (dBIC) between the BIC values obtained for the restricted (BIC_R) and unrestricted models (BIC_U) reveal the superiority of the unrestricted model over the restricted one when dBIC values are negative and with a high absolute value. In this example, dBIC=-20.71, thus indicating that the unrestricted model is the best option.

Besides a negative dBIC value, statistical significance is also required to conclude that one variable Granger causes the other one. The null hypothesis in this case is that y(t) does not Granger cause x(t). F-statistic is used to reject (or not) the null hypothesis by comparing its value to the critical value. The F-statistic is calculated as:

$$F = \frac{(SSE_R - SSE_U)/y_{lag}}{SSE_U/(N - DF)} \quad (9.12)$$

where ylag is the lag minimizing the BIC for the unrestricted model, SSE the sum of the squared residuals of the restricted (SSE_R) and the unrestricted models (SSE_U), N the number of samples available and DF the degrees of freedom (equation 9.13). The critical value is obtained using the F inverse cumulative distribution function considering 95% confidence intervals.

$$DF = xlag + ylag + 1 \quad (9.13)$$

Whenever the F statistic is greater than the critical value, the null hypothesis is rejected and causality from the timeseries y(t) to x(t) is considered to take place. In this example, the computed F statistic equals 20.78 while the critical value is much lower (3.84). Therefore, causality is detected from CePropo to the qCON index. The strength of this causal link is assessed by means of the causality index, computed as indicated in equation 9.11. Considering the causality from propofol dosage to qCON, since $\sigma_R^2 = 0.003$ and $\sigma_U^2 = 0.002$, the causality index results in $C_{Y\to X} = 0.33$. Therefore, CePropo proved to Granger cause qCON with statistical significance.

9.2.2 Experimental dataset

The analysis of causal interactions between physiological signals related to hemodynamic processes and those associated to brain activity was performed on the General Anesthesia Dataset 2. This dataset is composed by data from 88 female patients scheduled for elective gynecological surgeries under general anesthesia with propofol and remifentanil TIVA. REG signals were collected throughout the surgery, together with other clinical variables such as HR, MAP, EEG, the EEG index qCON and drug dosages. Details on the recorded dataset can be found in Chapter 3.

9.2.3 Data processing

REG data were screened for artefact rejection and preprocessed with linear filters. Geometric and Poincaré plot descriptors were calculated in 8s sliding windows, resulting in a new index value every second. In case artefacts were detected within the processed window, a NaN value was assigned. Segments with more than 50% of NaN values were excluded from analysis. Once all the time series for each proposed parameter were calculated, they were synchronized with all other data collected during the surgical procedures, such as hemodynamic variables, drug infusion dosages and events recorded during surgery.

The final set of variables to be analyzed for causality were: REG geometric features (Range, Δtmax, Δtmin, Δtmin-max, Slope (α), AreaSyst, δmax, δrange, CBVrel and CBFest), REG Poincaré plot descriptors (SD1, SD2, SDratio, SDarea, CCM and R), global hemodynamics (HR, MAP), the effect site concentrations of propofol and remifentanil (CePropo, CeRemi, respectively) and EEG parameters related to depth of anesthesia (qCON and the EEG bands δ, θ, α, β). The drug concentrations were directly recorded from the infusion pumps and required no further processing. The qCON index was also collected from the Conox device. Nonetheless, the energy in the canonic EEG bands was computed by means of the integral of the Fast Fourier Transform (FFT) of the EEG signal, downsampled at 256 Hz, accross the frequencies belonging to each frequency band.

Several events known to alter hemodynamics and/or EEG activity were selected in order to be analyzed for causality:

a) Steady state anesthesia (n=84): 400s periods in which effect site concentrations of propofol and remifentanil were constant and no surgical events took place.

b) Propofol infusion (n=29): periods from 200s before to 200s after the change of the target effect site concentration of propofol, while remifentanil was kept constant.

c) Remifentanil infusion (n=16) periods from 200s before to 200s after the change of the target effect site concentration of remifentanil, while propofol was kept constant.

d) Atropine infusion (n=16): periods from 200s before to 200s after the administration of atropine.

e) Ephedrine infusion (n=7): periods from 200s before to 200s after the administration of ephedrine.

f) Trendelenburg position (n=12): periods from 200s before to 200s after the positioning of the patient from the horizontal supine position to the Trendelenburg position.

g) Passive leg raising (n=48) periods from 200s before to 200s after the elevation of patient legs in preparation for surgery.

As an example, **Figure 9-4** includes a set of data recorded from one subject participating in the clinical trial. The anesthesia induction started at t=500s approximately, with the infusion of remifentanil and propofol. A decrease in qCON took place as a consequence of the effect of the drugs, resulting in the transition from the awake state to anesthesia around t=700s. In this example, events (a) steady state anesthesia and (c) remifentanil infusion can be observed: the first one begins right after the drug concentrations of propofol and remifenanil are lowered and stabilized, at t=1000s, and lasts for 1000s. Immediately afterwards, the remifentanil effect site concentration was increased, originating the new clinical event (c) to be processed.

For each type of event - from (a) to (g) - all possible causalities between pairs of variables were assessed through GC. The objective of this research is to study the causality between different physiological systems. For this reason, causalities among pairs of REG features were not considered for analysis, as well as the causal links between pairs of EEG-based parameters.

Among the set of clinical events in which causality was studied, the periods of steady state anesthesia were used as the reference: the results from the other events, such as atropine infusion or Trendelenburg positioning, were compared to those obtained during stable anesthesia. Besides the existence or absence of causality, and its occurrence along the clinical database, the time lags needed for each pair of variables to build the AR models required for GC causality assessment were also studied and compared to the reference clinical state of steady state anesthesia.

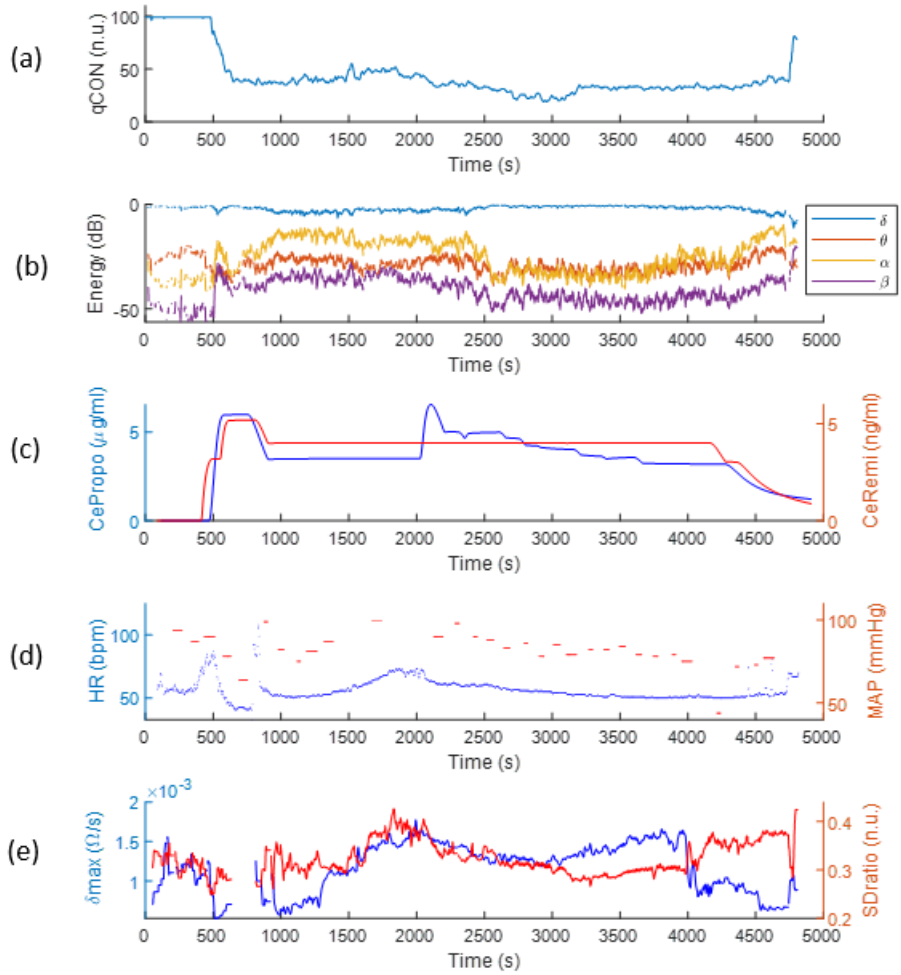

Figure 9-4 Example of clinical data recorded during an anesthetic procedure: (a) qCON index, (b) EEG frequency bands, (c) propofol and remifentanil effect site concentrations, (d) heart rate and mean arterial pressure and (e) δmax and SDratio REG features.

Causality diagrams were drawn for each event. Given a pair of variables X and Y, causality indices $C_{X\to Y}$ and $C_{Y\to X}$ were compared through statistical hypothesis testing. Normality of the data was assessed by means of a Kolmogorov-Smirnov test and subsequently, a student t-test or Mann-Whitney test was performed accordingly, considering statstical significance for $p<0.05$. Whenever causality indices were higher in one-way, with statistical

significance, a single direction of causality was considered, represented in the causality diagrams with a single arrow. If the statistical test could not be performed because there were not enough events available, both directions were considered in two different arrows. In case no statistical differences were detected between $C_{X\rightarrow Y}$ and $C_{Y\rightarrow X}$, a double arrow was used and the causality was interpreted as a closed loop interaction.

Moreover, for each event, Spearman correlations between the causality indices and patient demographics were calculated and considered as confounding factors for $p<0.01$, due to the large number of correlations being analyzed simultaneously. Only correlations reaching absolute values above 0.5 were included for analysis. Additionally, differences in age, height, weight or BMI, between the group of patients showing a causal relationship and the group of patients not presenting this interaction were assessed my means of hypothesis testing. A student T-test was used when samples were normally distributed, and a Mann-Whitney test otherwise. In both cases, the statistical significance was set to $p<0.01$, to account for the multiple testing performed even though the number of groups is limited to 2.

9.3 Results

9.3.1 Steady state anesthesia

Data from steady state anesthesia were processed to study GC among each pair of variables. The restricted and unrestricted models were built, resulting in the time lags provided in **Figure 9-5** for the GC – caused variable (x) and in **Figure 9-6** for the causing variable (y). The maxmium lag allowed for both was 10 samples (i.e. 10 seconds), however none of the pairs of variables under study reached this maximum.

Regarding x lags, REG parameters tended to show larger values, mainly for those related to the derivative of REG – δmax, δrange, CBVrel and CBFest - while other variables provided shorter optimal lags for the AR unrestricted models. The same situation is detected for y lags, where interactions among REG based parameters are the ones presenting the largest lags, while other pairs present lags typically smaller than 3 samples.

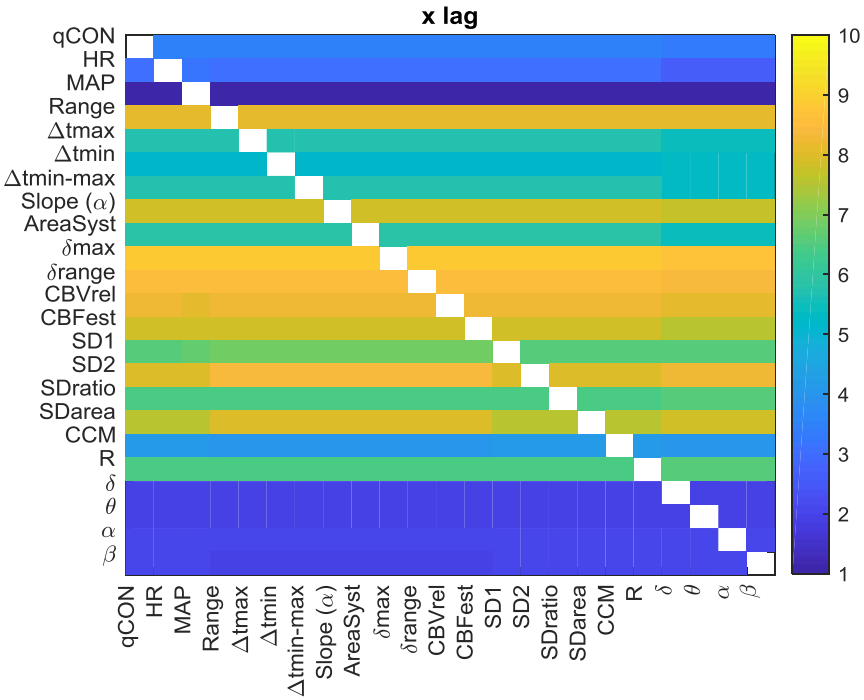

Figure 9-5 Optimal time lags for the GC caused variable (x lag) in the unrestricted AR model during steady state anesthesia. Columns contain the causing variables and rows the caused ones.

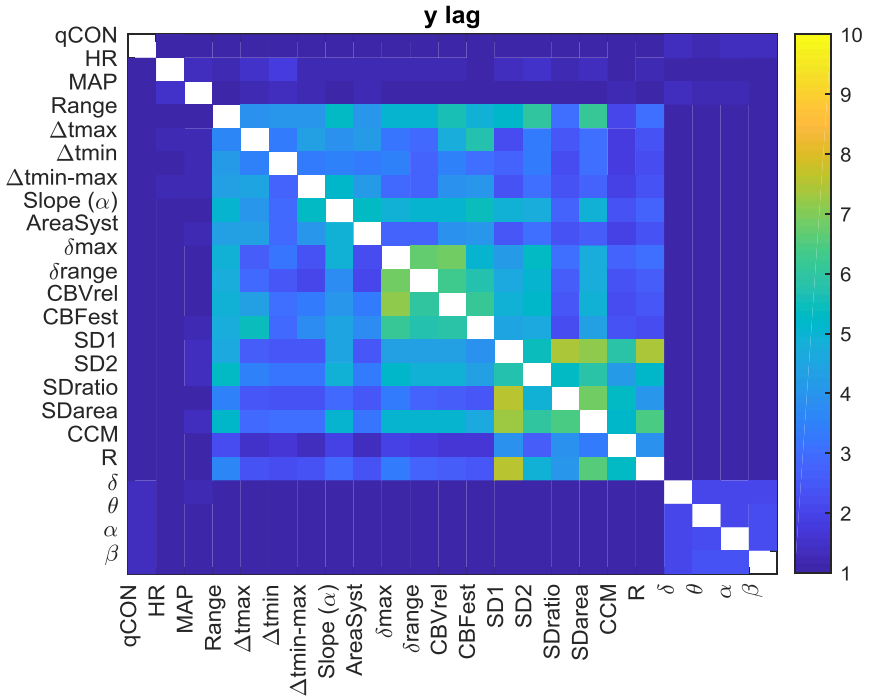

Figure 9-6 Optimal time lags for the GC causing variable (y lag) in the unrestricted AR model during steady state anesthesia. Columns contain the causing variables and rows the caused ones.

Once the time lags were defined, causality among each pair of variables was assessed. **Figure 9-7** shows the causal relationships between MAP and the geometrical features extracted from REG. All the geometric features showed causal relationships with MAP, the most significant ones being closed loop interactions between MAP and the slope of the REG wave (slope α), its maximum derivative (δmax) and CBVrel, and the causality from δrange towards MAP.

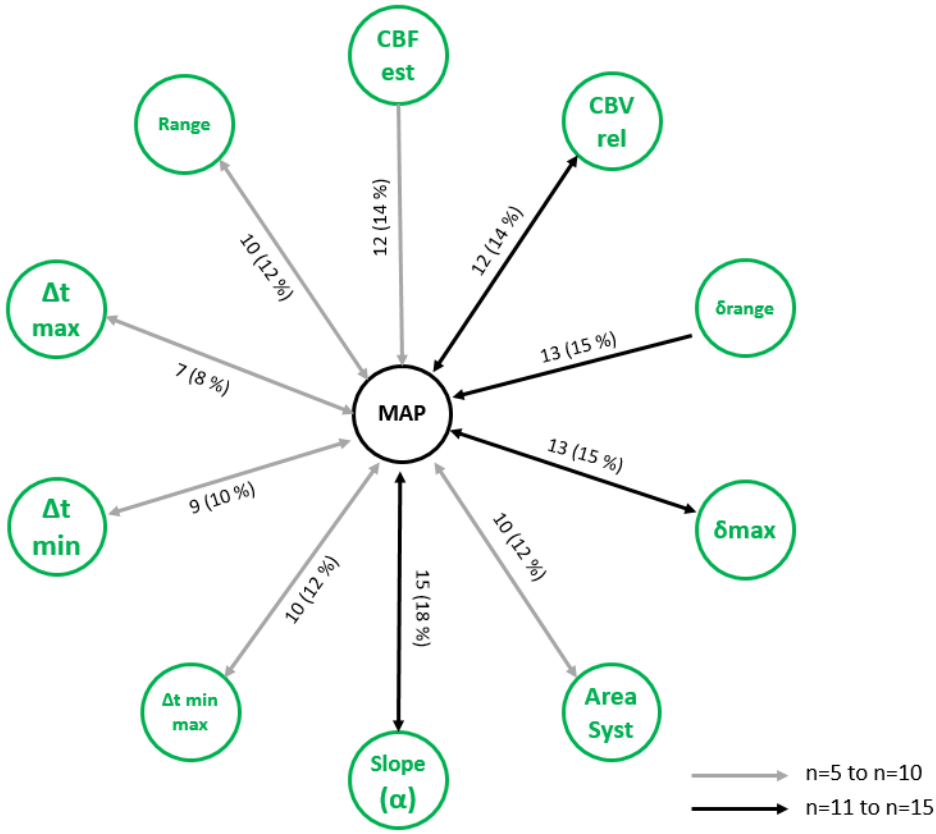

Figure 9-7 Causal relationships diagram between MAP and REG geometric features, where n represents the number patients presenting each causal interaction.

The causal relationships between REG linear features and HR are depicted in **Figure 9-8**: HR showed causal relationships with REG extracted features more often than MAP, with 33 patients presenting a closed loop interaction between δmax and HR. The slope (α), the Range, CBVrel and CBFest also showed closed loop interactions with HR. Moreover, unilateral causal relationships were also detected, with δrange, Δtmax and Δtmin presenting a causal effect on HR.

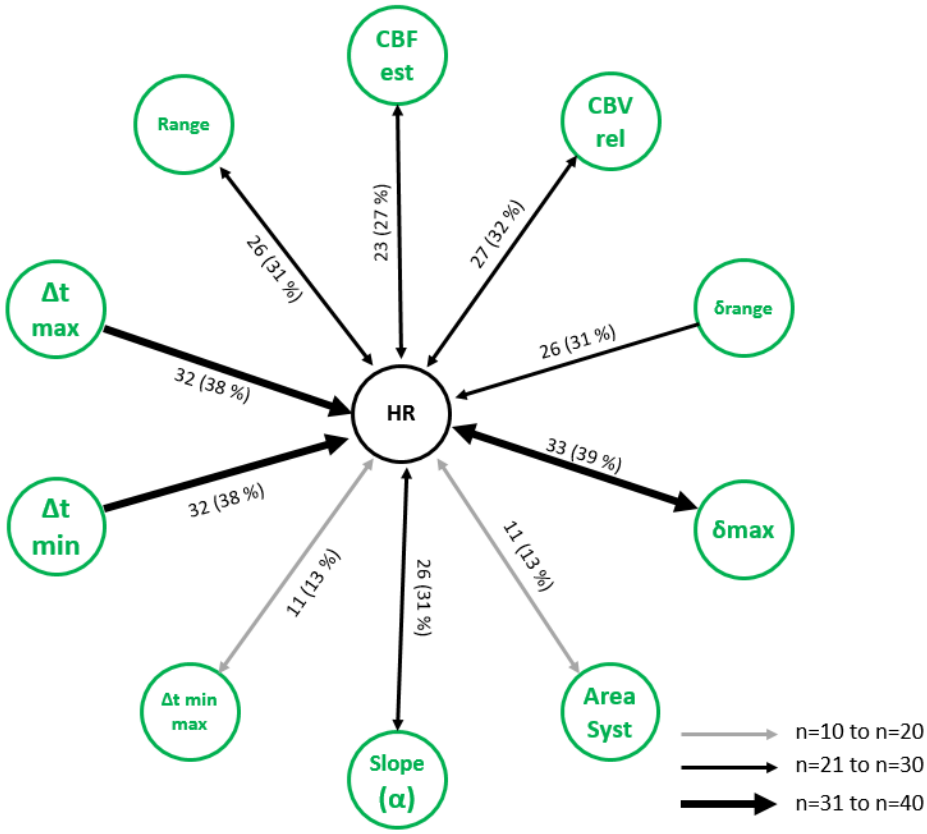

Figure 9-8 Causal relationships diagram between HR and REG geometric features, where n represents the number patients presenting each causal interaction.

The interactions between the Poincaré plot descriptors and MAP and HR are represented in **Figure 9-9**. HR showed stronger links than MAP. While all 6 descriptors presented closed loop relationships with MAP in a range of patients (n) between 10 and 20, SD2 and SDratio and R had a closed loop link with HR for 35, 32 and 31 patients, respectively. SDarea and, to a lesser extent, SD1, showed causal effects towards HR that were not recyprocal, while CCM was the feature presenting less occurences of causality.

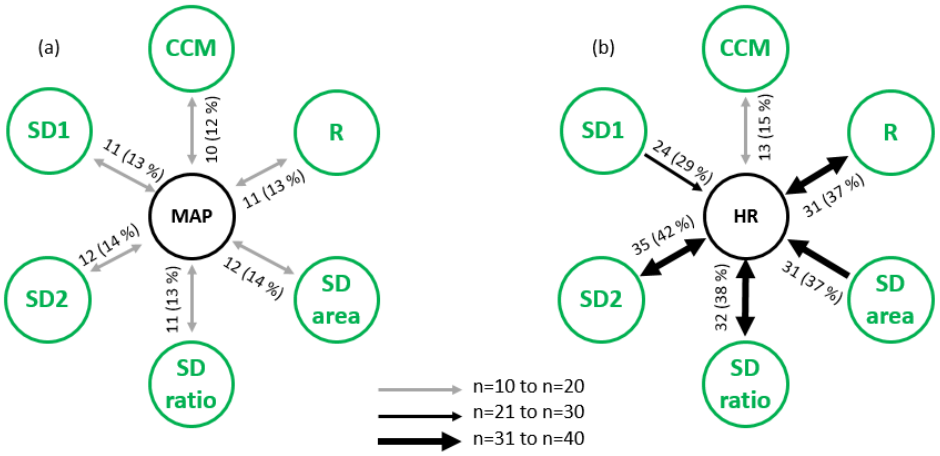

Figure 9-9 Causal relationships diagram between MAP and HR and REG Poincaré plot descriptors features, where n represents the number patients presenting each causal interaction.

Besides the causality among different measurements related to global and cerebral hemodynamics, the interactions between brain activity assessed by the EEG and REG features were also studied. The causal relationships between REG linear features and EEG energy bands is graphed in **Figure 9-10**. The relative energy in the δ band showed a closed loop relationship with Δtmax in more than 10 patients. Almost all REG geometric parameters, except δmax, presented causal relationships with this energy band, the majority of them being unilateral, from REG features towards δ band, except for Δtmax and δrange, that were closed loop interactions, and CBVrel, that presented a causal link from the δ band. Regarding θ, α and β bands,those showed less occurrences of causality with the geometric features extracted from REG signals, overall suggesting that lower frequencies are more related to linear changes in CBF than the higher ones, at least during steady state anesthesia.

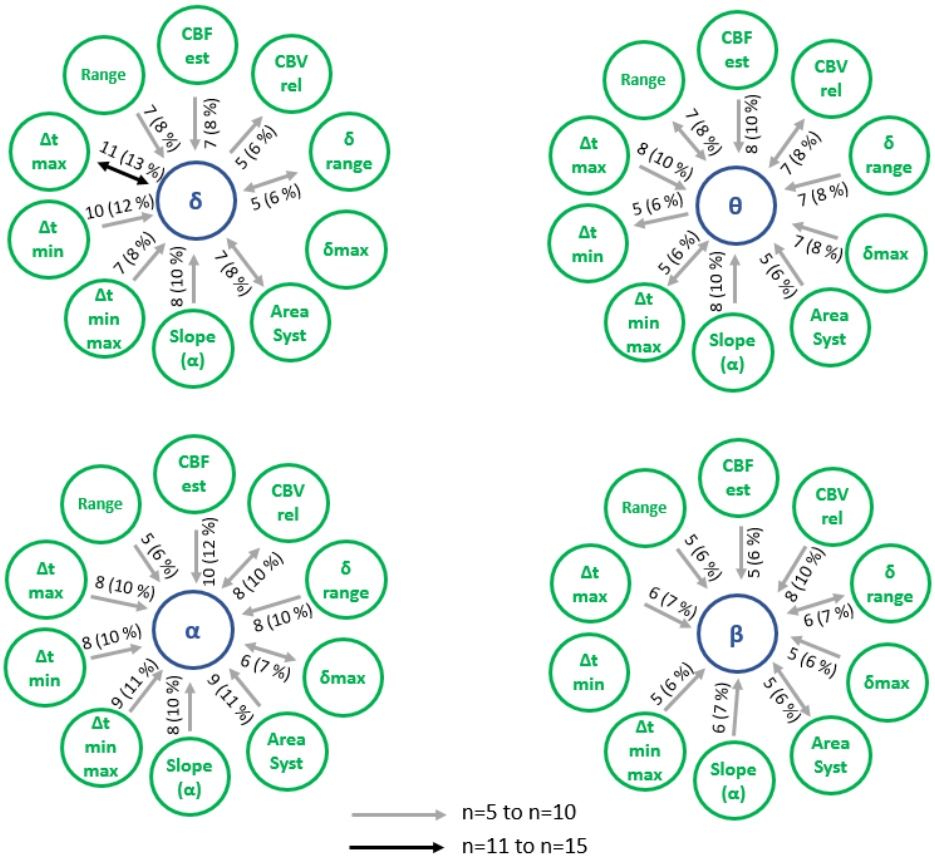

Figure 9-10 Causal relationships diagram between the energy of the EEG bands and REG geometric features, where n represents the number patients presenting each causal interaction.

Regarding the interactions between Poincaré plot descriptors and the energy in the canonical EEG bands (**Figure 9-11**), a low occurrence of causal relationships was detected, the majority being in the same direction, from the Poincaré plot descriptors towards the EEG bands, suggesting a stronger interaction from CBF to EEG than vice versa. It should also be noted that the β band was the one showing causal relationships with the fewest set of Poincaré descriptors, indicating that, as observed with linear REG features, lower frequencies present more causal links with REG descriptors.

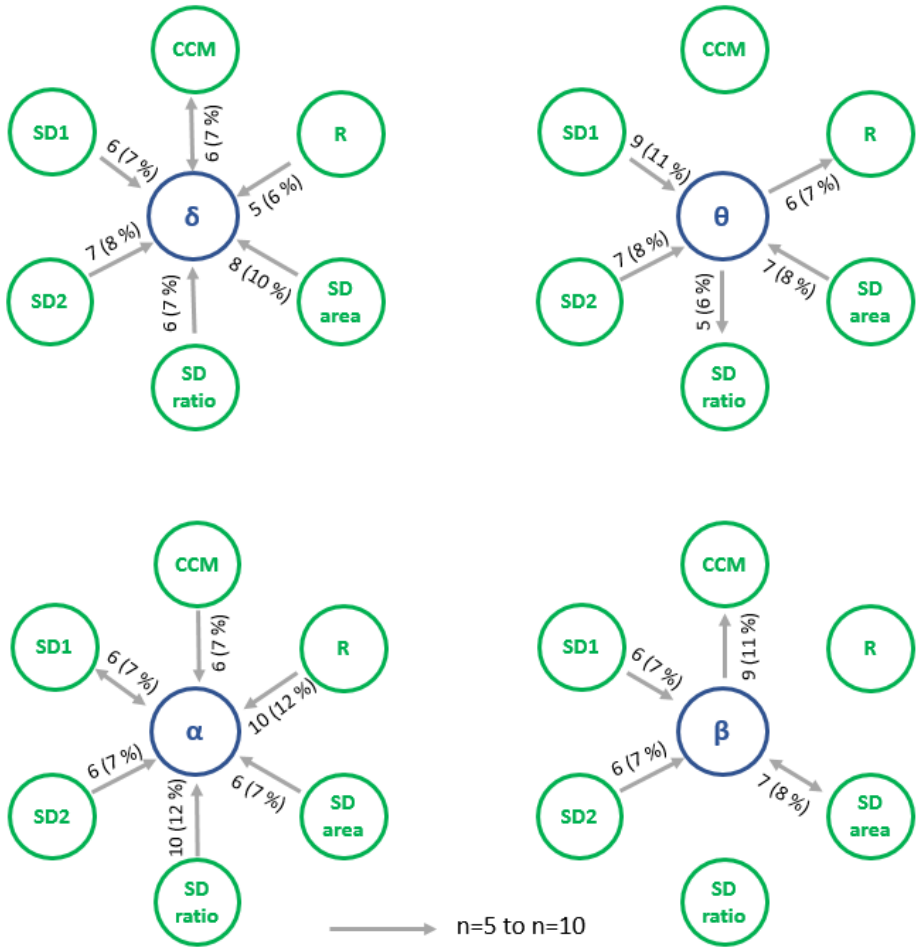

Figure 9-11 Causal relationships diagram between the energy of the EEG bands and REG Poincaré plot descriptors, where n represents the number patients presenting each causal interaction.

The depth of anesthesia index, qCON, integrates information from all the EEG spectrum and was analyzed as well for causal interactions with REG features. **Figure 9-12** depicts the relationship between qCON and the REG geometric features, showing a low occurrence of causal events. These results should be interpreted with caution and together with those provided under specific clinical scenarios detailed in this section, since due to the steady state conditions of anesthesia, qCON and frequency bands are not expected to

reveal important changes in the signal dynamics, resulting in lower causal intereactions.

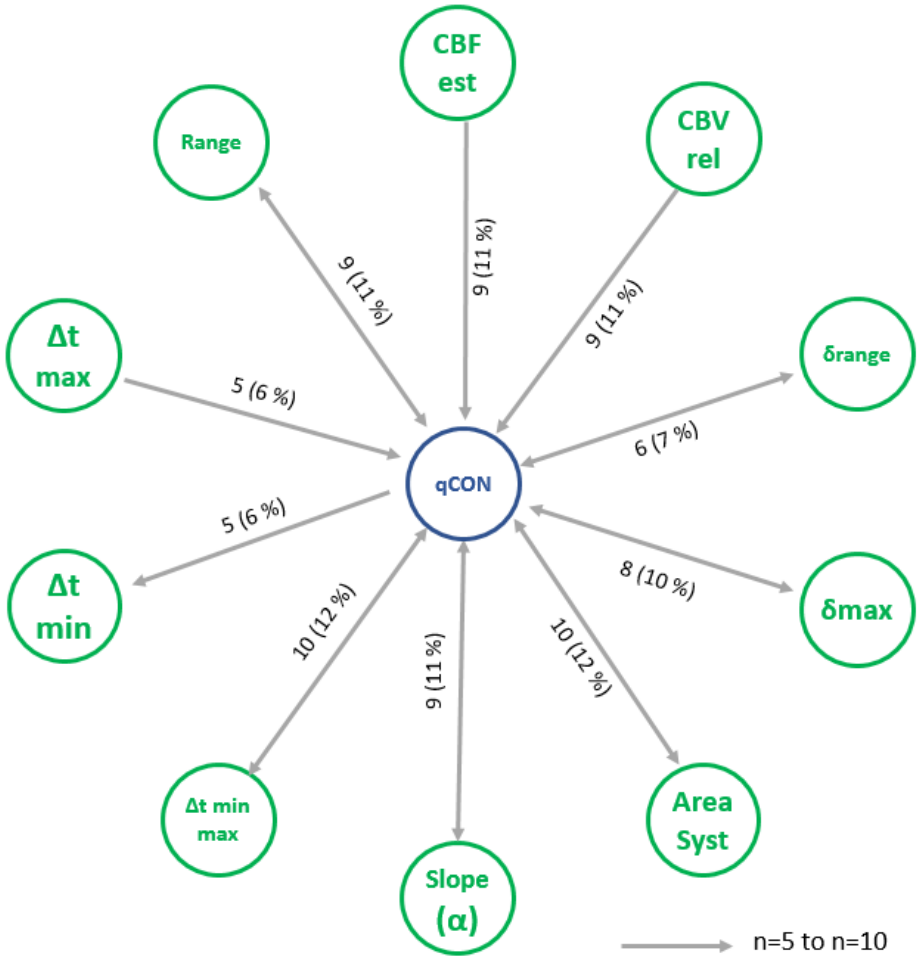

Figure 9-12 Causal relationships diagram between the qCON index and REG geometric features, where n represents the number patients presenting each causal interaction.

SD1 is the Poincaré plot descriptor with a stronger causality link with the depth of anesthesia index qCON, presenting a bilateral interaction, followed by SD2 (**Figure 9-13**). R and SDratio had a causal link from the qCON index towards the REG features, while SDarea showed the opposite causal direction and CCM revealed no relationship with the qCON index.

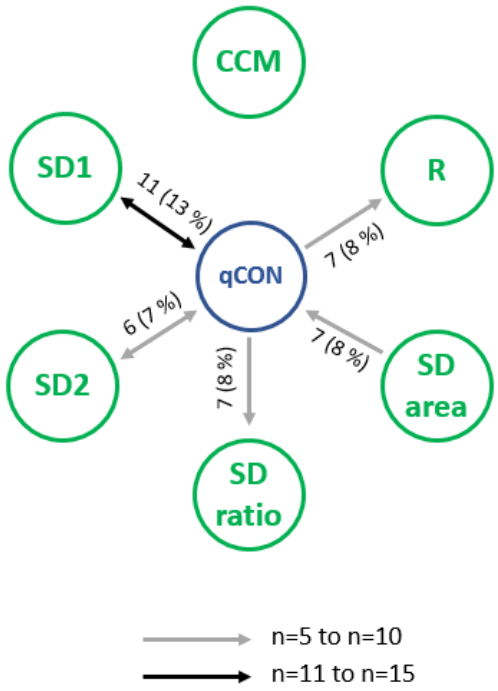

Figure 9-13 Causal relationships diagram between the qCON index and REG Poincaré plot descriptors, where n represents the number patients presenting each causal interaction.

An overview of the main interactions between HR, MAP, all EEG parameters, and CBF linear and nonlinear features is provided in **Figure 9-14**. REG geometric features represent the linear CBF estimators (CBF lin) while REG Poincaré plot descriptors correspond to the nonlinear CBF estimators (CBF PP). The occurrence of each interaction between a pair of variables in two groups was computed as the number of patients presenting at least a statistically significant causal relationship between any pair of features belonging to the two groups under analysis. Up to 99% of the analyzed patients showed a bilateral causal relationship between CBF lin and CBF PP parameters, since both sets of variables come from the same time series. Regarding the interactions between HR and CBF features, causalities from CBF to HR were more frequent than in the opposite direction, with the linear CBF features showing a stronger role over the nonlinear ones. This relevance of the linear features is preserved in the causality study from and to MAP,

even though in this case the causalities from MAP to the CBF features are more frequent than the opposite ones.

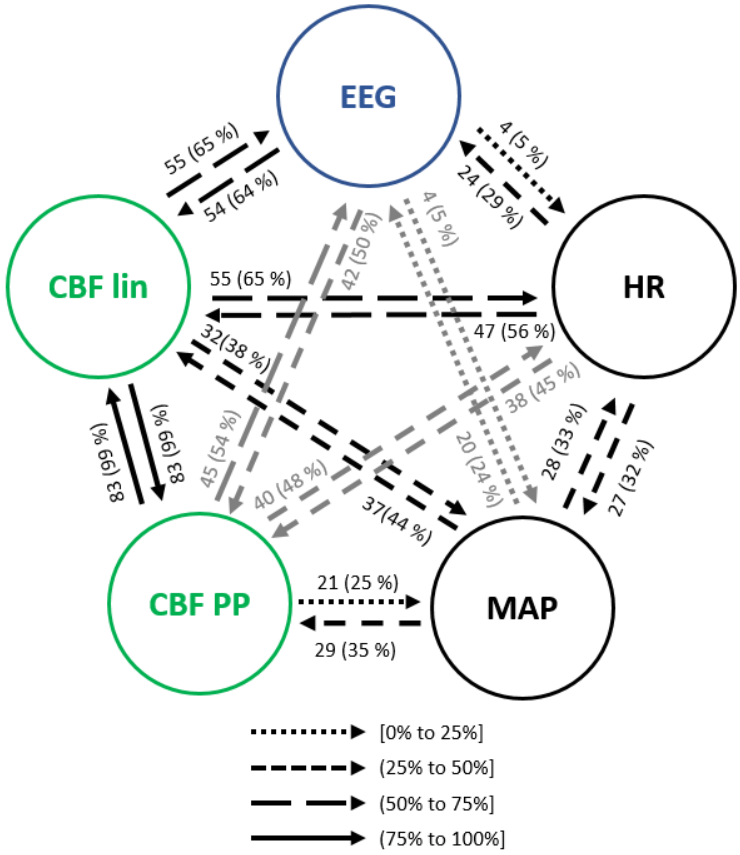

Figure 9-14 Main interactions between global hemodynamics (HR and MAP), EEG features and REG geometric features (CBF lin) and REG Poincaré plot (CBF PP) parameters during steady state anesthesia.

Both global and cerebral hemodynamics presented causal relationships with EEG activity. EEG had a similar occurrence of causality towards HR and MAP, while HR presented a higher rate of causality towards EEG than MAP. Regarding cerebral hemodynamics, the most relevant results rely on the 65% of causality from the CBF linear features to the EEG variables, which is one of the highest occurrences of interactions of the full system considered and therefore strongly suggests a modulation of EEG activity as a result of changes in the REG signals represented by their linear features. The Poincaré extracted features showed a lower occurrence of causality on EEG variables, but still higher than the ones provided by global hemodynamics. Finally, the

causality from EEG to CBF features was also higher for the linear features when compared to the nonlinear parameters extracted from REG signals.

No correlations were found between the causality indices and patient demographics. However, hypothesis testing comparing the age, height, weight and BMI of patients presenting causal relationships among pairs of variables with patients not presenting them showed statistical significant differences as summarized in table **Table 9-1**.

Table 9-1 Statistical differences of the hypothesis testing comparing the age, height, weight and BMI of patients presenting causal relationships among pairs of variables during steady state anesthesia with patients not presenting them.

FROM	TO	DEMOGRAPHIC	P-VALUE	CAUSALITY ↑
Δtmax	HR	age	0.0011	↓age
qCON	Δtmin-max	age	0.0067	↓age
qCON	AreaSyst	age	0.0067	↓age
α	SD1	age	0.0085	↓age
Range	δ	age	0.0055	↓age
Δtmin-max	α	age	0.0099	↓age
AreaSyst	α	age	0.0099	↓age
SD1	α	age	0.0083	↓age
SD2	α	age	0.0041	↓age
SDarea	α	age	0.0031	↓age
CBFest	δ	weight	0.0004	↑weight
HR	θ	weight	0.0016	↑weight
Range	θ	weight	0.0096	↑weight
slope(α)	θ	weight	0.0087	↑weight
Range	α	weight	0.0094	↑weight
δrange	α	weight	0.0023	↑weight
CBVrel	α	weight	0.0023	↑weight
CBFest	β	weight	0.0008	↑weight
δrange	α	BMI	0.0039	↑BMI
CBVrel	α	BMI	0.0039	↑BMI

Lower aged patients were prone to present causal links from REG features to EEG α band, through Δtmin-max, AreaSyst, SD1, SD2 and SDarea. Additonally, causality from Range to the δ band, from qCON to AreaSyst and Δtmin-max, from Δtmax to HR, and from the α band to SD1 was also identified in the patients presenting lower ages. While height did not show to be a significant factor, higher weight and BMI were detected in patients presenting causality links towards the EEG bands. The factors linked to those bands were CBFest, HR, Range, REG slope, δrange and CBVrel, and were mainly affecting the α and θ bands. Therefore, the link between REG features and EEG parameters seems to be enhanced by lower age and higher weight and BMI.

9.3.2 Propofol infusion

The time lags obtained for the combination of all the variables under analysis are provided in **Figure 9-15** and **Figure 9-16**. Regarding the lags for the Granger-caused variable (x lag), those related to REG variables are slightly lower than the ones obtained under steady state conditions, suggesting a closer coupling in the time domain. The propofol effect site concentration, CePropo, was added to the analysis since it is not constant in this scenario. However, it should only be considered as a causing variable, since it is collected from infusion pumps, resulting from the calculation of pharmacokinetic models and is not influenced by other physiological systems. CePropo showed smaller lags for EEG variables and higher values for interactions with cerebral hemodynamics.

The values obtained for the lags of the Granger causing variables (y lags) are represented in **Figure 9-16**, providing similar values to those obtained for anesthesia steady state conditions, with the propofol concentration reaching values between 1 and 2 samples.

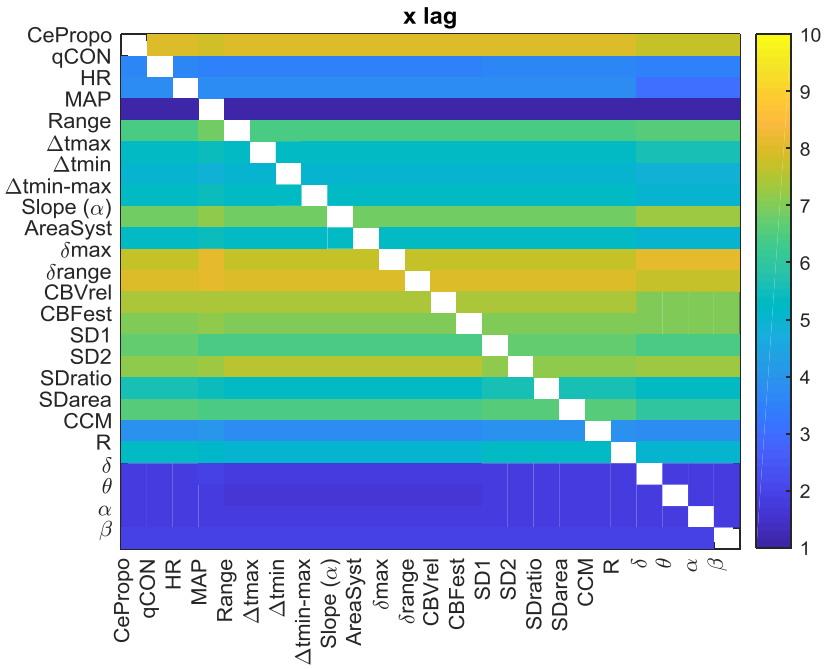

Figure 9-15 Optimal time lags for the GC caused variable (x lag) in the unrestricted AR model during changes in propofol concentration. Columns contain the causing variables and rows the caused ones.

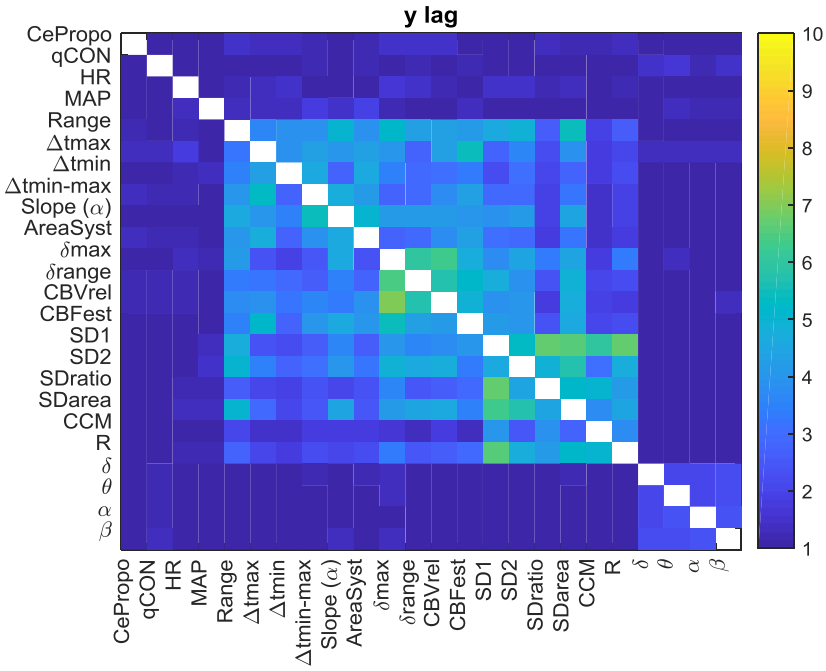

Figure 9-16 Optimal time lags for the GC causing variables (y lag) in the unrestricted AR model during changes in propofol concentration. Columns contain the causing variables and rows the caused ones.

The interactions from the propofol effect site concentration towards all the collected physiological data are represented in **Figure 9-17**. Causality in the opposite direction was not assessed since it does not have any clinical interpretation as previously stated. Among all the EEG bands, CePropo has the highest interaction with α, with similar results for its causality towards the qCON index. This indicates that the changes in propofol dosages are mainly affecting the α band and therefore projected in the overall depth of anesthesia assessment represented by the qCON index. The influence of CePropo in HR was detected in 21% of the patients, while causal relationships with MAP were limited to one patient. Regarding the effects of CePropo in the linear features extracted from REG signals, the causal relationships with higher occurrence were those towards Δtmin-max and AreaSyst, identified in 34% of the patients, followed by a 31% occurrence of causalities towards CBVrel, δmax and δrange. The less frequent interactions took place from CePropo to Δtmax and Δtmin. The Poincaré plot descriptors showed smaller occurrences, the higher ones associated to SD1, SDratio and R, suggesting that CePropo is affecting the short term variability of REG signals rather than the long term one.

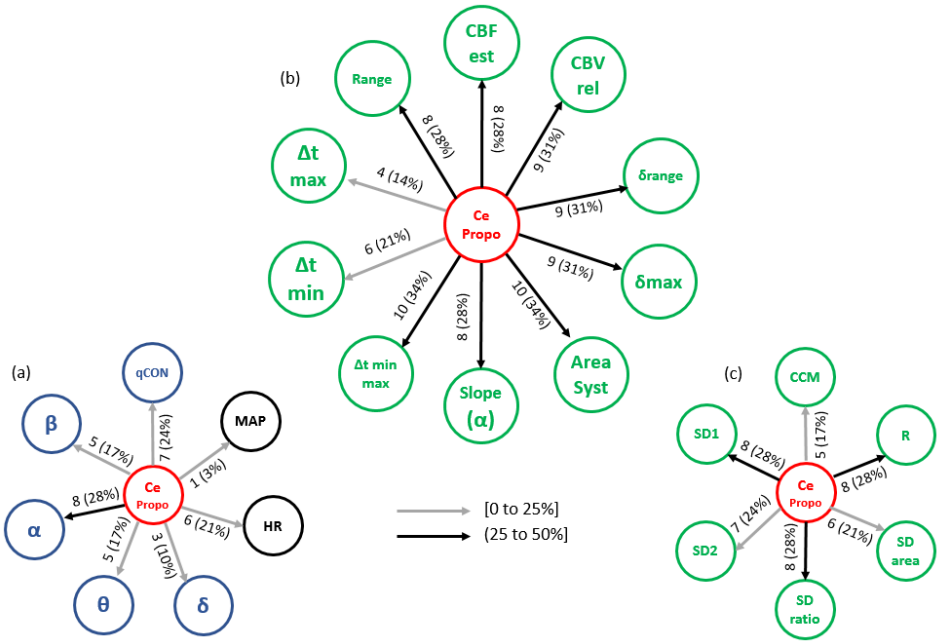

Figure 9-17 Causal interactions from CePropo to (a) EEG and global hemodynamics, (b) REG geometric features and (c) REG Poincaré plot descriptors.

Besides the direct effects of propofol concentration changes in all the physiological variables under study, the causal relationships among hemodynamics and EEG might also be affected by the administration of the hypnotic drug. **Figure 9-18** shows an overview of the existing causal interactions between general hemodynamics, cerebral hemodynamics and EEG related variables. Even though the detected interactions are similar to those during steady state anesthesia, several differences can be appreciated. For instance, the occurrence of causal interactions from HR and MAP towards CBF PP, CBF lin and EEG are higher, suggesting that changes in HR caused by propofol are projected in CBF and EEG. Additionally, causal effects from CBF lin to HR and EEG are also more frequent under propofol infusion, while the interactions between MAP and HR have a lower occurrence. Overall, changing the propofol effect site concentration ellicits a higher number of interactions from both cerebral and global hemodynamics towards EEG.

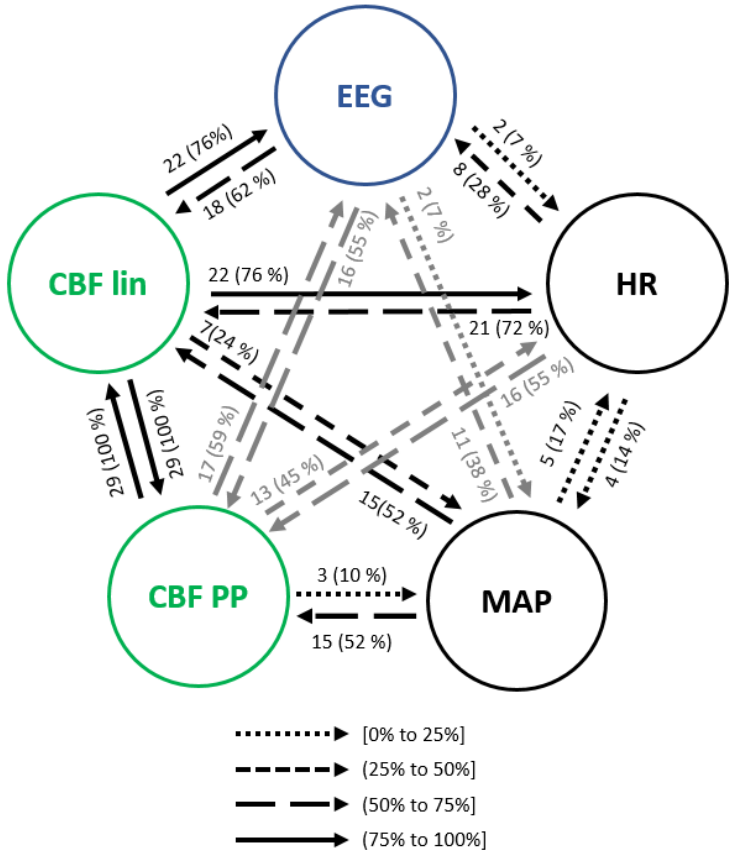

Figure 9-18 Causal interactions between EEG parameters, HR, MAP, REG geometric features (CBF lin) and REG Poincaré plot descriptors (CBF PP) during changes in propofol concentration.

Considering the influence of patient demographics in the causal analysis (**Table 9-2**), the group of patients in which the range of REG Granger-Caused HR showed to be taller than the group of patients not presenting interactions. Additionally, patients with higher BMI tent to present higher prevalence of causality from MAP to the REG slope (α) than those with lower BMI.

Table 9-2 Statistical differences of the hypothesis testing comparing the age, height, weight and BMI of patients presenting causal relationships among pairs of variables during changes in propofol concentration with patients not presenting them.

FROM	TO	DEMOGRAPHIC	P-VALUE	CAUSALITY ↑
Range	HR	height	0.0031	↑height
MAP	Slope (α)	BMI	0.0097	↑BMI

The causality indices and patient demographics did also show statistically significant correlations during changes in propofol effect site concentration (**Table 9-3**). Age proved to be correlated to the causality indices computed from REG features towards MAP, with the highest correlations obtained for the REG slope (α), δrange, CBFest, SDratio and R. Among those, the linear parameters presented increasing causality indices for increasing ages, while for the Poincaré based features the opposite behaviour was detected. Moreover, qCON also showed a causal link towards the REG slope (α) positively correlated with age.

The influence of patient's height in the causality indices was only relevant for the causal links from SDratio and R to MAP, with taller patients presenting higher causality indices. In contrast, weight showed a more determinant role: patients with higher weight presented lower causality indices from CePropo to MAP, from Δtmin to MAP and from CBFest to the EEG α band. Nonetheless, the highest correlations were detected for the causality links from the EEG θ band to Δtmin and AreaSyst, for which patients with higher weight resulted in higher causality indices.

Finally, BMI demonstrated to be relevant in the interactions between REG features and EEG. BMI was positively correlated with the causality indices form the EEG θ band to Δtmin-max and AreaSyst, while it presented a negative correlation with the indices calculated from Δtmin-max and AreaSyst to the δ band.

Table 9-3 Spearman correlation between the causality indices and patient demographic presenting statistical significance ($p<0.01$) during changes of propofol effect site concentration.

FROM	TO	DEMO-GRAPHIC	ρ	P-VALUE	CAUSALITY ↑
Slope (α)	MAP	age	0.523	0.0051	↑age
δrange	MAP	age	0.548	0.0031	↑age
CBFest	MAP	age	0.573	0.0018	↑age
SDratio	MAP	age	-0.553	0.0028	↓age
R	MAP	age	-0.535	0.0040	↓age
qCON	Slope (α)	age	0.574	0.0011	↑age
SDratio	MAP	height	0.537	0.0039	↑height
R	MAP	height	0.543	0.0035	↑height
CePropo	MAP	weight	-0.551	0.0029	↓weight
Δtmin	MAP	weight	-0.577	0.0016	↓weight
θ	Δtmin	weight	0.621	0.0003	↑weight
θ	AreaSyst	weight	0.618	0.0004	↑weight
CBFest	α	weight	-0.537	0.0026	↓weight
θ	Δtmin-max	BMI	0.518	0.0040	↑BMI
θ	AreaSyst	BMI	0.504	0.0054	↑BMI
Δtmin-max	δ	BMI	-0.524	0.0035	↓BMI
AreaSyst	δ	BMI	-0.569	0.0013	↓BMI

9.3.3 Remifentanil infusion

The optimal lags obtained for the caused variable in the analysis of segments in which remifentanil effect site concentration was modified are presented in **Figure 9-19**. No differences between those lags and the ones obtained for steady state anesthesia were detected. In this case, the concentration of remifentanil was included in the lag analysis since it is modified as well over time. However, only causalities from CeRemi towards other variables should be taken into account since, as discussed for CePropo, CeRemi data are the result of the calculation of a theoretical model and are not affected in any way by other physiological data: they only depend on patient demographics.

Results for the y lag analysis are depicted in **Figure 9-20**. Even though lags from previous analysis are preserved, slightly lower lags are obtained for the causal GC interaction among linear and nonlinear features of CBF.

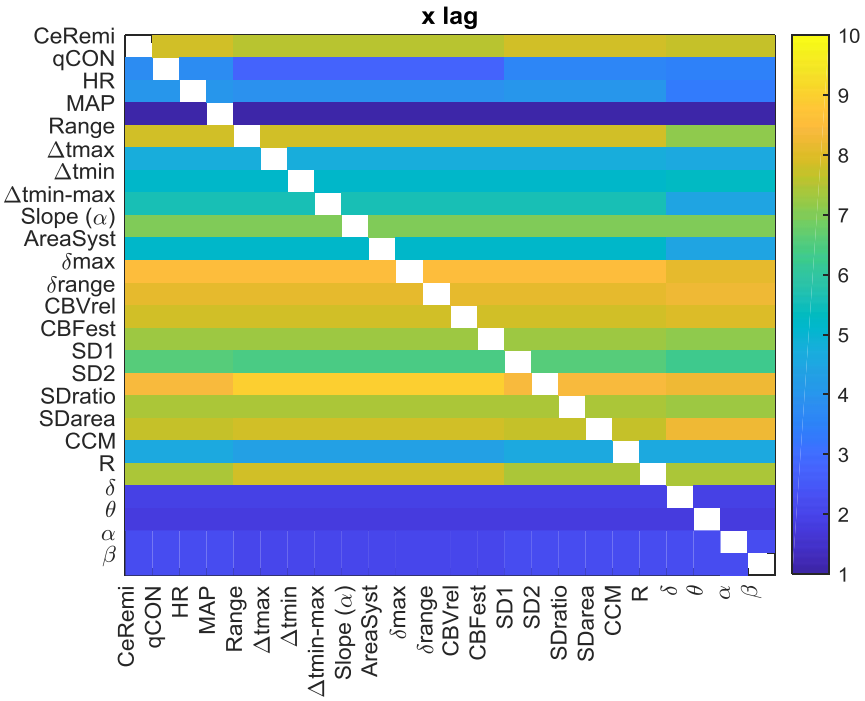

Figure 9-19 Optimal time lags for the GC caused variable (x lag) in the unrestricted AR model during changes in remifentanil concentration. Columns contain the causing variables and rows the caused ones.

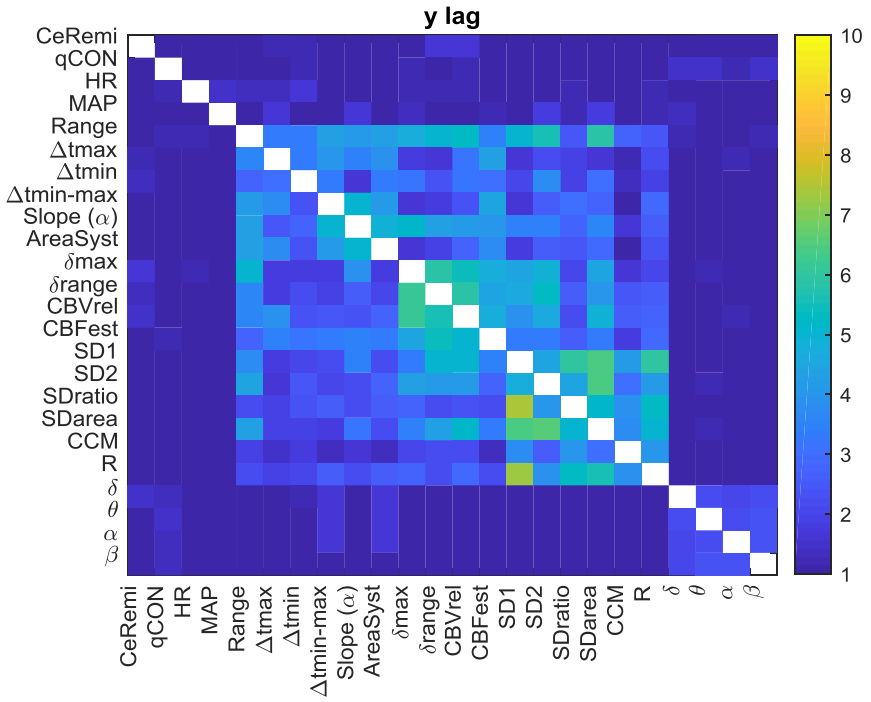

Figure 9-20 Optimal time lags for the GC causing variable (y lag) in the unrestricted AR model during changes in remifentanil concentration. Columns contain the causing variables and rows the caused ones.

Causal interactions from CeRemi towards EEG, global hemodynamics and CBF linear and nonlinear features are depicted in **Figure 9-21**. The effects of CeRemi on EEG variables have occurrences up to 25%, almost inexistent towards the qCON index, but slightly higher for α, θ and δ bands. However, GC relationships between CeRemi and global hemodynamics represented by HR and MAP were more frequent, reaching an incidence of 31% and 38%, respectively. Regarding the causal effects of CeRemi towards the linear features of CBF, the highest occurrences took place in the causality from CeRemi to CBVrel (up to 50%), followed by δrange and δmax (44%). The weakest causality was detected towards Δtmin-max and AreaSyst, and this is one of the main differences when comparing causal effects ellicited by CePropo and CeRemi. Finally, for the REG Poincaré plot descriptors, the most frequent interaction was from CeRemi to SD1, as detected as well in the CePropo analysis, suggesting that changes in remifentanil infusion did also affect short term variability of REG signals.

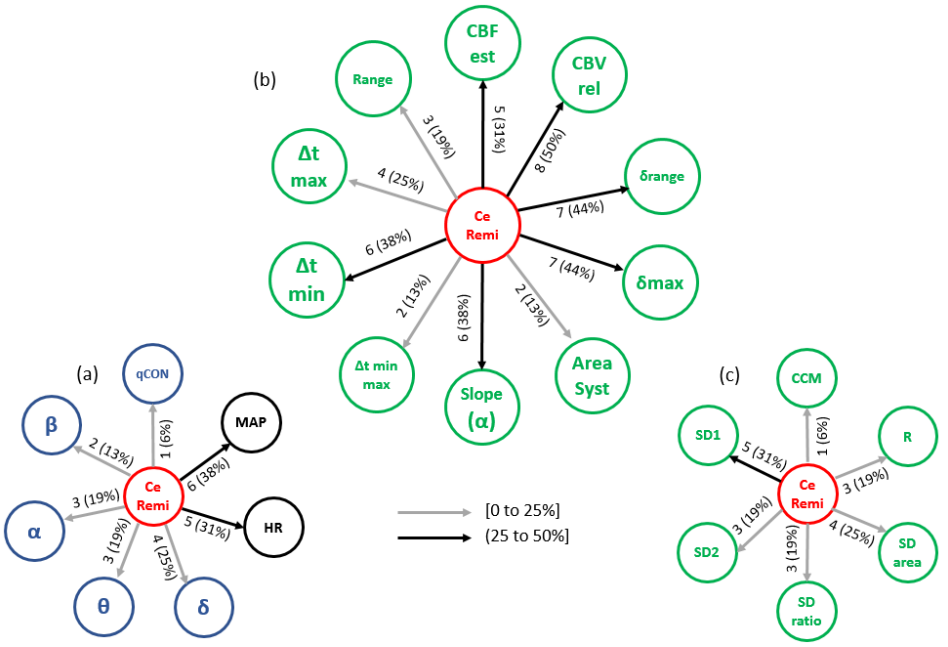

Figure 9-21 Causal interactions from CeRemi to (a) EEG related parameters ang global hemodynamics, (b) REG geometric features and (c) REG Poincaré plot descriptors.

The occurrence of causal interactions between HR, MAP, EEG and CBF linear and nonlinear parameters is presented in **Figure 9-22**. When compared to steady state anesthesia, the causal effects of HR on EEG and CBF linear features are enhanced, as well as the effects of CBF PP on EEG. On the contrary, causal relationships of CBF linear features on EEG have lower occurrence. Moreover, when comparing CeRemi changes to CePropo changes presented in section 9.3.2, causality from HR to EEG is much more frequent under CeRemi analysis, while causality from MAP to EEG decreases, allowing to consider that CePropo modulates EEG changes through MAP while CeRemi influences EEG by means of HR. With respect to other significant differences, it should also be mentioned that CBF linear and nonlinear features have less frequent causal links with EEG variables, when compared to the analysis of CePropo changes. This finding is consistent with the fact that propofol is acting at a cerebral level, reducing brain metabolism, while CeRemi has a less pronounced influence in EEG signals.

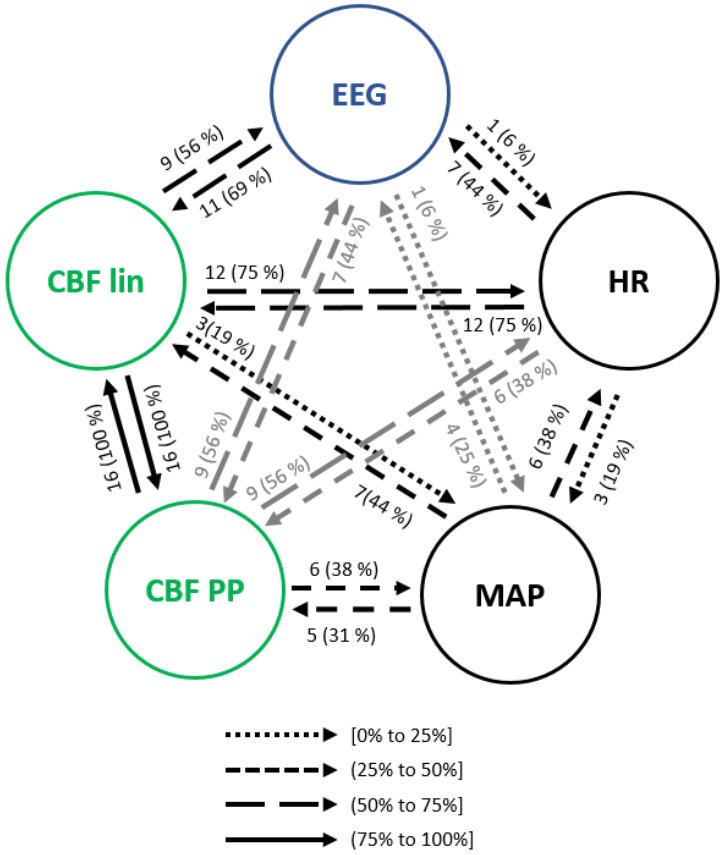

Figure 9-22 Causal interactions between EEG parameters, HR, MAP, REG geometric features (CBF lin) and REG Poincaré plot descriptors (CBF PP) during changes in remifentanil concentration.

No statistically significant differences were detected between patients presenting or not presenting causal relationships among the physiological variables under study. However, the causality indices obtained for several pairs of variables were highly correlated with patient demographics as summarized in **Table 9-4**. Age presented a positive correlation with the causality indices from CCM towards MAP, hence indicating that older patients presented higher causality indices between those two physiological parameters. Nonetheless, patient weight was the demographic variable showing more influence in the causal interactions detected under remifentanil dosage changes. For instance, the causality indices from Δtmin-max and AreaSyst towards HR showed a negative correlation with weight, suggesting that causality from REG to HR is enhanced in patients with lower weight. A

negative correlation was also obtained for the causal link from CBVrel to qCON, from EEG θ band to the slope of REG, and from the δ band to the Poincaré descriptor R, while positive correlations were found for the interactions from α to Δtmax, from β to δmax, from HR to SD1 and from HR to the θ band. Some of those results were replicated for the BMI analysis, namely the causality from β to δmax and from δ to R. Additionally, BMI presented a positive correlation with the causality index from CeRemi to SD2, and a negative one from δ to SDratio.

Table 9-4 Spearman correlation between the causality indices and patient demographic presenting statistical significance ($p<0.01$) during changes of remifentanil effect site concentration.

FROM	TO	DEMOGRAPHIC	ρ	P-VALUE	CAUSALITY ↑
CCM	MAP	age	0.668	0.005	↑age
CBVrel	qCON	weight	-0.698	0.003	↓weight
Δtmin-max	HR	weight	-0.707	0.002	↓weight
AreaSyst	HR	weight	-0.673	0.004	↓weight
α	Δtmax	weight	0.752	0.001	↑weight
θ	Slope (α)	weight	-0.643	0.007	↓weight
β	δmax	weight	0.640	0.008	↑weight
HR	SD1	weight	0.646	0.007	↑weight
δ	R	weight	-0.639	0.008	↓weight
HR	θ	weight	0.672	0.004	↑weight
β	δmax	BMI	0.637	0.008	↑BMI
CeRemi	SD2	BMI	0.645	0.007	↑BMI
δ	SDratio	BMI	-0.658	0.006	↓BMI
δ	R	BMI	-0.695	0.003	↓BMI

Those correlations suggest that links between general hemodynamics, EEG activity and REG descriptors under changes of remifentanil dosage are sensitive to the main characteristics of the patients being monitored, with weight being the key factor to be considered, influencing causality from REG to EEG and HR and from all frequency bands to REG descriptors.

9.3.4 Atropine infusion

Results for the x lag analysis obtained between each pair of variables during atropine infusion are presented in **Figure 9-23**. Differences were detected for all REG features when those were considered as the caused variables, presenting significantly lower time lags than those obtained for steady state anesthesia. However, regarding the EEG bands as caused variables, x lags were slightly increased, suggesting a different coupling under antropine anesthesia.

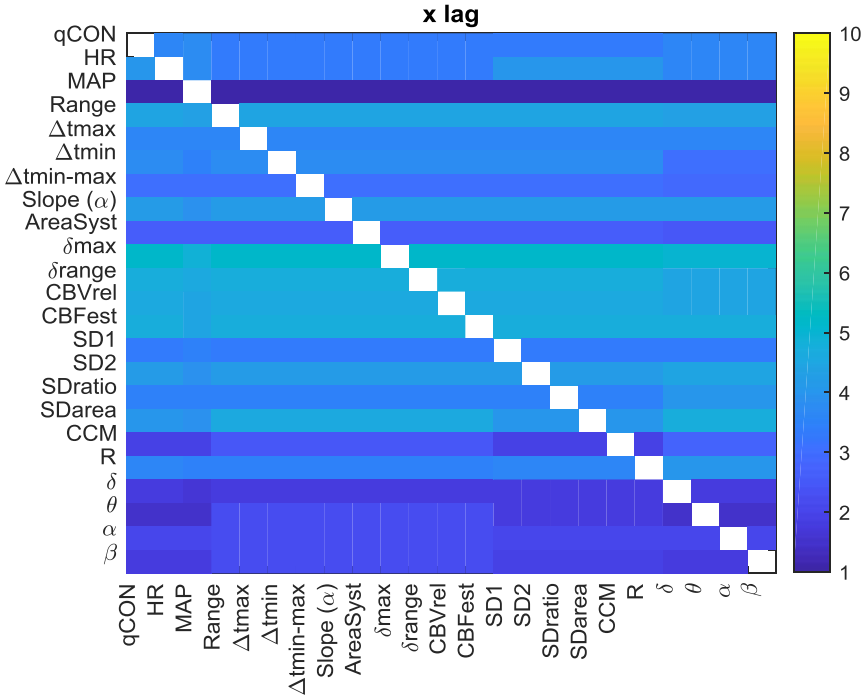

Figure 9-23 Optimal time lags for the GC caused variable (x lag) in the unrestricted AR model during atropine infusion. Columns contain the causing variables and rows the caused ones.

Analogously, those changes were also observed for y lags when compared to steady state anesthesia (**Figure 9-24**). Lags related to REG descriptors were reduced while those associated to the EEG frequency bands were either kept similar or slightly increased.

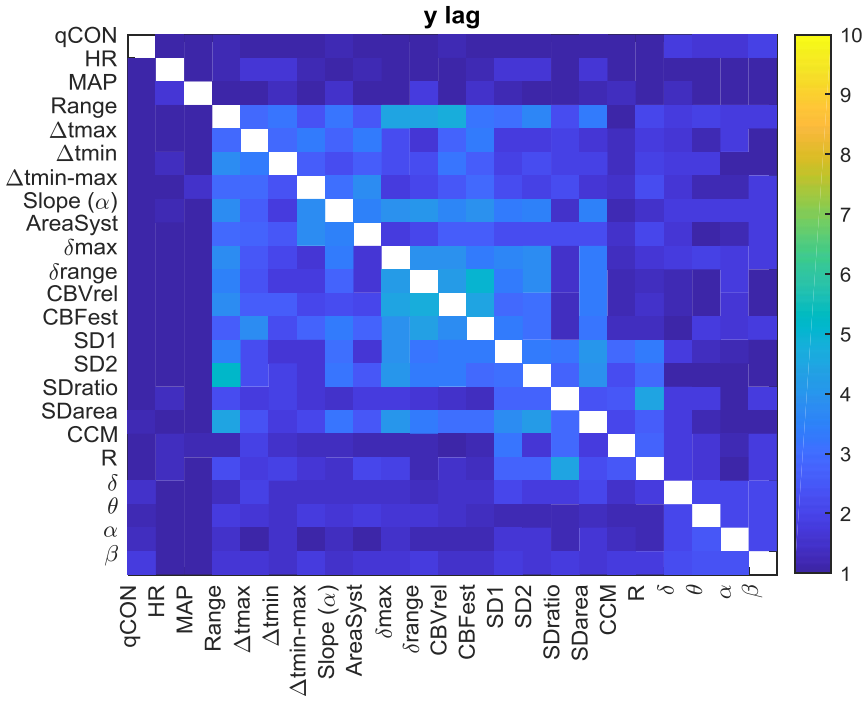

Figure 9-24 Optimal time lags for the GC causing variable (y lag) in the unrestricted AR model during atropine infusion. Columns contain the causing variables and rows the caused ones.

Figure 9-25 presents an overview of the interactions between EEG parameters, HR, MAP and CBF extracted features. Causalities emerging from HR were lower towards MAP and CBF lin when compared to steady state anesthesia, but higher towards CBF PP and EEG. Regarding MAP, the causal link towards CBF PP showed a higher occurrence for atropine infusion, while all other links were detected with a lower frequency. Finally, the analysis of the interactions between EEG and REG descriptors was enhanced during the administration of atropine, suggesting that this drug affects the electrical brain activity.

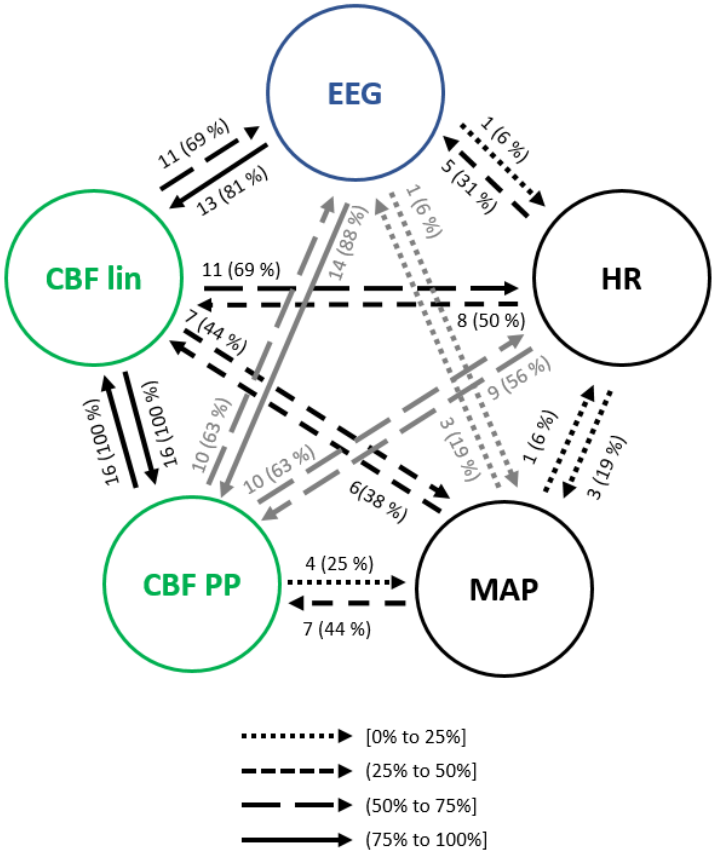

Figure 9-25 Causal interactions between EEG parameters, HR, MAP, REG geometric features (CBF lin) and REG Poincaré plot descriptors (CBF PP) during atropine infusion.

No statistical differences were detected between patients presenting or not presenting causal relationships among the set of variables under study. However, several correlations between the causality indices and the demographic data of the patients were identified as significant (**Table 9-5**). Age presented a negative correlation with the causality indices from qCON to δrange and from MAP to SD1, and a positive one from the REG features Δtmax, Δtmin and SD2 towards the EEG β band. This indicates that older patients present stronger causal links from REG to EEG.

Several correlations between height and the analyzed set of causal links were also found to be significant. For instance, the causality from the EEG α band to Δtmax had a negative correlation with height, while positive correlations were obtained from β to δrange, from θ to SD1, from θ to SDarea

and from HR to θ. Therefore, the links between EEG and CBF features during atropine infusion seem to be dependent on patient height.

Finally, weight was positively correlated with the causality index computed from CBVrel to the EEG δ band, as well as BMI. Additionally, BMI showed positive correlations from δmax, CBFest and SDarea towards the δ band, and from Δtmax towards β. Increased BMI is hence related to enhanced causality from REG features towards electrical brain activity.

Table 9-5 Spearman correlation between the causality indices and patient demographic presenting statistical significance ($p<0.01$) during atropine infusion.

FROM	TO	DEMOGRAPHIC	ρ	P-VALUE	CAUSALITY ↑
qCON	δrange	age	-0.638	0.0079	↓age
MAP	SD1	age	-0.736	0.0027	↓age
Δtmax	β	age	0.780	0.0010	↑age
Δtmin	β	age	0.689	0.0064	↑age
SD2	β	age	0.694	0.0059	↑age
α	Δtmax	height	-0.748	0.0021	↓height
β	δrange	height	0.715	0.0040	↑height
θ	SD1	height	0.693	0.0060	↑height
θ	SDarea	height	0.664	0.0095	↑height
HR	θ	height	0.664	0.0095	↑height
CBVrel	δ	weight	0.679	0.0095	↑weight
δmax	δ	BMI	0.798	0.0010	↑BMI
CBVrel	δ	BMI	0.749	0.0030	↑BMI
CBFest	δ	BMI	0.723	0.0048	↑BMI
SDarea	δ	BMI	0.688	0.0084	↑BMI
Δtmax	β	BMI	0.692	0.0078	↑BMI

9.3.5 Ephedrine infusion

The values obtained for the x lags of the GC unrestricted AR model are presented in **Figure 9-26**. Lags obtained when using the EEG bands as caused variables were similar to those computed for steady state anesthesia and atropine infusion. However, x lags for qCON and HR were higher under ephedrine infusion than for the other two scenarios. With respect to x lags for REG features, the obtained results were lower than for steady state anesthesia intervals but higher than under atropine infusion.

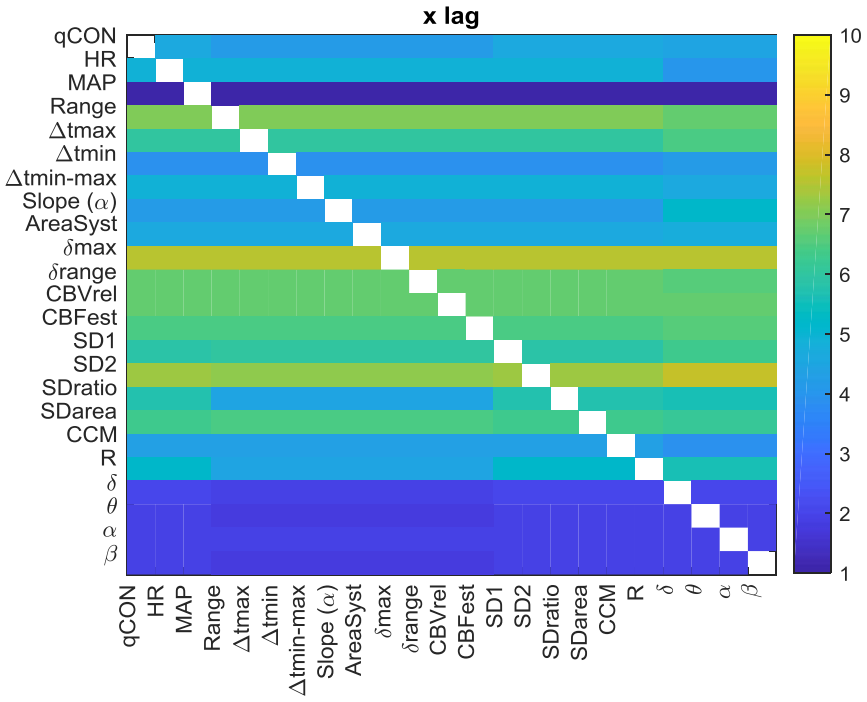

Figure 9-26 Optimal time lags for the GC caused variable (x lag) in the unrestricted AR model during ephedrine infusion. Columns contain the causing variables and rows the caused ones.

Regarding the y lags (**Figure 9-27**), those were slightly lower when compared to steady state anesthesia and to atropine infusion intervals. Especifically, links between REG features and energy in the canonical EEG bands presented lower lag values for ephedrine in both directions.

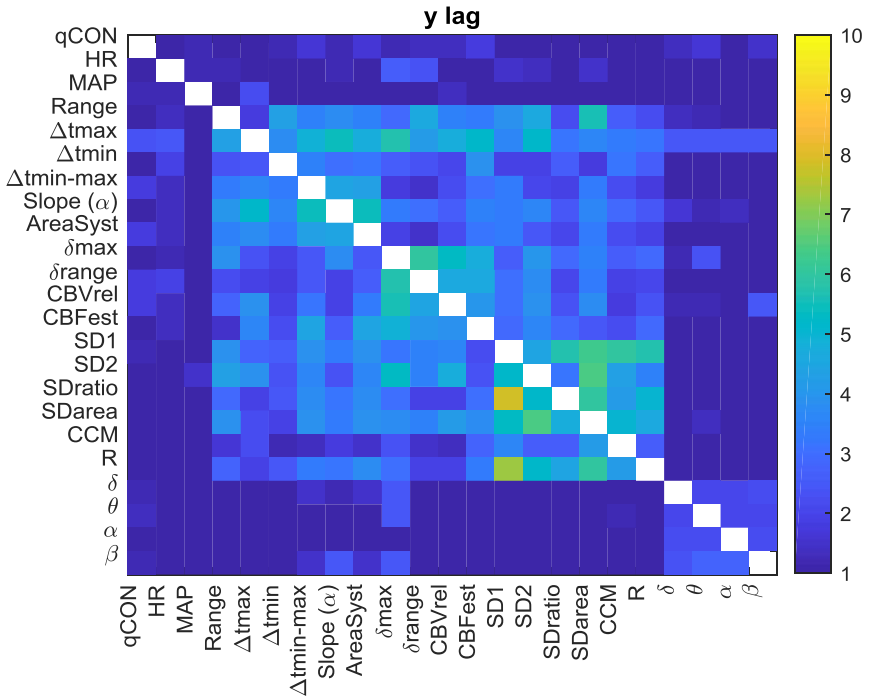

Figure 9-27 Optimal time lags for the GC causing variable (y lag) in the unrestricted AR model during ephedrine infusion. Columns contain the causing variables and rows the caused ones.

As with the previous clinical scenarios analyzed, the interactions between the main sets of physiological variables were analyzed to assess the relationship between hemodynamics and brain activity (**Figure 9-28**). One of the most relevant changes when compared to steady state anesthesia was the occurrence of the EEG causality towards CBF parameters, as well as the one from CBFlin to EEG and all causal links emerging from HR and MAP, suggesting that the cardiovascular effects of ephedrine are also projected in brain activity. Some of those effects were also detected during the infusion of another vasoactive drug, atropine, even though in that case the causalities emerging from MAP and HR were in general lower, while those from EEG to CBF PP and from CBFlin to both MAP and EEG were enhanced.

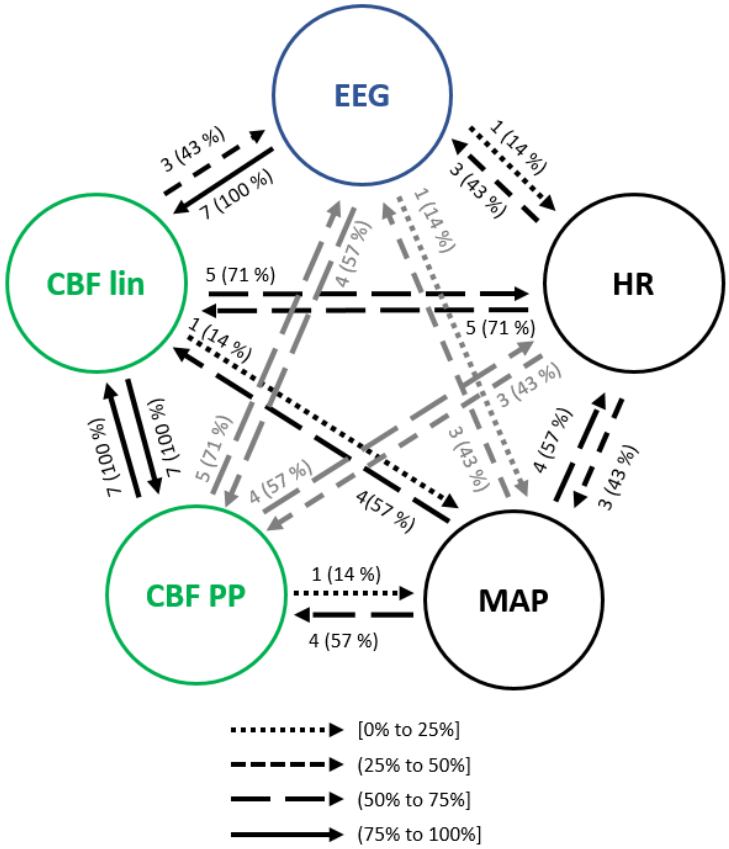

Figure 9-28 Causal interactions between EEG parameters, HR, MAP, REG geometric features (CBF lin) and REG Poincaré plot descriptors (CBF PP) during ephedrine infusion.

No statistical differences were detected between patients presenting and not presenting causal relationships. **Table 9-6** reflects the correlations between the causality indices and patient demographics. Age was not a relevant factor during ephedrine infusion. Decreasing height was associated to increased causality between CCM and the α EEG band. The highest correlation was detected between weight and the cauality index from the EEG δ band towards the REG slope (ρ=-0.955), followed by the one from the δ band towards the REG range (ρ=-0.901). Both correlations were also detected for BMI, suggesting that lower weight and BMI are associated to higher causality from EEG towards CBF features.

Table 9-6 Spearman correlation between the causality indices and patient demographic presenting statistical significance ($p<0.01$) during ephedrine infusion.

FROM	TO	DEMOGRAPHIC	ρ	P-VALUE	CAUSALITY ↑
CCM	α	height	-0.906	0.0095	↓height
δ	Range	weight	-0.955	0.0040	↓weight
δ	Slope(α)	weight	-0.901	0.0095	↓weight
δ	Range	BMI	-0.955	0.0040	↓BMI
δ	Slope(α)	BMI	-0.901	0.0095	↓BMI

9.3.6 Trendelenburg position

The transition of anesthetized patients from a supine position to Trendelenburg was assessed for causality. The x lags (**Figure 9-29**) were in general lower than the ones obtained for steady state anesthesia, with the caused variables Range and SD2 showing the highest x lags across all the possible causing parameters. Moreover, lags when considering HR as the caused variable were higher, mainly when the causing variables were CBF PP and EEG based features. Regarding the values obtained for the lags of the caused variables (**Figure 9-30**), y lags, those are almost coincident with those for steady state conditions, with a small decrease in the lags where interactions between different REG features were involved.

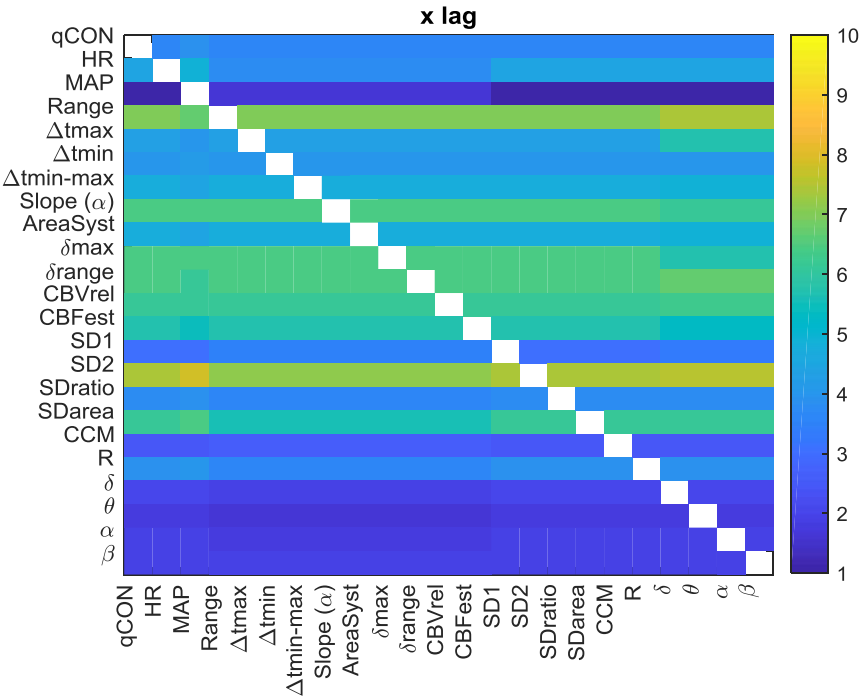

Figure 9-29 Optimal time lags for the GC caused variable (x lag) in the unrestricted AR model during Trendelenburg positioning. Columns contain the causing variables and rows the caused ones.

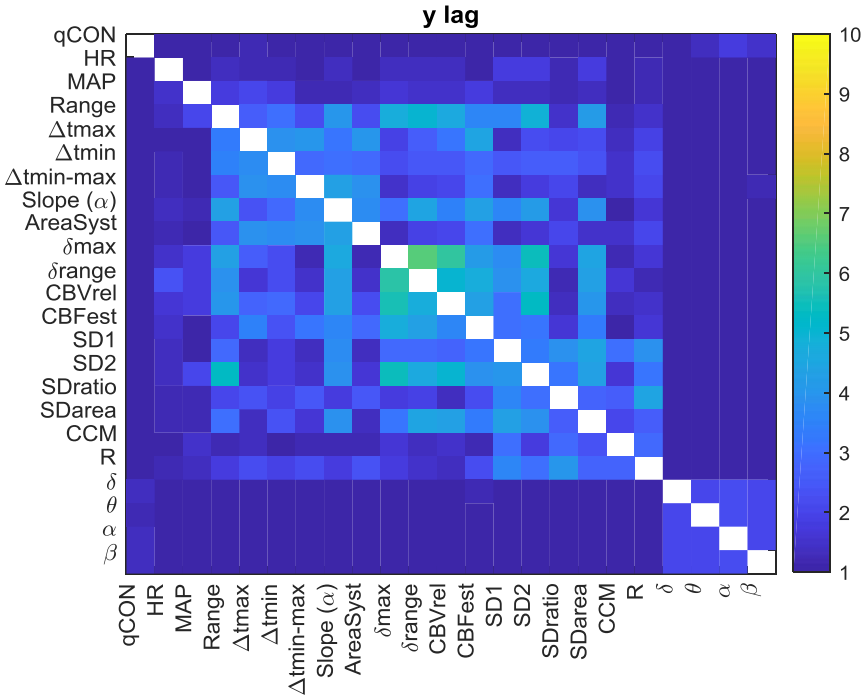

Figure 9-30 Optimal time lags for the GC causing variable (y lag) in the unrestricted AR model during Trendelenburg positioning. Columns contain the causing variables and rows the caused ones.

Considering the interactions between hemodynamics and brain activity signals (**Figure 9-31**), HR showed less influence in MAP when compared to steady state anesthesia, but higher causal effects on CBF features, up to 83% for the linear ones. On the contrary, MAP caused lower interactions than in steady state, except for CBF PP, which were significantly higher. Moreover, while causal links between EEG and CBF PP were enhanced during Trendelenburg positioning when compared to stable anesthesia, links between EEG and CBF linear features showed lower occurrence.

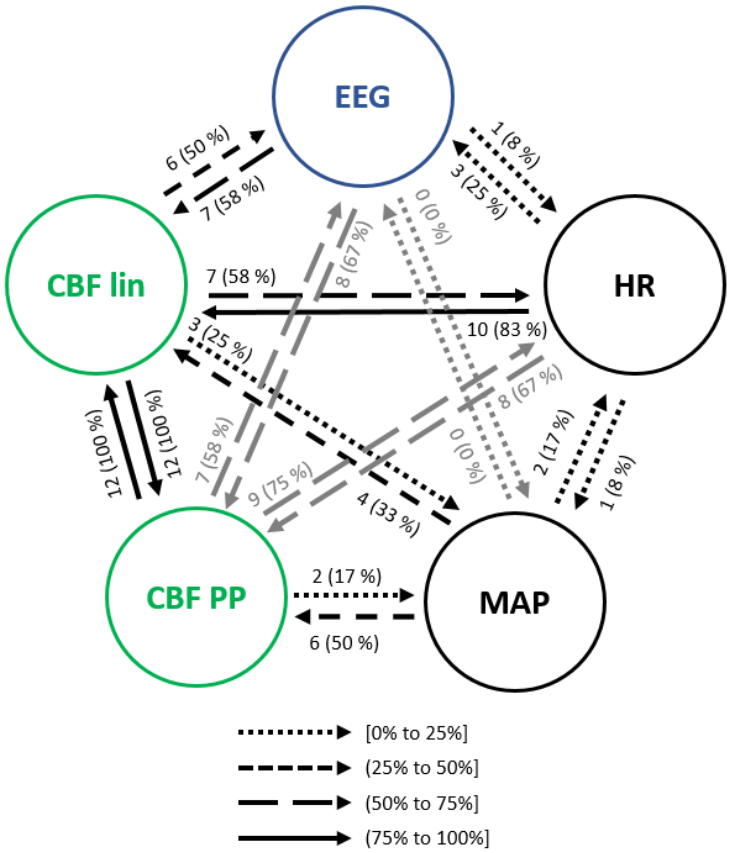

Figure 9-31 Causal interactions between EEG parameters, HR, MAP, REG geometric features (CBF lin) and REG Poincaré plot descriptors (CBF PP) during Trendelenburg positioning.

Regarding the influence of demographic characteristics of the patients in the causal relationships previously analyzed (**Table 9-7**), age showed a high negative correlation with the causality indices from HR to AreaSyst and Δtmin-max, indicating that the younger the patients the higher the causality from HR towards REG features.

The causality index from the depth of anesthesia index, qCON, towards Δtmin-max and AreaSyst was negatively correlated with height, as well as the causality index from CCM to the EEG α band and from HR to β, suggesting that taller patients presented weaker causal links among those pairs of variables. The role of weight was limited to two statistically significant correlations: one from δmax to qCON, presenting higher causality in patients

with less weight, and a second one from MAP to SD2, in which taller patients had higher causality index associated.

Finally, lower BMI was associated to an enhanced causality from several REG features (δmax, δrange and CBVrel) to the qCON index while higher BMI resulted in a stronger causality from δ to Range, from MAP to SD2 and from SD1 to θ.

Table 9-7 Spearman correlation between the causality indices and patient demographic presenting statistical significance ($p<0.01$) during Trendelenburg positioning.

FROM	TO	DEMO-GRAPHIC	ρ	P-VALUE	CAUSALITY ↑
HR	Δtmin-max	age	-0.866	0.0003	↓age
HR	AreaSyst	age	-0.894	0.0001	↓age
qCON	Δtmin-max	height	-0.789	0.0023	↓height
qCON	AreaSyst	height	-0.789	0.0023	↓height
CCM	α	height	-0.732	0.0068	↓height
HR	β	height	-0.732	0.0068	↓height
δmax	qCON	weight	-0.746	0.0053	↓weight
MAP	SD2	weight	0.872	0.0005	↑weight
δmax	qCON	BMI	-0.825	0.0017	↓BMI
δrange	qCON	BMI	-0.769	0.0053	↓BMI
CBVrel	qCON	BMI	-0.769	0.0053	↓BMI
δ	Range	BMI	0.734	0.0091	↑BMI
MAP	SD2	BMI	0.782	0.0070	↑BMI
SD1	θ	BMI	0.769	0.0053	↑BMI

9.3.7 Passive Leg Raise

The x lags obtained for the unrestricted AR model used to calculate GC between all the pairs of physiological variables analyzed are presented in **Figure 9-32**. It can be observed that all lags are lower than 6 for any pair of parameters and, therefore, smaller than those computed for either steady state anesthesia or the Trendelenburg positioning. The same effect takes place for y lags (**Figure 9-33**), even though in that case differences are smaller since those lags already presented small values in the aforementioned states.

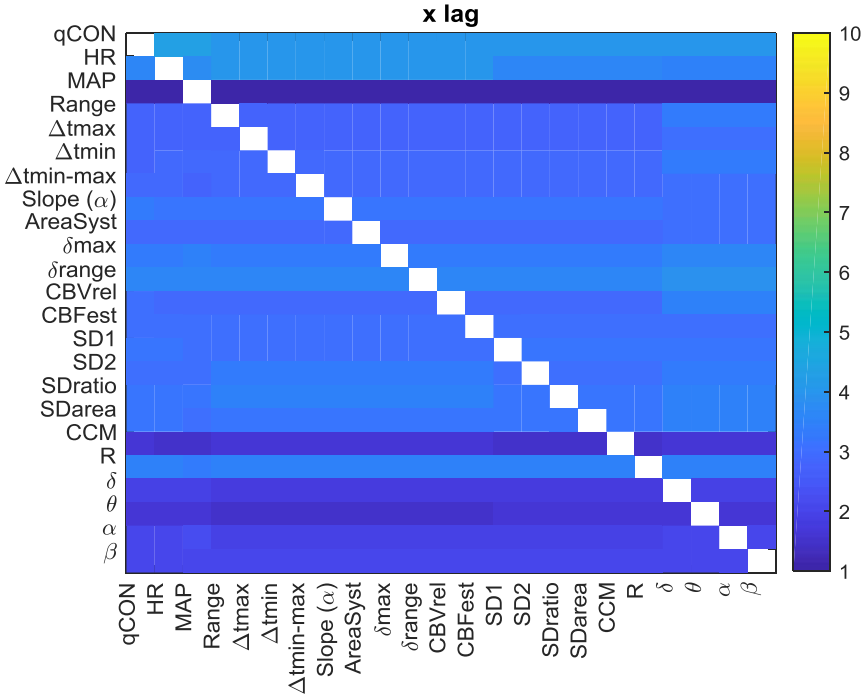

Figure 9-32 Optimal time lags for the GC caused variable (x lag) in the unrestricted AR model during passive leg raising. Columns contain the causing variables and rows the caused ones.

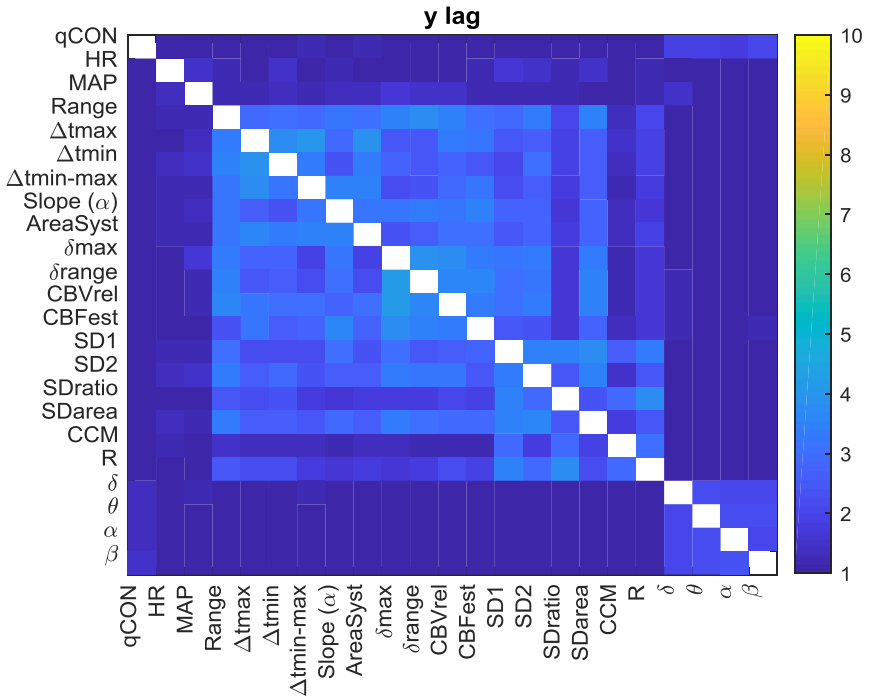

Figure 9-33 Optimal time lags for the GC causing variable (y lag) in the unrestricted AR model during passive leg raising. Columns contain the causing variables and rows the caused ones.

An overview of the global interactions among the physiological systems under study is presented in **Figure 9-34**. Besides the bidirectional link between linear and nonlinear CBF features, the most frequent causality during passive leg raising (PLR) takes place from CBF linear parameters towards EEG, suggesting that changes in cerebral hemodynamics are projected in brain activity. When compared to steady state anesthesia, higher casualities are detected, mainly from HR to CBF PP and EEG, from MAP to CBF features and, bilaterally, between CBF features and EEG. Addtionally, causality from EEG to CBF PP is increased during patient positioning.

Since both Trendelenburg and passive leg raise provoke hemodynamic changes, it is worth comparing the causal interactions between both situations. Causalities emerging from MAP have higher occurrence under passive leg raising, as well as the interactions from CBF features to brain activity variables,

and from EEG to CBF lin. However, causality from EEG to CBF PP is decreased, as well as from HR to CBF parameters.

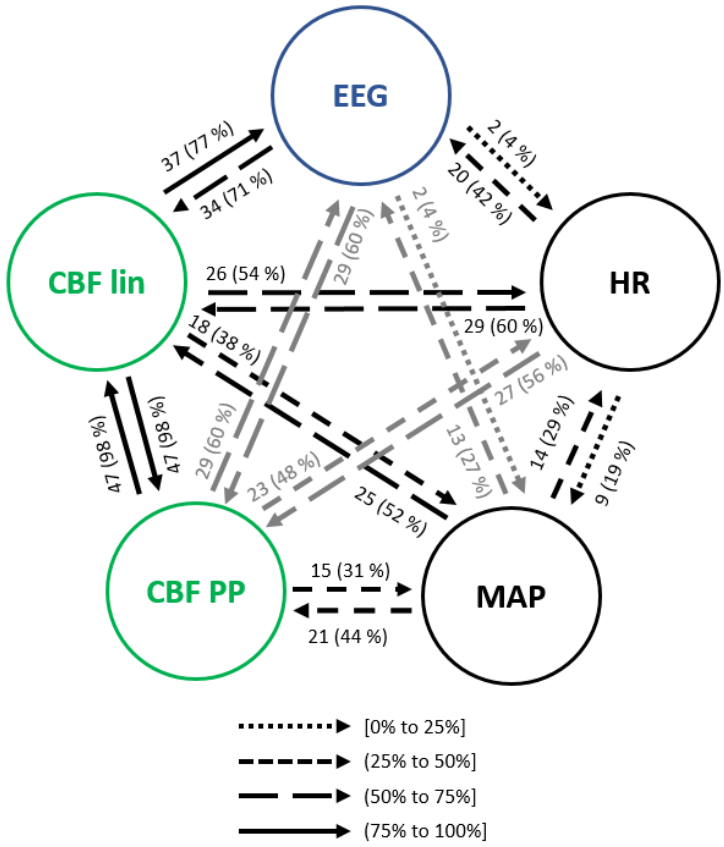

Figure 9-34 Causal interactions between EEG parameters, HR, MAP, REG geometric features (CBF lin) and REG Poincaré plot descriptors (CBF PP) during passive leg raising.

No statistically significant correlations were found between the causality indices and patient demographics, suggesting that the detected interactions were not dependent on patient characteristics. Additionally, patients presenting and not presenting causal relationship did not show any statistical difference in terms of age, height, weight or BMI.

9.4 Discussion

This chapter focused on the causal relationships existing between global hemodynamics, cerebral hemodynamics and EEG activity during steady state anesthesia as well as during certain events occurring during surgery, such as anesthetic concentration changes, the administration of vasoactive drugs and patient positioning.

Even though literature on causal interactions involving REG signals is not available, several studies on brain activity and general hemodynamics describing the so-called heart-brain interactions have been published during both natural sleep and anesthesia. For example, Faes et al. [285] analyzed causal relationships among HRV and EEG during a full night sleep of 10 subjects, observing a strong link between nonlinear beat-to-beat analysis and the power spectrum of the δ EEG band. Analogously, this EEG band was the one found in this study having a more frequent coupling with CBF measurements. A direct comparison of the incidence of this causality is not possible due to two main reasons: Faes and colleagues used the recordings of several hours, performed in 10 patients only, while in this study sample size was of 84 subjects but including only a few minutes of data. Nonetheless, other studies do also support this link between hemodynamics and brain networks, such as the ones presented by Jurysta et al. [306], [307].

A brain-heart causality study during propofol anesthesia was published by Wo et al. [300], concluding that causalities increased with depth of anesthesia and were stronger in the brain-heart direction than from the heart to the brain. Results obtained for the analysis herein presented suggest in fact that the most frequent interactions took place from cerebral hemodynamics to the EEG spectral densities(rather than in the opposite direction), that HR and MAP had closed loop relationships with cerebral hemodynamics and the depth of anesthesia index presented bilateral causal links with cerebral hemodynamics. Even though a larger physiological system was considered in this chapter, the obtained results are not consistent with those presented by Wo et al. Some differences exist in the study design, mainly based on the lowest age of the patients enroled in Wo's study, with a majority of males, and receiving as well midazolam. Further data should be collected under the same circumstances to figure out the root cause of the differences between both studies, since patient demographics have shown to play an important role both in the occurrence of causality and its strength.

Overall, the analysis of causal interactions during steady state anesthesia showed that hemodynamics and EEG activity are closely linked, often under closed loop interactions, and even though there is no consensus on the direction and strength of those links, their existence has been published by several research groups and has turned neurocardiology into a relevant topic under analysis[308], [309].

Besides the study of causal interactions among heart and brain hemodynamics and EEG activity during stable anesthesia periods, changes in the concentration of propofol were also analyzed to assess its influence in these causal links. The effects of propofol on hemodynamics are well-known, characterized by a MAP and HR depression, cerebral vasoconstriction and reduced CBF while preserving CAR[6]. However, no publications regarding the causality between hemodynamics and EEG during the infusion have been found by the author. The study performed in this work reveals that during a change in propofol dosage, the number of interactions between hemodynamics and brain activity increases. Changes in HR and MAP provoked changes in CBF and EEG, with CBF linear and nonlinear features causing EEG modulation. Moreover, one of the strongest links was found between the propofol effect site concentration and the EEG α band, which is consistent with the fact that propofol provokes a shift of the EEG energy towards this band [101]. Additionally, a causal link between the propofol concentration and the qCON index was detected as expected, since changes in hypnotic dosages should translate into changes in depth of anesthesia.

As presented in chapter 2, several propofol pharmacokinetic-pharmacodynamic models are used in routine clinical practice for induction and maintenance of propofol anesthesia. The parameters used in those models are exclusively based on patient demographics but do not take into account hemodynamics. Given the causal relationships between brain activity and hemodynamics, the inclusion of HR, MAP or CBF data in the models would probably make them more patient-specific and improve their accuracies. Several studies have been published on this topic. Sahinovic et al. [310] raised a concern on the use of propofol models in patients with brain tumours, since those might alter propofol kinetics and dynamics and loose accuracy. Furthermore, a new set of models called Physiologically-Based PK Models (PBPK) have been developed to account for the effects of hemodynamics in the currently used compartments models [311], since hemodynamic variables such as cardiac output have shown to be determinant for predicting the effects of propofol infusion [312], [313]. The results for propofol infusion in this work support the hypothesis that those new models

should be key for anesthesia personalization, thus enhancing the accuracy of TCI.

Similar conclusions can be drawn from the analysis of remifentanil concentration changes. The use of remifentanil is associated to depressed hemodynamics, preserving CAR but lowering CBF [6], and its administration together with propofol is known to produce some synergies in the modulation of the EEG waves and resulting depth of anesthesia index [314], [315]. The causal interactions between CeRemi and EEG related parameters revealed that the highest causality took place from CeRemi to the δ frequency band, followed by α, θ and β, but was almost inexistent with the qCON index. Those results are consistent with the EEG spectral analysis under remifentanil infusion published by Kortelainen et al.[316], that highlighted the influence of remifentanil in the EEG spectrogram rather than to limit its effects to synergies with propofol. Hence, remifentanil modified the spectral content of the EEG of the patients under study while the qCON index remained unaffected.

The causal relationships detected during CeRemi changes suggest that its causal effects in EEG, either directly or through hemodynamics, are less pronounced than those obtained for propofol, which is consistent with the fact that propofol is an hypnotic drug while remifentanil is an analgesic. Moreover, HR seems to be the link between CeRemi infusion and brain activity, while MAP played a more relevant role in propofol infusion.

Together with the effects of propofol and remifentanil in the EEG activity, the causal relationships induced by vasoactive drugs such as atropine and ephedrine were also studied in order to find out to which extent those drugs could affect brain activity and depth of anesthesia. Both drugs are often administered during anesthesia to compensante bradycardia and/or hypotension prokoved by hypnotics and analgesics, and are therefore producing HR and MAP increases to achieve hemodynamic stability. The results presented in this chapter provide information supporting the hypothesis that effects of atropine and ephedrine in EEG activity take place through the causal links between MAP, HR and CBF features towards EEG parameters, and vice versa.

In a recently published case study [317], atropine was administered to a patient presenting very low depth of anesthesia values, including EEG suppression and a bradycardia episode. After the atropine infusion,

hemodynamic stability was recovered together with recommended depth of anesthesia values. The authors relate this episode to cerebral hypoperfusion, therefore suggesting that causal interactions exist between hemodynamics and brain activity, and that those are modulated through CBF.

Analogously, Ishiyama et al. reported an increase in the depth of anesthesia index BIS as a consequence of ephedrine administration [318], further supporting the existence of EEG effects of vasoactive drugs due to the existing coupling between hemodynamics and brain activity.

Patient positioning was also considered as a potential factor influencing causal relationships between hemodynamics and EEG activity. Two different positions were assessed besides the standard supine position in steady state anesthesia: Trendelenburg and PLR. Both positioning strategies are known to provoke changes in general hemodynamics, mainly in MAP [319] [320], but information on their influence in EEG is scarce. Mallick et al. [321] reported the dependence between the depth of anesthesia index and the steepness of the Trendelenburg position, establishing a relationship between both variables. Considering the causal occurrences calculated in this work, HR and MAP do not seem to modulate directly EEG changes, but through alterations in CBF features that are further projected into EEG activity.

As part of the causality analysis, the role of patient demographics was assessed through correlation and hypothesis testing. Patient characteristics such as age, height, weight and BMI should be taken into account since those might enhance or prevent the existence of causal relationships and the intensity of the existing causal effects. For instance, during steady state anesthesia, lower ages were associated to a higher occurrence of causal links from CBF to EEG, as well as lower weight and BMI. However, the size of the database under study impaired a more detailed analysis of patient demographics in heart-brain links during anesthesia, being one of the limitations of this study.

Other limitations that should be noted are the low number of recordings for some of the analyzed events, such as atropine or ephedrine infusions, and the concomitant effects of different factors, as for example patient positioning taking place before or after a drug dosage change or the administration of a vasoactive drug. For example, the Schnieder model was used for the calculation of CePropo, while some authors have suggested that the ke0 time effect constant in this model should be larger [104]. This would imply that causal effects of CePropo are assessed with inaccurate time lags and therefore do not reflect the real brain effect of propofol but a faster version provided

by the models. Finally, all patients enrolled in the clinical trial were women, therefore not allowing to extend the conclusions to a generic population.

During the causality study, linear and nonlinear CBF features have been independently considered in order to assess their individual performance. Even though they showed a 100% of causal effects among them in the majority of events under test, they revealed different occurrences of causal relationships with brain activity and global hemodynamics. As an example, during propofol infusion, bilateral causality between linear CBF features and HR was much more frequent than between Poincaré plot descriptors of REG signals and HR, while those showed similar values during steady state anesthesia. In contrast, during atropine infusion, effects of MAP on CBF parameters were more frequent towards the Poincaré descriptors. The use of a larger dataset would allow to further compare the performance of both algorithms, but results herein presented suggest that they are closely related to each other but the integration of the information contained in both sets of features improves the assessment of causality.

9.5 Conclusions

As a conclusion, results from this study confirm the hypothesis that during general anesthesia causal interactions among global hemodynamics, cerebral hemodynamics and EEG neural activity take place. And, as a consequence, clinial decisions made to achieve hemodynamical stability have effects at a neural level, as well as changes in anesthetic dosages would interfere both in global and brain hemodynamics.

REG signals provided an assessment of brain hemodynamics, with both linear and nonlinear features contributing to the heart-brain interactions, revealing its potential as a monitoring tool for anesthesia management. Even though CBF estimators are not able to accurately predict anesthetic depth on their own as shown in Chapter 8, they contain information allowing to understand the coupling between hemodynamics and neural activity, and should therefore be integrated in routine clinical care, mainly in patients in which causal relationships might be impaired or altered due to pathological or intrinsic conditions, such as brain tumours or obesity, respectively.

Chapter 10

Conclusions and Future Work

Abstract

In this chapter, the most important contributions and findings of this Doctoral Thesis are summarized and discussed, highlighting the key concepts and limitations of the REG signal's ability to detect CBF changes during anesthetic procedures. Furthermore, to overcome the aforementioned limitations, several topics deserving further work are described.

10.1 Conclusions

The main objective of this Thesis was to assess the possibility to use rheoencephalography (REG) technology to track cerebral blood flow (CBF) changes during general anesthesia, applying advanced signal processing techniques for that purpose. In order to provide an answer to this research question, a roadmap with intermediate milestones was designed.

Firstly, a literature review of other CBF monitoring solutions was presented in Chapter 2, showing that the most accurate ones are invasive, while those adapted to routine clinical pratice are often surrogates of CBF, such as near infrared spectroscopy (NIRS) or Transcranial Doppler. This scenario places REG as a candidate to fill the gap of a cost effective, real time, noninvasive, bedside CBF monitor. However, previous publications on REG based on the extraction of linear features from the time domain representation of the signal showed poor correlations with clinical outcomes. For that reason, a review of possible techniques to be applied to REG recordings was performed, finally chosing Poincaré plot analysis and Entropy metrics as the two algorithms to be analyzed in this project, together with the classical approach of geometric features extraction.

Due to the noise typically embedded in physiological signals, before the application of any of the three aforementioned solutions, a filtering strategy was needed to cancel the noise in the recorded signals. Two options were assessed: classical time domain filters and a nonlinear filtering algorithm applied to the reconstructed attractor of REG signals. The comparison of those two filtering techniques showed that the nonlinear algorithm presented better performance assessed by the percentage root-mean-square error (PRD), especially in very noise datasets. However, there is a tradeoff between the accuracy in the recovered signals and the exectution time of the filters, with the linear filter showing a significantly smaller computational complexity. Therefore, both filtering options were used prior to the application of the geometric, Poincaré and Entropy processing to evaluate their effect in the information extracted from REG signals.

The first technique to be tested was the extraction of geometric features in the time domain, which was considered as a reference since it is the standard methodology followed in REG signal processing. A first feasibility test was performed using a respiration challenge to assess the ability of REG features to detect apneas. Only one of the paremeters, the systolic area of the pulse wave, showed significant differences between apnea and baseline recordings,

while all others remain unchanged or presented changes smaller than the variabiliy of their values. Despite of this poor outcome, the same geometric features were used to identify different anesthetic states in REG data recorded from surgical procedures under general anesthesia. Under this scenario, many parameters provided statistically significant differences, mainly in the identification of the transition between loss of consciousness (LOC) and steady state anesthesia. No clear advantages were found for the application of the nonlinear filter, thus suggesting that the linear filter would be a better option in a real time REG based monitor.

The second technique to be tested was the Poincaré plot analysis. The steps taken to process REG signals were analogous to those used for the standard processing through geometrical features. A first study in the REG signals recorded during apnea challenges showed that the performance of the Poincaré plot descriptors was better than the one obtained with the extraction of geometric features. This finding was key in the development of this research, since it demonstrated that nonlinear features outperformed the linear analysis and therefore new information could be obtained from REG signals that, to the extent of our knowledge, had not been explored before. Due to their relevance, the results from this analysis were compiled and published in an indexed journal. The Poincaré plot descriptors were also extracted from REG signals collected during general anesthesia and were able to identify differences among the states Awake, LOC and steady state anesthesia, both using the linear and nonlinear filters.

The third technique applied to REG recordings was based on the calculation of Entropy metrics. This strategy resulted in higher computational costs due to the calculation of the correlation integral, thus compromising its use in real time monitoring scenarios. As with the other two signal processing techniques, a first assessment was performed with signals recorded during apnea and baseline periods, followed by the analysis os REG signals collected during anesthetic procedures. Results were similar to those obtained for the Poincaré plot analysis, outperforming the geometrical features approach, and due to this relevance, were also published. Detection of apnea and differences among the anesthetic state of Awake, LOC and steady state anesthesia were possible through the entropy metrics proposed, namely by means of Approximate Entropy (ApEn) and Fuzzy Entropy (FuzzyEn).

The comparison of the three processing methods suggested that the extraction of the geometric features was not optimal to detect CBF changes in REG signals, presenting poor results for apnea detecton but similar results to the other two techniques for data recorded during anesthesia. The choice of the algorithm to be used for processing was much more relevant than the choice for the linear and nonlinear filter, which presented very limited impact in the obtained results. It should be noted that despite the statistically significant differences detected for many descriptors from the three types of analysis, they all presented large variabilities. Those might be due to the noise and fluctuations of the recorded signals as well as to the variability among patients. For that reason, age, weight, height and body mass index (BMI) were considered as potential confounding factors and the correlations between these demographic data and REG descriptors were caclulated. Age, weight and BMI were often correlated with the extracted features and their rates of change among anesthetic states, suggesting that patient characteristics influence the information on CBF carried by REG signals. Moreover, other clinical variables collected during anesthesia also provided significant correlations with the changes in the selected descriptors. The anesthetic depth assessed by the qCON index, heart rate (HR), mean arterial pressure (MAP) and the propofol dosage were correlated with the rates of change of the descriptors, as well as the remifentanil dosages even though, in this case, to a lesser extent.

Therefore, the geometric features extraction, the Poincaré plot descriptors and entropy metrics were able to track CBF changes provoked by an apnea challenge and different anesthetic states, influenced by patient characteristics and other physiological systems. Those results were considered promising for the use of REG in depth of anesthesia monitoring. Thus, the variables suitable for real time monitoring (geometric features and Poincaré plot descriptors, obtained from linearly filtered data) were used as inputs for a classifier aiming at assessing patient's wakefulness in anesthetic procedures. The obtained accuracy was limited, reaching a value of 70%, suggesting that REG features by themselves could not identify the wakefulness of the patients under general anesthesia. However, this accuracy was considered high enough to include the use of REG combined with other physiological data for patient monitoring during anesthetic procedures.

The causal relationships between REG signals and other physiological data were assessed to explore the adequacy and need for REG monitoring during surgery. Overall, considering all the surgical procedures, interactions between general hemodynamics, brain hemodynamics and

electroencephalographic activity (EEG) were detected, confirming the hypothesis that CBF is linked to both the hemodynamic stability and the brain activity modulated by anesthetic drugs. Additionally, specific events during the anesthetic procedures were analyzed as well, such as drug infusion, patient positioning and the administration of vasoactive drugs. In all those cases, causal interactions were detected, showing that decisions on drug dosages and patient positioning should be made considering both the hemodynamic stability and depth of anesthesia simultaneously, since hemodynamic changes might induce brain activity levels to increase or decrease, and viceversa.

Those findings confirm the initial hypothesis, showing that REG signals do carry information on CBF that would be useful for depth of anestheia monitoring. Some limitations should however be considered. Firstly, all patients participating on the general anesthesia based clinical trials were females, thus limiting the obtained results to this population. Secondly, REG outcomes were not cross validated with a widely accepted CBF monitor. The noninvasive monitors available in the market are usually CBF surrogates and, without prior evidence, decision was made not to perform a clinical trial with invasive methods due to ethical reasons. However, this Thesis provides enough background to justify the comparison with invasive and accurate CBF measurements to explore the possibility of using REG for standard clinical practice CBF monitoring.

The limitations herein mentioned have been used to define the future work priorities, to enhance the validity of the results obtained in this Doctoral Thesis. Nonetheless, the analyses developed so far have been key from a scientific, clinical and business perspective. From a scientific perspective, the results of this research project justify a new opportunity for REG signals, since the application of advanced signal processing techniques has shown to be effective in tracking CBF information embedded in REG recordings. Moreover, the interaction among different physiological networks has been further assessed and quantified, contributing to the knowledge on the effects of anesthetics in the brain and the mechanisms cooperating to achieve a succesful and stable anesthetic state. Considering the clinical benefits, CBF monitoring through REG could be extended to all kind of patients, even to those initially at low risk, making it possible to reduce the occurrence of adverse events that might sometimes have deleterious effects for patients.

Last, but not least, this research project has business implications. In addition to the publication of a patent, those results support the possibility of using an existing cardiac output monitor manufactured by Quantium Medical for CBF monitoring, broadening the clinical claims and applications of this medical device.

10.2 Future work

Even though the main findings herein described are promising for REG inclusion in standard clinical practice, further studies are needed to confirm this. For instance, the causal relations between EEG based variables and cerebral hemodynamics should be validated in larger databases including participants from both genders. Moreover, the clinical data used for development and validation in this Thesis are limited to anesthetic procedures performed under propofol and remifentanil total intravenous anesthesia (TIVA), and therefore clinical trials under other anesthetic regimens should be carried out as well to extend the potential use of REG to all anesthetic options.

Nonetheless, the main challenge should be validating REG outcomes with other CBF monitors available in the market. The most commonly used for bedside monitoring are surrogates of CBF, such as CBF velocity (CBFv) or NIRS, and a validation against those would not have allowed a conclusion on the feasibility of REG for CBF monitoring. The most accurate ones, such as Xenon-based methods, are invasive, and were not ethically justified without prior data supporting the advantages of using REG. The outcome of this Thesis provides evidence suggesting the utility of REG monitoring and therefore opens the possibility for interventional clinical trials that should be carried out. Moreover, those trials should integrate information on respiration, expired CO2 and blood density of each patient, to turn the relative measurements herein presented in absolute CBF values.

Furthermore, other applications besides anesthetic procedures could benefit from the use of REG, such as critically ill subjects and /or patients with brain tumors or trauma. In this research field, clinical trials are also being considered to evaluate the capabilities of REG under those circumstances, to integrate this low-cost technology in diagnostic flows to improve patient care.

Publications, Patents and Conference Contributions

Publications

González, C.; Jensen, E.W.; Gambús, P.L.; Vallverdú, M. Poincaré plot analysis of cerebral blood flow signals: Feature extraction and classification methods for apnea detection. PLoS One 2018, 13, e0208642

González, C.; Jensen, E.; Gambús, P.; Vallverdú, M. Entropy Measures as Descriptors to Identify Apneas in Rheoencephalographic Signals. Entropy 2019, 21, 605,e21060605.

Patents

C.González, E.W.Jensen. System and method for estimating the brain blood volume and/or brain blood flow and/or depth of anesthesia of a patient (2017). Patent Application Number EP17382364.2.

Conference Contributions

Escrivá Muñoz J, Galea Cazorla A, González Pijuan C, Vallverdú M, Caminal P, Jensen EW (2016). Generación de bioseñales sintéticas mediante series de Fourier variantes en el tiempo. XXXVII Jornadas de Automática, Madrid.

C.González, E.W.Jensen. P.L.Gambús M.Vallverdú. Cerebral blood flow changes assessed by system complexity measures applied to cerebral bioimpedance signals, International Society for Anaesthetic Pharmacology (ISAP) 2017, Boston, US.

References

[1] M. J. Cipolla, *The Cerebral Circulation*. Morgan & Claypool Life Sciences, 2009.

[2] E. Moss, "The cerebral circulation," *Contin. Educ. Anaesthesia, Crit. Care Pain*, vol. 1, no. 3, pp. 67–71, 2001.

[3] Z. Vrselja, H. Brkic, S. Mrdenovic, R. Radic, and G. Curic, "Function of circle of Willis.," *J. Cereb. Blood Flow Metab.*, vol. 34, no. 4, pp. 578–84, 2014.

[4] F. Walters, "Neuropharmacology - Intracranial Pressure and Cerebral Blood Flow," *Physiology*, vol. 8, pp. 29–37, 1998.

[5] L. Hill, S. Anaesthesia, R. O. Hospital, C. Gwinnutt, C. Neuroanaesthetist, and H. Hospital, "CEREBRAL PHYSIOLOGY PART 1 - CEREBRAL BLOOD FLOW AND PRESSURE ANAESTHESIA TUTORIAL OF THE WEEK 69 1 ST OCTOBER 2007 Part 1 : Cerebral Blood Flow," *Blood*, no. October, pp. 1–8, 2007.

[6] A. Dagal and A. M. Lam, "Cerebral autoregulation and anesthesia.," *Curr. Opin. Anaesthesiol.*, vol. 22, pp. 547–552, 2009.

[7] M. T. Mullen, J. S. McKinney, and S. E. Kasner, "Blood pressure management in acute stroke," *J. Hum. Hypertens.*, vol. 23, no. 9, pp. 559–569, 2009.

[8] A. Zauner and J. P. Muizelaar, "Brain metabolism and cerebral blood flow," *Head Inj.*, pp. 90–99, 1997.

[9] H. M. Shapiro, "Intracranial HypertensionTherapeutic and Anesthetic Considerations," *J. Am. Soc. Anesthesiol.*, vol. 43, no. 4, pp. 445–471, 1975.

[10] P. T. Fox and M. E. Raichle, "Focal physiological uncoupling of cerebral blood flow and oxidative metabolism during somatosensory stimulation

in human subjects.," *Proc. Natl. Acad. Sci. U. S. A.*, vol. 83, no. February 1986, pp. 1140–4, 1986.

[11] M. A. Mintun, B. N. Lundstrom, A. Z. Snyder, A. G. Vlassenko, G. L. Shulman, and M. E. Raichle, "Blood flow and oxygen delivery to human brain during functional activity: theoretical modeling and experimental data.," *Proc. Natl. Acad. Sci. U. S. A.*, vol. 98, no. 12, pp. 6859–6864, 2001.

[12] T. Westermaier *et al.*, "Controlled Hypercapnia Enhances Cerebral Blood Flow and Brain Tissue Oxygenation After Aneurysmal Subarachnoid Hemorrhage: Results of a Phase 1 Study," *Neurocrit. Care*, vol. 25, no. 2, pp. 205–214, 2016.

[13] E. B. Ringelstein, S. Van Eyck, and I. Mertens, "Evaluation of cerebral vasomotor reactivity by various vasodilating stimuli: comparison of CO2 to acetazolamide," *J. Cereb. Blood Flow Metab.*, vol. 12, no. 1, pp. 162–168, 1992.

[14] M. E. Raichle and F. Plum, "Hyperventilation and cerebral blood flow.," *Stroke.*, vol. 3, no. 5, pp. 566–575, 2015.

[15] G. Settakis, A. Lengyel, C. Molnár, D. Bereczki, L. Csiba, and B. Fülesdi, "Transcranial Doppler Study of the Cerebral Hemodynamic Changes During Breath-Holding and Hyperventilation Tests," *J. Neuroimaging*, vol. 12, no. 3, pp. 252–258, 2002.

[16] S. S. Kety and C. F. Schmidt, "The effects of active and passive hyperventilation on cerebral blood flow, cerebral oxygen consumption, cardiac output, and blood pressure of normal young men," *J. Clin. Invest.*, vol. 25, no. 1, p. 107, 1946.

[17] A. Kastrup, T.-Q. Li, G. H. Glover, and M. E. Moseley, "Cerebral Blood Flow-Related Signal Changes during Breath-Holding," *Am. J. Neuroradiol.*, vol. 20, no. 7, pp. 1233–1238, 1999.

[18] F. Molinari, W. Liboni, G. Grippi, and E. Negri, "Relationship between oxygen supply and cerebral blood flow assessed by transcranial Doppler and near-infrared spectroscopy in healthy subjects during breath-holding," *J. Neuroeng. Rehabil.*, vol. 3, no. 1, p. 16, 2006.

[19] A. Kastrup, G. Krüger, T. Neumann-Haefelin, and M. E. Moseley, "Assessment of cerebrovascular reactivity with functional magnetic resonance imaging: comparison of CO(2) and breath holding.," *Magn. Reson. Imaging*, vol. 19, no. 1, pp. 13–20, 2001.

[20] S. Kety and C. F. Schmidt, "The determination of cerebral blood flow in man by the use of nitrous oxide in low concentrations.," *Am. J. Physiol.*,

vol. 143, pp. 53–66, 1945.

[21] B. A. Sutherland, T. Rabie, and A. M. Buchan, “Laser Doppler flowmetry to measure changes in cerebral blood flow,” *Cereb. Angiogenes. Methods Protoc.*, pp. 237–248, 2014.

[22] O. M. Henriksen *et al.*, “Sources of Variability of Resting Cerebral Blood Flow in Healthy Subjects: A Study Using ^{133} Xe SPECT Measurements,” *J. Cereb. Blood Flow Metab.*, vol. 33, no. 5, pp. 787–792, 2013.

[23] J. A. Friedman and R. E. Anderson, “Techniques of intraoperative cerebral blood flow measurement,” *Neurosurg. Focus*, vol. 9, no. 5, pp. 1–5, 2000.

[24] C. A. Giller, P. Purdy, and W. W. Lindstrom, “Effects of inhaled stable xenon on cerebral blood flow velocity.,” *Am. J. Neuroradiol.*, vol. 11, no. 1, pp. 177–182, 1990.

[25] A. Zauner and J. P. Muizelaar, “Measuring cerebral blood flow and metabolism,” *Head Inj.*, pp. 217–27, 1997.

[26] M. Sethuraman, “Cerebral blood flow monitoring,” *J. Neuroanaesth. Crit. Care*, vol. 2, no. 3, p. 204, 2015.

[27] R. Kumar and J. A. Friedman, “Intraoperative angiography during cerebral aneurysm surgery,” *Neurocrit. Care*, vol. 11, no. 2, pp. 299–302, 2009.

[28] A. Sheinfeld and A. Eyal, “Photoacoustic thermal diffusion flowmetry,” *Biomed. Opt. Express*, vol. 3, no. 4, p. 800, 2012.

[29] S. Tewolde, K. Oommen, D. Y. C. Lie, Y. Zhang, and M.-C. Chyu, “Epileptic Seizure Detection and Prediction Based on Continuous Cerebral Blood Flow Monitoring--a Review,” *J. Healthc. Eng.*, vol. 6, no. 2, pp. 159–178, 2015.

[30] P. Vajkoczy, M. Schomacher, M. Czabanka, and P. Horn, “Monitoring Cerebral Blood Flow In Neurosurgical Intensive Care,” *Eur. Neurol. Dis.*, vol. 1, no. 2, pp. 8–10, 2007.

[31] S. Amin-Hanjani, G. Meglio, R. Gatto, A. Bauer, and F. T. Charbel, “The Utility of Intraoperative Blood Flow Measurement During Aneurysm Surgery Using an Ultrasonic Perivascular Flow Probe,” *Neurosurgery*, vol. 62, no. Supplement 3, p. SHC1346-SHC1353, 2008.

[32] T. Durduran and A. G. Yodh, “Diffuse correlation spectroscopy for non-invasive, micro-vascular cerebral blood flow measurement,” *Neuroimage*, vol. 85, pp. 51–63, 2014.

[33] C. Lindner *et al.*, “Cerebral metabolism and blood flow during bispectral index-controlled, propofol-induced anesthesia assessed by hybrid diffuse optics,” in *Clinical and Translational Biophotonics*, 2016, p. JW3A--29.

[34] E. Carrero, U. Weigel, J. Tercero, C. Lindner, P. Zirak, and N. Fabregas, “Noninvasive monitoring of cerebral blood flow in healthy volunteers:‘beach chair’ and hypercapnia challenges: 7AP3-10,” *Eur. J. Anaesthesiol.*, vol. 31, p. 116, 2014.

[35] R. M. Schell and D. J. Cole, “Cerebral monitoring: jugular venous oximetry.,” *Anesth. Analg.*, vol. 90, no. 3, pp. 559–566, 2000.

[36] K. Obtulowicz, “Bradykinin-mediated angioedema,” *Pol. Arch. Med. Wewn.*, vol. 126, no. 1–2, pp. 76–85, 2016.

[37] J. E. Desmedt and G. Cheron, “Central somatosensory conduction in man: neural generators and interpeak latencies of the far-field components recorded from neck and right or left scalp and earlobes.,” *Electroencephalogr. Clin. Neurophysiol.*, vol. 50, no. 5–6, pp. 382–403, Dec. 1980.

[38] F. F. Jobsis, “Noninvasive, infrared monitoring of cerebral and myocardial oxygen sufficiency and circulatory parameters,” *Science (80-.).*, vol. 198, no. 4323, pp. 1264–1267, 1977.

[39] J. M. Murkin and M. Arango, “Near-infrared spectroscopy as an index of brain and tissue oxygenation,” vol. 103, pp. 3–13, 2009.

[40] P. Taussky *et al.*, “Validation of frontal near-infrared spectroscopy as noninvasive bedside monitoring for regional cerebral blood flow in brain-injured patients,” *Neurosurg. Focus*, vol. 32, no. 2, p. E2, 2012.

[41] F. Hyder, R. G. Shulman, D. L. Rothman, R. G. Shulman, and L. Douglas, “A model for the regulation of cerebral oxygen delivery,” pp. 554–564, 1998.

[42] E. Ohmae *et al.*, “Cerebral hemodynamics evaluation by near-infrared time-resolved spectroscopy: correlation with simultaneous positron emission tomography measurements,” *Neuroimage*, vol. 29, no. 3, pp. 697–705, 2006.

[43] G. Schwarz, G. Litscher, R. Kleinert, and R. Jobstmann, “Cerebral oximetry in dead subjects.,” *J. Neurosurg. Anesthesiol.*, vol. 8, no. 3, pp. 189–193, 1996.

[44] P. W. McCormick, M. Stewart, M. G. Goetting, and G. Balakrishnan, “Regional cerebrovascular oxygen saturation measured by optical spectroscopy in humans.,” *Stroke*, vol. 22, no. 5, pp. 596–602, 1991.

[45] J. M. Murkin *et al.*, “Monitoring brain oxygen saturation during coronary bypass surgery: a randomized, prospective study,” *Anesth. Analg.*, vol. 104, no. 1, pp. 51–58, 2007.

[46] R. Bhatia *et al.*, “The application of near-infrared oximetry to cerebral monitoring during aneurysm embolization: a comparison with intraprocedural angiography,” *J. Neurosurg. Anesthesiol.*, vol. 19, no. 2, pp. 97–104, 2007.

[47] L. Bathala, M. M. Mehndiratta, and V. K. Sharma, “Transcranial doppler: Technique and common findings (Part 1),” *Ann. Indian Acad. Neurol.*, vol. 16, no. 2, p. 174, 2013.

[48] B. Hage *et al.*, “Functional Transcranial Doppler Ultrasound for High Temporal Resolution Measurement of Lateralization in Visual Memory and Visual Search Cognitive Tasks,” no. 1263181, pp. 1–4, 2015.

[49] I. K. Moppett and R. P. Mahajan, “Transcranial Doppler ultrasonography in anaesthesia and intensive care,” *Br. J. Anaesth.*, vol. 93, no. 5, pp. 710–724, 2004.

[50] V. Fodale, D. Schifilliti, A. Conti, T. Lucanto, G. Pino, and L. B. Santamaria, “Transcranial Doppler and anesthetics,” *Acta Anaesthesiol. Scand.*, vol. 51, no. 7, pp. 839–847, 2007.

[51] M. Bodo, “Studies in Rheoencephalography (REG),” *J. Electr. Bioimpedance*, vol. 1, no. 1, pp. 18–40, 2010.

[52] Y. E. Moskalenko, “Rheoencephalography: Past Popularity, Obvilion at Present and Optimistic Future,” *Int. J. Adv. Life Sci. Technol.*, vol. 2, no. 1, pp. 1–15, 2015.

[53] L. D. Montgomery, R. W. Montgomery, and R. Guisado, “Rheoencephalographic and electroencephalographic measures of cognitive workload: analytical procedures,” *Biol. Psychol.*, vol. 40, no. 1–2, pp. 143–159, 1995.

[54] J. J. Perez, “To what extent is the bipolar rheoencephalographic signal contaminated by scalp blood flow? A clinical study to quantify its extra and non-extracranial components,” *Biomed. Eng. Online*, vol. 13, no. 1, pp. 1–11, 2014.

[55] M. Yu and A. Yu, “Multifrequency REG: Fundamental Background, Informational Meaning and Ways of Data Analysis and Automation,” *Am. J. Biomed. Eng.*, vol. 2, no. 4, pp. 163–174, 2012.

[56] S. N. Davie and H. P. Grocott, “Impact of extracranial contamination on regional cerebral oxygen saturation: a comparison of three cerebral oximetry technologies.,” *Anesthesiology*, vol. 116, no. 4, pp. 834–40, 2012.

[57] J. J. Perez, E. Guijarro, J. Sancho, and A. Navarre, “Extraction of the Intracranial Component from the Rheoencephalographic Signal: A New Approach,” in *2006 International Conference of the IEEE Engineering in Medicine and Biology Society*, 2006, pp. 6064–6067.

[58] J. J. Pérez, E. Guijarro, and J. A. Barcia, “Quantification of intracranial contribution to rheoencephalography by a numerical model of the head,” *Clin. Neurophysiol.*, vol. 111, no. 7, pp. 1306–1314, 2000.

[59] D. Popovic *et al.*, “Assessment of cerebral blood flow autoregulation (CBF AR) with rheoencephalography (REG): studies in animals,” *J. Phys. Conf. Ser.*, vol. 434, p. 12042, 2013.

[60] M. Bodo, F. J. Pearce, L. Baranyi, and R. A. Armonda, “Changes in the intracranial rheoencephalogram at lower limit of cerebral blood flow autoregulation.,” *Physiol. Meas.*, vol. 26, no. 2, pp. S1-17, 2005.

[61] W. Traczewski, M. Moskala, D. Szwabowska, I. Goscinski, M. Krupa, and J. Polak, “The role of computerized rheoencephalography in the assessment of normal pressure hydrocephalus.,” *Neurol Neurochir Pol*, vol. 39, no. 4, pp. 287–293, 2005.

[62] M. Bodo, F. Pearce, and A. Garcia, “In vivo cerebral blood flow autoregulation studies using rheoencephalography,” *J. Phys.*, vol. 224, pp. 8–11, 2010.

[63] M. Bodo, F. J. Pearce, and R. A. Armonda, “Cerebrovascular reactivity: rat studies in rheoencephalography,” *Physiol. Meas.*, vol. 25, no. 6, pp. 1371–1384, 2004.

[64] Y. Moskalenko, “Fundamental Basis, Informational Meaning and Data Analysis of Multifrequency Reoencephalography,” *Adv. Biosci. Bioeng.*, vol. 1, no. 1, p. 8, 2013.

[65] J. Jacquy *et al.*, “Cerebral blood flow and quantitative rheoencephalography,” *Electroencephalogr. Clin. Neurophysiol.*, vol. 37, no. 5, pp. 507–511, 1974.

[66] S. Markovich, P. Scheinberg, S. Shafey, R. Namon, and R. Sano, “Clinical monopolar rheoencephalography.,” *J. Neurol. Sci.*, vol. 5, no. 2, pp. 267–72.

[67] L. D. Montgomery and C. R. Gleason, “Simultaneous use of rheoencephalography and electroencephalography for the monitoring of

cerebral function.," *Aviat. Sp. Environ. Med.*, vol. 63, no. 4, pp. 314–321, 1992.

[68] M. Bodo and F. J. Pearce, "Rheoencephalography (REG) as a Non-Invasive Monitoring Alternative for the Assessment of Brain Blood Flow," no. August 2004, pp. 16–18.

[69] K. Brazovskii, P. S. Jacov, and O. S. Umanskii, "Modelling the ability of rheoncephalography to measure cerebral blood flow," *J. Electr. Bioimpedance*, vol. 5, no. 1, p. 110, 2014.

[70] V. Bonhomme *et al.*, "Influence of anesthesia on cerebral blood flow, cerebral metabolic rate, and brain functional connectivity," *Curr. Opin. Anaesthesiol.*, vol. 24, no. 5, pp. 474–479, 2011.

[71] H. S. Jung, T. Y. Sung, H. Kang, J. S. Kim, and T. Y. Kim, "Cerebral blood flow change during volatile induction in large-dose sevoflurane versus intravenous propofol induction: Transcranial doppler study," *Korean J. Anesthesiol.*, vol. 67, no. 5, pp. 323–328, 2014.

[72] K. Engelhard and C. Werner, "The effects of general anesthesia and variations in hemodynamics on cerebral perfusion," *Appl. Cardiopulm. Pathophysiol.*, vol. 13, no. 2, pp. 157–159, 2009.

[73] C. Molnár, G. Settakis, P. Sárkány, S. Kálmán, S. Szabó, and B. Fülesdi, "Effect of sevoflurane on cerebral blood flow and cerebrovascular resistance at surgical level of anaesthesia: a transcranial Doppler study," *Eur. J. Anaesthesiol.*, vol. 24, no. 2, pp. 179–184, 2007.

[74] N. Goettel *et al.*, "Monitoring of cerebral blood flow autoregulation in adults undergoing sevoflurane anesthesia: a prospective cohort study of two age groups," *J. Clin. Monit. Comput.*, vol. 30, no. 3, pp. 255–264, 2016.

[75] S. Strebel, A. M. Lam, B. Matta, T. S. Mayberg, R. Aaslid, and D. W. Newell, "Dynamic and static cerebral autoregulation during isoflurane, desflurane, and propofol anesthesia.," *Anesthesiology*, vol. 83, no. 1, pp. 66–76, Jul. 1995.

[76] K. W. Grathwohl *et al.*, "Total intravenous anesthesia including ketamine versus volatile gas anesthesia for combat-related operative traumatic brain injury.," *Anesthesiology*, vol. 109, no. 1, pp. 44–53, 2008.

[77] C. Eng, A. M. Lam, T. S. Mayberg, C. Lee, and T. Mathisen, "The influence of propofol with and without nitrous oxide on cerebral blood flow velocity and CO2 reactivity in humans.," *Anesthesiology*, vol. 77, no. 5, pp. 872–9,

Nov. 1992.

[78] A. Conti, D. G. Iacopino, V. Fodale, S. Micalizzi, O. Penna, and L. B. Santamaria, “Cerebral haemodynamic changes during propofol-remifentanil or sevoflurane anaesthesia: Transcranial Doppler study under bispectral index monitoring,” *Br. J. Anaesth.*, vol. 97, no. 3, pp. 333–339, 2006.

[79] T. Manchandia, “Alterations In Regional Cerebral Blood Flow With Propofol Anesthesia Compared With Sevoflurane,” *Yale Med. Thesis Digit. Libr.*, 2012.

[80] K. K. Kaisti *et al.*, “Effects of sevoflurane, propofol and adjunct nitrous oxide on regional cerebral blood flow, oxygen consumption, and blood volume in humans,” *Anesthesiology*, vol. 99, no. 3, pp. 603–613, 2003.

[81] D. J. Miletich, A. D. Ivankovich, R. F. Albrecht, C. R. Reimann, R. Rosenberg, and E. D. McKissic, “Absence of autoregulation of cerebral blood flow during halothane and enflurane anesthesia.,” *Anesth. Analg.*, vol. 55, no. 1, pp. 100–9, 1976.

[82] V. Minville *et al.*, “The effects of spinal anesthesia on cerebral blood flow in the very elderly,” *Anesth. Analg.*, vol. 108, no. 4, pp. 1291–1294, 2009.

[83] U. Rao, “Comparison of hemodynamic and neuromuscular properties of rocuronium versus vecuronium in anesthesia,” *Int. J. Med. Sci. Public Heal.*, vol. 5, no. 8, pp. 1617–1621, 2016.

[84] M. E. Hudson, K. P. Rothfield, W. C. Tullock, and L. L. Firestone, “Haemodynamic effects of rocuronium bromide in adult cardiac surgical patients,” *Can. J. Anaesth.*, vol. 45, no. 2, p. 139, 1998.

[85] P. Bhagade, D. Wadaskar, and B. Tendolkar, “Assessment of haemodynamic stability with intubating dose of intravenous rocuronium bromide versus vecuronium bromide in predominantly stenotic valvular cardiac surgery patients,” *Int J Res Med Sci*, vol. 4, pp. 3219–3223, 2016.

[86] M. R. Tramer, R. A. Moore, and H. J. McQuay, “Propofol and bradycardia: causation, frequency and severity.,” *Br. J. Anaesth.*, vol. 78, no. 6, pp. 642–651, 1997.

[87] M. Matsuda, S. Yoneda, H. Gotoh, J. Handa, and H. Handa, “Effect of atropine on cerebrovascular responsiveness to carbon dioxide,” *J. Neurosurg.*, vol. 48, no. 3, pp. 417–422, 1978.

[88] W.-J. Choi, K. Lee, Y.-K. Kim, K.-J. Song, S.-M. Jeong, and G.-S. Hwang, “Vagolytic atropine attenuates cerebral vasodilation response during acute orthostatic hypotension,” *Korean J. Anesthesiol.*, vol. 68, no. 6, p.

594, 2015.

[89] M. Masjedi, F. Zand, A. P. Kazemi, and A. Hoseinipour, “Prophylactic effect of ephedrine to reduce hemodynamic changes associated with anesthesia induction with propofol and remifentanil,” *J. Anaesthesiol. Clin. Pharmacol.*, vol. 30, no. 2, p. 217, 2014.

[90] L. Meng *et al.*, “Effect of phenylephrine and ephedrine bolus treatment on cerebral oxygenation in anaesthetized patients,” *Br. J. Anaesth.*, vol. 107, no. 2, pp. 209–217, 2011.

[91] K. U. Koch *et al.*, “Effect of ephedrine and phenylephrine on brain oxygenation and microcirculation in anaesthetised patients with cerebral tumours: study protocol for a randomised controlled trial,” *BMJ Open*, vol. 7, no. 11, p. e018560, 2017.

[92] P. Soeding, “Effects of Positioning on Cerebral Oxygenation,” *Curr. Anesthesiol. Rep.*, vol. 3, no. 3, pp. 184–196, 2013.

[93] G. Kose and S. Hatipoglu, “Effect of head and body positioning on cerebral blood flow velocity in patients who underwent cranial surgery,” *J. Clin. Nurs.*, vol. 21, no. 13–14, pp. 1859–1867, 2012.

[94] S.-J. Kim, J. Y. Kwon, A.-R. Cho, H. K. Kim, and T. K. Kim, “The effects of sevoflurane and propofol anesthesia on cerebral oxygenation in gynecological laparoscopic surgery,” *Korean J. Anesthesiol.*, vol. 61, no. 3, p. 225, 2011.

[95] Y. Zhang, M. Jiménez-Herrera, C. Axelsson, and Y. Cheng, “Not bad: passive leg raising in cardiopulmonary resuscitation-a new modeling study,” *Front. Physiol.*, vol. 7, p. 665, 2017.

[96] M. A. Tooley, L. J. Grant, and A. R. Davies, “A microprocessor based instrument for the spectral analysis of the EEG in anaesthesia,” *Clin. Phys. Physiol. Meas.*, vol. 5, no. 4, p. 303, 1984.

[97] R. G. Bickford, “Automatic electroencephalographic control of general anesthesia,” *Electroencephalogr. Clin. Neurophysiol.*, vol. 2, no. 1, pp. 93–96, 1950.

[98] I. J. Rampil, “A primer for EEG signal processing in anesthesia,” *J. Am. Soc. Anesthesiol.*, vol. 89, no. 4, pp. 980–1002, 1998.

[99] L. D. Gugino, R. J. Chabot, L. S. Prichep, E. R. John, V. Formanek, and L. S. Aglio, “Quantitative EEG changes associated with loss and return of consciousness in healthy adult volunteers anaesthetized with propofol or

sevoflurane," *Br. J. Anaesth.*, vol. 87, no. 3, pp. 421–428, 2001.

[100] E. N. Brown, R. Lydic, and N. D. Schiff, "General anesthesia, sleep, and coma," *N. Engl. J. Med.*, vol. 363, no. 27, pp. 2638–2650, 2010.

[101] H. Schwilden, H. Stoeckel, and J. Schüttler, "Closed-loop feedback control of propofol anaesthesia by quantitative EEG analysis in humans," *Br. J. Anaesth.*, vol. 62, no. 3, pp. 290–296, 1989.

[102] J. C. Drummond, C. A. Brann, D. E. Perkins, and D. E. Wolfe, "A comparison of median frequency, spectral edge frequency, a frequency band power ratio, total power, and dominance shift in the determination of depth of anesthesia," *Acta Anaesthesiol. Scand.*, vol. 35, no. 8, pp. 693–699, 1991.

[103] T. P. Barnett, L. C. Johnson, P. Naitoh, N. Hicks, and C. Nute, "Bispectrum analysis of electroencephalogram signals during waking and sleeping," *Science (80-.).*, vol. 172, no. 3981, pp. 401–402, 1971.

[104] X. Borrat *et al.*, "Modeling the Influence of the A118G Polymorphism in the OPRM1 Gene and of Noxious Stimulation on the Synergistic Relation between Propofol and Remifentanil," *Anesthesiology*, vol. 6, no. 118, pp. 1395–1407, 2013.

[105] E. W. Jensen *et al.*, "Monitoring hypnotic effect and nociception with two EEG-derived indices, qCON and qNOX, during general anaesthesia," *Acta Anaesthesiol. Scand.*, vol. 58, no. 8, pp. 933–941, 2014.

[106] V. Chidambaran, A. Costandi, and A. D'Mello, "Propofol: A Review of its Role in Pediatric Anesthesia and Sedation," *CNS Drugs*, vol. 29, no. 7, pp. 543–563, 2015.

[107] B. Marsh, M. White, N. Morton, and G. N. C. Kenny, "Pharmacokinetic Model Driven Infusion of Propofol in Children," *Br. J. Anaesth.*, vol. 67, pp. 41–48, 1991.

[108] Y. E. J. Schnider, Thomas W, Minto Charles F, Gambus Pedro L, Andresen Corina, Goodale David B, Shafer Steven L, "The Influence of Method of Administration and Covariates on the Pharmacokinetics of Propofol in Adult Volunteers," *Anesthesiology*, vol. 88, pp. 1170–82, 1998.

[109] A. R. Absalom, V. Mani, T. De Smet, and M. M. R. F. Struys, "Pharmacokinetic models for propofol- Defining and illuminating the devil in the detail," *Br. J. Anaesth.*, vol. 103, no. 1, pp. 26–37, 2009.

[110] S. Sivasubramaniam, "Review of pharmacokinetic models for target controlled infusions in anesthesia," *Int. J. Basic Clin. Pharmacol.*, vol. 3, no. 3, p. 417, 2014.

[111] C. Jeleazcov *et al.*, “Pharmacodynamic modelling of the bispectral index response to propofol-based anaesthesia during general surgery in children,” *Br. J. Anaesth.*, vol. 100, no. 4, pp. 509–516, 2008.

[112] T. Kazama *et al.*, “Comparison of the effect-site keOs of propofol for blood pressure and EEG bispectral index in elderly and younger patients,” *J. Am. Soc. Anesthesiol.*, vol. 90, no. 6, pp. 1517–1527, 1999.

[113] C. F. Swinhoe *et al.*, “Evaluation of the predictive performance of a ‘ Diprifusor ’ TCI system,” pp. 61–67, 1998.

[114] J. Escrivá *et al.*, “Comparison of two cardiac output monitors, qCO and LiDCO, during general anesthesia,” *Mathews J. Anesth.*, vol. 1, no. 1, pp. 1–8, 2016.

[115] D. P. Bernstein, “A new stroke volume equation for thoracic electrical bioimpedance: theory and rationale.,” *Crit. Care Med.*, vol. 14, no. 10, pp. 904–909, 1986.

[116] M. Elgendi, “On the analysis of fingertip photoplethysmogram signals,” *Curr. Cardiol. Rev.*, vol. 8, no. 1, pp. 14–25, 2012.

[117] Y. A. Djawad, A. Mu’nisa, P. Rusung, A. Kurniawan, I. S. Idris, and M. Taiyeb, “Essential Feature Extraction of Photoplethysmography Signal of Men and Women in Their 20s,” *Eng. J.*, vol. 21, no. 4, pp. 259–272, 2017.

[118] A. Karagiannis, P. Constantinou, and D. Vouyioukas, “Biomedical time series processing and analysis methods: The case of empirical mode decomposition,” in *Advanced Biomedical Engineering*, IntechOpen, 2011.

[119] A. Subasi, “EEG signal classification using wavelet feature extraction and a mixture of expert model,” *Expert Syst. Appl.*, vol. 32, no. 4, pp. 1084–1093, 2007.

[120] S. Li, S. Jiang, S. Jiang, J. Wu, W. Xiong, and S. Diao, “A Hybrid Wavelet-Based Method for the Peak Detection of Photoplethysmography Signals,” in *Comp. Math. Methods in Medicine*, 2017.

[121] D. Elad, G. Soffer, U. Zaretsky, M. Wolf, and R. J. Shiner, “Time-frequency analysis of breathing signals: in vitro airway model.,” *Technol. Health Care*, vol. 9, no. 3, pp. 269–280, 2001.

[122] A. Mert and A. Akan, “Emotion recognition based on time–frequency distribution of EEG signals using multivariate synchrosqueezing transform,” *Digit. Signal Process.*, vol. 81, pp. 106–115, 2018.

[123] J. D. Campbell, C. G. Pretty, J. G. Chase, and P. J. Bones, “Near-Real-Time Detection of Pulse Oximeter PPG Peaks Using Wavelet Decomposition,” *IFAC-PapersOnLine*, vol. 51, no. 27, pp. 146–151, 2018.

[124] F. G. Nocetti, J. S. González, E. R. Acosta, and E. M. Hernández, “Towards the Simplified Computation of Time-Frequency Distributions for Signal Analysis,” *IFAC Proc. Vol.*, vol. 33, no. 6, pp. 169–174, 2000.

[125] K. Kiasaleh, *Biological signals classification and analysis*, vol. 465. Springer, 2015.

[126] U. R. Acharya, K. Chua, T.-C. Lim, , DORITHY, and J. Suri, “Automatic identification of epileptic EEG signals using nonlinear parameters,” *J. Mech. Med. Biol.*, vol. 9, pp. 539–553, 2009.

[127] O. Faust *et al.*, “Effects of mobile phone radiation on cardiac health,” *J. Mech. Med. Biol.*, vol. 11, no. 5, pp. 1241–1253, 2011.

[128] A. Accardo, M. Affinito, M. Carrozzi, and F. Bouquet, “Use of the fractal dimension for the analysis of electroencephalographic time series,” *Biol. Cybern.*, vol. 77, no. 5, pp. 339–350, 1997.

[129] A. Dabrowski, “Estimation of the largest Lyapunov exponent-like (LLEL) stability measure parameter from the perturbation vector and its derivative dot product (part 2) experiment simulation,” *Nonlinear Dyn.*, vol. 78, no. 3, pp. 1601–1608, 2014.

[130] A. H. Khandoker, C. Karmakar, M. Brennan, M. Palaniswami, and A. Voss, *Poincaré plot methods for heart rate variability analysis*. Springer, 2013.

[131] A. Di Ieva, E. M. Schmitz, and M. D. Cusimano, “Analysis of intracranial pressure: past, present, and future,” *Neurosci.*, vol. 19, no. 6, pp. 592–603, 2013.

[132] C.-W. Lu, M. Czosnyka, J.-S. Shieh, A. Smielewska, J. D. Pickard, and P. Smielewski, “Complexity of intracranial pressure correlates with outcome after traumatic brain injury,” *Brain*, vol. 135, no. 8, pp. 2399–2408, 2012.

[133] R. Hornero, M. Aboy, D. Abasolo, J. McNames, W. Wakeland, and B. Goldstein, “Complex analysis of intracranial hypertension using approximate entropy,” *Crit. Care Med.*, vol. 34, no. 1, pp. 87–95, 2006.

[134] O. Faust and M. G. Bairy, “Nonlinear analysis of physiological signals: a review,” *J. Mech. Med. Biol.*, vol. 12, no. 4, p. 1240015, 2012.

[135] W. M. Association, “World Medical Association Declaration of Helsinki: Ethical Principles for Medical Research Involving Human SubjectsWorld Medical Association Declaration of HelsinkiSpecial Communication,”

JAMA, vol. 310, no. 20, pp. 2191–2194, Nov. 2013.

[136] I. O. for Standardization, *Clinical Investigation of Medical Devices for Human Subjects: Good Clinical Practice*. International Organization for Standardization, 2011.

[137] T. R. H. Cutmore and D. A. James, "Identifying and reducing noise in psychophysiological recordings," *Int. J. Psychophysiol.*, vol. 32, no. 2, pp. 129–150, 1999.

[138] A. A. Fedotov, A. S. Akulova, and S. A. Akulov, "Denoising Pulse Wave Signal Based on Wavelet Decomposition," in *6th European Conference of the International Federation for Medical and Biological Engineering*, 2015, pp. 98–101.

[139] A. A. Fedotov and A. S. Akulova, "Adaptive filter for eliminating baseline wander of pulse wave signals," in *World Congress on Medical Physics and Biomedical Engineering, June 7-12, 2015, Toronto, Canada*, 2015, pp. 1018–1021.

[140] K. Pilt, K. Meigas, R. Ferenets, and J. Kaik, "Photoplethysmographic signal processing using adaptive sum comb filter for pulse delay measurement/Fotopletusmograafilise signaali tootlus pulsi viiteaja mootmisel adaptiivse kammfiltriga," *Est. J. Eng.*, vol. 16, no. 1, pp. 78–95, 2010.

[141] K. Nakajima, T. Tamura, and H. Miike, "Monitoring of heart and respiratory rates by photoplethysmography using a digital filtering technique," *Med. Eng. Phys.*, vol. 18, no. 5, pp. 365–372, 1996.

[142] K. Bendjelid, "The pulse oximetry plethysmographic curve revisited," *Curr. Opin. Crit. Care*, vol. 14, no. 3, pp. 348–353, 2008.

[143] N. Stuban and M. Niwayama, "Optimal filter bandwidth for pulse oximetry," *Rev. Sci. Instrum.*, vol. 83, no. 10, p. 104708, 2012.

[144] M. Elgendi, I. Norton, M. Brearley, D. Abbott, and D. Schuurmans, "Detection of a and b waves in the acceleration photoplethysmogram," *Biomed. Eng. Online*, vol. 13, no. 1, p. 139, 2014.

[145] M. Elgendi, I. Norton, M. Brearley, D. Abbott, and D. Schuurmans, "Systolic peak detection in acceleration photoplethysmograms measured from emergency responders in tropical conditions," *PLoS One*, vol. 8, no. 10, p. e76585, 2013.

[146] M. Elgendi *et al.*, "Towards investigating global warming impact on

human health using derivatives of photoplethysmogram signals," *Int. J. Environ. Res. Public Health*, vol. 12, no. 10, pp. 12776–12791, 2015.

[147] C. A. Robles-Rubio, K. A. Brown, and R. E. Kearney, "A new movement artifact detector for photoplethysmographic signals," in *2013 35th Annual International Conference of the IEEE Engineering in Medicine and Biology Society (EMBC)*, 2013, pp. 2295–2299.

[148] W. G. Kubicek, R. P. Patterson, and D. A. Witsoe, "Impedance cardiography as a noninvasive method of monitoring cardiac function and other parameters of the cardiovascular system," *Ann. N. Y. Acad. Sci.*, vol. 170, no. 1, pp. 724–732, 1970.

[149] Y. Liang, M. Elgendi, Z. Chen, and R. Ward, "An optimal filter for short photoplethysmogram signals," *Sci. data*, vol. 5, p. 180076, 2018.

[150] A. E. Awodeyi, S. R. Alty, and M. Ghavami, "On the filtering of photoplethysmography signals," in *2014 IEEE International Conference on Bioinformatics and Bioengineering*, 2014, pp. 175–178.

[151] K. Pilt, R. Ferenets, K. Meigas, L.-G. Lindberg, K. Temitski, and M. Viigimaa, "New photoplethysmographic signal analysis algorithm for arterial stiffness estimation," *Sci. World J.*, vol. 2013, 2013.

[152] R. Cawley and G.-H. Hsu, "Local-geometric-projection method for noise reduction in chaotic maps and flows," *Phys. Rev. A*, vol. 46, no. 6, p. 3057, 1992.

[153] M. G. Signorini, F. Marchetti, D. Bioingegneria, P. Milano, and S. Cerutti, "Applying nonlinear noise reduction in the analysis of heart rate variability," *IEEE Eng. Med. Biol. Mag.*, vol. 20, no. 2, pp. 59–68, 2001.

[154] A. V Oppenheim, J. R. Buck, and R. W. Schafer, *Discrete-time signal processing. Vol. 2*. Upper Saddle River, NJ: Prentice Hall, 2001.

[155] B. Zhang, J. Zhao, X. Chen, and J. Wu, "ECG data compression using a neural network model based on multi-objective optimization," *PLoS One*, vol. 12, no. 10, p. e0182500, 2017.

[156] R. Benzid, A. Messaoudi, and A. Boussaad, "Constrained ECG compression algorithm using the block-based discrete cosine transform," *Digit. Signal Process.*, vol. 18, no. 1, pp. 56–64, 2008.

[157] J. W. Mason, D. J. Ramseth, D. O. Chanter, T. E. Moon, D. B. Goodman, and B. Mendzelevski, "Electrocardiographic reference ranges derived from 79,743 ambulatory subjects," *J. Electrocardiol.*, vol. 40, no. 3, pp. 228–234, 2007.

[158] F. Bilotta, L. Fiorani, I. La Rosa, F. Spinelli, and G. Rosa, “Cardiovascular effects of intravenous propofol administered at two infusion rates: a transthoracic echocardiographic study,” *Anaesthesia*, vol. 56, no. 3, pp. 266–271, 2001.

[159] J. W. D. Lovett, R. Barchha, R. S. Lee, M. H. Little, and J. S. Watkinson, “Acute effects of ECT on the cerebral circulation in man. A computerized study by cerebral impedance plethysmography.,” *Eur. Neurol.*, vol. 12, no. 1, pp. 47–62, 1974.

[160] C. J. Kirkness, P. H. Mitchell, R. L. Burr, K. S. March, and D. W. Newell, “Intracranial pressure waveform analysis: clinical and research implications,” *J. Neurosci. Nurs.*, vol. 32, no. 5, p. 271, 2000.

[161] P. K. Eide, A. Sorteberg, G. Bentsen, P. B. Marthinsen, A. Stubhaug, and W. Sorteberg, “Pressure-derived versus pressure wave amplitude--derived indices of cerebrovascular pressure reactivity in relation to early clinical state and 12-month outcome following aneurysmal subarachnoid hemorrhage,” *J. Neurosurg.*, vol. 116, no. 5, pp. 961–971, 2012.

[162] M. Kosteljanetz, “Intracranial pressure: cerebrospinal fluid dynamics and pressure-volume relations.,” *Acta Neurol. Scand. Suppl.*, vol. 111, pp. 1–23, 1987.

[163] C. J. J. Avezaat and J. H. M. Van Eijndhoven, “Clinical observations on the relationship between cerebrospinal fluid pulse pressure and intracranial pressure,” *Acta Neurochir. (Wien).*, vol. 79, no. 1, pp. 13–29, 1986.

[164] A. Chakraborty, D. Sadhukhan, and M. Mitra, “An Automated Algorithm to Extract Time Plane Features From the PPG Signal and its Derivatives for Personal Health Monitoring Application,” *IETE J. Res.*, pp. 1–13, 2019.

[165] N. Mahri, K. B. Gan, R. Meswari, M. H. Jaafar, and M. A. Mohd. Ali, “Utilization of second derivative photoplethysmographic features for myocardial infarction classification,” *J. Med. Eng. Technol.*, vol. 41, no. 4, pp. 298–308, 2017.

[166] A. Sološenko, A. Petrenas, and V. Marozas, “Photoplethysmography-based method for automatic detection of premature ventricular contractions,” *IEEE Trans. Biomed. Circuits Syst.*, vol. 9, no. 5, pp. 662–669, 2015.

[167] J. Siedlecka, P. Siedlecki, and A. Bortkiewicz, “Impedance cardiography--Old method, new opportunities. Part I. Clinical applications.,” 2015.

[168] M. Packer *et al.*, "Utility of impedance cardiography for the identification of short-term risk of clinical decompensation in stable patients with chronic heart failure," *J. Am. Coll. Cardiol.*, vol. 47, no. 11, pp. 2245–2252, 2006.

[169] G. Gielerak, P. Krzesiński, E. Piotrowicz, and R. Piotrowicz, "The usefulness of impedance cardiography for predicting beneficial effects of cardiac rehabilitation in patients with heart failure," *Biomed Res. Int.*, vol. 2013, 2013.

[170] Z. Xiajuan, D. Ding, H. Yanyan, and H. Zhen, "Impedance cardiographic hemodynamic variables and hypertension in elderly Han residents," *Ups. J. Med. Sci.*, vol. 118, no. 2, pp. 80–86, 2013.

[171] P. Krzesiński, G. Gielerak, J. Kowal, and K. Piotrowicz, "Usefulness of impedance cardiography in optimisation of antihypertensive treatment in patients with metabolic syndrome: a randomised prospective clinical trial," *Kardiol. Pol. (Polish Hear. Journal)*, vol. 70, no. 6, pp. 599–607, 2012.

[172] W. G. Kubicek, J. N. Karnegis, R. P. Patterson, D. A. Witsoe, and R. H. Mattson, "Development and evaluation of an impedance cardiac output system.," *Aerosp. Med.*, vol. 37, no. 12, pp. 1208–12, Dec. 1966.

[173] R. J. Demeter, K. L. Parr, P. D. Toth, and J. R. Woods, "Use of noninvasive bioelectric impedance to predict cardiac output in open heart recovery," *Biol. Psychol.*, vol. 36, no. 1–2, pp. 23–32, 1993.

[174] H. H. Woltjer, H. J. Bogaard, G. J. Scheffer, H. I. Van Der Spoel, M. A. Huybregts, and P. M. De Vries, "Standardization of non-invasive impedance cardiography for assessment of stroke volume: comparison with thermodilution.," *Br. J. Anaesth.*, vol. 77, no. 6, pp. 748–752, 1996.

[175] A. W. Quail, F. M. Traugott, W. L. Porges, and S. W. White, "Thoracic resistivity for stroke volume calculation in impedance cardiography," *J. Appl. Physiol.*, vol. 50, no. 1, pp. 191–195, 1981.

[176] B. B. Sramek, D. M. Rose, and A. Miyamoto, "Stroke volume equation with a linear base impedance model and its accuracy, as compared to thermodilution and magnetic flowmeter techniques in humans and animals," in *Proceedings of the Sixth International Conference on Electrical Bioimpedance, Zadar, Yugoslavia*, 1983, vol. 38.

[177] H. H. Woltjer, H. J. Bogaard, P. De Vries, and others, "The technique of impedance cardiography: a review," 1997.

[178] B. R. Pickett and J. C. Buell, "Validity of cardiac output measurement by computer-averaged impedance cardiography, and comparison with

simultaneous thermodilution determinations," *Am. J. Cardiol.*, vol. 69, no. 16, pp. 1354–1358, 1992.

[179] J. L. Willems, J. O. S. Roelandt, H. De Geest, H. Kesteloot, and J. V Joossens, "The left ventricular ejection time in elderly subjects," *Circulation*, vol. 42, no. 1, pp. 37–42, 1970.

[180] M. B. Vestergaard and H. B. W. Larsson, "Cerebral metabolism and vascular reactivity during breath-hold and hypoxic challenge in freedivers and healthy controls," *J. Cereb. Blood Flow Metab.*, p. 0271678X17737909, 2017.

[181] P. D. Verdouw, J. Beaune, J. Roelandt, and P. G. Hygenholtz, "Stroke volume from central aortic pressure? A critical assessment of the various formulae as to their clinical value," *Basic Res. Cardiol.*, vol. 70, no. 4, pp. 377–389, 1975.

[182] W. B. Jones, L. L. Hefner, W. H. Bancroft, and W. Klip, "Velocity of blood flow and stroke volume obtained from the pressure pulse," *J. Clin. Invest.*, vol. 38, no. 11, pp. 2087–2090, 1959.

[183] M. Rasmussen *et al.*, "Cerebral Blood Flow, Blood Volume, and Mean Transit Time Responses to Propofol and Indomethacin in Peritumor and Contralateral Brain RegionsPerioperative Perfusion-weighted Magnetic Resonance Imaging in Patients with Brain Tumors," *Anesthesiol. J. Am. Soc. Anesthesiol.*, vol. 112, no. 1, pp. 50–56, 2010.

[184] S. Ederberg, A. Westerlind, E. Houltz, S.-E. Svensson, M. Elam, and S.-E. Ricksten, "The effects of propofol on cerebral blood flow velocity and cerebral oxygen extraction during cardiopulmonary bypass," *Anesth. Analg.*, vol. 86, no. 6, pp. 1201–1206, 1998.

[185] D. J. Morgan, G. A. Campbell, and D. P. Crankshaw, "Pharmacokinetics of propofol when given by intravenous infusion.," *Br. J. Clin. Pharmacol.*, vol. 30, no. 1, pp. 144–148, 1990.

[186] E. V Golanov, S. Yamamoto, and D. J. Reis, "Spontaneous waves of cerebral blood flow associated with a pattern of electrocortical activity," *Am. J. Physiol. Integr. Comp. Physiol.*, vol. 266, no. 1, pp. R204--R214, 1994.

[187] X. Liu, X.-H. Zhu, Y. Zhang, and W. Chen, "Neural origin of spontaneous hemodynamic fluctuations in rats under burst--suppression anesthesia condition," *Cereb. cortex*, vol. 21, no. 2, pp. 374–384, 2010.

[188] J. M. V. Calvo, A. G. Abad, E. R. Garrido, K. N. Chao, A. C. Orts, and J. L.

Tomás, “Transcranial Doppler ultrasound, bispectral index, and electroencephalographic monitoring of entropy during pediatric total intravenous anesthesia,” *Rev. Esp. Anestesiol. Reanim.*, vol. 57, no. 10, pp. 621–629, 2010.

[189] Q. Noirhomme *et al.*, “Bispectral index correlates with regional cerebral blood flow during sleep in distinct cortical and subcortical structures in humans,” *Arch. Ital. Biol.*, vol. 147, no. 1/2, pp. 51–57, 2009.

[190] D. Hoyer *et al.*, “Nonlinear analysis of heart rate and respiratory dynamics,” *IEEE Eng. Med. Biol. Mag.*, vol. 16, no. 1, pp. 31–39, 1997.

[191] D. A. Dimitriev, E. V Saperova, and A. D. Dimitriev, “State anxiety and nonlinear dynamics of heart rate variability in students,” *PLoS One*, vol. 11, no. 1, p. e0146131, 2016.

[192] A. Voss, R. Schroeder, A. Heitmann, A. Peters, and S. Perz, “Short-term heart rate variability—influence of gender and age in healthy subjects,” *PLoS One*, vol. 10, no. 3, p. e0118308, 2015.

[193] E. Ebrahimzadeh, M. Pooyan, and A. Bijar, “A novel approach to predict sudden cardiac death (SCD) using nonlinear and time-frequency analyses from HRV signals,” *PLoS One*, vol. 9, no. 2, p. e81896, 2014.

[194] K. Hayashi, T. Yamada, and T. Sawa, “Comparative study of Poincaré plot analysis using short electroencephalogram signals during anaesthesia with spectral edge frequency 95 and bispectral index,” *Anaesthesia*, vol. 70, no. 3, pp. 310–317, 2015.

[195] A. Xiong, X. Zhao, J. Han, and G. Liu, “Application of the chaos theory in the analysis of EMG on patients with facial paralysis,” in *Robot Intelligence Technology and Applications 2*, Springer, 2014, pp. 805–819.

[196] H. J. Son, Y. J. Jeong, H. J. Yoon, J.-H. Park, and D.-Y. Kang, “Visual and Quantitative Analysis Methods of Respiratory Patterns for Respiratory Gated PET/CT,” *Biomed Res. Int.*, vol. 2016, 2016.

[197] R. A. Hoshi, C. M. Pastre, L. C. M. Vanderlei, and M. F. Godoy, “Poincar{é} plot indexes of heart rate variability: relationships with other nonlinear variables,” *Auton. Neurosci.*, vol. 177, no. 2, pp. 271–274, 2013.

[198] M. Brennan, M. Palaniswami, and P. Kamen, “Do existing measures of Poincare plot geometry reflect nonlinear features of heart rate variability?,” *IEEE Trans. Biomed. Eng.*, vol. 48, no. 11, pp. 1342–1347, 2001.

[199] C. K. Karmakar, A. H. Khandoker, A. Voss, and M. Palaniswami, “Sensitivity of temporal heart rate variability in Poincaré plot to changes in

parasympathetic nervous system activity," *Biomed. Eng. Online*, vol. 10, no. 1, p. 17, 2011.

[200] A. Goshvarpour, A. Goshvarpour, and S. Rahati, "Analysis of lagged Poincare plots in heart rate signals during meditation," *Digit. Signal Process.*, vol. 21, no. 2, pp. 208–214, 2011.

[201] T. P. Thakre and M. L. Smith, "Loss of lag-response curvilinearity of indices of heart rate variability in congestive heart failure," *BMC Cardiovasc. Disord.*, vol. 6, no. 1, p. 27, 2006.

[202] B. Koichubekov *et al.*, "Informative Nature and Nonlinearity of Lagged Poincaré Plots Indices in Analysis of Heart Rate Variability," *Entropy*, vol. 19, no. 10, p. 523, 2017.

[203] C. Lerma, O. Infante, H. Pérez-Grovas, and M. V. José, "Poincaré plot indexes of heart rate variability capture dynamic adaptations after haemodialysis in chronic renal failure patients," *Clin. Physiol. Funct. Imaging*, vol. 23, no. 2, pp. 72–80, 2003.

[204] P. Contreras, R. Canetti, and E. R. Migliaro, "Correlations between frequency-domain HRV indices and lagged Poincar{é} plot width in healthy and diabetic subjects," *Physiol. Meas.*, vol. 28, no. 1, p. 85, 2006.

[205] F. Takens, "Detecting strange attractors in turbulence," in *Dynamical systems and turbulence, Warwick 1980*, Springer, 1981, pp. 366–381.

[206] G. D'Addio, G. D. Pinna, R. Maestri, G. Corbi, N. Ferrara, and F. Rengo, "Quantitative Poincaré plots analysis contains relevant information related to heart rate variability dynamics of normal and pathological subjects," in *Computers in Cardiology, 2004*, 2004, pp. 457–460.

[207] M. A. Woo, W. G. Stevenson, D. K. Moser, R. B. Trelease, and R. M. Harper, "Patterns of beat-to-beat heart rate variability in advanced heart failure," *Am. Heart J.*, vol. 123, no. 3, pp. 704–710, 1992.

[208] K. Hayashi, N. Mukai, and T. Sawa, "Poincaré analysis of the electroencephalogram during sevoflurane anesthesia," *Clin. Neurophysiol.*, vol. 126, no. 2, pp. 404–411, 2015.

[209] A. M. Fraser and H. L. Swinney, "Independent coordinates for strange attractors from mutual information," *Phys. Rev. A*, vol. 33, no. 2, p. 1134, 1986.

[210] A. M. Albano, J. Muench, C. Schwartz, A. I. Mees, and P. E. Rapp, "Singular-value decomposition and the Grassberger-Procaccia algorithm," *Phys.*

Rev. A, vol. 38, no. 6, p. 3017, 1988.

[211] G. P. King, R. Jones, and D. S. Broomhead, “Phase portraits from a time series: a singular system approach,” *Nucl. Phys. B-Proceedings Suppl.*, vol. 2, pp. 379–390, 1987.

[212] H. D. I. Abarbanel, R. Brown, and J. B. Kadtke, “Prediction in chaotic nonlinear systems: Methods for time series with broadband Fourier spectra,” *Phys. Rev. A*, vol. 41, no. 4, p. 1782, 1990.

[213] W. Chen, Z. Wang, H. Xie, and W. Yu, “Characterization of surface EMG signal based on fuzzy entropy,” *IEEE Trans. neural Syst. Rehabil. Eng.*, vol. 15, no. 2, pp. 266–272, 2007.

[214] A. Voss, C. Fischer, R. Schroeder, H. R. Figulla, M. Goernig, and others, “Segmented Poincaré plot analysis for risk stratification in patients with dilated cardiomyopathy,” *Methods Inf. Med.*, vol. 49, no. 5, pp. 511–515, 2010.

[215] J. Piskorski and P. Guzik, “Filtering poincare plots,” *Comput. methods Sci. Technol.*, vol. 11, no. 1, pp. 39–48, 2005.

[216] M. P. Tulppo, T. H. Makikallio, T. E. Takala, T. Seppanen, and H. V Huikuri, “Quantitative beat-to-beat analysis of heart rate dynamics during exercise,” *Am. J. Physiol. Circ. Physiol.*, vol. 271, no. 1, pp. H244--H252, 1996.

[217] C. K. Karmakar, A. H. Khandoker, J. Gubbi, and M. Palaniswami, “Complex Correlation Measure: a novel descriptor for Poincaré plot,” *Biomed. Eng. Online*, vol. 8, no. 1, p. 17, 2009.

[218] C. Wu *et al.*, “Age-related changes of normal cerebral and cardiac blood flow in children and adults aged 7 months to 61 years,” *J. Am. Heart Assoc.*, vol. 5, no. 1, p. e002657, 2016.

[219] S. Amin-Hanjani, X. Du, D. K. Pandey, K. R. Thulborn, and F. T. Charbel, “Effect of age and vascular anatomy on blood flow in major cerebral vessels,” *J. Cereb. Blood Flow Metab.*, vol. 35, no. 2, pp. 312–318, 2015.

[220] M. Selim, R. Jones, P. Novak, P. Zhao, and V. Novak, “The effects of body mass index on cerebral blood flow velocity,” *Clin. Auton. Res.*, vol. 18, no. 6, p. 331, 2008.

[221] P. Elliott, R. O’Hare, K. M. Bill, A. S. Phillips, F. M. Gibson, and R. K. Mirakhur, “Severe cardiovascular depression with remifentanil,” *Anesth. Analg.*, vol. 91, no. 1, pp. 58–61, 2000.

[222] M. T. Alkire, R. J. Haier, S. J. Barker, N. K. Shah, J. C. Wu, and J. Y. Kao,

"Cerebral metabolism during propofol anesthesia in humans studied with positron emission tomography," *Anesthesiol. J. Am. Soc. Anesthesiol.*, vol. 82, no. 2, pp. 393–403, 1995.

[223] M. T. Alkire, "Quantitative EEG correlations with brain glucose metabolic rate during anesthesia in volunteers," *Anesthesiol. J. Am. Soc. Anesthesiol.*, vol. 89, no. 2, pp. 323–333, 1998.

[224] S. M. Pincus, I. M. Gladstone, and R. A. Ehrenkranz, "A regularity statistic for medical data analysis," *J. Clin. Monit.*, vol. 7, no. 4, pp. 335–345, 1991.

[225] F. Beckers, D. Ramaekers, and A. E. Aubert, "Approximate entropy of heart rate variability: validation of methods and application in heart failure," *Cardiovasc. Eng. An Int. J.*, vol. 1, no. 4, pp. 177–182, 2001.

[226] X. Li, S. Yu, H. Chen, C. Lu, K. Zhang, and F. Li, "Cardiovascular autonomic function analysis using approximate entropy from 24-h heart rate variability and its frequency components in patients with type 2 diabetes," *J. Diabetes Investig.*, vol. 6, no. 2, pp. 227–235, 2015.

[227] N. Burioka *et al.*, "Approximate entropy in the electroencephalogram during wake and sleep," *Clin. EEG Neurosci.*, vol. 36, no. 1, pp. 21–24, 2005.

[228] G. M. H. Lee, S. Fattinger, A.-L. Mouthon, Q. Noirhomme, and R. Huber, "Electroencephalogram approximate entropy influenced by both age and sleep," *Front. Neuroinform.*, vol. 7, p. 33, 2013.

[229] J. Bruhn, H. Röpcke, and A. Hoeft, "Approximate entropy as an electroencephalographic measure of anesthetic drug effect during desflurane anesthesia," *Anesthesiol. J. Am. Soc. Anesthesiol.*, vol. 92, no. 3, pp. 715–726, 2000.

[230] J. S. Richman and J. R. Moorman, "Physiological time-series analysis using approximate entropy and sample entropy," *Am. J. Physiol. Circ. Physiol.*, vol. 278, no. 6, pp. H2039--H2049, 2000.

[231] S. Ahmadi, N. Sepehri, C. Wu, and T. Szturm, "Sample Entropy of Human Gait Center of Pressure Displacement: A Systematic Methodological Analysis," *Entropy*, vol. 20, no. 8, p. 579, 2018.

[232] F. Wang, H. Wang, and R. Fu, "Real-Time ECG-based detection of fatigue driving using sample entropy," *Entropy*, vol. 20, no. 3, p. 196, 2018.

[233] D. Zhang, H. Ding, Y. Liu, C. Zhou, H. Ding, and D. Ye, "Neurodevelopment in newborns: a sample entropy analysis of electroencephalogram,"

Physiol. Meas., vol. 30, no. 5, p. 491, 2009.

[234] L. Montesinos, R. Castaldo, and L. Pecchia, "On the use of approximate entropy and sample entropy with centre of pressure time-series," *J. Neuroeng. Rehabil.*, vol. 15, no. 1, p. 116, 2018.

[235] J. M. Yentes, N. Hunt, K. K. Schmid, J. P. Kaipust, D. McGrath, and N. Stergiou, "The appropriate use of approximate entropy and sample entropy with short data sets," *Ann. Biomed. Eng.*, vol. 41, no. 2, pp. 349–365, 2013.

[236] S. Simons, P. Espino, and D. Abásolo, "Fuzzy entropy analysis of the electroencephalogram in patients with Alzheimer's disease: is the method superior to sample entropy?," *Entropy*, vol. 20, no. 1, p. 21, 2018.

[237] S. Lu, X. Chen, J. K. Kanters, I. C. Solomon, and K. H. Chon, "Automatic Selection of the Threshold Value R for Approximate Entropy," *IEEE Trans. Biomed. Eng.*, vol. 55, no. 8, pp. 1966–1972, 2008.

[238] C. Liu *et al.*, "Comparison of different threshold values r for approximate entropy: application to investigate the heart rate variability between heart failure and healthy control groups," *Physiol. Meas.*, vol. 32, no. 2, p. 167, 2010.

[239] K. H. Chon, C. G. Scully, and S. Lu, "Approximate entropy for all signals," *IEEE Eng. Med. Biol. Mag.*, vol. 28, no. 6, 2009.

[240] J. F. Restrepo, G. Schlotthauer, and M. E. Torres, "Maximum approximate entropy and r threshold: A new approach for regularity changes detection," *Phys. A Stat. Mech. its Appl.*, vol. 409, pp. 97–109, 2014.

[241] C. E. Shannon, "A mathematical theory of communication," *Bell Syst. Tech. J.*, vol. 27, no. 3, pp. 379–423, 1948.

[242] D. Q. Phung, D. Tran, W. Ma, P. Nguyen, and T. Pham, "Using Shannon Entropy as EEG Signal Feature for Fast Person Identification.," in *ESANN*, 2014, vol. 4, no. 1, pp. 413–418.

[243] C. Granero-Belinchon, S. Roux, P. Abry, M. Doret, and N. Garnier, "Information theory to probe intrapartum fetal heart rate dynamics," *Entropy*, vol. 19, no. 12, p. 640, 2017.

[244] A. Porta *et al.*, "Measuring regularity by means of a corrected conditional entropy in sympathetic outflow.," *Biol. Cybern.*, vol. 78, no. 1, pp. 71–78, 1998.

[245] S. Guzzetti *et al.*, "Linear and non-linear 24 h heart rate variability in chronic heart failure," *Auton. Neurosci. Basic Clin.*, vol. 86, no. 1, pp. 114–

119, 2000.

[246] L. Faes, G. Nollo, and A. Porta, “Mechanisms of causal interaction between short-term RR interval and systolic arterial pressure oscillations during orthostatic challenge,” *J. Appl. Physiol.*, vol. 114, no. 12, pp. 1657–1667, 2013.

[247] A. U. Viola, E. Tobaldini, S. L. Chellappa, K. R. Casali, A. Porta, and N. Montano, “Short-term complexity of cardiac autonomic control during sleep: REM as a potential risk factor for cardiovascular system in aging,” *PLoS One*, vol. 6, no. 4, p. e19002, 2011.

[248] T. D. Pham, T. C. Thang, M. Oyama-Higa, and M. Sugiyama, “Mental-disorder detection using chaos and nonlinear dynamical analysis of photoplethysmographic signals,” *Chaos, Solitons & Fractals*, vol. 51, pp. 64–74, 2013.

[249] M. Borowska, “Entropy-based algorithms in the analysis of biomedical signals,” *Stud. Logic, Gramm. Rhetor.*, vol. 43, no. 1, pp. 21–32, 2015.

[250] A. Porta *et al.*, “Information domain analysis of cardiovascular variability signals: evaluation of regularity, synchronisation and co-ordination,” *Med. Biol. Eng. Comput.*, vol. 38, no. 2, pp. 180–188, 2000.

[251] A. Porta *et al.*, “Entropy, entropy rate, and pattern classification as tools to typify complexity in short heart period variability series,” *IEEE Trans. Biomed. Eng.*, vol. 48, no. 11, pp. 1282–1291, 2001.

[252] S. M. Pincus and W.-M. Huang, “Approximate entropy: statistical properties and applications,” *Commun. Stat. Methods*, vol. 21, no. 11, pp. 3061–3077, 1992.

[253] A. Wolf, J. B. Swift, H. L. Swinney, and J. A. Vastano, “Determining Lyapunov exponents from a time series,” *Phys. D Nonlinear Phenom.*, vol. 16, no. 3, pp. 285–317, 1985.

[254] S. M. Pincus and A. L. Goldberger, “Physiological time-series analysis: what does regularity quantify?,” *Am. J. Physiol. Circ. Physiol.*, vol. 266, no. 4, pp. H1643--H1656, 1994.

[255] P. Castiglioni and M. Di Rienzo, “How the threshold ‘r’ influences approximate entropy analysis of heart-rate variability,” in *Computers in Cardiology, 2008*, 2008, pp. 561–564.

[256] R. Alcaraz, D. Abásolo, R. Hornero, and J. J. Rieta, “Optimal parameters study for sample entropy-based atrial fibrillation organization analysis,”

Comput. Methods Programs Biomed., vol. 99, no. 1, pp. 124–132, 2010.

[257] P. Castiglioni *et al.*, "Assessing sample entropy of physiological signals by the norm component matrix algorithm: Application on muscular signals during isometric contraction," in *Engineering in Medicine and Biology Society (EMBC), 2013 35th Annual International Conference of the IEEE*, 2013, pp. 5053–5056.

[258] D. E. Lake, J. S. Richman, M. P. Griffin, and J. R. Moorman, "Sample entropy analysis of neonatal heart rate variability," *Am. J. Physiol. Integr. Comp. Physiol.*, vol. 283, no. 3, pp. R789--R797, 2002.

[259] M. J. Lewis and A. L. Short, "Sample entropy of electrocardiographic RR and QT time-series data during rest and exercise," *Physiol. Meas.*, vol. 28, no. 6, p. 731, 2007.

[260] L. A. Zadeh, "Fuzzy sets," *Inf. Control*, vol. 8, no. 3, pp. 338–353, 1965.

[261] H.-B. Xie, W.-T. Chen, W.-X. He, and H. Liu, "Complexity analysis of the biomedical signal using fuzzy entropy measurement," *Appl. Soft Comput.*, vol. 11, no. 2, pp. 2871–2879, 2011.

[262] C. Liu and L. Zhao, "Using fuzzy measure entropy to improve the stability of traditional entropy measures," in *Computing in Cardiology*, 2011, pp. 681–684.

[263] C. C. Mayer, M. Bachler, M. Hörtenhuber, C. Stocker, A. Holzinger, and S. Wassertheurer, "Selection of entropy-measure parameters for knowledge discovery in heart rate variability data," *BMC Bioinformatics*, vol. 15, no. 6, p. S2, 2014.

[264] A. Bošković, T. Lončar-Turukalo, N. Japundžić-Žigon, and D. Bajić, "The flip-flop effect in entropy estimation," in *2011 IEEE 9th International Symposium on Intelligent Systems and Informatics*, 2011, pp. 227–230.

[265] M. Aktaruzzaman and R. Sassi, "Parametric estimation of sample entropy in heart rate variability analysis," *Biomed. Signal Process. Control*, vol. 14, pp. 141–147, 2014.

[266] D. Cuesta-Frau *et al.*, "Measuring body temperature time series regularity using approximate entropy and sample entropy," in *2009 Annual International Conference of the IEEE Engineering in Medicine and Biology Society*, 2009, pp. 3461–3464.

[267] M. Gospodinov and E. Gospodinova, "The effect of obesity on heart rate variability in healthy subjects," 2017.

[268] R. K. Begg, M. Palaniswami, and B. Owen, "Support vector machines for

automated gait classification," *IEEE Trans. Biomed. Eng.*, vol. 52, no. 5, pp. 828–838, 2005.

[269] P. Melillo, A. Jovic, N. De Luca, and L. Pecchia, "Automatic classifier based on heart rate variability to identify fallers among hypertensive subjects," *Healthc. Technol. Lett.*, vol. 2, no. 4, pp. 89–94, 2015.

[270] M. Nardelli, G. Valenza, A. Greco, A. Lanata, and E. P. Scilingo, "Recognizing emotions induced by affective sounds through heart rate variability," *IEEE Trans. Affect. Comput.*, vol. 6, no. 4, pp. 385–394, 2015.

[271] Y. Isler, A. Narin, M. Ozer, and M. Perc, "Multi-stage classification of congestive heart failure based on short-term heart rate variability," *Chaos, Solitons & Fractals*, vol. 118, pp. 145–151, 2019.

[272] R. J. Urbanowicz, M. Meeker, W. La Cava, R. S. Olson, and J. H. Moore, "Relief-based feature selection: introduction and review," *J. Biomed. Inform.*, vol. 85, pp. 189–203, 2018.

[273] K. Kira and L. A. Rendell, "A practical approach to feature selection," in *Machine Learning Proceedings 1992*, Elsevier, 1992, pp. 249–256.

[274] A. Y. Ng and M. I. Jordan, "On discriminative vs. generative classifiers: A comparison of logistic regression and naive bayes," in *Advances in neural information processing systems*, 2002, pp. 841–848.

[275] J. Chhatwal, O. Alagoz, M. J. Lindstrom, C. E. Kahn Jr, K. A. Shaffer, and E. S. Burnside, "A logistic regression model based on the national mammography database format to aid breast cancer diagnosis," *Am. J. Roentgenol.*, vol. 192, no. 4, pp. 1117–1127, 2009.

[276] C. Combes, F. Kadri, and S. Chaabane, "Predicting hospital length of stay using regression models: application to emergency department," 2014.

[277] K.-J. Wang, B. Makond, and K.-M. Wang, "Modeling and predicting the occurrence of brain metastasis from lung cancer by Bayesian network: a case study of Taiwan," *Comput. Biol. Med.*, vol. 47, pp. 147–160, 2014.

[278] D. A. Morales *et al.*, "Predicting dementia development in Parkinson's disease using Bayesian network classifiers," *Psychiatry Res. NeuroImaging*, vol. 213, no. 2, pp. 92–98, 2013.

[279] L. Breiman, J. H. Friedman, C. J. Stone, R. A. Olshen, and C. J. Stone, *Classification and regression trees*. CRC press, 1984.

[280] C. J. Sims, L. Meyn, R. Caruana, R. B. Rao, T. Mitchell, and M. Krohn,

"Predicting cesarean delivery with decision tree models," *Am. J. Obstet. Gynecol.*, vol. 183, no. 5, pp. 1198–1206, 2000.

[281] C. L. Tsien, H. S. Fraser, W. J. Long, and R. L. Kennedy, "Using classification tree and logistic regression methods to diagnose myocardial infarction," *Medinfo*, vol. 98, 1998.

[282] J. M. Evans and W. L. Davies, "Monitoring anesthesia," *Clin. Anesth*, vol. 2, pp. 243–262, 1984.

[283] C. W. J. Granger, "Investigating Causal Relations by Econometric Models and Cross-spectral Methods," *Econometrica*, vol. 37, no. 3, pp. 424–438, 1969.

[284] M. Javorka, B. Czippelova, Z. Turianikova, Z. Lazarova, I. Tonhajzerova, and L. Faes, "Causal analysis of short-term cardiovascular variability: state-dependent contribution of feedback and feedforward mechanisms," *Med. Biol. Eng. Comput.*, pp. 1–12, 2016.

[285] L. Faes, D. Marinazzo, F. Jurysta, and G. Nollo, "Linear and non-linear brain--heart and brain--brain interactions during sleep," *Physiol. Meas.*, vol. 36, no. 4, p. 683, 2015.

[286] L. Faes, G. Nollo, and K. H. Chon, "Assessment of granger causality by nonlinear model identification: Application to short-term cardiovascular variability," *Ann. Biomed. Eng.*, vol. 36, no. 3, pp. 381–395, 2008.

[287] A. Porta *et al.*, "Effect of age on complexity and causality of the cardiovascular control: Comparison between model-based and model-free approaches," *PLoS One*, vol. 9, no. 2, 2014.

[288] G. Nollo, L. Faes, A. Porta, R. Antolini, and F. Ravelli, "Exploring directionality in spontaneous heart period and systolic pressure variability interactions in humans: implications in the evaluation of baroreflex gain.," *Am. J. Physiol. Hear. Circ. Physiol.*, vol. 288, no. 4, pp. H1777-85, 2005.

[289] L. Faes, G. Nollo, and A. Porta, "Information domain approach to the investigation of cardio-vascular, cardio-pulmonary, and vasculo-pulmonary causal couplings," *Front. Physiol.*, vol. 2 NOV, no. November, pp. 1–13, 2011.

[290] M. Riedl, A. Suhrbier, H. Stepan, J. Kurths, and N. Wessel, "Short-term couplings of the cardiovascular system in pregnant women suffering from pre-eclampsia.," *Philos. Trans. R. Soc. A Math. Phys. Eng. Sci.*, vol. 368, no. 1918, pp. 2237–50, 2010.

[291] A. Porta *et al.*, "Cardiovascular control and time domain Granger causality:

insights from selective autonomic blockade," *Philos. Trans. R. Soc. A Math. Phys. Eng. Sci.*, vol. 371, no. 1997, p. 20120161, 2013.

[292] C. Juan-Cruz, C. Gómez, J. Poza, A. Fernández, and R. Hornero, "Assessment of effective connectivity in Alzheimer's disease using Granger causality," in *Converging clinical and engineering research on neurorehabilitation ii*, Springer, 2017, pp. 763–767.

[293] R. Coben and I. Mohammad-Rezazadeh, "Neural connectivity in epilepsy as measured by Granger causality," *Front. Hum. Neurosci.*, vol. 9, p. 194, 2015.

[294] M. Lee *et al.*, "Connectivity differences between consciousness and unconsciousness in non-rapid eye movement sleep: a TMS--EEG study," *Sci. Rep.*, vol. 9, no. 1, p. 5175, 2019.

[295] N. Nicolaou and J. Georgiou, "Neural Network--Based Classification of Anesthesia/Awareness Using Granger Causality Features," *Clin. EEG Neurosci.*, vol. 45, no. 2, pp. 77–88, 2014.

[296] N. Nicolaou, S. Hourris, P. Alexandrou, and J. Georgiou, "EEG-based automatic classification of 'awake'versus 'anesthetized'state in general anesthesia using Granger causality," *PLoS One*, vol. 7, no. 3, p. e33869, 2012.

[297] A. B. Barrett *et al.*, "Granger causality analysis of steady-state electroencephalographic signals during propofol-induced anaesthesia," *PLoS One*, vol. 7, no. 1, p. e29072, 2012.

[298] A. Duggento *et al.*, "Globally conditioned Granger causality in brain--brain and brain--heart interactions: a combined heart rate variability/ultra-high-field (7 T) functional magnetic resonance imaging study," *Philos. Trans. R. Soc. A Math. Phys. Eng. Sci.*, vol. 374, no. 2067, p. 20150185, 2016.

[299] A. Greco, L. Faes, V. Catrambone, R. Barbieri, E. P. Scilingo, and G. Valenza, "Lateralization of Directional Brain-Heart Information Transfer during Visual Emotional Elicitation," *Am. J. Physiol. Integr. Comp. Physiol.*, 2019.

[300] D.-O. Won, B.-R. Lee, K.-S. Seo, H. J. Kim, and S.-W. Lee, "Alteration of coupling between brain and heart induced by sedation with propofol and midazolam," *PLoS One*, vol. 14, no. 7, p. e0219238, 2019.

[301] G. Schwarz, "Estimating the dimension of a model," *Ann. Stat.*, vol. 6, no. 2, pp. 461–464, 1978.

[302] H. Akaike, “A new look at the statistical model identification,” in *Selected Papers of Hirotugu Akaike*, Springer, 1974, pp. 215–222.

[303] P. Zhang, “On the convergence rate of model selection criteria,” *Commun. Stat. Methods*, vol. 22, no. 10, pp. 2765–2775, 1993.

[304] N. Nicolaou and J. Georgiou, “Autoregressive model order estimation criteria for monitoring awareness during anaesthesia,” in *IFIP International Conference on Artificial Intelligence Applications and Innovations*, 2013, pp. 71–80.

[305] F. J. Fabozzi, S. M. Focardi, S. T. Rachev, and B. G. Arshanapalli, *The basics of financial econometrics: Tools, concepts, and asset management applications*. John Wiley & Sons, 2014.

[306] F. Jurysta *et al.*, “A study of the dynamic interactions between sleep EEG and heart rate variability in healthy young men,” *Clin. Neurophysiol.*, vol. 114, no. 11, pp. 2146–2155, 2003.

[307] F. Jurysta *et al.*, “The link between cardiac autonomic activity and sleep delta power is altered in men with sleep apnea-hypopnea syndrome,” *Am. J. Physiol. Integr. Comp. Physiol.*, vol. 291, no. 4, pp. R1165--R1171, 2006.

[308] Z. Chen, P. Venkat, D. Seyfried, M. Chopp, T. Yan, and J. Chen, “Brain--heart interaction: cardiac complications after stroke,” *Circ. Res.*, vol. 121, no. 4, pp. 451–468, 2017.

[309] N. Scherbakov and W. Doehner, “Heart--brain Interactions in Heart Failure,” *Card. Fail. Rev.*, vol. 4, no. 2, p. 87, 2018.

[310] M. M. Sahinovic, D. J. Eleveld, T. Miyabe-Nishiwaki, M. Struys, and A. R. Absalom, “Pharmacokinetics and pharmacodynamics of propofol: changes in patients with frontal brain tumours,” *BJA Br. J. Anaesth.*, vol. 118, no. 6, pp. 901–909, 2017.

[311] H. M. Jones and K. Rowland-Yeo, “Basic concepts in physiologically based pharmacokinetic modeling in drug discovery and development,” *CPT pharmacometrics Syst. Pharmacol.*, vol. 2, no. 8, pp. 1–12, 2013.

[312] R. N. Upton, G. L. Ludbrook, C. Grant, and A. M. Martinez, “Cardiac output is a determinant of the initial concentrations of propofol after short-infusion administration,” *Anesth. Analg.*, vol. 89, no. 3, p. 545, 1999.

[313] Y. U. Adachi, M. Satomoto, H. Higuchi, and K. Watanabe, “The determinants of propofol induction time in anesthesia,” *Korean J. Anesthesiol.*, vol. 65, no. 2, p. 121, 2013.

[314] D. Copot, R. De Keyser, and C. Ionescu, “Drug interaction between

propofol and remifentanil in individualised drug delivery systems," *IFAC-PapersOnLine*, vol. 48, no. 20, pp. 64–69, 2015.

[315] S. E. Kern, G. Xie, J. L. White, and T. D. Egan, "A response surface analysis of propofol--remifentanil pharmacodynamic interaction in volunteers," *Anesthesiol. J. Am. Soc. Anesthesiol.*, vol. 100, no. 6, pp. 1373–1381, 2004.

[316] J. Kortelainen, M. Koskinen, S. Mustola, and T. Seppänen, "Effects of remifentanil on the spectrum and quantitative parameters of electroencephalogram in propofol anesthesia," *Anesthesiol. J. Am. Soc. Anesthesiol.*, vol. 111, no. 3, pp. 574–583, 2009.

[317] Y. Jo *et al.*, "Sudden Bispectral Index Reduction and Suppression Ratio Increase Associated with Bradycardia in a Patient Undergoing Breast Conserving Surgery," *J. Neurocritical Care*, vol. 11, no. 1, pp. 39–42, 2018.

[318] T. Ishiyama, T. Oguchi, T. Iijima, T. Matsukawa, S. Kashimoto, and T. Kumazawa, "Ephedrine, but not phenylephrine, increases bispectral index values during combined general and epidural anesthesia," *Anesth. Analg.*, vol. 97, no. 3, pp. 780–784, 2003.

[319] N. Zorko, D. Mekiš, and M. Kamenik, "The influence of the Trendelenburg position on haemodynamics: comparison of anaesthetized patients with ischaemic heart disease and healthy volunteers," *J. Int. Med. Res.*, vol. 39, no. 3, pp. 1084–1089, 2011.

[320] S. Fakhari, E. Bilehjani, H. Farzin, H. Pourfathi, and M. Chalabianlou, "The effect of passive leg-raising maneuver on hemodynamic stability during anesthesia induction for adult cardiac surgery," *Integr. Blood Press. Control*, vol. 11, p. 57, 2018.

[321] S. Mallick, A. Das, S. Dutta, S. Chattopadhyay, T. Das, and R. Banu, "A Prospective, double-blinded randomized controlled study comparing two different Trendelenburg tilts in laparoscopically assisted vaginal hysterectomy positioning," *J. Nat. Sci. Biol. Med.*, vol. 6, no. 1, p. 153, 2015.